# THERMODYNAMIC AND MATERIAL PROPERTIES OF REVERSIBLE CLUSTER FORMATION - APPLICATION TO CONCENTRATED PROTEIN SOLUTIONS

by

P. Douglas Godfrin

A dissertation submitted to the Faculty of the University of Delaware in partial fulfillment of the requirements for the degree of Doctor of Philosophy in Chemical Engineering

Summer 2015

© 2015 P. Douglas Godfrin
All Rights Reserved

ProQuest Number: 3730189

All rights reserved

INFORMATION TO ALL USERS
The quality of this reproduction is dependent upon the quality of the copy submitted.

In the unlikely event that the author did not send a complete manuscript
and there are missing pages, these will be noted. Also, if material had to be removed,
a note will indicate the deletion.

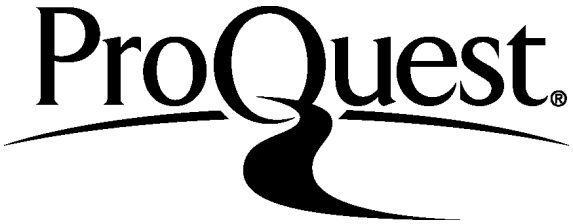

ProQuest 3730189

Published by ProQuest LLC (2015). Copyright of the Dissertation is held by the Author.

All rights reserved.
This work is protected against unauthorized copying under Title 17, United States Code
Microform Edition © ProQuest LLC.

ProQuest LLC.
789 East Eisenhower Parkway
P.O. Box 1346
Ann Arbor, MI 48106 - 1346

# THERMODYNAMIC AND MATERIAL PROPERTIES OF REVERSIBLE CLUSTER FORMATION - APPLICATION TO CONCENTRATED PROTEIN SOLUTIONS

by

P. Douglas Godfrin

Approved: _____

Abraham M. Lenhoff, Ph.D.
Chair of the Department of Chemical and Biomolecular Engineering

Approved: _____

Babatunde A. Ogunnaike, Ph.D.
Dean of the College of Engineering

Approved: _____

James G. Richards, Ph.D.
Vice Provost for Graduate and Professional Education

I certify that I have read this dissertation and that in my opinion it meets the academic and professional standard required by the University as a dissertation for the degree of Doctor of Philosophy.

Signed: _____

Norman J. Wagner, Ph.D.
Professor in charge of dissertation

I certify that I have read this dissertation and that in my opinion it meets the academic and professional standard required by the University as a dissertation for the degree of Doctor of Philosophy.

Signed: _____

Yun Liu, Ph.D.
Professor in charge of dissertation

I certify that I have read this dissertation and that in my opinion it meets the academic and professional standard required by the University as a dissertation for the degree of Doctor of Philosophy.

Signed: _____

Eric M. Furst, Ph.D.
Member of dissertation committee

I certify that I have read this dissertation and that in my opinion it meets the academic and professional standard required by the University as a dissertation for the degree of Doctor of Philosophy.

Signed: _____

Christopher J. Roberts, Ph.D.
Member of dissertation committee

I certify that I have read this dissertation and that in my opinion it meets the academic and professional standard required by the University as a dissertation for the degree of Doctor of Philosophy.

Signed: _____

Paul Butler, Ph.D.
Member of dissertation committee

## ACKNOWLEDGEMENTS

Completing this dissertation is an achievement of a life-long goal of mine. As with any wish, my desire to become a Ph.D. is a bit selfish in that it expected much of those around me with little reward other than my satisfaction. For those efforts, I hope that my humble recognition of their immense influence on my success can provide some form of compensation.

First, I'd like to thank my advisors Norm Wagner and Yun Liu for their unparalleled knowledge and expertise of seemingly every relevant area of soft matter science. Similar to wave phenomena, there always exists a possibility of destructive interference when multiple personal styles of scientific thought and study are combined. However, I believe that Norm and Yun provided an incredibly constructive environment (interference is far too inappropriate here) from which I have benefited immensely. Norm's energetic and enthusiastic approach to scientific exploration, as well as social interests, is contagious and one I hope to emulate. I'm also incredibly fortunate and grateful to have been able to travel around the world with Norm from California to Iceland, Scotland and France. Yun's tireless and meticulous pursuit of fundamental physics is both impressive and rewarding to be associated with. Having a fellow New England sports fan to celebrate and commiserate with was just an added bonus. In the end, their guidance and input has been invaluable to my success in writing this dissertation and in my development as a scientist.

My education started a (relatively) long time ago now and I owe those who helped prepare me for the rigor of my doctoral research. Starting in my home town of North Smithfield, RI, the diversity of teaching styles I encountered through the public schools helped me identify the ways I learn best. I am also proud to be an alumni of Chemical Engineering at the University of Virginia, where I owe a large part of my

success to my classmates and the passionate and insightful professors I was fortunate to learn from.

I also owe a great deal of gratitude to my friends, throughout all these stages, who have been a source of entertainment and motivation. Thanks to them, I have been able to "work to live" rather than "live to work" by distracting me when I'm focused to the point of being oblivious of the world.

Finally, to my family, I want to express all of my love and thanks for their patience and support. I wandered into uncharted territory by pursuing a doctorate degree and my family encouraged me to continue my education. My two brothers, Nate and Mike, have always been a great source of love and fun and have been a bigger component of my happiness and success than they may realize. Thank you to my parents, Kim and Phil, for supporting my path away from Rhode Island, and most of my family, to follow my passion. I love you both and I am constantly reminded, directly and indirectly, of how much that love is reciprocated. As a result of leaving, though, I met my fiancée Meghan while an undergrad at UVa. She is a source of comfort, pride and motivation and helps me reach my fullest potential. She has been very patient and supportive of my long road to completing the Ph.D. degree and I thank and love her immensely for that and so much more.

## TABLE OF CONTENTS

**LIST OF TABLES** . . . . . **xii**
**LIST OF FIGURES** . . . . . **xiii**
**ABSTRACT** . . . . . **xxx**

**Chapter**

**1 INTRODUCTION** . . . . . **1**

1.1 Colloidal Particles as Engineered Materials . . . . . 1
1.2 The Chemistry of Colloidal Interactions . . . . . 4
1.3 Interactions and Phase Behavior . . . . . 8
1.4 Solution Viscosity - The Influence of Interactions . . . . . 12
1.5 Landmark Observations . . . . . 15

1.5.1 Cluster Formation Fundamentals . . . . . 15
1.5.2 Cluster Configuration and Solution Microstructure . . . . . 17
1.5.3 Cluster Dynamics . . . . . 19
1.5.4 Experimental Identification . . . . . 22
1.5.5 Clusters in the Biopharmaceutical Industry . . . . . 23

1.6 Dissertation Goals and Outline . . . . . 24

REFERENCES . . . . . **27**

**2 METHODOLOGY: THEORY, SIMULATIONS, AND EXPERIMENTS** . . . . . **39**

2.1 Background . . . . . 39
2.2 Thermodynamics of Colloidal Systems . . . . . 39

2.2.1 Interaction Potentials . . . . . 41
2.2.2 Structural Functions . . . . . 42

2.2.3 Integral Equation Theory . . . . . 46

2.3 Monte Carlo Simulations . . . . . 47
2.4 Small Angle Neutron Scattering . . . . . 48
2.5 Neutron Spin Echo . . . . . 50
2.6 Dynamic Light Scattering . . . . . 52
2.7 Rheology . . . . . 53
2.8 Materials and Sample Preparation . . . . . 55

REFERENCES . . . . . **56**

**3 INTERMEDIATE RANGE ORDER AND OTHER STRUCTURAL FEATURES OF COMPETING INTERACTIONS 60**

3.1 Introduction . . . . . 60
3.2 Methodology . . . . . 61

3.2.1 Simulation Details . . . . . 61
3.2.2 Phase Transition Calculations . . . . . 63
3.2.3 Decomposing the Structure Factor . . . . . 65

3.3 Self-consistency and Implications of Defining a Cut-off Distance . . . 66
3.4 State Definitions . . . . . 69
3.5 Phase Behavior . . . . . 72
3.6 Cut-off Distance as a Probe of Solution Structure . . . . . 75

3.6.1 Monomer Dominated IRO Peak . . . . . 75
3.6.2 Analyzing Moments of the Cluster Size Distribution . . . . . 76
3.6.3 Distinguishing Percolated States . . . . . 78

3.7 Decomposing Contributions to the Solution Structure . . . . . 83
3.8 Conclusions . . . . . 88

REFERENCES . . . . . **90**

**4 GENERALIZED PHASE BEHAVIOR AND PROPERTIES OF CLUSTER FLUIDS . . . . . 96**

4.1 Introduction . . . . . 96
4.2 Simulation and Analysis Methods . . . . . 97

4.2.1 Simulation Protocol . . . . . 97
4.2.2 Thermodynamics of a Reference Attractive System . . . . . 98

4.2.3 State Definitions . . . 101

4.3 Results and Discussion . . . 103

4.3.1 Corresponding States of the Reference Potentials . . . 103
4.3.2 Generalized Cluster State Diagram . . . 107
4.3.3 IRO Peaks in Clustered States . . . 111
4.3.4 Internal Cluster Structure in Clustered Fluids . . . 112
4.3.5 Role of Long-Range Repulsion . . . 118

4.4 Conclusions . . . 123

REFERENCES . . . **125**

**5 A MODEL PROTEIN WITH COMPETING INTERACTIONS TO STUDY THEIR EFFECT ON DYNAMICS AND VISCOSITY 132**

5.1 Introduction . . . 132
5.2 Materials and Methods . . . 134

5.2.1 Sample Preparation . . . 134
5.2.2 Small Angle Neutron and X-ray Scattering . . . 137
5.2.3 Simulation Protocol . . . 140
5.2.4 Neutron Spin Echo . . . 140
5.2.5 Microrheology . . . 142

5.3 Low Concentration Structure and Dynamics . . . 142
5.4 High Concentration Interactions, Structure and Dynamics . . . 147

5.4.1 SANS Experiments and Analysis . . . 147
5.4.2 NSE Experiments and Analysis . . . 158

5.5 IRO Structure and Glassy Dynamics at High Concentration . . . 165
5.6 Testing the Representation of Lysozyme Viscosity by Colloidal Models 179
5.7 Viscosity Predictions . . . 186
5.8 Effective Cluster Properties from a New SALR Viscosity Model . . . 189
5.9 Conclusions . . . 192

REFERENCES . . . **194**

**6 EFFECT OF SMALL LONG-LIVED CLUSTERS ON THE VISCOSITY OF CONCENTRATED MONOCLONAL**

**ANTIBODY FORMULATIONS** . . . . . **206**

6.1 Introduction . . . . . 206
6.2 Materials and Methods . . . . . 208
6.3 Influence of mAb Association on Solution Viscosity . . . . . 210

6.3.1 Solution Viscosity . . . . . 210
6.3.2 Small Angle Neutron Scattering . . . . . 212
6.3.3 Low Concentration Structure and Dynamics . . . . . 216
6.3.4 Structure at High Concentration . . . . . 218
6.3.5 Dynamics at High Concentration . . . . . 220
6.3.6 Cluster-Viscosity Correlation . . . . . 227

6.4 Influence of Solvent . . . . . 230
6.5 Conclusions . . . . . 234

REFERENCES . . . . . **236**

**7 VISCOUS RESPONSE OF LARGE TRANSIENT CLUSTERS IN CONCENTRATED MONOCLONAL ANTIBODY FORMULATIONS** . . . . . **241**

7.1 Introduction . . . . . 241
7.2 Materials and Experimental Techniques . . . . . 244

7.2.1 Materials . . . . . 244
7.2.2 Small Angle Neutron Scattering . . . . . 244
7.2.3 Form Factor Modeling . . . . . 246
7.2.4 Neutron Spin Echo . . . . . 252
7.2.5 Dynamic Light Scattering . . . . . 252
7.2.6 Rheology . . . . . 253

7.3 Results . . . . . 254

7.3.1 Low Concentration Behavior . . . . . 257
7.3.2 High Concentration Behavior . . . . . 260

7.4 Discussion . . . . . 266

7.4.1 Hydrodynamic Effects . . . . . 267
7.4.2 Shear Thinning and Effective Structure Size . . . . . 271
7.4.3 Effective mAb-mAb Interactions and Concentrated Solution Microstructure . . . . . 275

7.4.4 Microscopic Contributions to the Viscosity . . . . . 280
7.4.5 Comparison of mAb1, mAb2, and mAb3 . . . . . 287

7.5 Conclusions . . . . . 290

REFERENCES . . . . . **291**

**8 CONCLUSIONS AND FUTURE WORK . . . . . 298**

8.1 Conclusions . . . . . 298
8.2 Future Work . . . . . 300

8.2.1 A Model One-Component Cluster Forming System . . . . . 301
8.2.2 Developing More Accurate Models of Cluster Interactions, Growth, and Viscosity . . . . . 303
8.2.3 Representing Colloidal Shape and Interaction Anisotropy by the Reference Interaction Site Model . . . . . 306

REFERENCES . . . . . **309**

**Appendix**

**A MICROMECHANICAL MODEL OF CLUSTER FLUID DYNAMICS AND VISCOSITY . . . . . 312**

A.1 Introduction . . . . . 312
A.2 Modeling the Effect of Competing Interactions on the Dynamics . . . 314
A.3 Modeling the Effect of Competing Interactions on the Viscosity . . . 319
A.4 Cluster-Cluster Interactions . . . . . 321

REFERENCES . . . . . **325**

## LIST OF TABLES


4.1 The inverse range of attraction, inverse range of repulsion, relative strength of repulsion to attraction, and cut-off distance are provided for all HSDY ($z_1$, $z_2$, $\lambda$, $r_c$) and LJY ($\alpha$, $1/\xi$, $A$, $r_c$) potentials used in this chapter. . . . . 100

5.1 Radii of gyration extracted from SAXS experiments at low lysozyme concentration without salt for both $H_2O$ and $D_2O$ as solvents. . . . 144

5.2 A compilation of parameters determined from fits to the SANS data at several values of $\phi$ and $T$, including the fitted volume fraction ($\phi_{fit}$), strength of attraction and repulsion ($K_1$ and $K_2$, respectively), range of attraction and repulsion ($z_1$ and $z_2$, respectively), and neutron SLD contrast $(\Delta\rho)^2$. The Baxter parameter ($\tau_B$), representing the effective strength of attraction, calculated from each combination of potential parameters is provided for each solution condition (to be discussed later). . . . . 148

5.3 Estimates of $D_{short}/D_{long}$ and shear thinning shear rate from DLS results. . . . . 172

7.1 A compilation of apparent molecular weights and standard deviations ($\sigma$), determined from SANS data, at low mAb3 concentrations under each set of temperature and salt conditions studied. . . . . 258

7.2 All fitting parameters extracted from fits to the SANS patterns in Fig. 7.20 are compiled together for each protein concentration (mg/mL) and temperature at both salt conditions. The table includes the strength and range of interactions, protein concentration, effective radius and extracted volume fraction. . . . . 277

## LIST OF FIGURES


1.1 A schematic representation of the hierarchical relationship between microscopic and macroscopic properties used to engineer materials. 2

1.2 (a) Interaction potentials of HS (black solid line), short range attraction (red dashed line) and long range attraction (blue dotted line) are plotted together for comparison. Representations of the phase behavior resulting from the corresponding potentials in (a) are plotted for (b) hard sphere, (c) short range attractive and (d) long range attractive fluids. Letters distinguish the type of phase in each region of the diagrams. The dashed line in (d) represents the triple point (gas-liquid-solid coexistence). . . . . 9

1.3 (a) Four SALR interaction potentials are plotted together with the same range and strength of attraction but varying range and strength of repulsion. (b) The configuration energy per particle is plotted for each of the potentials in (a) with the corresponding colors using simulation results form [81] (symbols) and new numerical calculations (lines) of close-packed spherical configurations, an example of which is shown in the inset. . . . . 16

1.4 The difference in transient (#1), dynamic (#2) and permanent (#3) clusters are distinguished according to the time scale of their dynamic correlations. Though structurally correlated, cluster #1 is never dynamically correlated while cluster #2 diffused together for a finite time and cluster #3 moves collectively for an extended time period. 20

1.5 The structure factor of an SALR system and a HS system are compared for a system at $\phi = 0.15$. . . . . 22

2.1 Two functional representations of an SALR potential, the HSDY and LJY potentials, are compared. . . . . 42

2.2 A characteristic structure factor (left) and pair distribution function (right) for a hard sphere fluid are shown with a physical representation. . . . . 43

2.3 The structure factors of colloidal systems with potentials including HS (black dashed line), attractive (red dash-dot-dot line), repulsive (blue dotted line) and SALR (green solid line) interactions are compared at the same volume fraction. . . . . 45

2.4 An ideal configuration of an NSE spectrometer. The neutron beam enters the first coil and passes through a spin ($\pi$) flipper before interacting with the sample. Scattered neutrons then pass through the second coil before being analyzed and detected on the two-dimensional detector. . . . . 51

2.5 The (A) cone and plate, (B) couette, and (C) capillary viscometer geometries used during rheological measurements in this work are depicted with their characteristic parameters. . . . . 54

3.1 The hard sphere double Yukawa (HSDY) potential, black line, used throughout this chapter ("full HSDY") is plotted with the attractive component of the potential, red dashed line ("attractive HSDY"), used to estimate phase transitions of a purely attractive reference system in order to provide context to the HSDY state points. . . . 64

3.2 Cluster size distributions, $N(s)$, calculated for a hard sphere fluid at a volume fraction of 0.15 using a range of cut-off distances. The effect of this distance defining connectivity on the apparent distribution of cluster sizes is significant. . . . . 67

3.3 A comparison of $N(s)$ resulting from three different cut-off distances for three states points to be discussed in more detail later: (a) state B, (b) state C, and (c) state E. Filled points are calculations from HSDY simulations while lines are HS results. . . . . 69

3.4 Cluster size distributions, N(s), are plotted together for each of the six state points studied, which fall into four categories of states: dispersed fluid (states A and B), clustered fluid (state C), cluster percolated (state D), and random percolated (states E and F). . . 70

3.5 The phase diagram shows the relative location of six state points of a HSDY fluid with $z_1 = 10$, $z_2 = 0.5$, and $\lambda = 0.1$. The state points represent dispersed fluid systems (diamonds), clustered systems (square), cluster percolated systems (circle), and "randomly" percolated systems (triangles). The reference attractive potential, outlined in the text, is used to estimate the binodal (grey solid line) and percolation transition (grey dotted line). . . . . 73

3.6 The $S(q)$ (open dots) and contribution of cluster-cluster correlations $S_{CC}(q)$ (filled dots) are shown for states B, E, and F (all at $T^* = 0.46$). $S(q)$ results are compared with IET calculations (solid lines). For clarity, simulation and IET results are shifted vertically for states B and E by a value of 1.5 and 0.5, respectively. . . . . 74

3.7 The dependence of the fraction of particles contained in clusters $X_{clusters}$ on $r_c$ for state A (open diamonds) and state B (filled diamonds). . . . . 75

3.8 (a) Comparison of $S(q)$ for state A (dotted line) and state B (solid line) and their corresponding partial structure factor contributions (triangles and circles, respectively) for connectivity defined by $r_c = 1.035$. (b) The magnitude of $S(q)$, $S_{MM}(q)$, and $S_{CC}(q)$ for state A relative to state B as a function of $q$-value. . . . . 77

3.9 The product of the average and skewness of the cluster size distribution are plotted as a function of cut-off distance for (a) HS fluids at three volume fractions and (b) each of the six HSDY state points studied here. The trend in this parameter with $r_c$ appears to be a distinguishing feature of clustered states. . . . . 78

3.10 The cluster size distribution for three values of $r_c$ ( 1.005, 1.035, and 1.2424) for (a) state D and (b) state E. . . . . 79

3.11 The $g_{CC}(r)$ as well as the intra-cluster and inter-cluster components are shown for cut-off distances of (a) 1.005, (b) 1.035, and (c) 1.2424 for state D. The snapshots (d-f) are of a characteristic configuration with the corresponding $r_c$ of the plot above and show particles within a given cluster as the same color. . . . . 80

3.12 The same details as given in Fig. 3.11 for percolated state E. . . . . 81

3.13 The relative magnitude of the IRO peak compared to its maximum value as a function of the cut-off distance. For comparison, the data are plotted relative to the cut-off distance at which 50% of the sampled configurations contain a percolated cluster. . . . . 82

3.14 Structure factors and the three partial structure factor contributions are shown for (a) state A, (b) state B, (c) state C, (d) state D, (e) state E, and (f) state F. The diversity of microstructures that produce an IRO peak is direct evidence of the inaccuracy in using it as an indication of cluster formation. . . . . 85

3.15 IRO peak magnitudes are shown for state points along the two isotherms studied. Trend in IRO peak height with volume fraction are distinctly different when below the critical reduced temperature ($T^* = 0.25$) compared to systems outside the two phase region of the reference attractive system ($T^* = 0.46$). . . . . 86

3.16 The average number of neighbors, IRO peak height $S(q_c)$ and IRO peak location $q_c$ are given for all six HSDY states studied. . . . . 87

4.1 The HSDY1 (solid line) and LJY1 (dashed line) potentials from Table 4.1 are shown as representative of each function form of interaction potential. The attractive component of the potential (dotted lines) is used as a reference potential. . . . . 99

4.2 Characteristic cluster size distributions used to define each state point are shown for each of the four states identified in SALR systems (specifically for potential HSDY1): dispersed, clustered, random percolated and cluster percolated states. . . . . 102

4.3 Interaction potentials are plotted for each condition in Table 4.1. Each has a different color and lines alternate between solid and dotted for clarity. . . . . 104

4.4 (a) The critical reduced temperature is plotted for HSDY (filled stars) and LJY (open stars) systems as a function of the effective range of attraction for a SW fluid with the same $\tau_B$ value $(1 + \delta)$. Also plotted are literature results for SW[24] (solid line) and Yukawa[34] (dotted line) fluids. (b) Two definitions of the effective range of attraction (dashed lines) for SW potentials are shown compared to potential LJY2 (solid line). Open stars in (a) correspond to the definition of $\delta$ with the same color in (b). . . . . 105

4.5 The Baxter parameters at the critical point of each HSDY (filled stars) and LJY (open stars) potential are plotted relative to the prediction from ELCS (dashed line)[33] as a function of the effective range of attraction. . . . . 106

4.6 The location of the IRO peak $q_c$ appears to be a universal (linear) function of an effective strength of attraction represented by $(T^*/T_c^*)(1 - B_{2c}^*)$. Diamonds are simulation results of new states studied in this chapter, triangles are from Ref. [40] and squares are from Ref. [3]. . . . . 107

4.7 (a) Binodals corresponding to a subset of the potentials studied in this chapter are plotted together. The inset shows the associated reference attractive potential of each binodal with the same line color and style. (b) Binodal lines of all reference attractive potential are normalized by their respective critical points and shown to overlap (except for HSDY5, LJY3, and LJY4 that are discussed in the text). 108

4.8 Normalizing several state diagrams according to ELCS,[33] a generalized phase diagram for clustered states is produced. New state points from this chapter are combined with literature results from Ref. [40], Ref. [32] and Ref. [7] (orange, dark cyan, and grey points, respectively). The color of each state point corresponds with the potential in Fig. 4.3 used in that simulation. Four distinct regions are found for dispersed (up-right), clustered (down-right), random percolated (criss-cross), and cluster percolated (vertical). . . . . 110

4.9 The magnitude of IRO peaks are plotted as a function of reduced volume fraction. All clustered and cluster percolated states lie above an apparent critical magnitude of $\sim 2.7$ (dashed line) separating them from monomer and monomer percolated states below this value. Filled symbols are from the new simulations performed here, open symbols are from Ref. [7], and half-filled symbols are from Ref. [32]. 112

4.10 Average coordination number $\langle N \rangle$ is plotted as a function of average cluster size $\langle s \rangle$. The minimum value of $\langle N \rangle = 2.4$ (dashed line) for rigidity percolated[21] separates dispersed fluids from all other states. Clustered and cluster percolated states are further distinguished by Eqn. 4.7 (solid line). Open symbols are taken from Ref. [7]. . . . . 114

4.11 (a) The dependence of $\langle N \rangle$ on cluster size is plotted for spherical clusters with four different crystal lattices and Eq. 4.7. The bulk values of $\langle N \rangle$ for each crystal structure are also provided. (b) Normalizing $\langle N \rangle$ of the four crystal lattices by Eq. 4.7 produces constant values, which appear to increase linearly with the crystal volume fraction ($\phi_{crys}$) relative to the FCC lattice ($\phi_{crit}$). The equivalence point of the coordination numbers provides an estimate of the minimum volume fraction needed to form clustered states ($0.384 \pm 0.035$). . . . . 115

4.12 The HSDY1 potential is plotted with a variety of $z_2$ values with a fixed value of $B^*_{2c}$. The inset highlights the shift in the magnitude and position of maximum energy of $U(r)/kT$. . . . . 118

4.13 To maintain a constant value of $B_{2c}^*$ for HSDY1, the value of (a) $z_1$ and (b) $\lambda$ shift as a function $z_2$. The shift in the maximum energy is also plotted in (a). Clustered (squares) and dispersed (diamonds) states at ($T^* = 0.25$, $\phi = 0.05$) are plotted in (b) relative to the conditions at which spherical clusters with close packed structures can form clusters as described in the text (dashed lines). . . . . 120

4.14 The (a) magnitude of the IRO peak and (b) average number of neighbors for clustered (squares) and dispersed (diamonds) fluids at varying values of $z_2$ (and $\langle s \rangle$) for the HSDY1 potential. Clustered and dispersed fluids are distinguished in (a) by $S(q_c) = 2.7$ (solid line) and in (b) by $\langle N \rangle = 2.4$ (dashed line). . . . . 122

5.1 Estimates of protein volume fraction, $\phi$, as a function of lysozyme weight fraction, $X_L$, using definitions as discussed in the main text of a "hydrated" protein $r_{hydr}$ and "dry" protein with experimental intrinsic volume $r_{dry}$, average crystal size $r_{avg}$ and hydrodynamic DLS size $r_{DLS}$. . . . . 136

5.2 Scattering intensities (with arbitrary units, a.u.) obtained by SAXS are plotted for several lysozyme samples. The effect of solvent conditions are compared for samples with 0 mg/mL (open symbols) and 8.7 mg/mL (filled symbols) sodium chloride at a protein concentration of 4 mg/mL in $D_2O$ (triangles) and $H_2O$ (squares). A sample at 1 mg/mL (circles) in $H_2O$ is provided to represent the form factor. . . . . 143

5.3 Structures factors of low concentration lysozyme samples in $H_2O$ (open symbols) and $D_2O$ (half-filled symbols) are compared at 25°$C$ for several protein concentrations. . . . . 145

5.4 The structure factor of a 50 mg/mL lysozyme sample at 25°$C$ in $H_2O$ and $D_2O$ obtained by SAXS and SANS, respectively, are plotted together to demonstrate the similarity of results in both solvents and by both experimental techniques. . . . . 146

5.5 The absolute scattering intensity, $I(q)$, is plotted for several 1-D SANS profiles (symbols) relative to the best fits (lines) using the HSDY potential at 5°$C$ (blue), 25°$C$ (green) and 50°$C$ (red). All data sets except that at ($\phi = 0.0399$, $T = 25°C$) are shifted for clarity. . 149

5.6 The neutron SLD contrast determined from fits to the SANS data is plotted as a function of fitted lysozyme volume fraction for $T = 5°C$ (blue), $T = 25°C$ (green) and $T = 50°C$ (red). Estimated values (line) assuming roughly 16% of hydrogen-deuterium exchange are provided for comparison. . . . . 150

5.7 Structure factors, $S(q)$, obtained by normalizing experimental $I(q)$ data (filled symbols) are plotted relative to best fits (lines) and MC simulation results using the extracted potential parameters (open symbols) for protein volume fractions labeled at the left of each row at $5°C$ (left column), $25°C$ (middle column) and $50°C$ (right column). 151

5.8 Interaction potentials extracted from best fits to SANS data at (a) $5°C$, (b) $25°C$ and (c) $50°C$ are plotted for a range of protein volume fractions. . . . . 153

5.9 Cluster size distributions, $N(s)$, determined from MC simulations are plotted as a function of cluster size, $s$, at $5°C$ (blue circles), $25°C$ (green triangles) and $50°C$ (red squares) for four volume fractions labeled in each panel. The lines are best fits of $N(s)$ using a Weibull distribution function discussed in the text. . . . . 154

5.10 Empirical fits (lines) to the volume fraction dependence of the HSDY parameters (symbols) for (a) attraction strength, $K_1$, (b) repulsion strength, $K_2$ and (c) repulsion range, $z_2$ extracted from fits to SANS data. . . . . 157

5.11 The ISF (symbols) at several $q$-values are shown for a lysozyme sample at $\phi = 0.2981$ and $T = 25°C$ with the best fits (lines) using a single exponential function up to only 25 ns to remain within the short-time limit. . . . . 159

5.12 The $q$-dependence of the collective diffusion coefficient, extracted from fits to the ISF obtained by NSE, is plotted for several lysozyme samples at large volume fractions for $5°C$, $25°C$ and $50°C$. The lines represent the average value determined in the high-$q$ asymptotic limit to estimate $D_S/D_0$. . . . . 160

5.13 (a) Short-time self diffusion coefficients (symbols) extracted from the high-$q$ asymptotic limit shown in Fig. 5.12 are plotted relative to HS (solid line) and CS (dotted line) estimates as well as empirical fits (dashed lines). (b) Effective hydrodynamic radii, $R_h/R_0$, estimated from values of $D_S/D_0$ are plotted as a function of $\phi$ for each of the three temperatures studied. . . . . 161

5.14 The experimental ISF (symbols) of lysozyme samples at several conditions and $q$-values are plotted with best fits (lines) using a double exponential function over the full correlation time range up to 50 ns. . . . . 162

5.15 Empirical fits (lines) to the volume fraction dependence of the normalized (a) monomer and (b) cluster diffusion coefficients and (c) the scaling factor of clusters (symbols) determined from the high-$q$ asymptotic limit of each parameter extracted from fits to NSE data. 163

5.16 Comparison of effective, normalized short-time self diffusion coefficients determined from fits to the ISF using a single exponential, $D_{1ex}$, and a double exponential, $D_{2ex}$. Both methods of fitting show great agreement, but the weighted combination of two coefficients in the double exponential method produces large uncertainties (error bars). . . . . 165

5.17 Viscosities (symbols) are plotted as a function of shear rate at several temperatures for (a) $\phi = 0.2070$, (b) $\phi = 0.2509$ and (c) $\phi = 0.3448$ along with fits of the zero shear viscosity (lines). (d) Specific viscosities in the zero shear limit (filled circles) are plotted as a function of protein volume fraction at several temperatures relative to HS estimates according to the Brady model (open squares) and RMW-MCT model (line). . . . . 167

5.18 The product of relative viscosity and short time self diffusion (symbols) is plotted similar to a Generalized Stokes-Einstein-Sutherland relation as a function of volume fraction relative to HS expectations (dashed line). . . . . 169

5.19 Comparison of long-time self diffusion estimated by the reciprocal of the experimentally determined zero-shear viscosity (y-axis) and MCT scaling of experimental $D_S/D_0$ from NSE (x-axis). The black line is the equivalence point. The inset shows the same plot on a linear scale to clarify the correlation at low $\phi$ (high $D_L/D_0$). . . . . 171

5.20 The mean squared displacement of all lysozyme solutions at short times determined from NSE (filled symbols) and long times determined from viscosity measurements (open symbols) are plotted on a normalized time scale relative to trends expected for four types of dynamic states determined previously.[47] Lysozyme in all solution conditions appears diffusive at $t < \tau$, but deviates from fluid-like behavior at $t > \tau$ at elevated $\phi$ and low $T$. . . . . 173

5.21 (a) The specific viscosity of lysozyme is plotted as a function of short-time (filled symbols) and long-time (open symbols) self diffusivity, relative to calculations for HS fluids (solid and dotted lines, respectively). The inset provides examples of fits to the ISF. (b) Structure factors are plotted for several state points, indicating the formation of IRO peaks. . . . . 175

5.22 Structure factors are plotted for samples with volume fractions $\phi = 0.1215$ (triangles), $\phi = 0.2070$ (diamonds) and $\phi = 0.2509$ (circles) at $T = 5°C$ (blue), $T = 25°C$ (green) and $T = 50°C$ (red) to highlight shifts in the IRO peak magnitude. . . . . 176

5.23 Lysozyme state points are plotted on the AHS phase diagram (open symbols represent estimates of $\tau_B$ for state points that could not be fit by IET) along with the percolation transition of an SALR system with repulsion representative of lysozyme interactions (gray dotted line). Shaded regions represent dispersed fluids (blue vertical), random percolated (magenta diagonal) and a new local glassy state determined from MSD data (black criss-cross). . . . . 178

5.24 Lysozyme zero-shear vicsosity (symbols) is plotted for three temperatures as a function of volume fraction according to (a) the dry definition and (b) the hydrated definition. Best fits of HS estimates using the Eilers (solid line), Maron-Pierce (dashed line) and Mooney (dotted lines) equations are also provided. . . . . 181

5.25 Lysozyme zero-shear vicsosity (symbols) is plotted for three temperatures as a function of volume fraction according to (a) the dry definition and (b) the hydrated definition. Best fits using the KW attractive model (lines) are provided using a single value of $\tau_B$ for a given temperature provided in the legend, where HS indicates $\tau_B = \infty$. . . . . 182

5.26 (a) Experimental lysozyme diffusivity ("Full") is plotted relative to HS (black line) and CS (pink line) trends and estimates using the KW attractive model ("Att") with values of $\tau_B$ extracted from fits to SANS data. (b) Lysozyme viscosity data are normalized according to a weakly attractive model (symbols) and plotted relative to HS expectations (line), which should be identical if the viscosity was driven purely by attractive forces. . . . . 183

5.27 Combined contributions to the viscosity from the Brownian and Interaction terms determined from experimental results (symbols) are plotted relative to the HS estimate (line). Deviations above the HS line are indicative of predominantly repulsive contributions to increases in viscosity while points below the HS line represent attractive driven enhancements to the viscosity. . . . . 185

5.28 Values of (a) $X_{clus}$, (b) $D_{mon}$ and (c) $D_{clus}$ determined from simultaneously fitting the diffusivity parameters using the double exponential model fits to NSE data (discussed in the main text) are plotted for $T = 5°C$ (blue), $T = 25°C$ (green) and $T = 50°C$ (red). 187

5.29 Lysozyme viscosity data (symbols) are compared to estimates using the viscosity model (colored lines) developed in the Appendix by estimating cluster sizes using diffusion data as well as HS estimates (black line). . . . . 188

5.30 Values extracted from simultaneous fits to effective diffusion coefficients and viscosities of lysozyme are plotted as a function of $\phi$ for the density of clusters (lines and open squares), $\rho_c$, and cluster size (filled circles), $N$. . . . . 190

5.31 Zero-shear viscosity is plotted as a function of the estimated cluster size for three temperatures, indicating an apparent lack of universal relationship between these two parameters. . . . . 191

6.1 The viscosity of mAb1 (circles) and mAb2 (triangles) is plotted (a) as a function of protein concentration without added NaCl and (b) at 150 mg/mL antibody concentration as a function of added salt concentration. Measurements conducted at 5 $°C$ and 25 $°C$ are represented by blue and red symbols, respectively. . . . . 211

6.2 The reduced zero-shear viscosity of mAb1 (circles) and mAb2 (triangles) is plotted relative to hard sphere expectations (solid line) as a function of protein concentration without added NaCl (at $T = 25°C$). . . . . 212

6.3 (a) Absolute scattering intensity and (b) effective structure factors from SANS of mAb1 (circles) and mab2 (triangles) samples at 150 mg/mL with 0 mM (open symbols) and 150 mM (filled symbols) added NaCl. The form factor (open black triangles) in (a) is a 5 mg/mL sample. All data sets were studied at 25 $°C$. Only a fraction of all points in each data set are included for clarity. . . . . 213

6.4 SANS 1-D scattering profiles of (a) mAb1 and (b) mAb2 at 5 $°C$ and 25 $°C$ for three concentrations. Corresponding effective structure factors are plotted for (c) mAb1 and (d) mAb2. All samples studied have 0 mM sodium chloride. Only a fraction of all points in each data set are included for clarity. . . . . 215

6.5 (a) The radius of gyration determined from a Guinier analysis of SAXS data and (b) the hydrodynamic radius estimated from DLS results at 25 $°C$ are plotted for low mAb concentrations. . . . . 217

6.6 Apparent molecular weights determined from SAXS results are plotted as a function of protein concentration for mAb1 (circles) and mAb2 (triangles) both with 0 mM NaCl (open symobls) and 150 mM added NaCl (filled symbols) at 25 $°C$. . . . . 219

6.7 The short-time collective diffusion coefficients determined from NSE data are plotted as a function of $q$-value for solutions of mAb1 at (a) 5 $°C$ and (c) 25 $°C$ and for mAb2 at (b) 5 $°C$ and (d) 25 $°C$. Samples with 0 mM NaCl are open symbols and those with 150 mM NaCl added are filled symbols. The lines represent the average value used to determine the short-time self diffusion coefficient. . . . . 222

6.8 Short-time self diffusion coefficients are plotted as a function of protein concentration for formulations with salt concentrations of (a) 0 mM and (b) 150 mM at 5 $°C$ (blue symbols) and 25 $°C$ (red symbols). For clarity, filled circles and open triangles represent mAb1 and mAb2 samples, respectively, at both salt conditions. The same symbols are used for the normalized values $D_s/D_0$ with (c) 0 mM and (d) 150 mM added NaCl. . . . . 223

6.9 Effective hydrodynamic radii of mAb1 clusters are shown relative to protein concentration at 5 $°C$ (blue symbols) and 25 $°C$ (red symbols) for salt concentrations of 0 mM (open symbols) and 150 mM (filled symbols). . . . . 226

6.10 (a) The average separation distance between nearest mAbs (solid line), $d_{avg}$, is compared against the effective hydrodynamic diameter (dashed lines) of a mAb monomer and dimer as a function of protein concentration. (b) Maximum theoretical effective $R_h/R_0$ (solid line) as a function of concentration compared to estimates from NSE for mAb1 at $5°C$ and $25°C$. . . . . 228

6.11 The reduced zero-shear viscosities of mAb1 (circles) and mAb2 (triangles) are compared between formulations of $D_2O$ (empty symbols) and $H_2O$ (half-filled symbols) at $25°C$ and 0 mM NaCl. These results are plotted relative to HS predictions (solid line). . . 231

6.12 Values of $R_g$ determined from SAXS data are shown for mAb1 (circles) and mAb2 (triangles) samples with (a) 0 mM and (b) 150 mM added sodium chloride salt. Formulations in $H_2O$ are half-filled samples and in $D_2O$ are empty and filled symbols (0 mM and 150 mM NaCl, respectively). . . . . 232

6.13 The same symbols as in Fig. 6.12 are used to distinguish the apparent molecular weight of formulations in $H_2O$ and $D_2O$. . . . . 233

7.1 Scattering intensities are plotted as a function of $q$-value for six different mAb form factor structures represented by the 12 bead model, shown below (inset highlights the middle $q$-range). . . . . 247

7.2 (a) Scattering intensities and (b) decoupling functions are plotted over a range of $q$-values for four dimer form factors constructed from the 12 bead model shown below. . . . . 249

7.3 (a) The mAb3 crystal structure is shown, with each domain given a different color. The best fit structures from the 12-bead model of a 2 mg/mL mAb3 sample with (b) 0 mM and (c) 50 mM sodium sulfate salt. The monomeric structure is compared with the crystal structure in (b). . . . . 250

7.4 The decoupling functions corresponding to the best fit structures pictured in Fig. 7.3 are plotted as a function of $q$-value. The range of $q$-values over which smearing of protein interactions becomes significant, $\beta(q) < 0.1$, is shifted between the monomer and dimer structures. . . . . 251

7.5 The (a) absolute magnitude and (b) reduced zero-shear viscosity is plotted for all conditions of mAb3 concentration, temperature, and salt content studied. The viscosity under all conditions increases significantly with protein concentration while reducing temperature and increasing salt content have similar effects on the magnitude of the relative viscosity. . . . . 255

7.6 Reduced 1-D scattering profiles are plotted on the same scale for several mAb concentrations with (a) 0 mM and (b) 50 mM added sodium sulfate salt. The addition of salt leads to significantly higher intensities at low $q$-values, indicating the presence of larger scale structures. . . . . 256

7.7 A comparison of (a) the $R_g$ extracted from Guinier analysis of low concentration SANS data and (b) the $R_h$ estimated from DLS data. While both methods agree quite well, mAb3 shows signatures of cluster formation in the presence of 50 mM sodium sulfate, even at low protein concentrations. . . . . 257

7.8 SANS profiles are plotted for two 2 mg/mL mAb3 samples representative of the form factor with best fits using the 12 bead model. Both sodium sulfate concentrations are plotted, with the sample at 50 mM sodium sulfate shifted by a factor of 3 for clarity. 260

7.9 Characteristic correlation decay curves (symbols) from (a) neutron spin echo and (b) dynamic light scattering experiments are plotted with their corresponding exponential function fits (lines) for a 100 mg/mL mAb3 sample at $5°C$ and $25°C$ and with 0 mM and 50 mM sodium sulfate salt. . . . . 261

7.10 Collective diffusion coefficients (symbols) extracted from fits to the NSE data with (a) 0 mM and (b) 50 mM sodium sulfate salt are plotted as a function of $q$-value. The average value in the limit of high $q$-values (lines) indicates the short-time self diffusion coefficient under each set of conditions. . . . . 262

7.11 The magnitude of the contribution of the fast mode ($X_1$) is plotted as a function of mAb3 concentration for each of the four solution conditions studied. . . . . 263

7.12 (a) Collective diffusion coefficients and (b) short-time self diffusion coefficients normalized by the bare diffusion of a mAb3 monomer, $D_0$, are plotted separately on the same scale. Deviations due to the presence of sodium sulfate are significant for long time collective motion (a), but relatively insignificant for the short-time mobility of individual moving units. . . . . 264

7.13 Absolute short-time self diffusion coefficients of mAb1 (circles), mAb2 (squares) and mAb3 (diamonds) in $D_2O$ buffers are compared as a function of protein concentration. . . . . 265

7.14 The effective hydrodynamic radius of the moving unit with 50 mM sodium sulfate is plotted as a function of temperature and protein concentration. . . . . 266

7.15 The effective hydrodynamic functions are plotted at (a) zero $q$-value, $H(0)$, and (b) the $q$-value of the monomer peak, $H(q_m)$ relative to HS (solid line) and CS (dashed line) fluids. . . . . 269

7.16 The hydrodynamic functions at $q_m$ determined from experimental results for samples with 0 mM (open symbols) and 50 mM (filled symbols) salt are fit with the inverse of the high frequency viscosity represented by Eq. 7.11 (dashed and solid lines, respectively). . . . 270

7.17 The shear rate dependence of the viscosity is plotted for a range of mAb3 concentrations (in mg/mL) for samples without added sodium sulfate at (a) $5°C$ and (b) $25°C$ and samples with 50 mM $Na_2SO_4$ at (c) $5°C$ and (d) $25°C$. . . . . 272

7.18 (a) A Cross model scaling of the viscosity is plotted as a function of stress for samples that display shear thinning behavior. All curves appear nearly identical, indicating that structural deformation is controlled by stress. Also plotted are (b) the characteristic structural lengthscale at the point of shear thinning and (c) values of $L$ normalized by the corresponding radius of gyration for each salt condition listed in the legend. (d) The zero shear viscosity scales well with the cube of the lengthscale. . . . . 273

7.19 Proposed long time and length scale ($L$) solution microstructures and corresponding fundamental moving units over short time and length scales ($2R_{eff}$) are compared under both salt conditions. Without salt, structures contain a dispersion of monomers and dynamic clusters (composed of monomers). With 50 mM sodium sulfate, transient networks form due to weak association of long-lived dimers. . . . . 275

7.20 The structure factor (symbols) is plotted for samples with (a) 0 mM and (b) 50 mM sodium sulfate salt for several mAb3 concentrations at $5°C$ and $25°C$ with $S(q)$ fits (lines) using the HSDY potential and corresponding $\beta(q)$. Only a fraction of all points in each data set are included for clarity. . . . . 276

7.21 Potentials extracted from fits to the SANS data using the 12 bead model for samples with (a) 0 mM and (b) 50 mM sodium sulfate. Antibodies interact purely attractively in the presence of salt, which screens the weak, long-range repulsion found in samples without salt. 278

7.22 A pictorial representation of mAb3 (a) monomers without salt and (b) dimers with salt used to capture trends in protein interactions. The effective distances are those of the green spheres relative to the structure center of mass, which relate well with potential features in Fig. 7.21. . . . . 279

7.23 The experimental mAb3 viscosity (symbols) are compared with estimates of HS fluids (gray region) and interacting proteins calculated using parameters from NSE and SANS data (blue-red region). The ranges reflect differences in effective hydrodynamic radii and interaction parameters as a function of solution conditions. The upper (blue) portion of the HSDY range reflects low temperature samples while the lower (red) HSDY estimates represent higher temperatures. . . . . 281

7.24 (a) The absolute zero-shear viscosity is plotted with fits (solid lines) using a polymer based entanglement model and their extrapolation over the full concentration range (dotted lines). (b) The estimates of effective aggregate size (solid lines) from the entanglement model fits are plotted relative to structural lengthscales (symbols) determined from shear thinning behavior. . . . . 283

7.25 The viscosity is plotted according to the linearized Ross-Minton equation, where non-linearity indicates concentration dependent self-association, for (a) 0 mM and (b) 50 mM added sodium sulfate using viscosities at two different shear rates. The solid lines are used to estimate the intrinsic viscosity (provided in the corresponding pane). . . . . 285

7.26 (a) The reduced zero-shear viscosity is plotted for each solution condition as a function of protein concentration with fits (solid lines) using the modified Ross-Minton equation while allowing $k/\nu$ to vary. (b) Corresponding values of $k/\nu$ extracted from the fits in (a) with each solution condition having identical symbols. . . . . 287

7.27 The concentration dependence of the zero-shear viscosity is compared for multiple antibodies and formulation conditions. Results are provided for mAb3 in $D_2O$ (diamonds) from this chapter[16] and literature results of mAb3 in $H_2O$ (triangles)[22] and mAb1 (circles) and mAb2 (squares) in $D_2O$.[48] . . . . . 288

7.28 The viscosity of each of the mAbs and solution conditions presented in Fig. 7.27 at mAb concentrations of 50 mg/mL (diagonal bars) and 100 mg/mL (cris-cross bars). . . . . 289

8.1 A hypothetical two dimensional microstructure is shown with three clusters. One particle in each cluster is shown with a dotted line connecting it to the cluster center of mass and an arrow depicting the directionality of the net force acting on it. Each particle is labeled as it would be distinguished, with a cluster size, $s$, and coordination number, $N$. . . . . 304

8.2 Two 12 sphere representations of monoclonal antibodies are shown side by side with each position labeled as it would in the RISM formalism. . . . . 307

A.1 The effective ISF (red squares) for a hypothetical two-component system of HS particles with radii of 1.54 nm (blue circles) and 4 nm (purple circles) is plotted relative to the model of short-time diffusivity (line) of an SALR system of monomers and clusters. . . . 315

A.2 The radii of gyration are plotted as a function of cluster size, $N$, or spherical clusters with FCC (circles) and BCC (squares) crystal structures along with a line representative of the expected power-law for a fractal dimension, $d_f$, of 2.77. . . . . 316

A.3 The magnitude of $S(q)$ for an FCC (left) and BCC (right) cluster structure as a function of $N$ and several values of $d_f$. . . . . 317

A.4 The change in $S(q)$ magnitude with cluster size, $N$, is plotted as a function of fractal dimension for an FCC (circles) and BCC (squares) internal cluster structure and a line of best fit represented by Eq. A.6. 318

A.5 The hydrodynamic (gold) and effective compact cluster (red) radii are represented relative to clusters of 16, 12, 10, and 14 particle (clockwise from bottom). The bottom cluster (green) is a spherical FCC cluster on which the calculations of the effective (red) sphere sizes are partially based. The remaining clusters are characteristic of those expected to form in lysozyme systems, for which the hydrodynamic radii capture the more diffuse structure. . . . . 324

## ABSTRACT

Colloidal particles and "soft matter" materials are essential parts of many consumer goods we utilize in all facets of life. The utility of these materials stems from their chemical and structural versatility, ease of customization, and response to external stimuli. As a result, soft materials are ubiquitous in industries such as electronics, performance composites, personal care, cosmetics, paints and pharmaceuticals. Engineering these materials relies on a fundamental understanding of their phase behavior and structure-property relationships that dictate various microstructural states for particular applications. Regardless of the chemistry of various colloids, whether they are particles, polymers, micelles, or proteins, the combination of interaction forces (e.g., dispersion, hydrogen bonding, hydrophobic, electrostatic) can be represented as an effective potential energy field, or interaction potential, which determines the diversity of equilibrium and non-equilibrium states. This thesis examines the influence of a combination of a short-range attraction (SA) and long-range repulsion (LR), ubiquitous to protein systems, on the phase behavior and associated material properties.

The competition of attractive and repulsive forces is unique in its ability to produce self-assembled clusters with a preferred size. This type of cluster has been observed in a variety of materials. For example, the biopharmaceutical industry is concerned with large solution viscosities in highly concentrated therapeutic formulations that are hypothesized to arise from cluster formation. In general, SALR (or competing) interactions may have a significant impact on material properties stemming from the large diversity of states they may form. Thus, theoretical calculations and experimental observation of thermodynamic and material properties (e.g., viscosity) are necessary to more accurately understand the phase behavior of SALR systems.

Characteristic features of cluster formation in SALR systems are investigated and identified using scattering techniques. In contrast to early experimental studies, the presence of a unique intermediate range order (IRO) peak in small angle scattering patterns is found not to be an experimental representation of cluster formation. Using the particle level details provided by Monte Carlo (MC) simulations, several microstructures are studied and distinguished using well defined definitions according to the cluster size distribution. The contribution to the scattering intensity is decomposed into correlations between monomers and clusters. The results indicate that a significant contribution to the IRO peak is from monomers in each type of microstructure. Some specific properties of this peak are found to be useful identifiers of clustered states in the one phase region.

The widely used extended law of corresponding states for colloidal systems with only an SA interaction is extended in this thesis to systems with competing interactions. A generalized phase diagram for systems with isotropic SALR potentials has been identified to distinguish different liquid states including clustered fluid states. Fluids with a preferred cluster size driven by SALR interactions are identified using MC simulations, and are found to form exclusively within the two-phase region of a purely attractive reference system. The additional repulsion frustrates phase separation, driving particle localization on intermediate range order (IRO) length scales. Multiple potential forms and interaction parameter sets are investigated and demonstrate identical behavior, ensuring that this generalized phase diagram is a generic feature of systems with competing interactions. This phase diagram serves as an effective and efficient method of identifying cluster formation for the community.

A model protein solution is used to experimentally study the relation between cluster formation and dramatic increases in viscosity. Using neutron scattering techniques, the structure and dynamics of this nearly isotropic system under concentrated conditions are accurately quantified. Interaction parameters are extracted by fitting neutron scattering data with a thermodynamically self-consistent integral equation theory. The extent of cluster formation is identified by mapping these states onto the new

generalized phase diagram and generating structures using MC simulations. Unique glassy-like behavior and large viscosities are shown to arise from structures with IRO. A new viscosity model is developed for SALR systems to capture the additional impact of cluster interactions.

These methods are applied to understand the anomalously large viscosities sometimes apparent in concentrated monoclonal antibody solutions, which are used as biopharmaceutical therapeutics. The formation of dynamic clusters had been hypothesized to be the underlying driving force behind the viscosity increase at higher concentration. Three different mAbs are studied over a wide range of commercially relevant formulation conditions to distinguish the thermodynamic properties of viscous solutions. The formation of long-lived dimers is consistently found to cause the larger viscosities. Differences in the magnitude depend on the subsequent association of these small clusters into supramolecular structures. Model systems could be used as a foundation to semi-quantitatively characterize the extent of cluster formation and its influence on viscosity.

# Chapter 1

# INTRODUCTION

## 1.1 Colloidal Particles as Engineered Materials

Modern processes and devices call for highly specific material properties in order to optimize manufacturing operations and/or enhance the user experience (subsequently maximizing margins and profitability). Rarely does a pure material optimize or even meet all the requirements for a given application. Most materials must be engineered, either as a composite or a unique synthetic material, to obtain properties that satisfy a range of specifications such as thermal and mechanical stability (e.g. turbine blades), chemical stability and conductivity (e.g. photovoltaics), or colloidal stability and bio-compatibility (e.g. pharmaceuticals). Engineering these preferred macroscopic or bulk properties is accomplished by directly altering the material's microscopic properties. The inherent correlation between bulk and microscopic properties is typically referred to as a structure-property relationship, although the structure is not always the only criteria of merit. Linking the pertinent parameters on such disparate length-scales requires a hierarchy of knowledge regarding material behavior as shown in Fig. 1.1.

Represented in Fig. 1.1 is a pyramid at the top of which is a given application for which a material must be developed. The final product is supported by increasingly larger, and more fundamental, layers of supporting information that include the material's bulk properties, its phase behavior, the microscopic interactions, and finally its chemistry. Phase behavior lies directly below properties as it indicates which state of matter is most stable, whether thermodynamically or kinetically, at a given set of environmental conditions. For example, whether a material is a solid or a liquid clearly

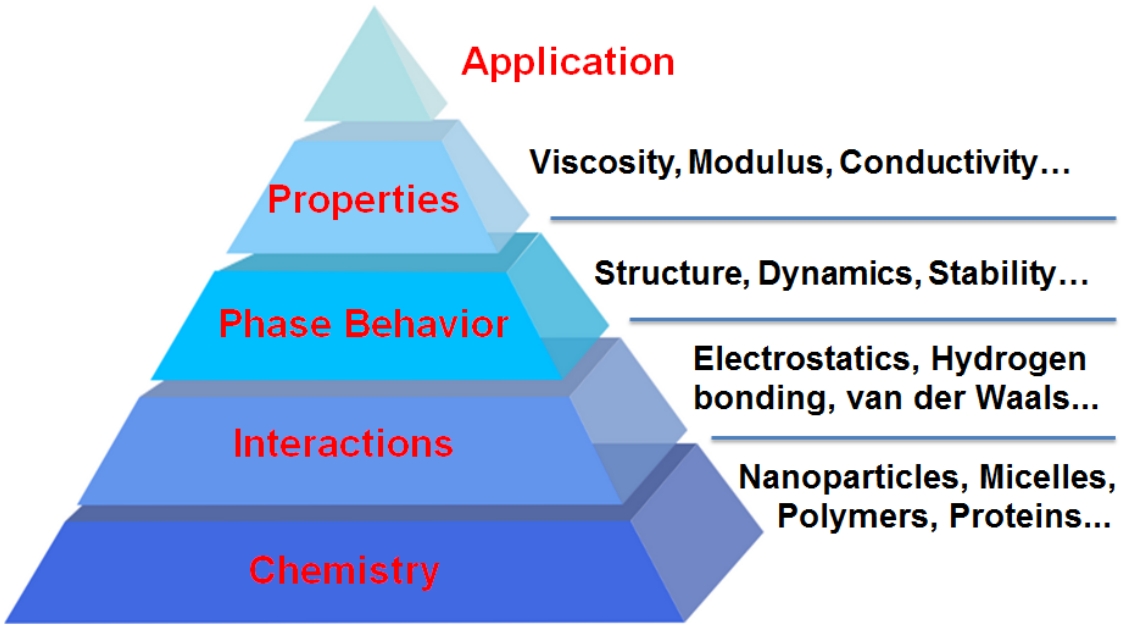


**Figure 1.1:** A schematic representation of the hierarchical relationship between microscopic and macroscopic properties used to engineer materials.

plays a significant role in determining material properties. One of the most fundamental intensive properties, material density, is typically utilized in a phase diagram to distinguish between these states. Since van der Waals proposed a new equation of state in 1873,[97] for which he won a Nobel prize in 1910, the coexistence of a low and high density state (and phase behavior in general) has been understood in terms of interactions between atoms or particles.[2, 35, 46] The strength and range of these interactions are dictated by the underlying chemistry of the materials of interest.[48, 50] In the case of pure materials, these interactions are dictated by the atomic structure. However, colloidal particles provide a platform for customizing the chemistry, size, and shape of particles to have direct control over these microscopic forces.

Colloidal particles, typically silica, titania, or gold spheres but also inclusive of polymers (e.g., poly-(methylmethacrylate), PMMA) and proteins (essentially polymers of amino acids), are versatile materials important to the electronics, performance composites, personal care, cosmetics, paint, food and biopharmaceutical industries, among

others. They are also of great fundamental scientific interest due to their size scale, typically within the range of a few nanometers to hundreds of microns, which allow their structure and dynamics to be treated independently of the solvent (only Angstroms in size).[48] In addition, their chemistry can be tuned to create a customized potential energy field by which two particles interact, referred to as an interaction potential. The effective interactions can be tuned by manipulating the chemistry of these particles and the solvent within which they are dispersed.[50] Having control over these properties then provides a method to study the impact of interactions on the phase behavior, which is the foundation for further study of material properties.

In this dissertation, the particular combination of short range attraction (SA) and long range repulsion (LR) is examined to quantify the corresponding phase behavior and associated solution viscosity at a range of environmental conditions. The competition of two potential features provides an opportunity to engineer a diverse set of structural states, which may offer desirable properties through reproducible spontaneous structures.[83, 87] Therefore, engineering materials with SALR interactions will benefit from developing a direct connection between dispersion microstructure (and its associated properties) and the inter-particle potential. Further understanding of these complex systems will build upon the well established behavior of systems with the more fundamental interactions of which SALR potentials are composed.

SALR systems are of particular interest as they can produce liquid states comprised of equilibrium clusters.[14, 15, 16, 75, 82, 85, 93, 94] Colloidal dispersions with these competing interactions are of great scientific interest due to the diversity of materials they represent. These include polymer nanocomposites,[66] colloidal dispersions,[14, 85] as well as several types of proteins including membrane proteins,[18, 70] globular proteins[16, 75, 93] and therapeutic monoclonal antibodies.[52, 101] Each of these materials has demonstrated the ability to form equilibrium clusters due to SALR interactions, though their impact on material properties is not fully understood. For example, several studies within the biopharmaceutical industry on concentrated

solutions of therapeutic proteins have hypothesized that cluster formation is the underlying cause for large viscosities that are detrimental to the manufacturing and delivery of these invaluable drugs.[56, 101, 103] Hence, the importance of each tier in Fig. 1.1 will be addressed before presenting important advances in the understanding of cluster fluids as Landmark Observations.

## 1.2 The Chemistry of Colloidal Interactions

Despite the large size differences between individual atoms and colloidal particles, their behavior can be represented within the same framework of an effective interaction potential. When the distances over which these forces act are normalized by the corresponding size of the individual unit, the potentials of a nitrogen atom with a diameter $\sigma \approx 1.2$ Å and, for example, that of a $1.0\mu m$ diameter PMMA particle could be remarkably similar (though the type of interaction(s) responsible for their respective potentials will most likely be different). Therefore, with respect to the equilibrium thermodynamic structure, these two systems (atomic and colloidal) can serve as proxies of each other. In the case of a colloidal particle, the potential is an "effective" potential since the forces are mediated by the solvent that is considered a continuous medium. However, atomic forces are the result of quantum mechanical fluctuations of electrons relative to the nucleus in a vacuum.[48] Equilibrium pockets with a high probability of finding an electron, known as orbitals, vary in size and shape depending on the energy state of a given electron bound to the nucleus.[102] Large gradients in electron density within these orbitals can produce a dipole, which is a closely coupled pair of oppositely charged points in space. Therefore, similar to a bar magnet, fluctuations in electron density produce forces between atoms, generally referred to as dispersion forces or van der Waals (vdW) forces, which can be decomposed into induced-induced, induced-permanent and permanent-permanent dipole interactions (though vdW forces do not include hydrogen bonds, these are also an important class of dipole interactions).

Distinguishing an atomic dipole as permanent or induced depends on the chemical composition of a given molecule and how the individual atoms interact. Permanent

dipoles exist in molecules that are held together by sharing electrons in communal orbital space surrounding adjacent nuclei.[102] Therefore, regions of high and low electron density remain in a particular orientation to maintain a stable chemical structure. The interaction between two permanent dipoles is known as the Keesom force. A prevalent example of a highly directional interaction between two permanent dipoles is a hydrogen bond, which is an orientation dependent association of a hydrogen atom in one molecule with an electron pair of an electronegative atom in another molecule.

In contrast, the location of electrons bound to a particular atom fluctuate and can perturb the surrounding electromagnetic field. These perturbations can subsequently influence the location of electrons bound to an adjacent atom, creating an induced dipole. Theoretical calculations of electromagnetic fluctuations indicate that, after averaging over all possible orientations, the resulting vdW forces have a dependence on inter-atomic spacing of $F(r) \sim 1/r^6$.[48] A manifestation of the Pauli exclusion principle, which states that two electrons can not exist in the same quantum state (classically interpreted as not occupying the same physical space), is that a very short range repulsive force is also produced between atoms. As a result, atomic interactions are typically represented by a Lennard-Jones 12-6 interaction potential of the form $U(r) = 4(r^{-12} - r^{-6})/T^*$, where $1/T^*$ is the magnitude of attraction strength.[79]

These microscopic quantum mechanical forces can be extended to colloidal interactions by integrating the volume of a body composed of atoms.[45] The functional form (i.e., the dependence on center-of-mass separation) of dispersion forces varies depending on the type of bodies interacting (e.g., walls or spheres), but generally the form $F(r) \sim 1/r^\alpha$ is used, where the range of colloidal interactions ($\alpha < 6$) is much longer compared to atomic materials ($\alpha = 6$),[48] though this is not strictly true for macromolecules such as proteins. Colloidal bodies also have a unique capability for their dispersion interactions to be customized. The constant of proportionality between the magnitude of dispersion forces and the range of interaction, referred to as a Hamaker constant, can be manipulated via the chemical composition of the particles and the suspending medium. While vdW forces are always attractive for atoms, they

can be made attractive, repulsive or zero for colloids by choosing materials with an appropriate refractive index.[48, 50]

An additional consideration for colloidal particles is the interaction with solvent molecules. The cumulative rearrangement of this sea of small molecules introduces an interesting phenomenon of random fluctuations by a colloidal particle, known as Brownian motion.[13] Einstein demonstrated that this "random" motion is Gaussian in nature for most cases and is a thermally regulated process due to particle-solvent collisions.[32] Interestingly, as particles diffuse via Brownian motion they create flow fields in the medium that can then produce shear forces on other particles, potentially quite far away, known as hydrodynamic interactions.[28, 67] Hydrodynamic interactions involve multiple particles and therefore, inherently depend on the equilibrium microstructure, making quantitative calculations very difficult. Typically, however, the net effect is to resist particle motion. As the density of colloids increases, hydrodynamic interactions will become a significant contribution to the cumulative forcefield of all interactions imposed on a given particle.[67]

In addition to forces of hydrodynamic and quantum mechanical origin, effective interactions between colloids can be induced from other features of their chemical composition. Additional attractive forces can be generated from a solute being partially or completely immiscible in the suspending medium. Also known as the hydrophobic force, the resulting association of solutes is driven by a minimization of free energy accomplished by reducing the surface area of interfaces with high interfacial energy. Also, introducing a second component of much smaller size than the original one (but still large relative to solvent molecules) into a suspension may induce an apparent attraction between larger particles. This so called depletion attraction is induced by maximizing the free volume available to the smaller, non-interacting solutes due to overlap of excluded regions surrounding the larger ones. If the small solutes do interact with the larger ones, they may also cause bridging attraction in which they weakly bind to two (or more) entities, holding them in close proximity.

Repulsive interactions are typically present, which stabilize colloids from these

associative driving forces. Steric repulsion is a physical barrier simply caused by the finite volume of molecules preventing neighbors from coming into contact. Further, Coulomb repulsion is an electrostatic repulsive force between two charged solutes of the same sign due to the perturbation of the local electric field (a repulsive analog to the vdW force). The magnitude and range of repulsion varies depending on the charge of the solute, the permittivity of the solvent and concentration of small counter-ions. A simple mathematical representation is provided by Debye-Hückel theory, which relates the surface potential (related to the surface charge via the Grahame equation) to the interaction potential. The counter-ions play an important role by forming a diffuse density distribution around a charged particle, known as a Debye layer,[48] which screens the charge on the surface of a solute from a neighboring solute and is thereby called a screened Coulomb repulsion.

A powerful capability of colloidal suspensions is the customization of the effective interaction potential by combining these various forces. Historical precedent for this has been set since the study of colloidal stability using the DLVO potential, which combined attractive dispersion forces and Coulomb repulsion.[29, 73] Further, it is quite common for multiple attractive forces to contribute to the total attraction in the effective interaction potential. In the interest of producing SALR interactions, previous work has combined large charged colloidal particles with "built-in" repulsive interactions with smaller non-adsorbing, randomly coiled polymers to induce a depletion attraction.[14, 53, 86, 93] Other studies have taken advantage of a material that naturally produces SALR interactions, small globular proteins (specifically, lysozyme).[15, 16, 34, 62, 75, 91, 93] Although several other compositions could produce these forces that may better suit a particular application, for now these two systems have provided a powerful framework to experimentally corroborate theoretical and simulation studies.

## 1.3 Interactions and Phase Behavior

While several observations of various structural states in SALR systems, including cluster fluids, have been presented in the literature, relatively little progress has been made in physically rationalizing or summarizing the conditions at which they form. In particular, while a wide range of microstructures can be produced with several tuning parameters (i.e., strength and range of interactions), it is a daunting task to explore the full parameter space of an SALR potential. Therefore, a theory for the generalization of the phase behavior of systems with competing interactions will facilitate the development of structure-property relationships for these systems by enabling the rapid location of interesting states exhibiting clusters. Fortunately, a consequence of the fact that an SALR potential is a summation of an attractive and a repulsive potential is that SALR phase diagrams contain aspects of the phase behavior observed in purely attractive systems and purely repulsive systems. Therefore, previous studies of these "simpler" systems can be used as a basis for understanding the more complex influence of competing interactions.

By choosing appropriate chemistry, the influence of the effective interaction potential can be systematically studied as demonstrated in Fig. 1.2. The simplest interaction is a hard sphere (HS) interaction, where the finite size of the particle produces an excluded volume in which no two particles can exist simultaneously. Theoretical calculations demonstrate that the HS phase diagram includes a single equilibrium phase transition between a fluid at a volume fraction of $\phi = 0.494$ and a crystal at $\phi = 0.545$, shown in Fig. 1.2b.[49] Such samples can be generated experimentally by matching the refractive index of particle and solvent (i.e., removing vdW forces by reducing the magnitude of the Hamaker constant) and/or grafting a steric stabilization layer on the surface of the colloid. Previous experimental work demonstrated this technique nearly quantitatively reproduced the HS phase behavior.[76] Interestingly, non-equilibrium transitions can exist at large volume fractions if samples have sufficient polydispersity to prevent crystallization.[2] In particular, HS samples have a glass transition at $\phi \approx 0.58$ forming a disordered solid (not shown in Fig. 1.2).[76] In addition to a

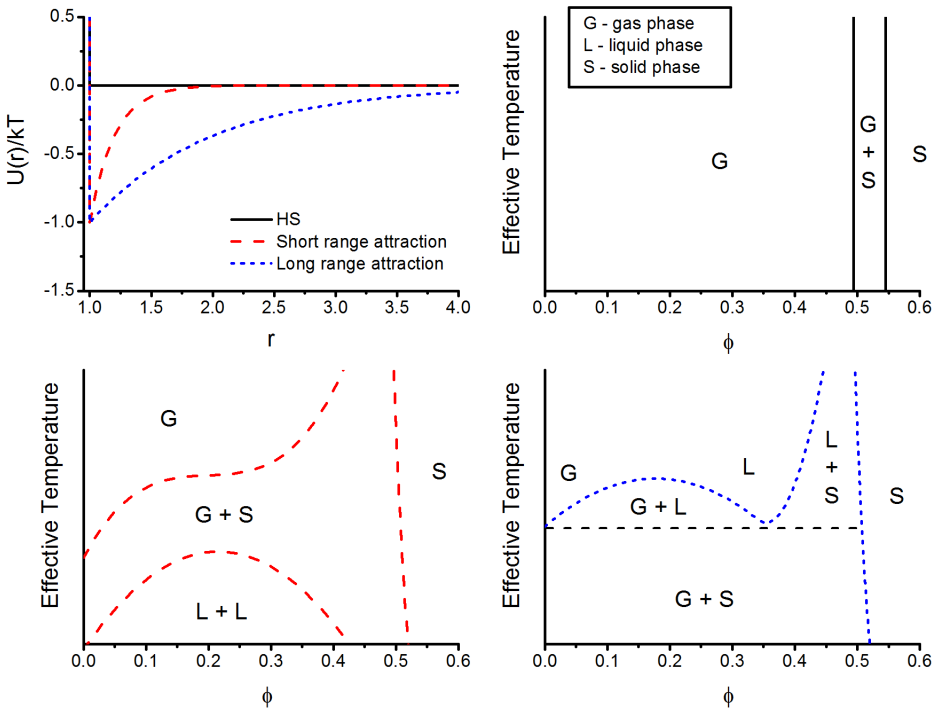


**Figure 1.2:** (a) Interaction potentials of HS (black solid line), short range attraction (red dashed line) and long range attraction (blue dotted line) are plotted together for comparison. Representations of the phase behavior resulting from the corresponding potentials in (a) are plotted for (b) hard sphere, (c) short range attractive and (d) long range attractive fluids. Letters distinguish the type of phase in each region of the diagrams. The dashed line in (d) represents the triple point (gas-liquid-solid coexistence).

divergence of zero-shear viscosity and the onset of a yield stress,[67] particles in an ideal glass become dynamically arrested, which is indicated by a plateau in the auto-correlation function due to density fluctuations representative of non-ergodicity (i.e., non-equilibrium behavior).[98, 99]

Attractive interactions, with two additional tuning parameters (i.e., attraction strength and range), produce much more diverse phase behavior that is acutely sensitive to the range of attraction, which is graphically represented by comparing the diagrams in Fig. 1.2.[2, 5, 35, 36, 68] The equilibrium phase behavior of long range attraction contains a gas-liquid-solid triple point in addition to separate gas-liquid and liquid-solid coexistence regions.[2, 35, 68] (These features are reminiscent of atomic systems, as the Lennard-Jones potential falls into this category). As the range is reduced, the gas-liquid (or liquid-liquid) coexistence becomes metastable within the gas-solid region.[35, 36] This liquid-liquid region can typically be accessed due to the slow dynamics of crystallization and/or particle size polydispersity. Several studies have demonstrated that, if attractive forces are less than roughly 10% of a particle diameter, this two phase region can be normalized onto a generalized phase diagram, referred to as the extended law of corresponding states.[55, 71, 72]

While Fig. 1.2 represents the qualitative trends in colloidal systems with *isotropic* HS and attractive interactions, the phase behavior can become significantly different if the interactions are *anisotropic*. Although throughout this dissertation the use of isotropic interaction potentials will be utilized to numerically extract parameters to describe the effective forces between colloids, it is important to recognize the significance of directionality on their behavior. This fact is particularly relevant to proteins (as will be explored in detail later in this dissertation), which typically have a complex distribution of surface residues responsible for protein-protein interactions. Recent experimental and modeling work demonstrated the accuracy of a so called "patchy" model in representing the interactions between lysozyme that could successfully reproduce the experimentally observed phase behavior.[42] A more expansive theoretical investigation has also demonstrated the quantitative changes in phase behavior as a function of the

number of patches and their angle of (purely attractive) interaction.[89] For example, Ref. [89] showed an expansion of one-phase liquid stability over a broader range of solution conditions with increasing patches and angle of interaction, which would greatly influence the resulting properties affiliated with the fluid microstructure.

Short range attraction can induce an equilibrium connectivity known as percolation, in which at least one cluster spans the sample volume. Stochastic models and simulations demonstrate that percolation precedes liquid-liquid phase separation.[20, 68, 84] This transition depends on the strength and range of attraction and can have a significant impact on the dynamics in these systems.

Attraction also produces a rich landscape of non-equilibrium states (not shown in Fig. 1.2) in addition to the diverse equilibrium phase diagram. In the limit of very weak attraction (i.e., a HS fluid), attractive systems will transition through the so called "repulsive driven" glass (RPG) transition at high volume fractions. Additionally, these systems contain an "attractive-driven" glass (ADG) transition at sufficiently strong attraction and high volume fractions.[80] A kinetically arrested state at intermediate $\phi$ has also been found that precedes the ADG transition, known as gelation.[104] Despite the difference in their volume fractions, gels and glasses are similar in that the viscosity diverges and a yield stress develops, indicating a mechanically robust structure. However, the physical origin of gelation remains heavily debated. Gel states have been shown to correlate with both random percolation[31] and rigidity percolation,[96] but have also been associated with an arrested spinodal decomposition.[63]

As may be expected, introducing two additional parameters to a potential with HS plus attractive interactions, by combining with it a repulsive interaction resulting in an SALR potential, produces an even richer variety of structural and dynamic states with distinct properties. Simulations have demonstrated that systems with *long range attraction* and longer range repulsion (or *LALR* interactions) may still have a stable gas-liquid coexistence, similar to systems with purely long range attraction.[4, 21] However, the two-phase region of LALR systems is much more complex as compared to long range attractive systems,[3, 22] consisting of spontaneous micro-phase separation

into self-assembled structures with similar geometry to block copolymers,[23] which in and of themselves have a rich phase behavior.[6]

In the case of *SALR* interactions, this dissertation will demonstrate that the phase behavior of systems with competing interactions is very similar to purely short-range attractive systems. In particular, the phase behavior of these two systems will be shown to be so similar that the extended law of corresponding states[71] can be used to construct a normalized phase diagram for SALR systems, analogous to that for purely attractive interactions.[40] The most significant differences between SA and SALR phase behavior is that the additional LR interactions shift the liquid-liquid binodal to lower temperatures[51] and the percolation transition to smaller volume fractions.[95] Below the percolation line, simulations indicate that equilibrium fluids of clusters form at sufficiently strong attraction in balance with repulsion.[38, 40, 82, 94] At higher volume fractions, clusters can act as building blocks of more complex microstructures leading to cluster-induced glassy states[53] or gelation.[14, 40, 82] These macromolecular structures likely have a significant influence on the solution viscosity, to be discussed in the next section, which heightens the importance of more accurately and generally identifying the phase space of these states to further study their properties.

### 1.4 Solution Viscosity - The Influence of Interactions

Viscosity, $\eta$, is one of the most important physical properties to the manufacturing and use of nearly every consumer product. The formulation of materials ranging from toothpaste to paint must be carefully optimized to maintain the structural integrity and flow behavior necessary for the application of interest. Simultaneously, the properties must be suitable for the unit operations needed to initially produce each product. Therefore, an accurate model of solution viscosity as a function of concentration and interactions can serve as a powerful tool for successfully engineering a wide range of materials. This is true whether one is traversing up or down the pyramid in Fig. 1.1. In the case of SALR systems, previously developed models for HS and

attractive systems can serve as a foundation, similar to the phase behavior, but the simultaneous influence of competing forces presents significant challenges.

Phase diagrams provide an important physical rationalization for the behavior of colloidal suspension viscosity, which is intricately related to the microstructure. The viscosity represents the stress supported under flow when applied at a given shear rate. Therefore, the stress depends on the relative timescale of the imposed flow and the microscopic mechanisms of particle relaxation (i.e., rearrangement) that dissipate stress.[67] In the limit of small shear rates the static microstructure (whether equilibrium or non-equilibrium) is essentially unperturbed. Hence, the resistance to "flow" by this structure is reflected in the zero-shear viscosity, $\eta_{r0}$, measured under these conditions. The dynamic corollary of $\eta_{r0}$ is an oscillatory shear force imposed at a fast enough frequency that the equilibrium structure is essentially unchanged, known as the high-frequency viscosity, $\eta_{\infty}$, which is representative of purely hydrodynamic forces. At high shear rates, perturbations alter the solvent flow field relative to the static microstructure since the particles, which are orders of magnitude slower than solvent molecules, can be considered to remain static. Therefore, the stress response in the low or high shear limit can be estimated according to the sample's equilibrium structural state within the phase diagram.

Glass transitions in HS and attractive (specifically, adhesive hard sphere) colloidal systems serve as a useful example of the viscosity dependence on the microstructural state. At elevated volume fraction, approaching either the RDG or ADG transitions, the zero-shear viscosity diverges. Prior to the glassy state, these samples become non-ergodic due to dynamic arrest and a majority of the population of particles coming into direct contact with several neighboring particle. By definition, once becoming a glass, the particles are caged by many neighbors and no longer move on long length-scales. Therefore, these dynamically arrested structures resist shear flow and produce the divergence in viscosity. In fact, both the structural and dynamic parameters are proportional to the proximity of the sample volume fraction to an effective maximum volume fraction, $\phi_{max}$, which has been closely associated with the experimentally

identified glass transition.[78] By accounting for both contributions, they accurately account for the power law behavior of the viscosity according to the semi-empirical relation $\lim_{\phi \to \phi_{max}} \eta_{r0} \propto (\phi - \phi_{max})^{-2}$.[11] In the case of the ADG transition, which depends on the strength and range of attraction, this divergent behavior can then be used to accurately identify $\phi_{max}$ for a given interaction potential.[54, 77]

As a macroscopic material property, viscosity is a manifestation of several microscopic parameters that make modeling its dependence on solution conditions quite challenging.[67] While empirical models utilize the glass transition as an upper limit to estimate the viscosity at high volume fractions, calculations for samples at intermediate $\phi$ requires knowledge of the microscopic properties. Decomposing the microstructural contributions to stress dissipation under shear flow has proven to be a powerful and reliable method.[11, 58] In particular, the viscosity can be differentiated into hydrodynamic, Brownian, and inter-particle contributions.[11]

Each viscosity contribution term highlights the importance of interactions, structure, and dynamics. The hydrodynamic contribution is a many-body interaction that is difficult to calculate. Therefore, it is determined by experimentally measuring the high-frequency viscosity. The Brownian and inter-particle terms are proportional to the self diffusion coefficient and the probability of finding two particles in contact, which can be estimated using thermodynamics. However, since the steady-state microstructure is a perturbation of the equilibrium structure under flow, the resulting viscosity model will depend on the specific flow field. As a simplification, most models estimate the viscosity by assuming only minor perturbations to the equilibrium microstructure.[11]

By combining the three individual contributions, the viscosity can be estimated as an expansion in terms of the particle volume fraction. A widely used representation includes only one- and two-body contributions through the form

$$\eta_{r0}(\phi) = 1 + 2.5\phi + k_H\phi^2 + O(\phi^3) \tag{1.1}$$

where $k_H$ is the Huggins coefficient. This functional form can be directly compared with experimental viscosity data to quantitatively estimate the contribution of particles

and their interactions, as well as the subsequent structure and dynamics resulting from those interactions, to the solution viscosity. In this sense, Eq. 1.1 turns a rheology experiment into a probe of thermodynamic and dynamic properties.

In contrast, Eq. 1.1 can be used as a tool to predict solution viscosity by estimating Huggins coefficients. Values of $k_H$ have been theoretically predicted for HS fluids with equilibrium liquid[100] and shear-induced[7] structures. Similar calculations have also produced Huggins coefficients for charged and attractive colloids. For purely repulsive systems, $k_H$ is a function of the Debye length[11] and for weakly attractive systems it is a function of the well depth of the potential, whether an adhesive hard sphere,[24] square well,[8] or some other functional form.

Although exact for dilute solutions, extending the approach presented in Eq. 1.1 to concentrated solutions requires approximating many-body calculations. Thus, the development of accurate predictive models for attractive and especially SALR systems becomes quite difficult. As of yet, no definitive theory exists for systems with SALR interactions. In part, this is due to the novelty of SALR systems. This thesis will build upon previous models developed separately for an attractive and a repulsive force by combining their most effective features into a functional form that represents the cumulative contribution of SALR interactions. Many of these details are provided in the Appendix.

## 1.5 Landmark Observations

### 1.5.1 Cluster Formation Fundamentals

Cluster formation was shown to theoretically occur from the combination of short range attraction and long range repulsion by Sciortino, et al.[81] The attractive force draws particles together and initiates association into larger aggregates. If left unimpeded, aggregation will continue until the aggregate is so large that it either spans the whole system or precipitates out of solution (if the particle and solvent densities are sufficiently mismatched). However, the accumulation of repulsion on each of the individual particles within a cluster eventually becomes large enough to prevent further

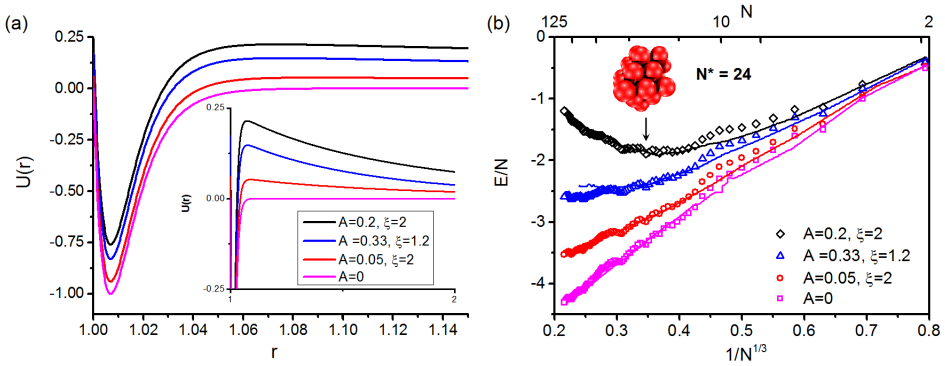


**Figure 1.3:** (a) Four SALR interaction potentials are plotted together with the same range and strength of attraction but varying range and strength of repulsion. (b) The configuration energy per particle is plotted for each of the potentials in (a) with the corresponding colors using simulation results form [81] (symbols) and new numerical calculations (lines) of close-packed spherical configurations, an example of which is shown in the inset.

growth. If the repulsive force is sufficiently strong, it would prevent any aggregation from taking place. Therefore, a delicate balance of a weak but non-zero repulsion and a relatively strong attractive well (however, not so deep particles are unable to escape) are necessary for the formation of equilibrium clusters with a finite size.

Achieving the necessary delicate balance of attraction and repulsion to form a cluster is manifested as a minimum in the configuration energy as a function of cluster size.[69, 81] Previous work relied on a complex basin-hopping algorithm in Monte Carlo (MC) simulations to identify the ground state (zero temperature, infinite dilution) configuration that minimized the free energy.[81] The calculations utilized an interaction potential that combined a short range equivalent of Lennard-Jones type attraction (known as the $2\alpha-\alpha$ form, with $\alpha = 100$ rather than $\alpha = 6$) with a screened Coulomb repulsion, examples of which are provided in Fig. 1.3a. However, these cluster configurations can also be accurately represented by a spherical close-packed crystal structure.[69] The similarity of simulation and analytical calculation results is demonstrated for all four potentials in Fig. 1.3b. The top curve has a clear energy minimum as a function of cluster size, indicating a stable cluster of about 24 particles.

The other three potentials have insufficient repulsion and therefore, the configuration energy continually decreases with increasing size. Thus, systems with these potentials are expected to exhibit bulk phase separation rather than form a clustered fluid, at least at zero temperature. With a simple extension of the model, four orders of magnitude of both interaction parameters are sampled to observe stable cluster formation.[69]

### 1.5.2 Cluster Configuration and Solution Microstructure

The simple ground state calculations demonstrating the fundamentals of cluster formation were a significant step in understanding what clusters are and the conditions under which they form. However, at finite temperature and concentration the influence of entropy and Brownian motion become significant contributions to the free energy landscape of colloidal systems with SALR interactions, and the sum of these interactions determines whether clusters are energetically favorable.[82, 94] For example, entropy favors a highly polydisperse cluster size distribution compared to enthalpy, which as shown in Fig. 1.3 would result in a single minimum energy cluster size. To accomplish a similar calculation for a sample at finite $\phi$ and $T$, the free energy of a particular cluster size would need to be calculated while accounting for the ensemble average microstructure within which it exists. Simulations provide an effective means to quantify cluster properties under experimentally relevant conditions.[1, 37]

While simulations are powerful techniques that offer significant details into the solution microstructure, they can be time consuming. Therefore, efforts have been made to develop models to predict the onset of clustering. Models developed thus far estimate an average cluster size in a monodisperse solution, which may simplify determining the conditions at which significant clustering occurs.[30, 43] As a result, these calculations treat clustering analogously to micellization.[30, 44, 103] However, these models miss potentially important details such as the cluster polydispersity and internal configuration and rely on input parameters such as cluster surface energy that are very difficult to experimentally identify (and likely infeasible to determine).

Identifying the additional influence of entropy and excluded volume on cluster formation at finite temperature and concentration can be accomplished by quantifying the cluster size distribution via simulation techniques. To do so requires defining a separation distance between particles, within which they are considered connected or associated.[25] This is a point of contention in the soft matter community involved in studying cluster formation and will be discussed in more detail in later chapters. However, features of the resulting cluster size distribution are used to define various types of structural states. As such, evolution of extensive clustering has been found to occur at relatively small concentrations and temperatures.[38, 40, 82, 94, 95]

Previous work has also observed the effect of interaction potential parameters on cluster shape via experimental and simulation studies. Studies of a relatively short range repulsion ($0.5\sigma$ and $0.65\sigma$) demonstrate that larger clusters are quite condensed with a fractal dimension between 2.1 and 2.5 while smaller clusters are more linear with a fractal dimension of about 1.5.[14, 82, 95] However, large clusters can transition from relatively compact to more elongated, with a fractal dimension of about 1.3, by making the repulsion very strong while still short ranged or longer ranged ($2\sigma$) while still weak.[94, 95] Under very strong attractive interactions, more spherical clusters are preferred at smaller sizes[82, 94] due to the larger driving force for aggregation. In addition to the interaction parameters, cluster structure is also dependent on temperature and particle volume fraction. However, cluster fluids are generally observed at low to intermediate $\phi$ and relatively low temperature.

Depending on the volume fraction, as well as the interactions, the cluster size distribution may show a predominant cluster structure in solution. An experimental system with a small range of repulsion formed predominantly small (more spherical) clusters at low volume fractions ($\phi \leq 0.08$) until becoming larger, and thus more linear, above $\phi \sim 0.1$.[14] Simulations using similar interaction parameters corroborated these results.[82] Within these experimental[14, 85] and simulation[82, 94] studies, small clusters at small $\phi$ exist in equilibrium with monomers. In contrast, the large linear clusters eventually percolated at larger volume fractions ($\phi \approx 0.14$). Thus, in addition

to stable, reversible aggregates, clusters can act as building blocks that aggregate into larger structures.[14, 16, 38, 82, 85, 94]

### 1.5.3 Cluster Dynamics

In practice, clusters have both structural and dynamic features that determine their stability. Clustered fluids are composed of reversible aggregates with a preferred average size (with finite polydispersity) that coexist with individual particles.[69, 81, 82, 94] The equilibrium coexistence of monomers and clusters indicates that clusters likely have a finite lifetime. The delicate balance of relatively weak attraction and (typically) weaker repulsion dictates that, if sufficient thermal energy is available to a given particle, a finite probability exists for it to "escape" a cluster. Types of clusters can be categorized according to the timescale of this process into regimes of transient, dynamic and permanent clusters as depicted in Fig. 1.4.[75] While transient clusters can be defined as the instantaneous or random dynamic correlation of 2 or more particles, dynamic and permanent clusters can be distinguished by their lifetime relative to the characteristic diffusion time of a single particle. A dynamic cluster exists over a similar timescale as a single particle diffuses its own size, while the timescale over which particles in a permanent cluster remain correlated can be orders of magnitude longer.

An interesting feature of colloidal systems with competing interactions is the possibility that structural correlations can be independent of dynamic correlations. Depending on the solution conditions, the dynamic behavior of colloidal particles interacting with an SALR potential can be diffusive or kinetically arrested, yet under both conditions these systems have been observed to contain structural correlations over intermediate range lengthscales. Originally observed in molecular glasses, intermediate range order has been associated with clusters of molecules.[33, 64] It is hypothesized that these clusters then become percolated, which may cause the hindered mobility associated with glassy behavior.[33] In addition to this additional order

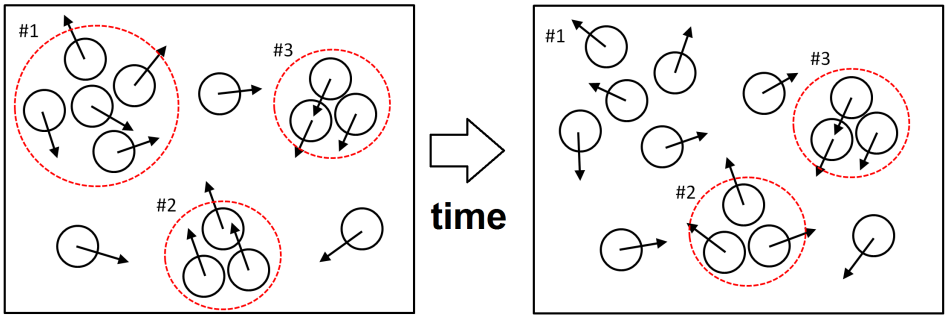


**Figure 1.4:** The difference in transient (#1), dynamic (#2) and permanent (#3) clusters are distinguished according to the time scale of their dynamic correlations. Though structurally correlated, cluster #1 is never dynamically correlated while cluster #2 diffused together for a finite time and cluster #3 moves collectively for an extended time period.

at intermediate lengthscales, molecular glasses contain structural order over short distances and disorder over long distances and thus, resemble molecular liquids. However, molecular liquids remain mobile over sufficiently long times such that they behave as fluids, despite the fact that molecules in these liquids are percolated. Therefore, this lack of intermediate range order is correlated with diffusive motion. Hence, in general, the structure and dynamics of molecular systems are directly related. Similarly, in the case of purely attractive colloidal materials, Hansen and Verlet identified a correlation between the magnitude of the monomer peak in the solution structure factor with the freezing transition (i.e., kinetic arrest).[46] In contrast, due to the prevalence of IRO in systems with competing interactions, identifying the state of a colloidal SALR system will require measurements of particle dynamics in addition to the solution structure.

Equilibrium clusters in an SALR system should be distinguished from widely studied systems of fractal aggregates, or flocs, that form irreversibly. Both flocs and clusters can form in systems with SALR interactions, but the primary attractive well is much deeper to cause flocculation and the repulsive strength is insufficient or non-existent to prevent further growth. One important difference between flocs and reversible clusters is their stability. Floc size grows irreversibly and continuously in

the reaction- or diffusion-limited regimes until it percolates or sediments.[57, 65] In contrast, clusters in an SALR system can have a thermodynamically preferred size distribution and these clusters are reversible, or in other words, particles within the clusters may have a finite rate of exchange with particles in the bulk. Despite the long lifetime of permanent clusters, the net repulsive force that stabilizes them to a particular size ensures that their growth is suspended and that they remain in equilibrium. Nevertheless, clusters can still interact to form larger structures, but the effective interactions between these structures are primarily repulsive.[69, 81]

Several studies have provided examples of cluster-induced kinetic arrest. Both simulations and theoretical calculations demonstrate that, for the right combination of potential parameters, clusters can form Wigner crystals or glasses comprised of clusters.[53, 81, 94] For less repulsive inter-cluster interactions, percolation (and therefore possibly gelation[31]) can occur with increasing volume fraction as a result of association between clusters rather than monomers.[14, 16, 53, 82, 85, 86, 94] Thus, clustered states can exhibit many properties similar to those found for traditional colloidal dispersions, but the pertinent dynamic parameters pertain to the mobility of clusters as opposed to monomers.

Due to the importance of short-time dynamics on the viscosity, it is critical to model the diffusion of particles, and possible clusters, in SALR systems. A significant hurdle to this task is the inherent polydispersity of cluster sizes and their finite lifetime.[75] If clusters exist as equilibrium aggregates, it may be possible for the particles composing a cluster to freely exchange between the cluster and monomer "state". Further, clusters can potentially associate into larger scale structures. Therefore, care must be taken to ensure that the different timescales associated with different types of clusters in SALR systems can be distinguished by experimental techniques. Recent work on highly concentrated solutions of lysozyme[34, 39, 62, 75] and monoclonal antibody proteins[103] have taken some initial steps in distinguishing individual cluster mobility and their collective motion by comparing neutron scattering and light scattering techniques that probe time scales differing by multiple orders of magnitude. In

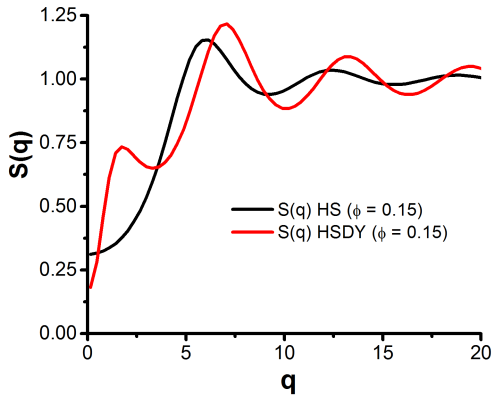


**Figure 1.5:** The structure factor of an SALR system and a HS system are compared for a system at $\phi = 0.15$.

the short time limit, shorter than the apparent lifetime of a cluster, the self-diffusion coefficient can be used to estimate the hydrodynamic radius of clusters.[75, 103]

### 1.5.4 Experimental Identification

Several methods have been used to observe the formation of clusters experimentally. For micron-sized particles, clusters can be directly imaged using confocal microscopy.[14, 53, 85, 86, 93] By direct tracking of particle movements, these experiments can yield a distribution of cluster sizes as well as information regarding their diffusivity and lifetime. Unfortunately, the resolution limit of microscopy prevents its use in studying colloids on the nanometer size scale, such as proteins. The typical technique of choice for these material is small angle scattering experiments. However, which features can be used to experimentally identify clustered fluids in nanoscale SALR systems is still debated in literature.[15, 60, 61, 62, 75, 88, 90, 92, 93]

Given the disordered structure of any fluid state, the extent of order is typically represented by a function called the pair distribution function, $g(r)$, which represents the probability of finding a neighboring particle at a distance $r$ from a reference particle. Small angle scattering experiments are able to obtain the solution structure factor,

$S(q)$, which can be calculated from $g(r)$ through a Fourier transformation. $S(q)$ is a function of $q$-vector, or momentum transfer, where $q \propto 2\pi/r$. Features of both $g(r)$ and $S(q)$ obtained experimentally can be compared with thermodynamic calculations to be discussed in Chapter 2.

Early small angle X-ray and neutron scattering studies of lysozyme protein[91, 93] identified an interesting peak at small $q$-values, indicative of structural correlations over intermediate range lengthscales (or intermediate range order). An example of such a peak in the $S(q)$ of an SALR system is provided in Fig. 1.5 relative to a HS fluid at the same volume fraction. This anomalous low-$q$ peak was considered to arise from cluster formation and hence, termed the cluster peak.[93] Simulation studies and thermodynamic calculations of $S(q)$ have determined the dependence of the low-$q$ peak position and magnitude on SALR potential parameters.[9, 12, 59] Cluster states estimated in this way have been mapped onto an effective SALR system phase diagram.[26] However, recent experimental studies[62, 75] have provided evidence that low-$q$ peaks are not necessarily a consequence of forming clusters of a preferred size, but are a general repercussion of SALR interactions resulting in a distribution of cluster sizes. Hence, the physical significance of cluster fluid phases demarcated in SALR phase diagrams according to the presence of a low-$q$ peak is unclear. As a result, further study is required to confirm the phase space of cluster fluids, which will be explored further in this dissertation.

### 1.5.5 Clusters in the Biopharmaceutical Industry

Given that proteins are naturally able to produce SALR interactions due to their chemistry, the biopharmaceutical industry is concerned with possible detrimental effects of clustering in therapeutic protein solutions. Understanding cluster formation by these "large molecules" at higher concentrations is important for improving pharmaceutical production and product stability and providing new and better delivery methods. Human therapeutics based on monoclonal antibodies (mAb) and other protein-based biologics (drugs derived from biological sources) have grown into one of

the largest sectors of the pharmaceutical market in the past few decades.[27, 47] The high selectivity and reproducibility of antibodies combined with few side effects has made these materials successful in treating several forms of cancer and a broad range of auto-immune disorders such as rheumatoid arthritis, psoriasis, Crohn's disease and transplant rejection.[27, 47]

Clarification of the phase behavior of clustering systems is of significant technological importance for biological materials, ranging from model globular proteins to therapeutic mAbs. Recent experimental work on high concentration solutions of mAbs[10, 17, 56, 74, 103, 105] and lysozyme[15, 16, 19, 34, 62, 75, 93] suggest extensive formation of clusters in solution. In particular, the presence of mAb clusters has been shown to strongly affect the solution viscosity and hypothesized to depend on the type of clusters formed.[41, 103] These commercial products provide an important framework to test the current understanding of the fundamental driving forces leading to the complex and diverse range of structures produced by SALR interactions as well as the implication of these structures on the solution viscosity.

### 1.6 Dissertation Goals and Outline

Due to the social and economic importance of soft matter materials, the main goal of this dissertation is to develop the theoretical understanding and experimental methods to explore the prevalent, but poorly understood colloidal systems with SALR interactions, with the intent to apply these developments to protein solutions. The discussion thus far has presented several proposed features of competing interactions, including the formation of cluster fluids and its effect on the solution viscosity. Developing a further understanding of these two features will have a significant impact on all colloidal materials with competing interactions. Within this diverse range of materials, biopharmaceutical therapeutic products can serve as an important and pertinent test of the current understanding of materials with SALR interactions and how to engineer their properties. To begin to address the remaining questions of cluster formation and stability, this work will focus on the hypotheses that (1) a generalized phase diagram

of cluster states exists and that, building upon this phase behavior, (2) cluster fluids can be identified as a significant driving force behind the observed increase in solution viscosity in certain concentrated protein solutions. By setting a precedent with this particular class of SALR systems, the fundamental connection between competing interactions, clusters and solution viscosity can be extended to understand the behavior and properties of colloidal materials in general, but based on a more solid theoretical foundation.

The progression of chapters through this dissertation will be concerned with these two hypothesis and therefore, two components of Fig. 1.1 for colloidal dispersions with competing interactions. By defining inter-particle interactions with an SALR potential, the scientific method will be used to explore (1) the influence of these interactions on the phase behavior relative to simpler interaction potentials as well as (2) the solution viscosity of new structural states composed of clusters. These broad initiatives have been decomposed into several successive fundamental studies, requiring a comprehensive combination of simulation and experimental techniques to identify characteristic properties of cluster fluids. The unique experimental and analytical framework developed in this dissertation will be separated into its individual components for each to be described in detail in Chapter 2.

In order to explore the material properties of cluster fluids, the solution conditions at which they form must first be determined. However, no experimentally accessible signatures, such as the magnitude and/or location of peaks in $S(q)$ or $g(r)$, have been confirmed as representative of clustered states. Identification of clusters will be accomplished through the use of detailed analysis of particle-level simulations. A thermodynamically relevant, but specific definition will be developed to distinguish clustered states based on the distribution of cluster sizes in the microstructure (Chapter 3). Next, these characteristics will be utilized with a variety of SALR potentials to map the regions of phase space where clustered states are formed. By appropriately normalizing these results, the compilation of all state points produces a generalized phase diagram of clustered states (Chapter 4), applicable to a wide range of materials

and conditions.

With a theoretical understanding of the conditions leading to cluster formation observed experimentally, the remaining fundamental task is to quantify the influence of clusters on solution viscosity. The globular protein, lysozyme, is used as a model experimental system to study the connection between structure and dynamics and the cluster-viscosity relationship. Initially, the interactions, structure, and dynamics are characterized in detail over a wide range of concentration and temperature. Significant viscosities as well as glassy dynamics are found to be qualitatively related to structural heterogeneity stemming from intermediate range order. The influence of these large-scale structures is quantified by developing a novel viscosity model that associates effective cluster-cluster interactions with the increase in viscosity. As a result, the model can extract an effective measure of cluster formation in these solutions (Chapter 5).

Finally, these fundamental studies are used as a foundation for identifying clustered states in formulations of biopharmaceutical therapeutic proteins. Specifically, two monoclonal antibodies are used as representative examples of cluster forming mAb formulations that produce large viscosities. Despite their more complex structure and interactions, the structural and dynamical features are semi-quantitatively related to the viscosity. In particular, formulation composition and protein surface chemistry are correlated with effective inter-protein interactions to provide generic metrics to identify clustering in these materials. One mAb is found to produce elongated, long-lived dimers that raise the viscosity due to enhanced excluded volume and repulsive inter-cluster interactions (Chapter 6). The other system appears to form small clusters at low concentrations with little effect on viscosity, which merge at higher concentrations to form large-scale, transient clusters leading to large viscosities (Chapter 7). These results are summarized and discussed with proposed future work in the conclusion of the dissertation (Chapter 8).

## REFERENCES


[1] Allen, M. P., and Tildesley, D. J. *Computer Simulation of Liquids*. Oxford University Press, 1987.

[2] Anderson, V. J., and Lekkerkerker, H. N. W. Insights into phase transition kinetics from colloid science. *Nature 416*, 6883 (2002), 811–815.

[3] Archer, A. J., Ionescu, C., Pini, D., and Reatto, L. Theory for the phase behaviour of a colloidal fluid with competing interactions. *J. Phys. Condens. Matter 20*, 41 (Oct. 2008), 415106.

[4] Archer, A. J., and Wilding, N. Phase behavior of a fluid with competing attractive and repulsive interactions. *Phys. Rev. E 76*, 3 (Sept. 2007), 1–14.

[5] Asherie, N., Lomakin, A., and Benedek, G. Phase Diagram of Colloidal Solutions. *Phys. Rev. Lett. 77*, 23 (Dec. 1996), 4832–4835.

[6] Bates, F. S., and Fredrickson, G. H. block copolymers-designer soft materials. *Phys. Today 52* (1999), 32.

[7] Bergenholtz, J., Brady, J. F., and Vicic, M. The non-Newtonian rheology of dilute colloidal suspensions. *J. Fluid Mech. 456* (Apr. 2002), 239–275.

[8] Bergenholtz, J., and Wagner, N. J. The Huggins Coefficient for the Square-Well Colloidal Fluid. *Ind. Eng. Chem. Res. 33*, 10 (1994), 2391–2397.

[9] Bomont, J.-M., Bretonnet, J.-L., and Costa, D. Temperature study of cluster formation in two-Yukawa fluids. *J. Chem. Phys. 132*, 18 (2010), 184508.

[10] Borwankar, A. U., Dinin, A. K., Laber, J. R., Twu, A., Wilson, B. K., Maynard, J. a., Truskett, T. M., and Johnston, K. P. Tunable equilibrium nanocluster dispersions at high protein concentrations. *Soft Matter 9*, 6 (2013), 1766.

[11] Brady, J. F. The rheological behavior of concentrated colloidal dispersions. *J. Chem. Phys. 99*, 1 (1993), 567.

[12] Broccio, M., Costa, D., Liu, Y., and Chen, S.-H. The structural properties of a two-Yukawa fluid: Simulation and analytical results. *J. Chem. Phys. 124*, 8 (Feb. 2006), 084501.

[13] Brown, R. A brief account of microscopical observations made in the months of June, July and August 1827, on the particles contained in the pollen of plants; and on the general existence of active molecules in organic and inorganic bodies. *Philos. Mag. Ser. 2 4* (1828), 161–173.

[14] Campbell, A., Anderson, V., van Duijneveldt, J. S., and Bartlett, P. Dynamical Arrest in Attractive Colloids: The Effect of Long-Range Repulsion. *Phys. Rev. Lett. 94*, 20 (May 2005), 1.

[15] Cardinaux, F., Stradner, A., Schurtenberger, P., Sciortino, F., and Zaccarelli, E. Modeling equilibrium clusters in lysozyme solutions. *Europhys. Lett. 77*, 4 (Feb. 2007), 48004.

[16] Cardinaux, F., Zaccarelli, E., Stradner, A., Bucciarelli, S., Farago, B., Egelhaaf, S. U., Sciortino, F., and Schurtenberger, P. Cluster-Driven Dynamical Arrest in Concentrated Lysozyme Solutions. *J. Phys. Chem. B 115*, 22 (June 2011), 7227.

[17] Castellanos, M. M., Pathak, J. a., and Colby, R. H. Both protein adsorption and aggregation contribute to shear yielding and viscosity increase in protein solutions. *Soft Matter 10*, 1 (2014), 122.

[18] Charbonneau, P., and Reichman, D. Phase behavior and far-from-equilibrium gelation in charged attractive colloids. *Phys. Rev. E 75*, 5 (May 2007), 1.

[19] Chen, S.-H., Broccio, M., Liu, Y., Fratini, E., and Baglioni, P. The two-Yukawa model and its applications: the cases of charged proteins and copolymer micellar solutions. *J. Appl. Crystallogr. 40*, s1 (Apr. 2007), s321–s326.

[20] Chiew, Y. C., and Glandt, E. D. Percolation behaviour of permeable and of adhesive spheres. *J. Phys. A. Math. Gen. 16*, 11 (1983), 2599–2608.

[21] Ciach, A. Mesoscopic theory for inhomogeneous mixtures. *Mol. Phys. 109*, 7-10 (Apr. 2011), 1101–1119.

[22] Ciach, A., and Gozdz, W. T. Mesoscopic description of network-forming clusters of weakly charged colloids. *Condens. Matter Phys. 13*, 2 (2010), 23603.

[23] Ciach, A., Pkalski, J., and Góźdź, W. T. Origin of similarity of phase diagrams in amphiphilic and colloidal systems with competing interactions. *Soft Matter 9*, 27 (2013), 6301.

[24] Cichocki, B., and Felderhof, B. U. Diffusion coefficients and effective viscosity of suspensions of sticky hard spheres with hydrodynamic interactions. *J. Chem. Phys. 93*, September (1990), 4427.

[25] Coniglio, A., Angelis, U. D., and Forlani, A. Pair connectedness and cluster size. *J. Phys. A. Math. Gen. 10*, 7 (1977), 1123.

[26] Costa, D., Caccamo, C., Bomont, J.-M., and Bretonnet, J.-L. Theoretical description of cluster formation in two-Yukawa competing fluids. *Mol. Phys. 109*, 23-24 (2011), 2845–2853.

[27] Daugherty, A. L., and Mrsny, R. J. Formulation and delivery issues for monoclonal antibody therapeutics. *Adv. Drug Deliv. Rev. 58*, 5-6 (Aug. 2006), 686–706.

[28] Deen, W. M. *Analysis of Transport Phenomena*. Oxford University Press, New York, 1998.

[29] Derjaguin, B. On the repulsive forces between charged colloidal particles and on the theory of slow coagulation and stability of lyophobe sols. *Trans. Faraday Soc. 35* (1940), 203–215.

[30] Destainville, N., and Foret, L. Thermodynamics of nanocluster phases: A unifying theory. *Phys. Rev. E 77*, 5 (May 2008), 1–5.

[31] Eberle, A. P. R., Wagner, N. J., and Castañeda Priego, R. Dynamical Arrest Transition in Nanoparticle Dispersions with Short-Range Interactions. *Phys. Rev. Lett. 106*, 10 (Mar. 2011), 1.

[32] Einstein, A. Über die von der molekularkinetischen Theorie der Wärme geforderte Bewegung von in ruhenden Flüssigkeiten suspendierten Teilchen. *Ann. Phys. 322*, 8 (1905), 549–560.

[33] Elliott, S. R. Medium-range structural order in covalent amorphous solids. *Nature 354* (1991), 445.

[34] Falus, P., Porcar, L., Fratini, E., Chen, W.-R., Faraone, A., Hong, K., Baglioni, P., and Liu, Y. Distinguishing the monomer to cluster phase transition in concentrated lysozyme solutions by studying the temperature dependence of the short-time dynamics. *J. Phys. Condens. Matter 24*, 6 (Feb. 2012), 064114.

[35] Foffi, G., McCullagh, G., Lawlor, A., Zaccarelli, E., Dawson, K., Sciortino, F., Tartaglia, P., Pini, D., and Stell, G. Phase equilibria and glass transition in colloidal systems with short-ranged attractive interactions: Application to protein crystallization. *Phys. Rev. E 65*, 3 (Mar. 2002), 031407.

[36] Frenkel, D. Colloidal encounters: a matter of attraction. *Science (80-. ). 314*, 5800 (Nov. 2006), 768–9.

[37] Frenkel, D., and Smit, B. *Understanding Molecular Simulations: From Algorithms to Applications*. Academic Press, 2002.

[38] Godfrin, P. D., Castañeda Priego, R., Liu, Y., and Wagner, N. J. Intermediate range order and structure in colloidal dispersions with competing interactions. *J. Chem. Phys. 139*, 15 (2013), 154904.

[39] Godfrin, P. D., Hudson, S. D., Hong, K., Porcar, L., Falus, P., Wagner, N. J., and Liu, Y. Excess viscous response from intrinsic structural heterogeneity caused by competing potential features. *Submitt. to Phys. Rev. Lett.* (2015).

[40] Godfrin, P. D., Valadez-Pérez, N. E., Castañeda Priego, R., Wagner, N. J., and Liu, Y. Generalized phase behavior of cluster formation in colloidal dispersions with competing interactions. *Soft Matter 10* (2014), 5061.

[41] Godfrin, P. D., Zarzar, J., Zarraga, I. E., Porcar, L., Falus, P., Wagner, N. J., and Liu, Y. Hierarchical cluster formation and its effect on the viscosity of concentrated monoclonal antibody formulations. *Submitt. to J. Phys. Chem. B* (2015).

[42] Gögelein, C., Nägele, G., Tuinier, R., Gibaud, T., Stradner, A., and Schurtenberger, P. A simple patchy colloid model for the phase behavior of lysozyme dispersions. *J. Chem. Phys. 129*, 8 (Aug. 2008), 085102.

[43] Groenewold, J., and Kegel, W. K. Colloidal cluster phases, gelation and nuclear matter. *J. Phys. Condens. Matter 16*, 42 (Oct. 2004), S4877–S4886.

[44] Hadgiivanova, R., Diamant, H., and Andelman, D. Kinetics of surfactant micellization: a free energy approach. *J. Phys. Chem. B 115*, 22 (June 2011), 7268–80.

[45] Hamaker, H. The Londonvan der Waals attraction between spherical particles. *Physica 4*, 1 (1937), 1058–1072.

[46] Hansen, J.-P., and Verlet, L. Phase transitions of the Lennard-Jones System. *Phys. Rev. 184*, 1 (1969), 151–161.

[47] Harris, R. J., Shire, S. J., and Winter, C. Commercial manufacturing scale formulation and analytical characterization of therapeutic recombinant antibodies. *Drug Dev. Res. 61*, 3 (Mar. 2004), 137–154.

[48] Hiemenz, P. C., and Rajagopalan, R. *Principles of Colloid and Surface Chemistry*, 3rd editio ed. Taylor & Francis Group, 1997.

[49] Hoover, W. G., and Ree, F. H. Melting Transition and Communal Entropy for Hard Spheres. *J. Chem. Phys. 49*, 1968 (1968), 3609.

[50] Israelachvili, J. N. *Intermolecular and Surface Forces*, 3rd editio ed. Elsevier, 2011.

[51] Jiang, T., and Wu, J. Cluster formation and bulk phase behavior of colloidal dispersions. *Phys. Rev. E 80*, 2 (Aug. 2009), 1–8.

[52] Johnston, K. P., Maynard, J. A., Truskett, T. M., Borwankar, A. U., Miller, M. A., Wilson, B. K., Dinin, A. K., Khan, T. A., and Kaczorowski, K. J. Concentrated Dispersions of Equilibrium Protein Nanoclusters That Reversibly Dissociate into Active Monomers. *ACS Nano 6*, 2 (Jan. 2012), 1357.

[53] Klix, C. L., Royall, C. P., and Tanaka, H. Structural and Dynamical Features of Multiple Metastable Glassy States in a Colloidal System with Competing Interactions. *Phys. Rev. Lett. 104*, 16 (Apr. 2010), 165702.

[54] Krishnamurthy, L.-N., and Wagner, N. J. The influence of weak attractive forces on the microstructure and rheology of colloidal dispersions. *J. Rheol. (N. Y. N. Y). 49*, 2 (2005), 475.

[55] Largo, J., Miller, M. A., and Sciortino, F. The vanishing limit of the square-well fluid: the adhesive hard-sphere model as a reference system. *J. Chem. Phys. 128*, 13 (Apr. 2008), 134513.

[56] Lilyestrom, W. G., Yadav, S., Shire, S. J., and Scherer, T. M. Monoclonal antibody self-association, cluster formation, and rheology at high concentrations. *J. Phys. Chem. B 117*, 21 (May 2013), 6373–84.

[57] Lin, M. Y., Lindsay, H. M., Weitz, D. A., Ball, R. C., Klein, R., and Meakin, P. Universality in colloid aggregation. *Nature 339* (1989), 360.

[58] Lionberger, R. A., and Russel, W. B. Microscopic theories of the rheology of stable colloidal dispersions. *Adv. Chem. Phys. 111* (2000), 399–474.

[59] Liu, Y., Chen, W.-R., and Chen, S.-H. Cluster formation in two-Yukawa fluids. *J. Chem. Phys. 122*, 4 (Jan. 2005), 44507.

[60] Liu, Y., Fratini, E., Baglioni, P., Chen, W.-R., and Chen, S.-H. Effective Long-Range Attraction between Protein Molecules in Solutions Studied by Small Angle Neutron Scattering. *Phys. Rev. Lett. 95*, 11 (Sept. 2005), 2–5.

[61] Liu, Y., Fratini, E., Baglioni, P., Chen, W.-R., Porcar, L., and Chen, S.-H. Liu et al. Reply. *Phys. Rev. Lett. 96*, 21 (June 2006), 219802.

[62] Liu, Y., Porcar, L., Chen, J., Chen, W.-r., Falus, P., Faraone, A., Fratini, E., Hong, K., and Baglioni, P. Lysozyme protein solution with an intermediate range order structure. *J. Phys. Chem. B 115*, 22 (June 2011), 7238.

[63] Lu, P. J., Zaccarelli, E., Ciulla, F., Schofield, A. B., Sciortino, F., and Weitz, D. A. Gelation of particles with short-range attraction. *Nature 453*, 7194 (May 2008), 499.

[64] Martin, J. D., Goettler, S. J., Fossé, N., and Iton, L. Designing intermediate-range order in amorphous materials. *Nature 419*, 6905 (Sept. 2002), 381–4.

[65] Meakin, P. Formation of fractal clusters and networks by irreversible diffusion-limited aggregation. *Phys. Rev. Lett. 51*, 13 (1983), 1119.

[66] Meth, J. S., Zane, S. G., Chi, C., Londono, J. D., Wood, B. A., Cotts, P., Keating, M., Guise, W., and Weigand, S. Development of Filler Structure in Colloidal Silica-Polymer Nanocomposites. *Macromolecules 44* (2011), 8301–8313.

[67] Mewis, J., and Wagner, N. J. *Colloidal Suspension Rheology*. Cambridge University Press, New York, 2012.

[68] Miller, M., and Frenkel, D. Phase diagram of the adhesive hard sphere fluid. *J. Chem. Phys. 121*, 1 (July 2004), 535.

[69] Mossa, S., Sciortino, F., Tartaglia, P., and Zaccarelli, E. Ground-state clusters for short-range attractive and long-range repulsive potentials. *Langmuir 20*, 24 (2004), 10756–10763.

[70] Mulheran, P., Pellenc, D., Bennett, R., Green, R., and Sperrin, M. Mechanisms and Dynamics of Protein Clustering on a Solid Surface. *Phys. Rev. Lett. 100*, 6 (Feb. 2008), 068102.

[71] Noro, M. G., and Frenkel, D. Extended corresponding-states behavior for particles with variable range attractions. *J. Chem. Phys. 113*, 8 (2000), 2941.

[72] Orea, P., Tapia-Medina, C., Pini, D., and Reiner, A. Thermodynamic properties of short-range attractive Yukawa fluid: simulation and theory. *J. Chem. Phys. 132*, 11 (Mar. 2010), 114108.

[73] Overbeek, J. T. G. Recent Developments in the Understanding of Colloid Stability. *J. Colloid Interface Sci. 58*, 2 (1977), 408.

[74] Pathak, J. A., Sologuren, R. R., and Narwal, R. Do Clustering Monoclonal Antibody Solutions Really Have a Concentration Dependence of Viscosity ? *Biophys. J. 104* (2013), 1–11.

[75] Porcar, L., Falus, P., Chen, W.-R., Faraone, A., Fratini, E., Hong, K., Baglioni, P., and Liu, Y. Formation of the Dynamic Clusters in Concentrated Lysozyme Protein Solutions. *J. Phys. Chem. Lett. 1*, 1 (Jan. 2010), 126.

[76] Pusey, P. N., and van Megen, W. Phase behaviour of concentrated suspensions of nearly hard colloidal spheres. *Nature 320* (1986), 340–342.

[77] Rueb, C. J., and Zukoski, C. F. Rheology of suspensions of weakly attractive particles: Approach to gelation. *J. Rheol. (N. Y. N. Y). 42*, 6 (1998), 1451.

[78] Russel, W. B., Wagner, N. J., and Mewis, J. Divergence in the low shear viscosity for Brownian hard-sphere dispersions: At random close packing or the glass transition? *J. Rheol. (N. Y. N. Y). 57*, 6 (2013), 1555.

[79] Sandler, S. I. *Chemical, Biochemical, and Engineering Thermodynamics*. 2006.

[80] Sciortino, F. Disordered materials: One liquid, two glasses. *Nat. Mater. 1* (2002), 145–146.

[81] Sciortino, F., Mossa, S., Zaccarelli, E., and Tartaglia, P. Equilibrium Cluster Phases and Low-Density Arrested Disordered States: The Role of Short-Range Attraction and Long-Range Repulsion. *Phys. Rev. Lett. 93*, 5 (July 2004), 5.

[82] Sciortino, F., Tartaglia, P., and Zaccarelli, E. One-dimensional cluster growth and branching gels in colloidal systems with short-range depletion attraction and screened electrostatic repulsion. *J. Phys. Chem. B 109*, 46 (2005), 21942.

[83] Sear, R. P., Chung, S. W., Markovich, G., Gelbart, W. M., and Heath, J. R. Spontaneous patterning of quantum dots at the air-water interface. *Phys. Rev. E 59*, 6 (June 1999), R6255–8.

[84] Seaton, N. A., and Glandt, E. D. Aggregation and percolation in a system of adhesive spheres. *J. Chem. Phys. 86*, 8 (1987), 4668.

[85] Sedgwick, H., Egelhaaf, S. U., and Poon, W. C. K. Clusters and gels in systems of sticky particles. *J. Phys. Condens. Matter 16*, 42 (Oct. 2004), S4913–S4922.

[86] Segrè, P., Prasad, V., Schofield, A., and Weitz, D. A. Glasslike Kinetic Arrest at the Colloidal-Gelation Transition. *Phys. Rev. Lett. 86*, 26 (June 2001), 6042.

[87] Seul, M., and Andelman, D. Domain Shapes and Patterns: The Phenomenology of Modulated Phases. *Science (80-. ). 267*, 5197 (1995), 476–483.

[88] Shukla, A., Mylonas, E., Di Cola, E., Finet, S., Timmins, P., Narayanan, T., and Svergun, D. I. Absence of equilibrium cluster phase in concentrated lysozyme solutions. *Proc. Natl. Acad. Sci. U. S. A. 105*, 13 (Apr. 2008), 5075–80.

[89] Smallenburg, F., and Sciortino, F. Liquids more stable than crystals. *Nat. Phys. 9* (2013), 554–558.

[90] Stradner, A., Cardinaux, F., Egelhaaf, S. U., and Schurtenberger, P. Do equilibrium clusters exist in concentrated lysozyme solutions? *Proc. Natl. Acad. Sci. U. S. A. 105*, 44 (2008), E75.

[91] Stradner, A., Cardinaux, F., and Schurtenberger, P. A small-angle scattering study on equilibrium clusters in lysozyme solutions. *J. Phys. Chem. B 110*, 42 (Oct. 2006), 21222–31.

[92] Stradner, A., Cardinaux, F., and Schurtenberger, P. Comment on Effective Long-Range Attraction between Protein Molecules in Solution Studied by Small Angle Neutron Scattering. *Phys. Rev. Lett. 96*, 21 (June 2006), 219801.

[93] Stradner, A., Sedgwick, H., Cardinaux, F., Poon, W. C. K., Egelhaaf, S. U., and Schurtenberger, P. Equilibrium cluster formation in concentrated protein solutions and colloids. *Nature 432*, 7016 (Nov. 2004), 492.

[94] Toledano, J. C. F., Sciortino, F., and Zaccarelli, E. Colloidal systems with competing interactions: from an arrested repulsive cluster phase to a gel. *Soft Matter 5*, 12 (2009), 2390.

[95] Valadez-Pérez, N. E., Castañeda Priego, R., and Liu, Y. Percolation in colloidal systems with competing interactions: the role of long-range repulsion. *RSC Adv. 3* (2013), 25110.

[96] Valadez-Pérez, N. E., Liu, Y., Eberle, A. P. R., Wagner, N. J., and Castañeda Priego, R. Dynamical arrest in adhesive hard-sphere dispersions driven by rigidity percolation. *Phys. Rev. E 88*, 6 (2013), 060302(R).

[97] van der Waals, J. D. *On the continuity of the gas and liquid state*. PhD thesis, Leiden University, 1873.

[98] van Megen, W., Mortensen, T., Williams, S., and Müller, J. Measurement of the self-intermediate scattering function of suspensions of hard spherical particles near the glass transition. *Phys. Rev. E 58*, 5 (1998), 6073–6085.

[99] van Megen, W., and Underwood, S. M. Change in Crystallization Mechanism at the Glass-Transition of Colloidal Spheres. *Nature 362* (1993), 616–618.

[100] Wagner, N. J., and Woutersen, A. T. J. M. The viscosity of bimodal and polydisperse suspensions of hard spheres in the dilute limit. *J. Fluid Mech. 278* (1994), 267–287.

[101] Yadav, S., Laue, T. M., Kalonia, D. S., Singh, S. N., and Shire, S. J. The influence of charge distribution on self-association and viscosity behavior of monoclonal antibody solutions. *Mol. Pharm. 9*, 4 (Apr. 2012), 791–802.

[102] Yates, J. T., and Johnson, J. K. *Molecular Physical Chemistry for Engineers*. University Science Books, 2007.

[103] Yearley, E. J., Godfrin, P. D., Perevozchikova, T., Zhang, H., Falus, P., Porcar, L., Nagao, M., Curtis, J., Gawande, P., Taing, R., Zarraga, I. E., Wagner, N. J., and Liu, Y. Observation of small cluster formation in concentrated monoclonal antibody solutions and its implications to solution viscosity. *Biophys. J. 106*, 8 (2014), 1763–1770.

[104] Zaccarelli, E. Colloidal gels: equilibrium and non-equilibrium routes. *J. Phys. Condens. Matter 19*, 32 (Aug. 2007), 1–61.

[105] Zarraga, I. E., Taing, R., Zarzar, J., Luoma, J., Hsiung, J., and Patel, A. High Shear Rheology and Anisotropy in Concentrated Solutions of Monoclonal Antibodies. *J. Pharm. Sci. 102*, 8 (2013), 2538–2549.

# Chapter 2

# METHODOLOGY: THEORY, SIMULATIONS, AND EXPERIMENTS

## 2.1 Background

Cluster fluids are an equilibrium state of matter that have a unique combination of structural and dynamic features. Previous studies have discussed these characteristics, but the feasibility of experimentally distinguishing these states is still unclear in the literature. Therefore, this work aims to develop a rigorous methodology to identify clustered states and utilize this framework to study their properties.

Accurately quantifying clustered states and their associated properties requires several approaches. The foundation of these characterization efforts is a thermodynamic description of equilibrium behavior. Therefore, a short discussion of important statistical thermodynamic functions is presented with respect to colloidal particles. Detailed information of cluster microstructure is extracted from simulations used to generate equilibrium configurations in conjunction with calculations of thermodynamic parameters. This work will be corroborated with small angle neutron scattering, dynamic light scattering, and rheology experiments. These theoretical, simulation and experimental techniques are outlined in detail below.

## 2.2 Thermodynamics of Colloidal Systems

Several methods are available to study the structure and phase behavior of systems with a given interaction potential, including experimentation, simulation and theoretical calculations. Each has their own merits and deficiencies. Through experimentation, the phase(s) produced at each state point can be directly observed, but this technique requires several samples to be prepared and may also require multiple experimental techniques to accurately distinguish between phases. Several types of simulation

protocols, such as the canonical and Gibbs ensemble Monte Carlo (MC) methods, enable the calculation of phase behavior for a model potential of interaction, but require some *a priori* knowledge of the states to be examined. Theoretical approaches have also been used to calculate phase transitions, including Barker-Henderson, thermodynamic, and discrete perturbation theories, integral equation theory (IET) approaches with various closure relations, and density functional theory.[26] As with simulation methods, theoretical calculations require the definition of some pre-determined distinction between states. In this work, experimental techniques, canonical ensemble MC simulations, and IET calculations will be used to characterize solution structure and produce phase diagrams of SALR systems. The fundamental concepts, upon which these methods are based and unified, are borne from statistical thermodynamics.

The solution structure of liquids are difficult to quantify due to the relatively high density and the inherent disorder in their structure. An important concept is that each system (defined by the density and interaction potential) contains an ensemble of configurations that are each weighted to produce an average structure. Under any set of sample conditions, a material is continuously fluctuating and attempting to reach a minimum on a complex energy landscape that is a function of every particle's coordinates and momentum.[19, 26] Despite this complexity, the ergodic hypothesis postulates that if a system is in equilibrium the (stochastic) ensemble average of a given thermodynamic property is identical to the time average.[25]

Within the context of ergodicity, calculating a weighted average structure is a function of all realizable configurations.[13] Depending on the potential and the relative spacing of each set of particles within a particular configuration, that realization of the system may have a low configurational energy and therefore be a low point on the energy landscape. As a result, that orientation would be preferred, occurring more frequently than others and therefore be heavily weighted in the average structure of the system. Artificially creating millions of configurations and performing such a weighting is exactly the premise of MC simulations. Theoretical calculations attempt to avoid the time consuming task of realizing these configurations by estimating the statistical

weighting using relations of varying orders of simplification.

### 2.2.1 Interaction Potentials

Several functional forms have been used to represent the SALR potential, typically with variations of the attractive term. Repulsive interactions are well known to be accurately represented by a Yukawa form in accordance with Debye-Hückel theory.[15] Throughout this work two SALR potentials will be referenced. A representative potential of each type is shown in Fig. 2.1.

The first type of potential used, known as a hard sphere double Yukawa (HSDY) potential, combines hard sphere excluded volume with an additional short range attraction and a longer range repulsion as:

$$\frac{U_{HSDY}(r)}{kT} = \begin{cases} \infty & r \leq 1 \\ \left(\frac{1}{r}\right)\left( - K_1 \exp[-z_1(r-1)] + K_2 \exp[-z_2(r-1)]\right) & r > 1, \end{cases} \tag{2.1}$$

where $r$ is the particle-particle separation normalized by the particle diameter ($\sigma$), $z_1$ and $z_2$ are the inverse ranges of attraction and repulsion, respectively, and $K_1$ and $K_2$ are the strengths of attraction and repulsion, respectively. The equation can be recast as a function of reduced temperature, $T^* = (K_1 - K_2)/k_BT$, which represents the relative strength of the well depth to thermal energy, and the relative strength of attraction to repulsion, $\lambda$, such that $K_1 = 1/[T^*(1-\lambda)]$ and $K_2 = \lambda/[T^*(1-\lambda)]$.

The HSDY potential is a widely studied model potential chosen for its demonstrated ability to qualitatively reproduce the solution structure and phase behavior of protein and micellar solutions and thus, its applicability to experimentally relevant systems.[7, 18, 29] Further, the HSDY potential has been demonstrated by previous integral equation theory calculations to form intermediate range order (IRO) peaks pertinent to cluster fluids.[4, 5, 8, 16] Though the model potential is not derived from specific molecular interactions, it is widely adopted because it quantitatively represents the total effective force acting between particles.[14]

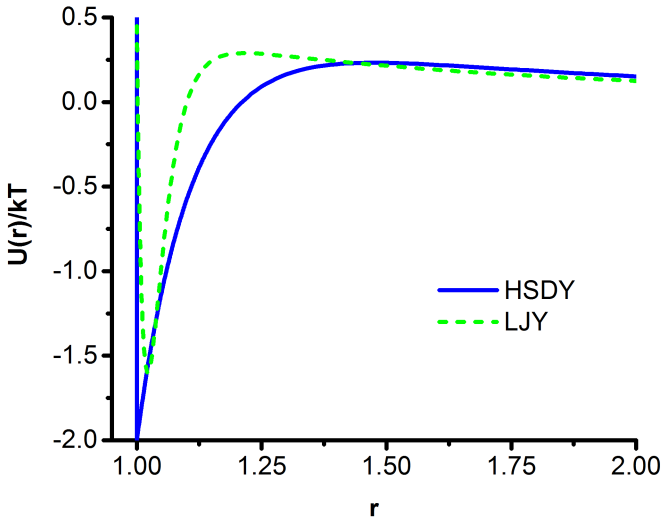


**Figure 2.1:** Two functional representations of an SALR potential, the HSDY and LJY potentials, are compared.

Another convenient and popular choice is a pair wise potential that combines a Leonard-Jones $2\alpha$ - $\alpha$ form of short range attraction with a longer range Yukawa repulsion, called the Leonard-Jones-Yukawa (LJY) interaction potential:

$$\frac{U_{LJY}(r)}{kT} = \frac{1}{T^*}\left[4\left(r^{-2\alpha} - r^{-\alpha}\right) + A\left(\frac{\xi}{r}\right)\exp\left(\frac{-r}{\xi}\right)\right]. \tag{2.2}$$

where $\alpha$ is inversely related to the range of attraction, $\xi$ is the range of repulsion, and $A$ is the ratio of strength of repulsion to strength of attraction. This potential has been previously shown to produce clustered and percolated states[28, 30] and is representative of attractive interactions arising from dispersion forces.[15]

### 2.2.2 Structural Functions

Structure can be quantified by particle correlation functions, which are typically represented by the pair distribution function, $g(r)$. The pair distribution function is

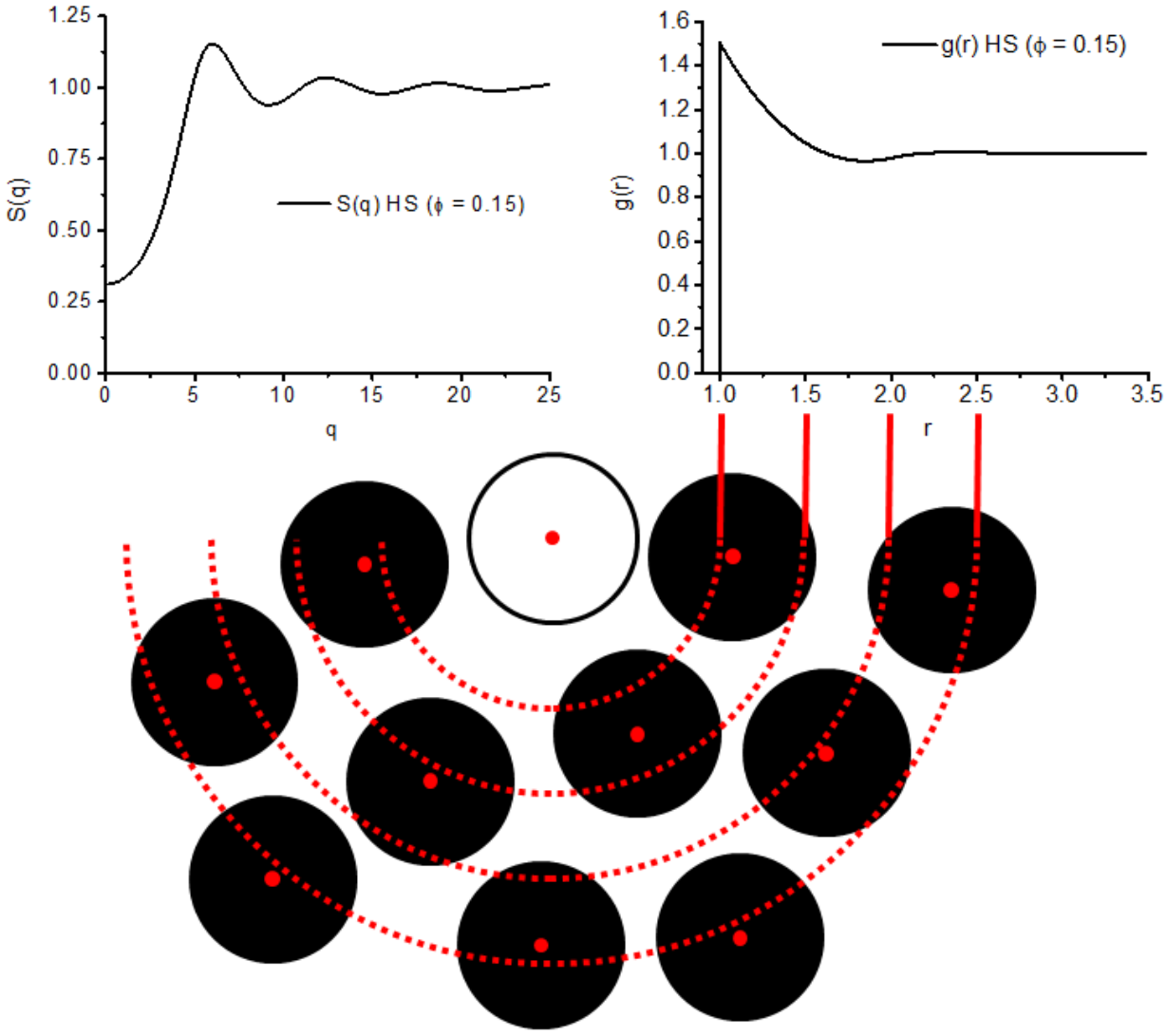


**Figure 2.2:** A characteristic structure factor (left) and pair distribution function (right) for a hard sphere fluid are shown with a physical representation.

the normalized probability of finding two particles a distance $r_{12}$ apart in the presence of all possible configurations of the remaining particles:

$$g(r_{12}) = \frac{V^2}{N^2}\frac{1}{Z_N}\int\cdots\int \exp[-\beta U_N(r_3\cdots r_N; r_{12})]\mathrm{d}r_3\cdots\mathrm{d}r_N \tag{2.3}$$

where $N$ is the number of particles, $V$ is the volume of the system, $\beta = \frac{1}{kT}$, $U_N$ is the energy of the given configuration of $N$ particles, and $Z_N$ is the configuration integral

$$Z_N(r_1\cdots r_N) = \int\cdots\int \exp[-\beta U_N(r_1\cdots r_N)]\mathrm{d}r_1\cdots\mathrm{d}r_N \tag{2.4}$$

that represents a Boltzmann average probability of all possible configurations that can be realized in a sample of $N$ particles in a volume $V$.[13] As an example, the regularly repeated spacing between particles in crystals would produce sharp peaks at those distances defining the crystal structure. However, the inherent disorder in fluids will produce broad peaks corresponding to spherical isotropic shells of particles oriented relative to some central particle. Figure 2.2 provides a representative $g(r)$ for a hard sphere fluid (at a volume fraction $\phi = 0.15$), which contains a characteristic peak at contact followed by a depletion zone and a weak secondary peak. The pictorial representation at the bottom of Fig. 2.2 highlights the various shells within which the centers of neighboring particles reside relative to the central (unfilled) sphere. Eq. 2.3 clearly indicates the direct impact of the interaction potential on the resulting average microstructure and thus the phase behavior.

An experimentally relevant function that is directly obtained from small angle scattering measurements is the inter-particle structure factor, $S(q)$. The structure factor is the Fourier transformation of a function of the radial distribution function:

$$S(q) = 1 + \rho\int_0^\infty \frac{\sin(qr)}{qr}[g(r) - 1]4\pi r^2\mathrm{d}r \tag{2.5}$$

which is a function of particle separation $r$, solution density $\rho$ and the scattering vector $q$ defined as

$$q = \left(\frac{4\pi}{\lambda}\right)\sin\left(\frac{\theta}{2}\right) \tag{2.6}$$

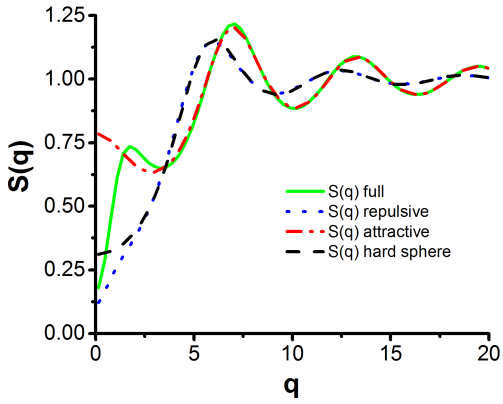


**Figure 2.3:** The structure factors of colloidal systems with potentials including HS (black dashed line), attractive (red dash-dot-dot line), repulsive (blue dotted line) and SALR (green solid line) interactions are compared at the same volume fraction.

with the incident wavelength, $\lambda$, and scattering angle, $\theta$, as parameters.[13, 19, 25] This function will produce peaks similar to that observed in $g(r)$ that will appear in the frequency spectrum at $q$-values corresponding to roughly $2\pi/q$. The resulting $S(q)$ for the hard sphere fluid at $\phi = 0.15$ is also provided in Fig. 2.2. The peaks in $S(q)$ result from the frequency of density fluctuations due to the particle excluded volume. In addition to its experimental relevance, $S(q)$ provides a more sensitive measurement of long lengthscale correlations compared to $g(r)$, which will be important for conditions that produce clusters.

In particular, the influence of interactions on the solution structure factor are most prevalent at small $q$-values that represent intermediate to large lengthscales. Several $S(q)$ examples are compared in Fig. 2.3 for different forms of interaction potentials, with the HS result serving as a basis to interpret the effect of the interactions. From the specific scenario present in Fig. 2.3, the general implication of attractive forces is shown as an increase in the magnitude of $S(q)$ at low-$q$, while repulsive forces decrease the magnitude. A physical interpretation arises from the relationship between the isothermal compressibility, $\chi_T$, and the zero $q$-value limit of the structure factor:

$S(0) = k_B T \rho \chi_T$, where $\rho$ is the particle density.[19, 25] For example, more repulsive systems will resist compression more strongly and therefore the change in volume with pressure will decrease via $\chi_T$ and thus $S(0)$. Interestingly, SALR interactions are capable of producing a unique feature introduced in Chapter 1. Although not observed for all SALR potentials, an appropriate combination of attraction and repulsion results in a peak at small $q$-values, which is never observed in the $S(q)$ produced by other isotropic potentials.

### 2.2.3 Integral Equation Theory

Integral equation theory (IET) calculates the pair distribution function by first decomposing $g(r_{12})$ into a direct and indirect component, as proposed by Ornstein and Zernike. The resulting Ornstein-Zernike (OZ) equation is typically written in terms of a "total correlation function", $h(r_{12})$, that represents the change in probability of finding a second particle a distance $r_{12}$ from a central particle due to its presence.[22] The two contributions to the OZ equation

$$h(r_{12}) = g(r_{12}) - 1 = c(r_{12}) + \rho \int c(r_{13}) h(r_{23}) \mathrm{d}r_3 \tag{2.7}$$

are the direct component captured by the "direct correlation function", $c(r_{12})$, and the indirect component represented by the integral term. In essence, $c(r_{12})$ represents the direct influence of particle 1 on particle 2, while the indirect component is a result of the direct influence of particle 1 on particle 3 that in turn influences particle 2. The relation is more conveniently written in reciprocal space, as the convolution theorem can be applied to the Fourier transform of the indirect term resulting in

$$\hat{H}(k) = \hat{C}(k) + \rho \hat{C}(k) \hat{H}(k) \tag{2.8}$$

where $\hat{H}(k)$ and $\hat{C}(k)$ are the Fourier transforms of $h(r_{12})$ and $c(r_{12})$, respectively. Both $h(r_{12})$ and $c(r_{12})$ must be solved simultaneously, which requires the second component of IET – a closure relation. One can imagine that the indirect interaction between two particles by a third particle can be perpetuated *ad infinitum* with any number of

"middle man" particles. Therefore, closure relations are used, and named, for their resolution of this issue by relating higher order interactions to some combination of the individual two-body interactions involved.

Throughout this work, a thermodynamically self-consistent closure relation will be used that has been outlined previously and demonstrated as highly accurate for SALR potentials.[5, 16] The closure utilizes the rHMSA functional form

$$h(r)+1=\exp\left[\frac{-U_{rep}(r)}{kT}\right]\left(1+\frac{\exp\left[f(r)\left(h(r)-c(r)-\frac{U_{att}(r)}{kT}\right)\right]-1}{f(r)}\right) \tag{2.9}$$

where $r$ has replaced $r_{12}$, $U_{att}(r)$ and $U_{rep}(r)$ are the attractive and repulsive components of the potential, respectively, $f(r)=1-e^{-1/(\alpha r)}$, and $\alpha$ is a mixing parameter shifted to equate the compressibility calculated by both the virial equation and fluctuation routes (i.e., to fulfill thermodynamic self-consistency).[5, 16]

### 2.3 Monte Carlo Simulations

In order to study the microstructure of colloidal suspensions with SALR interactions in more detail, MC simulations using the Metropolis algorithm[1, 11] are used to generate configurations consisting of 1728 particles in the canonical (NVT) ensemble with periodic boundary conditions. Each configuration is weighted, or accepted, according to a Boltzmann factor, $e^{-\beta U_N}$. Starting from a simple cubic lattice, each system is thermalized for 2x10$^7$ steps, where a step is the (attempted) move of a single particle. After equilibration, thermodynamic and structural parameters are averaged over 4x10$^4$ independent configurations. The initial displacement distance of 0.1, where all distances are normalized by the particle diameter $\sigma$, is dynamically adjusted to maintain an acceptance ratio of 30%. All parameters were averaged over 10 different seeds to reduce the intrinsic uncertainties. System size effects were also monitored under a few conditions, but in all cases $N=1728$ particles provided a reasonable system size to optimize the computational time.

As a typical representation of the inter-particle structure obtained from scattering experiments, the ensemble average pair distribution function and structure factor

are calculated for each state. All particle configurations are used to calculate the average $g(r)$ using direct summation according to:

$$g(r) = \frac{V^2}{N^2}\left\langle \sum_{i=1}^{N}\sum_{j=1}^{N} \frac{\delta(r_{ij}-r)}{V} \right\rangle \tag{2.10}$$

using standard methods,[1, 11] where $\delta$ is the Dirac delta function. To avoid artificial long-range correlations due to implementing periodic boundary conditions, the box size sets the upper limit of distances for which $g(r)$ is calculated. The solution structure factor is then determined by combining Eq. 2.10 with Eq. 2.5. All other pertinent calculations using simulated configurations are outlined in the appropriate chapter.

## 2.4 Small Angle Neutron Scattering

Small angle neutron scattering (SANS) experiments were conducted on the D-22 and D-33 beamlines at the Institut Laue-Langevin (ILL) in Grenoble, France and on the NG-3 (now NG-B30), NG-7, and NG-B10 (nSoft) beamlines at the NIST Center for Neutron Research (NCNR) in Gaithersburg, MD. The scattering intensity was obtained over scattering vectors (or $q$-values) ranging from 0.0028 $\text{Å}^{-1}$ to 0.5296 $\text{Å}^{-1}$. Samples were studied at multiple temperatures using either quartz Hellma (banjo) cells or standard NCNR SANS cells with quartz windows with a 1 mm pathlength. All samples were studied using a water bath with a temperature control of roughly $0.1°C$. The main goal of these studies is to extract effective interaction parameters under various conditions by fitting experimental $S(q)$ functions with the above IET calculations, according to Eq. 2.5.

Scattering intensity is initially obtained on a two-dimensional detector. Absolute scattering intensities on each pixel are determined by normalizing the sample intensity by several important factors, including the background and sample cell scattering and their corresponding transmissions. The normalization procedure is documented in Ref. [17], which was conducted using software provided by the NCNR and ILL, depending on the facility that was used to obtain the raw data. Finally, one-dimensional intensities

are obtained by an annular average over all pixels within a ring with a radial distance and thickness corresponding to a particular $q$-value.

The scattering intensity, $I(q)$, from a solution of *spherically isotropic*, monodisperse scatterers is:[31]

$$I(q) = \phi V(\Delta\rho)^2 P(q) S(q) + B \tag{2.11}$$

Here, $q$ is the scattering vector defined in Eq. 2.6, $B$ is the background scattering intensity, $\phi$ is the particle volume fraction, $V$ is the particle volume, and $\Delta\rho$ is the scattering length density different between the particle and solvent. The remaining functions of $q$ are the inter-particle structure factor, $S(q)$, also defined previously in Eq. 2.5, and the normalized form factor, $P(q)$, which is the Fourier transform of the intra-particle density correlations,

$$P(q) = \frac{1}{V_p{}^2}\langle |F(q)|^2 \rangle \tag{2.12}$$

where $V_p$ is the volume of a particle and

$$F(q) = \frac{1}{V}\int_{V_p} \rho(r) e^{-iq*r} \mathrm{d}r \tag{2.13}$$

In the case of a uniform spherical particle of radius, $R_p$, the form factor is simply

$$P(q) = \left[\frac{3}{qR_p}\left(\frac{\sin(qR_p) - (qR_p)\cos(qR_p)}{(qR_p)^2}\right)\right]^2 \tag{2.14}$$

In practice $P(q)$ is typically obtained by the scattering intensity of a dilute sample and subsequently fitted with appropriate models to extract relevant parameters.

In the case of dispersions of non-spherical particles, the intra- and inter- particle structure factor, $P(q)$ and $S(q)$, can no longer be conveniently decoupled. Under such conditions, as will be encountered later in this work, the total scattering intensity becomes

$$I(q) = \phi V(\Delta\rho)^2 P(q) S_{eff}(q) + B \tag{2.15}$$

where $S_{eff}(q) = 1 + \beta(q)[S(q) - 1]$ is an effective structure factor and $\beta(q)$ is a decoupling function[6, 18] defined as

$$\beta(q) = \frac{|\langle F(q) \rangle|^2}{\langle |F(q)|^2 \rangle} \tag{2.16}$$

Once an appropriate structure is found to model the form factor, $\beta(q)$ can be numerically calculated as it is only a function of intra-particle orientation. Normalizing $S_{eff}(q)$ by $\beta(q)$ to produce $S(q)$ subsequently allows the underlying interactions to be modeled using IET. However, current numerical methods are only able to determine *spherically symmetric* interaction potentials. Considering the anisotropic shape of the particles, such a representation is likely inaccurate and the resulting interaction parameters need to be interpreted carefully.

## 2.5 Neutron Spin Echo

Neutron spin echo (NSE) experiments were conducted on the IN-15 beamline at the ILL in Grenoble, France.[27] Samples were prepared on site, pipetted into 1 mm square quartz cells, and stored in a custom temperature controlled sample chamber. All samples were allowed 30 to 60 minutes to reach thermal equilibrium at each of the temperatures studied. Intermediate scattering functions (ISF), represented as $F_s(q,t)$, were obtained up to correlation times of 50 ns at 30 to 35 $q$-values ranging from 0.03 $\text{Å}^{-1}$ to 0.20 $\text{Å}^{-1}$ at each sample condition studied.

NSE experiments measure the ISF by directly detecting on a two-dimensional detector the shift in polarization of an initially polarized neutron beam due to its interaction with the sample at a range of correlation times. The experimental set-up is represented in Fig. 2.4, which shows the path of the neutron beam through the first and second magnetic fields ("coils") located before and after the sample, respectively.[12] Different Fourier times are acquired by changing the field strength of the two main coils at a given neutron wavelength. Specifically, a larger field strength and wavelength produce a longer correlation time.

The final state of a given neutron depends on its initial state and the dynamics of the sample, which will cause the state of the neutron to change (if they interact). While the beam contains neutrons with a spread of velocities (or wavelengths or energy), the amount of time an individual neutron spends in the first coil depends on its specific velocity. As a result, the direction of its polarization will rotate (or "process") an

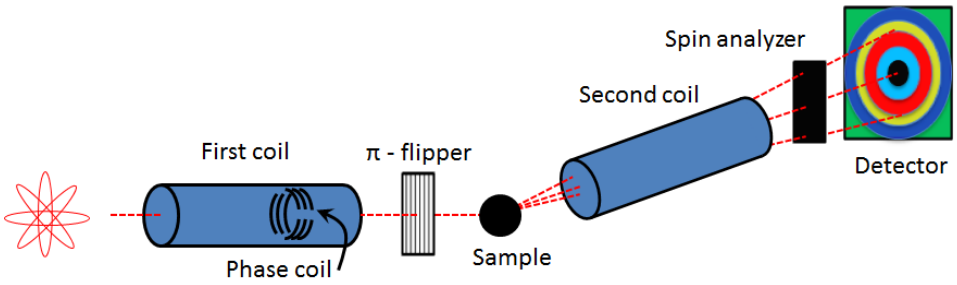


**Figure 2.4:** An ideal configuration of an NSE spectrometer. The neutron beam enters the first coil and passes through a spin ($\pi$) flipper before interacting with the sample. Scattered neutrons then pass through the second coil before being analyzed and detected on the two-dimensional detector.

amount proportional to the field strength and its speed. Upon interacting with the sample, three things may happen to any given neutron. The neutron may have it's spin flip with a probability of 2/3, it may scatter at a particular angle (or $q$-value) from its original trajectory, and it may lose or gain energy relative to it's initial state. The quantum mechanical probability of spin flipping is accounted for by a procedure known as polarization analysis, which sets the lower and upper limit of the total polarization of the beam. The corresponding $q$-value of each pixel on the detector is determined in the same manner as with SANS measurements, as shown by the various rings on the detector in Fig. 2.4. Finally, any change in a neutron's velocity due to quasi-elastic scattering causes it to spend a different amount of time in the second coil compared to the first coil, resulting in a change in polarization.

Due to the quantum mechanical nature of neutrons, combined with an inherent polydisperse distribution of wavelengths (velocities) within the neutron beam, a pattern of intensities will appear on the detector that reflects the relative probability of a given neutron to traverse the instrument geometry and arrive at that given location (or $q$-value). An additional "phase coil" sits within the first coil that shifts the strength of its magnetic field relative to the second coil, which alters the observed intensity. Changing the phase coil field strength probes the phase shift in the polarization of the neutron

beam by creating an offset in the total field strength between the first and second main coils. As a result, the intensity as a function of phase coil field strength is a damped cosine functional form. The phase coil field strength producing an intensity maximum is known as the echo point and depends only on the mean and standard deviation of the neutron beam's wavelength. The scattering intensity of a sample measured at the echo point is directly related to the polarization. An ISF for that sample is acquired at a given $q$-value and Fourier time by normalizing its polarization by that of an ideal elastic scatterer under the same conditions.[24]

In the short-time limit, the ISF can be fit with a single exponential decay to extract a $q$-dependent collective diffusion coefficient, $D_c(q)$, according to

$$\frac{F_s(q,t)}{F_s(q,0)} = \exp[-q^2 D_c(q) t] \tag{2.17}$$

where $D_c(q) = D_0 \frac{H(q)}{S(q)}$.[2, 21] $H(q)$ is the hydrodynamic function, which represents the change in particle diffusion at a given $q$-value (lengthscale) caused by solvent flows resulting from the motion of nearby particles. In the limit of large $q$-values,$S(q)$ approaches a value of 1 and $\lim_{q\to\infty} H(q) = \frac{D_s}{D_0}$, where $D_s$ is the short-time self diffusion coefficient. Consequently, $\lim_{q\to\infty} D_c(q) = D_s$.[10, 23]

## 2.6 Dynamic Light Scattering

A DynaPro NanoStar instrument (Wyatt Technology Corp., Santa Barbara, CA) was used for dynamic light scattering (DLS) measurements over a range of conditions. All samples were allowed to thermally equilibrate at each temperature for 30 minutes before taking 5 independent measurements of the scattered intensity over a correlation time range of 500 to 5x$10^7$ ns. The instrument was operated with a 663 nm wavelength laser at 90° scattering angle. The scattering wave vector was calculated according to $q = \frac{4\pi n}{\lambda}\sin(\frac{\theta}{2})$, where n is the refractive index of the sample.

The output from the DLS experiments is a digital autocorrelation of the scattered intensity. When normalized by the average count rate at the given scattering vector, the output function is related to the heterodyne autocorrelation function,

$F_1(q,t)$,[3] according to the Siegert relation[15]

$$\frac{C(q,t)}{[I(q)]^2} = 1 + A\left|\frac{F_1(q,t)}{F_1(q,0)}\right|^2 \tag{2.18}$$

The heterodyne and self-intermediate scattering functions are related by $F_1(q,t) = \langle N\rangle F_s(q,t)$,[3] from which the collective diffusion coefficient can be extracted as demonstrated in Eq. 2.17. The parameter A is a coherence factor and is an instrument-dependent fitting parameter. Additionally, the data can be analyzed using the Cumulant method according to

$$\frac{F_s(q,t)}{F_s(q,0)} = \exp\left[-q^2 D_c(q)t\right]\left(1 + \frac{\mu}{2}t^2 - \cdots\right) \tag{2.19}$$

which captures non-linearity by the first order deviation term $\mu$, where the variance of the average diffusion coefficient is related to $\sigma^2 \propto \mu/(q^2 D_c(q))$.

In the limit of infinite dilution, where $D_c(q) \approx D_0$, the hydrodynamic radius, $R_h$, of the particle of interest can be estimated by the Stokes-Einstein relation[20]

$$R_h = \frac{kT}{6\pi\eta_s D_0} \tag{2.20}$$

where $k$ is the Boltzmann constant, $T$ is the temperature, and $\eta_s$ is the solvent viscosity.

## 2.7 Rheology

Viscosities were obtained for each sample by means of either a bulk rheometer or a capillary viscometer. The details of each geometry used will be described in the appropriate chapter. However, in general the viscosity, $\eta$, is defined as the ratio of an applied shear stress, $\tau$, to the resulting shear rate, $\dot{\gamma}$, when subjected to that shear force. While the viscosity is independent of shear rate for a Newtonian fluid, many colloidal dispersions display more complex rheological behavior such as shear thinning or thickening in which the viscosity decreases or increases with increasing shear rate, respectively.[20] Therefore, viscosity data is obtained as a function of shear rate for all samples and solution conditions of interest.

In the case of a bulk rheometer, the shear stress is applied as a torque, $T$, to turn a cylindrically symmetric confining wall relative to a stationary wall with a well

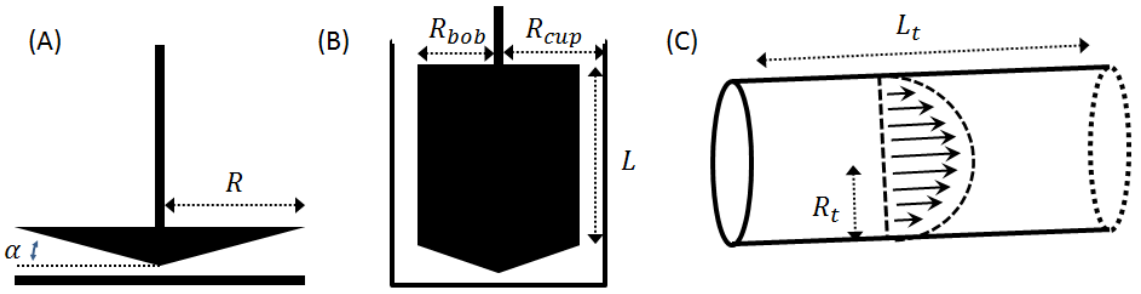


**Figure 2.5:** The (A) cone and plate, (B) couette, and (C) capillary viscometer geometries used during rheological measurements in this work are depicted with their characteristic parameters.

defined gap separating them. The two geometries used in this work are a cone and plate and a coaxial cylinder, or couette, configuration, shown in panes (A) and (B) of Fig. 2.5, respectively. A cone is defined by its radius, $R$, and cone angle, $\alpha$. In a cone and plate geometry, the plate is stationary below the sample while the cone rotates with a stress of $\tau = \frac{3T}{2\pi R^3}$ and shear rate of $\dot{\gamma} = \frac{\Omega}{\alpha}$, where $\Omega$ is the rotational velocity.[20] Under these conditions, the shear rate is the same at all points within the sample as long as the cone angle is sufficiently small. A couette geometry is composed of a cup with radius, $R_{cup}$, and a bob with radius, $R_{bob}$, and length, $L$. Typically the cup acts as the stationary outer wall while the bob, as the inner wall, rotates. Unlike the cone and plate geometry, the shear stress and shear rate vary in a couette cell as a function of the radial distance from the center of the bob, $r$. At any given position, $r$, the bob imposes a shear stress of $\tau(r) = \frac{T}{2\pi L r}$ with an average shear rate of $\dot{\gamma} = \frac{\Omega(R_{cup}+R_{bob})}{2(R_{cup}-R_{bob})}$.[20]

A capillary viscometer measures the viscosity by imposing a pressure driven flow through a cylindrical tube of radius, $R_t$, and length, $L_t$, depicted in pane (C) of Fig. 2.5. Once again, the shear stress under these conditions is a function of the radial position within tube according to $\tau(r) = \frac{\Delta P r}{8L_t}$, where $\Delta P$ is the pressure drop across the tube.[9, 20] The shear rate is defined as the value at the wall of the tube, which is the maximum value due to the parabolic flow profile (assuming Newtonian flow with no slip boundary conditions). To account for any non-Newtonian flow behavior, the

shear rate is calculated using the Rabinowitsch-Mooney equation[20]

$$\dot{\gamma}(r) = \frac{Q}{3R^3}\left(3 + \frac{\mathrm{d}(\ln Q)}{\mathrm{d}(\ln[\tau(R_t)])}\right) \tag{2.21}$$

## 2.8 Materials and Sample Preparation

Experimental investigation of cluster phenomena are accomplished by studying formulations of several proteins. In particular, experimental parts of this work study the behavior of a model globular protein lysozyme as well as three different commercially available therapeutic proteins produced by Genentech, Inc. known as monoclonal antibodies (mAbs). Lysozyme was obtained from MP Biomedicals and carefully purified to remove ion impurities, minimizing the residual ion content. Samples were prepared by dissolving the purified lyophilized lysozyme in deuterium oxide, $D_2O$. Low concentration samples ($< 300$ mg/mL) were filtered through $0.22\mu m$ filters, while higher concentrations required $0.45\mu m$ filters as these samples were too viscous to filter through smaller pore sizes. High concentration samples ($\leq 350$ mg/mL) were prepared at 50 $^\circ C$ to aid in dissolution during reconstitution due to their resulting high viscosities. All mAbs are humanized IgG1 proteins expressed in Chinese hamster ovarian (CHO) cells. The antibodies were subsequently purified in multiple chromatography steps before being dialyzed into various buffers in deuterium oxide ($D_2O$), the details of which will be discussed in the appropriate chapter.

## REFERENCES


[1] Allen, M. P., and Tildesley, D. J. *Computer Simulation of Liquids*. Oxford University Press, 1987.

[2] Banchio, A. J., and Nägele, G. Short-time transport properties in dense suspensions: from neutral to charge-stabilized colloidal spheres. *J. Chem. Phys. 128*, 10 (Mar. 2008), 104903.

[3] Berne, B. J., and Pecora, R. *Dynamic Light Scattering*, dover edit ed. John Wiley and Sons, New York, 2000.

[4] Bomont, J.-M., Bretonnet, J.-L., and Costa, D. Temperature study of cluster formation in two-Yukawa fluids. *J. Chem. Phys. 132*, 18 (2010), 184508.

[5] Bomont, J.-M., Bretonnet, J.-L., Costa, D., and Hansen, J.-P. Communication: thermodynamic signatures of cluster formation in fluids with competing interactions. *J. Chem. Phys. 137*, 1 (July 2012), 011101.

[6] Chen, S.-H. Small angle neutron scattering studies of the structure and interaction in micellar and microemulsion systems. *Annu. Rev. Phys. Chem. 37* (1986), 351–399.

[7] Chen, S.-H., Broccio, M., Liu, Y., Fratini, E., and Baglioni, P. The two-Yukawa model and its applications: the cases of charged proteins and copolymer micellar solutions. *J. Appl. Crystallogr. 40*, s1 (Apr. 2007), s321–s326.

[8] Costa, D., Caccamo, C., Bomont, J.-M., and Bretonnet, J.-L. Theoretical description of cluster formation in two-Yukawa competing fluids. *Mol. Phys. 109*, 23-24 (2011), 2845–2853.

[9] Deen, W. M. *Analysis of Transport Phenomena*. Oxford University Press, New York, 1998.

[10] Falus, P., Porcar, L., Fratini, E., Chen, W.-R., Faraone, A., Hong, K., Baglioni, P., and Liu, Y. Distinguishing the monomer to cluster phase transition in concentrated lysozyme solutions by studying the temperature dependence of the short-time dynamics. *J. Phys. Condens. Matter 24*, 6 (Feb. 2012), 064114.

[11] Frenkel, D., and Smit, B. *Understanding Molecular Simulations: From Algorithms to Applications*. Academic Press, 2002.

[12] Gahler, R., Golub, R., Habicht, K., Keller, T., and Felber, J. Space-time description of neutron spin echo spectrometry. *Phys. B 229* (1996), 1–17.

[13] Hansen, J.-P., and McDonald, I. R. *Theory of Simple Liquids*, 3rd editio ed. Elsevier, Oxford, 2006.

[14] Helgeson, M. E., and Wagner, N. J. Colloidal interactions mediated by end-adsorbing polymer-like micelles. *J. Chem. Phys. 135*, 8 (Aug. 2011), 084901.

[15] Hiemenz, P. C., and Rajagopalan, R. *Principles of Colloid and Surface Chemistry*, 3rd editio ed. Taylor & Francis Group, 1997.

[16] Kim, J. M., Castañeda Priego, R., Liu, Y., and Wagner, N. J. On the importance of thermodynamic self-consistency for calculating clusterlike pair correlations in hard-core double Yukawa fluids. *J. Chem. Phys. 134*, 6 (Feb. 2011), 064904.

[17] Kline, S. R. Reduction and analysis of SANS and USANS data using IGOR Pro. *J. Appl. Crystallogr. 39* (2006), 895–900.

[18] Liu, Y., Chen, W.-R., and Chen, S.-H. Cluster formation in two-Yukawa fluids. *J. Chem. Phys. 122*, 4 (Jan. 2005), 44507.

[19] McQuarrie, D. *Statistical Mechanics*. University Science Books, 2000.

[20] Mewis, J., and Wagner, N. J. *Colloidal Suspension Rheology*. Cambridge University Press, New York, 2012.

[21] Nagele, G. On the dynamics and structure of charge-stabilized suspensions. *Phys. Rep. 272*, 5-6 (1996), 215–372.

[22] Ornstein, L. S., and Zernike, F. Accidental deviations of density and opalescence at the critical point of a single substance. *KNAW, Proc. 17* (1914), 793.

[23] Porcar, L., Falus, P., Chen, W.-R., Faraone, A., Fratini, E., Hong, K., Baglioni, P., and Liu, Y. Formation of the Dynamic Clusters in Concentrated Lysozyme Protein Solutions. *J. Phys. Chem. Lett. 1*, 1 (Jan. 2010), 126.

[24] Rosov, N., Rathgeber, S., and Monkenbusch, M. Neutron Spin Echo Spectroscopy at the NIST Center for Neutron Research. In *Scatt. from Polym.* 2009, ch. 7, pp. 103–116.

[25] Sandler, S. *An Introduction to Applied Statistical Thermodynamics*. John Wiley and Sons, 2011.

[26] Sandler, S. I. *Chemical, Biochemical, and Engineering Thermodynamics*. 2006.

[27] Schleger, P., Ehlers, G., Kollmar, A., Alefeld, B., Barthelemy, J. F., Casalta, H., Farago, B., Giraud, P., Hayes, C., Lartigue, C., Mezei, F., and Richter, D. The sub-neV resolution NSE spectrometer IN15 at the Institute Laue Langevin. *Phys. B 266* (1999), 49–55.

[28] Sciortino, F., Tartaglia, P., and Zaccarelli, E. One-dimensional cluster growth and branching gels in colloidal systems with short-range depletion attraction and screened electrostatic repulsion. *J. Phys. Chem. B 109*, 46 (2005), 21942.

[29] Shukla, A., Mylonas, E., Di Cola, E., Finet, S., Timmins, P., Narayanan, T., and Svergun, D. I. Absence of equilibrium cluster phase

in concentrated lysozyme solutions. *Proc. Natl. Acad. Sci. U. S. A. 105*, 13 (Apr. 2008), 5075–80.

[30] Toledano, J. C. F., Sciortino, F., and Zaccarelli, E. Colloidal systems with competing interactions: from an arrested repulsive cluster phase to a gel. *Soft Matter 5*, 12 (2009), 2390.

[31] Zemb, T., and Lindner, P. *Neutrons, X-rays and Light: Scattering Methods Applied to Soft Condensed Matter*. Elsevier B.V., Amsterdam, 2002.

# Chapter 3

# INTERMEDIATE RANGE ORDER AND OTHER STRUCTURAL FEATURES OF COMPETING INTERACTIONS

## 3.1 Introduction

Early observations of cluster formation in SALR systems were accomplished with micron sized colloidal particles, which could be observed directly by microscopy.[7, 42, 43, 45] However, clustering of nanoparticles is much more difficult to observe as they are unable to be resolved by microscopy techniques and therefore it remains an active area of research. This intriguing state of matter has been studied with the use of lysozyme, a globular protein whose chemistry has been found to naturally produce a combination of short range attractive and long range repulsive interactions.[8, 10, 13, 30, 37] Previous work has inferred the formation of clusters in aqueous lysozyme solutions from small angle neutron scattering (SANS) measurements. Theoretical integral equation theory (IET) calculations and simulation studies have demonstrated that the same SALR interactions capable of producing clusters can also produce an additional peak in the structure factor at small scattering angles or $q$-values experimentally accessible by SANS.[5, 6, 17, 29] The simultaneous study of colloidal and lysozyme systems initially linked this low-$q$ peak to the formation of an ordered solution phase of clusters, where the additional peak was attributed to the correlation of stable clusters in solution.[45] Several studies have also observed low-$q$ peaks in the scattering patterns of lysozyme solutions under specific conditions.[8, 10, 13, 30, 37]

Recent work has brought into question the use of this low-$q$ peak as an experimental indicator of cluster formation.[30] By studying both the structure and dynamics of lysozyme, the magnitude of the low-$q$ peak was found to decrease while the effective hydrodynamic radius (related to the average cluster size) increased. In general,

peak formation in a scattering pattern signifies the presence of a correlation length between scattering centers in a sample. Consequently, this low-$q$ peak has recently been suggested to arise from *intermediate range order* (IRO) between scattering centers, of which a fluid consisting of clusters is only one specific scenario.[20, 30] While scattering patterns contain the contributions from all scattering centers, it is desirable to distinguish the contributions from particles within different structures, such as those contained in clusters. Direct particle simulations thus provide particle-level details of the cluster size distributions and corresponding contributions to the structure factor. By distinguishing cluster and monomer species, the contributions leading to the IRO peak can be explicitly calculated.

The goal of this chapter is to separate the correlation of monomers and clusters as distinct species within SALR systems and quantify their relative contributions to the formation of an IRO peak in the structure factor.[20] Monte Carlo (MC) simulations are used to study a model system with realistic interactions parameters across a range of volume fractions to assess the validity of using the IRO peak as an indicator of cluster formation. The microstructure of several states exhibiting IRO are decomposed into contributions from monomer, cluster, and cross correlations. A new, self-consistent method is proposed to identify the state conditions at which clustered fluids exist based on the cluster size distribution. This method provides an unambiguous classification of states in SALR systems and a method by which to identify them in practice. The structure of each state and its relation with the IRO peak are discussed in detail. The work detailed in this chapter is published in [20].

## 3.2 Methodology

### 3.2.1 Simulation Details

All simulations in this chapter were performed using the protocol outlined in Chapter 2. Particle interactions are defined by the hard sphere double Yukawa (HSDY)

potential using the parameters $\lambda = 0.1$, $z_1 = 10$, and $z_2 = 0.5$ for all state points. Physically, the value of $z_1$ reflects the relative interaction range of a short-range attraction observed among globular proteins (roughly 10 % of the globular protein diameter).[13, 30] The values of $\lambda$ and $z_2$ represent long range and relatively weak repulsion, as in the case of proteins with low ionic strength and small surface charge and/or relatively strong attractive forces. Practically, this parameter set was chosen because it was observed to produce an IRO peak in the structure factor over a range of reduced temperatures and volume fractions by previous studies.[4, 17, 25] Here, the pair distribution function $g(r)$ and structure factor $S(q)$ of the system are calculated by direct summation and averaged over the trajectory using standard methods.[1, 19] At significantly large strengths of attraction, or small reduced temperatures ($T^* < 0.25$), the system energy and pressure could not reach a steady value (i.e., a thermodynamically stable state) after 1x10$^8$ simulation steps, such that $T^* = 0.25$ is the practical lower limit for these investigations.

Particles within any given configuration can be distinguished as monomers or contained in a cluster. If two neighboring particles are within some cut-off distance $r_c$ of each other, they are defined as belonging to a specific cluster. Particles not contained in a cluster are referred to as monomers. This calculation determines the cluster size distribution, $n(s)$, or the relative population of aggregates ranging from monomers to clusters of each possible size. Here, the cluster size distribution is normalized by the cluster size, $s$, and system size, $N_p = 1728$:

$$N(s) = \left(\frac{s}{N_p}\right) n(s) \tag{3.1}$$

similar to that used previously.[14, 44] The function $N(s)$ represents the average fraction of particles contained in clusters of size $s$ as opposed to the average number of clusters of $s$ particles existing in the system. $N(s)$ provides a normalized function for all cluster sizes, while $n(s)$ is biased towards smaller cluster sizes. The normalized cluster size distribution, $N(s)$, henceforth referred to as the cluster size distribution, is used to identify the state of the fluid at each state point. The sensitivity of statistical

thermodynamic calculations to the cut-off distance are studied in detail in the next section.

Each sampled configuration is also tested for dynamic percolation, defined as when a cluster spans the entire system size in at least one dimension for 50% of the time. Such a cluster is effectively infinite in size when periodic boundary conditions are employed and is denoted as a percolated cluster. Dynamic percolation at a given state point is defined when at least 50% of the configurations sampled contain at least one percolated cluster.[41] States that fulfill this criterion can be further distinguished as cluster percolated states, rather than random percolated states, which will be discussed later.

### 3.2.2 Phase Transition Calculations

Liquid-liquid phase separation (binodal) in an HSDY system is difficult to calculate. However, it is known that the addition of a long-range repulsion to attractive potentials shifts the liquid-liquid coexistence region to lower temperatures.[24] Therefore, a convenient reference system in identifying the HSDY states is the phase behavior of a corresponding purely attractive potential. Here, the attractive component of the HSDY potential is taken as a reference potential, shown in Fig. 3.1, and defined as:

$$\frac{U_{ref}(r)}{kT} = \begin{cases} \infty & r < 1 \\ \frac{1}{T^*(1-\lambda)r}(-e^{-z_1(r-1)} + \lambda e^{-z_2(r-1)}) & 1 \leq r \leq r_c \\ 0 & r > r_c \end{cases} \tag{3.2}$$

where $r_c = 1.2424$ for the given set of interaction parameters used in this chapter. The rationale for using this as the cut-off distance defining connectivity will be discussed in more detail in the next section.

The binodal of the reference attractive potential is calculated using discrete perturbation theory (DPT) calculations.[3, 11, 47, 48, 49] DPT represents the interaction potential by numerous discrete square well-like steps and is known to calculate accurate gas-liquid binodals and critical points. The dynamic percolation transition line of

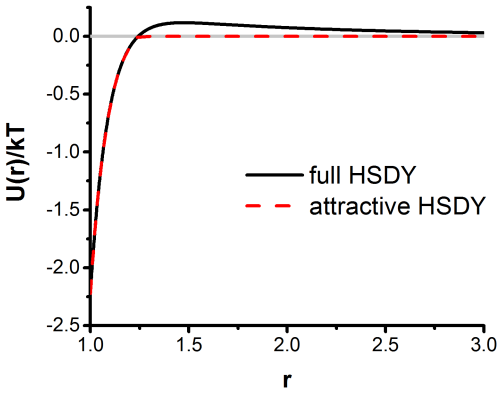


**Figure 3.1:** The hard sphere double Yukawa (HSDY) potential, black line, used throughout this chapter ("full HSDY") is plotted with the attractive component of the potential, red dashed line ("attractive HSDY"), used to estimate phase transitions of a purely attractive reference system in order to provide context to the HSDY state points.

the reference attractive fluid is estimated by the phenomenological model proposed by Miller and Frenkel[33] for an adhesive hard sphere fluid:

$$\rho_{perc}(\tau_B) = \frac{-10.09 + 182.4\tau_B + 606.9\tau_B^2 + 15.31\tau_B^3}{1.0 + 507.9\tau_B + 548.9\tau_B^2} \tag{3.3}$$

where $\rho_{perc}$ is the particle density at percolation for a given Baxter parameter $\tau_B$,[2, 33] which is a representative measure of the strength of attraction. For this calculation, the reference potential is mapped to an adhesive hard sphere fluid in agreement with the Noro-Frenkel extended law of corresponding states for systems with short range attraction.[36] The reference potential is first integrated to determine the reduced second virial coefficient $B_2^*$ according to

$$B_2^* = \frac{B_2}{B_2^{HS}} = 1 + 3\int_1^{r_c} \left(1 - \exp\left[\frac{-U^{ref}(r)}{kT}\right]\right) r^2 \mathrm{d}r \tag{3.4}$$

which is converted to $\tau_B$ by the relationship

$$\tau_B = \frac{1}{4(1 - B_2^*)}. \tag{3.5}$$

### 3.2.3 Decomposing the Structure Factor

In order to understand the influence of competing interactions in SALR systems on the resulting structure, the system is decomposed into its individual constituents. In this regard, monomers and clusters are treated as distinct components in a pseudo-two-component solution. As this work is concerned with clusters in general rather than those of a specific size, individual particles are segregated into monomer or cluster categories.

The definition of this pseudo-two-component fluid comprised of monomers and clusters enables calculating the total structure factor with respect to the partial structure factors for each component as:[35]

$$S(q) = x_M S_{MM}(q) + x_C S_{CC}(q) + \sqrt{2 x_M x_C} S_{MC}(q). \tag{3.6}$$

Here, subscripts represent the type of particle (M for monomers and C for particles in a cluster), $x_i$ represents the fraction of each type of particle in the current configuration of the system, and the structure contributions arise from the monomer-monomer, $S_{MM}(q)$, monomer-cluster, $S_{MC}(q)$, and cluster-cluster, $S_{CC}(q)$, correlations. By definition, correlations involving clusters are calculated by summing over each individual particle within a cluster. Therefore, $S_{CC}(q)$ is to be distinguished from a correlation between the centers of mass of the clusters in solution.

The three partial structure factors are calculated by the relationship between the structure factor and the radial distribution function:

$$S_{ij}(q) = \delta_{ij} + \rho (x_i x_j)^{\frac{1}{2}} \int_0^\infty \frac{\sin(qr)}{qr} [g_{ij}(r) - 1] 4\pi r^2 \mathrm{d}r, \tag{3.7}$$

where $\delta_{ij}$ is the Kronecker delta and $\rho$ is the fluid density. The radial distribution function of each contribution is calculated according to:

$$g_{ij}(r) = V^2 \left\langle \sum_{i=1}^{n_i} \sum_{j=1}^{n_j} \frac{\delta(r_{ij} - r)}{n_i n_j V} \right\rangle, \tag{3.8}$$

where subscripts $(i, j)$ represent the component, $n_{(i,j)}$ is the number of particles of each component in a given configuration, and $V$ is the volume. Restricting the calculation

of Eq. 3.8 to include only particles contained in clusters, and explicitly accounting for each particle within the double summation, generates cluster-cluster correlations defined by $g_{cc}(r)$, the radial distribution function of clustered particles. This function represents the degree of order between clusters and helps in distinguishing between structural states formed by SALR systems. Corresponding cluster-cluster structure factors, $S_{CC}(q)$, can be further decomposed into intra- and inter-cluster correlations by counting only those particles within the same or different clusters, respectively.

### 3.3 Self-consistency and Implications of Defining a Cut-off Distance

The details of the microstructure are sensitive to the cut-off distance used to define connectivity.[20] Subsequently, the prevalence of clusters will influence the relative contribution of monomer and cluster correlations to the solution structure factor. Therefore, prior to understanding the influence of cluster formation on the structure, this section explores the sensitivity of the cluster size distribution to the choice of $r_c$.

Groupings or clusters of particles arise naturally in any fluid state regardless of interactions, simply due to density fluctuations.[23, 50] Therefore, an arbitrary definition of cut-off distance can produce clustering and percolation without physical significance. To provide a meaningful interpretation of solution structure, a self-consistent representation of connectivity is rationalized and used in this chapter. The cut-off distance, $r_c$, is defined here as the separation at which the HSDY potential first reaches net zero interaction energy beyond the attractive well: $r_c = 1.2424$. According to this definition, two particles are connected if they experience an attractive interactions with each other. This cut-off distance is independent of temperature and is intuitively related to the range of attraction that drives particle aggregation. Therefore, it is consistent with the potential used to produce the phase behavior of a reference system of purely attractive particles. By distinguishing states according to the structural features resulting from this connectedness, their location in the phase space of this reference system can provide additional understanding of the relative influence of attractive and repulsive forces.

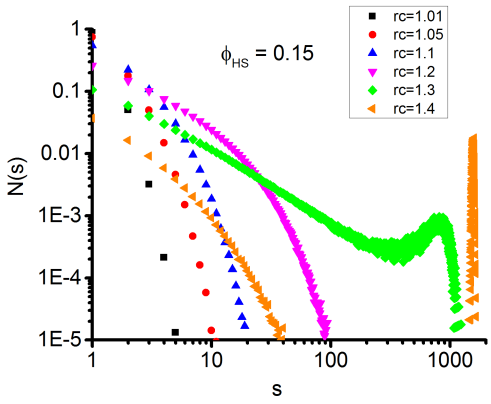


**Figure 3.2:** Cluster size distributions, $N(s)$, calculated for a hard sphere fluid at a volume fraction of 0.15 using a range of cut-off distances. The effect of this distance defining connectivity on the apparent distribution of cluster sizes is significant.

By defining a geometric connection between hard sphere (HS) particles, HS cluster size distributions can be used as a basis to compare with those found in the HSDY system. The HS $N(s)$ function is always monotonically decreasing with cluster size until the percolation transition is reached. Figure 3.2 shows the cluster size distributions for hard sphere systems at a volume fraction of 0.15 and a range of relevant cut-off distances. At small enough values of $r_c$ the cluster size distribution monotonically decreases with cluster size, while at a large cut-off distance (1.4) the system incorporates almost all particles into a single large cluster indicative of percolation. This shift in the connectedness from varying $r_c$ in a HS system directly indicates the sensitivity of $N(s)$ and the importance of choosing a physically significant value.

Three cut-off distances that reflect characteristic length scales of the HSDY interaction potential are tested. These distances represent (1) the separation distance at which the energy barrier for a particle to leave its nearest neighbor is 1.5 kT ($r_c = 1.035$ for $T^* = 0.46$), (2) the particle separation at which the interaction energy is zero ($r_c = 1.2424$), and (3) the separation distance of the energy maximum ($r_c = 1.4744$).

Choice (1) is associated with the separation distance at which the energy barrier to escape the primary attractive well is sufficient to suppress about 80% of escape attempts. Thus, it can be thought of as representative of a dynamic connectedness cut-off distance. Choice (3) is rationalized as being inclusive of all attractive forces, as the force is the derivative of the potential energy function. Again, this is related more closely with the dynamics as would influence the results in Molecular Dynamics (MD) simulations. Choice (2) is more directly related with equilibrium thermodynamic properties. Previous works have focused on choice (3) to investigate the system structure[9, 40, 46] while this work will rely on choice (2).

Comparing cluster size distributions at multiple cut-off distances will help confirm that the methodology used to distinguish states is not sensitive to $r_c$. The effect of competing interactions on the cluster size distribution will be reflected in the difference between the $N(s)$ of a given HSDY system and a HS system at the same volume fraction. $N(s)$ functions calculated using the three cut-off distances mentioned above are compared in Fig. 3.3 for three state points studied in this chapter. The states shown in Fig. 3.3 will be referred to throughout this chapter as (a) state B, (b) state C, and (c) state E, which represent different types of states (to be defined in the following section) that for now are not necessary to distinguish. Regardless of the cut-off distance defined, characteristic features of the cluster size distribution corresponding to each state remain consistent.

The HSDY interactions clearly shift the $N(s)$ to larger clusters when compared with the HS systems with the same $r_c$ for all three states. Only for state E at the largest $r_c$ do the HSDY and HS functions overlap. This indicates the simulation box is influencing the calculations, but also that the definition of connectivity may be inappropriately large. Similarly, while the cluster size distribution of state B remains larger than the HS value, the two begin to approach each other at larger cut-off distances even before the onset of percolation. The same can be said for state C. However, the HS fluid is unable to reproduce the unique appearance of a peak in the $N(s)$ of State

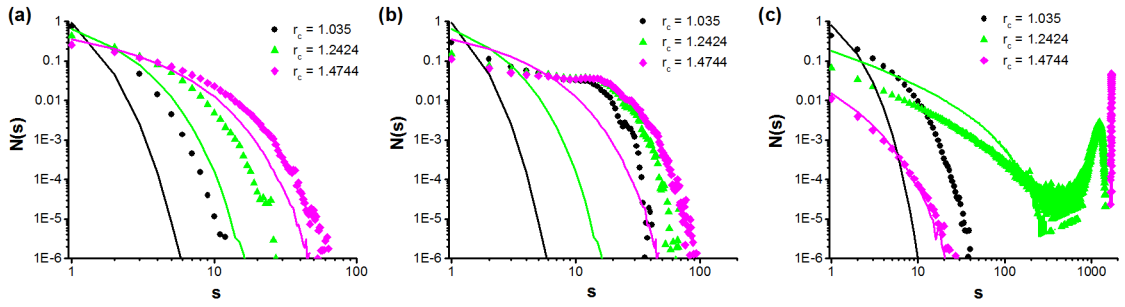


**Figure 3.3:** A comparison of $N(s)$ resulting from three different cut-off distances for three states points to be discussed in more detail later: (a) state B, (b) state C, and (c) state E. Filled points are calculations from HSDY simulations while lines are HS results.

C, which is used to define a clustered state. The maximum seen in $N(s)$ of the clustered state can only form due to the competing HSDY potential features. The peak shifts slightly in position and magnitude with $r_c$, but remains as a distinct feature. Therefore, if a particular state point is a clustered state according this definition, then the choice of cut-off distance will not influence this distinction. However, varying $r_c$ will shift the extent of clustering and influence the relation between $N(s)$ and $S(q)$ and the relative magnitude of each species' contribution. When $r_c$ is too large the effect of interactions becomes convoluted with random density fluctuations observed in HS fluids. For these reasons, it appears that the definition of $r_c = 1.2424$ is the most physically representative value (of the options tested previously and explored here) to define connectivity and will be thermodynamically consistent when compared with the phase behavior.

### 3.4 State Definitions

Simulations are performed on six state points exhibiting an IRO peak in $S(q)$. These state points are defined as: State A ($\phi = 0.01$, $T^* = 0.25$), State B ($\phi = 0.05$, $T^* = 0.46$), State C ($\phi = 0.05$, $T^* = 0.25$), State D ($\phi = 0.15$, $T^* = 0.25$), State E ($\phi = 0.15$, $T^* = 0.46$), and State F ($\phi = 0.25$, $T^* = 0.46$). States are determined according to

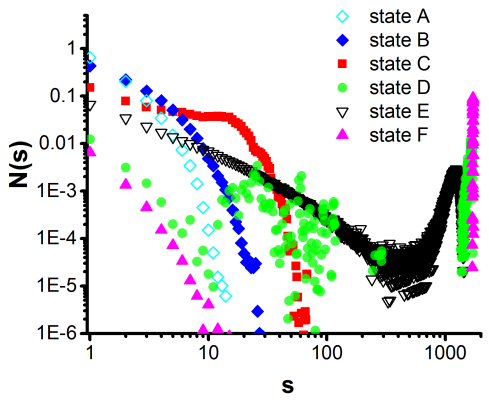


**Figure 3.4:** Cluster size distributions, N(s), are plotted together for each of the six state points studied, which fall into four categories of states: dispersed fluid (states A and B), clustered fluid (state C), cluster percolated (state D), and random percolated (states E and F).

the cluster size distribution and fraction of percolated configurations and are classified as dispersed fluid (A, B), clustered (C), cluster percolated (D), and random percolated (E, F) states. The cluster size distributions of all six states are shown in Fig. 3.4. The method of determining percolated clusters described in the Simulation Details section is used to identify a percolated state. By combining the cluster size distribution, percolation criterion, and details of the inter-particle structure, a cluster percolated state can also be defined. In this state, the percolated cluster is comprised of well-defined particle clusters, in contrast to the "usual" random percolation state.

Features of the cluster size distribution are used to distinguish dispersed and clustered states. When $N(s)$ is monotonically decreasing with cluster size, the state point is defined as a dispersed fluid state. The most probable species are monomers and there is no preferred cluster size within the distribution. Note that this is similar to a hard sphere fluid, as shown in Fig. 3.2 in the previous section. The development of a probability maximum in $N(s)$ at a size larger than a monomer is used to identify a state as a cluster fluid. Previous studies have defined clustered states by an average cluster size greater than two.[10, 31] However, it is uncertain if the (random, polydisperse)

cluster sizes of a state defined in this manner are a significant contribution to the material properties. Further, $N(s)$ of such states is similar in appearance to a HS fluid. Requiring clustered fluids to contain a peak in $N(s)$ is more indicative of a state whose properties result from the dominant cluster species. While monomers may be the most abundant single species in solution by the definition of a cluster fluid imposed here, they are typically less prevalent than the total amount of particles in all clusters (i.e., $N(1) < \sum_{x=2}^{N_p} N(x)$), though this is not strictly a requirement.

Examining the six states points in Fig. 3.4, both state points A and B have a monotonically decreasing distribution of cluster sizes and are correspondingly defined as dispersed fluids. As may be expected, the probability of finding clusters $(1 - N(1))$ increases with volume fraction with these two states. State C has a peak in $N(s)$ and is therefore a clustered state. It has almost 85% of particles in clusters with most of those being roughly the most preferred size of around 12 particles. The finite peak in the cluster size distribution indicates a dominating size scale, although the distribution of sizes is broad. Note that the percolated states (states D, E, and F) exhibit a large peak at a large cluster size corresponding to the box size, but this should not be confused with the cluster peak defined as a local maximum in $N(s)$ indicating the formation of finite-size particle clusters. According to Fig. 3.4, at least 93% of particles in each of the percolated states are part of a cluster, with varying amounts of those contributing to the percolated cluster.

Although the features presented in Fig. 3.4 cannot distinguish the three percolated states, their cluster size distributions differ in shape. In particular, the cluster size distribution for state D exhibits a weak peak at roughly the same preferred size as state C, which is at a lower volume fraction but the same temperature. This distinguishes state D from states E and F, which have cluster size distributions typical of percolated fluids.[50] Further analysis of the microstructure as a function of $r_c$ (discussed in a later section) will demonstrate that state D is fundamentally different from states E and F, despite all three exhibiting percolation.

### 3.5 Phase Behavior

All six state points, now appropriately defined, are mapped onto the phase diagram of reduced temperature $T^*$ as a function of volume fraction $\phi$ in Fig. 3.5. Also included, for perspective, are the binodal (phase separation) line and percolation transition of the reference attractive fluid defined earlier. By comparison, the two-phase region of the HSDY system is expected to exist at lower temperatures than studied here ($T^* < 0.25$) where simulations were unable to equilibrate. Technically, all six HSDY state points are metastable (one-phase) systems within the bulk gas-solid coexistence region of the HSDY phase diagram,[24] (see Fig. 1.2c for an analogous example of a purely short-range attractive system) but these states exist in equilibrium in these simulations.

In general, dispersed fluid states transition to clustered states upon lowering temperature. Progressively increasing the volume fraction from state B to E and F leads to percolation, which is qualitatively consistent with the reference attractive system,[15, 33] as shown by the dotted line, or even a hard-sphere fluid.[16] Interestingly, a clustered and a cluster percolated state are found within the binodal of the reference state diagram. Thus, the long-range repulsion in an HSDY system frustrates the phase separation expected in its absence (i.e., pure attraction). Increasing volume fraction at this lower temperature leads to the percolation of clusters of a preferred size. The microstructure of the cluster percolated state might then have a preferred lengthscale set by the clusters. This difference could be important for the material properties of gels and glasses formed from such systems, such as ceramics, zeolites,[18, 32, 38] and membranes[12, 34] in which clusters act as intermediates.

The results shown here suggest that the binodal of an appropriately defined reference attractive potential may act as an indicator of clustered states. This hypothesis will be explored in more detail in the following chapter. The relative location of these states will provide a physical basis to understand the formation of IRO peaks in $S(q)$.

Three of these state points (at a constant $T^*$ of 0.46) are shown in Fig. 3.6 to highlight the trend in the magnitude of their IRO peaks. The total structure factor

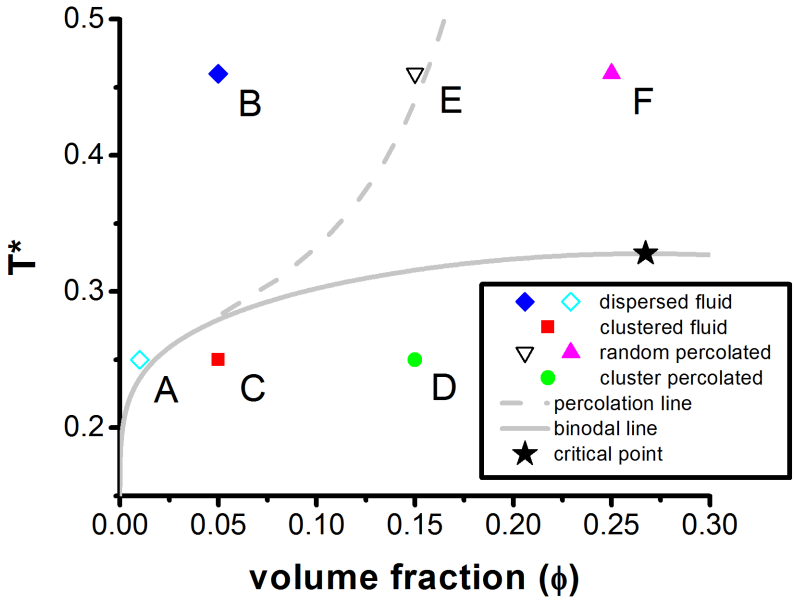


**Figure 3.5:** The phase diagram shows the relative location of six state points of a HSDY fluid with $z_1 = 10$, $z_2 = 0.5$, and $\lambda = 0.1$. The state points represent dispersed fluid systems (diamonds), clustered systems (square), cluster percolated systems (circle), and "randomly" percolated systems (triangles). The reference attractive potential, outlined in the text, is used to estimate the binodal (grey solid line) and percolation transition (grey dotted line).

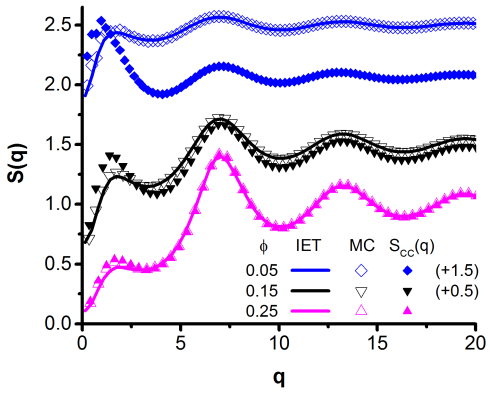


**Figure 3.6:** The $S(q)$ (open dots) and contribution of cluster-cluster correlations $S_{CC}(q)$ (filled dots) are shown for states B, E, and F (all at $T^* = 0.46$). $S(q)$ results are compared with IET calculations (solid lines). For clarity, simulation and IET results are shifted vertically for states B and E by a value of 1.5 and 0.5, respectively.

and the partial structure factor of particles in clusters (i.e., cluster-cluster correlations) obtained from MC simulations are given for states B, E, and F. The dependence of IRO peak formation on temperature and volume fraction has been studied previously by integral equation theory.[4, 17, 25, 29] These studies have assumed that a direct connection exists between the formation of an IRO peak and the formation of a clustered state. Contrary to these previous works, all three states studied here exhibit an IRO peak. The magnitude clearly decreases with increasing volume fraction and simultaneously, cluster-cluster correlations, $S_{CC}(q)$, are an increasingly large contribution to the total structure. Figure 3.6 shows that the IRO peak is not trivially indicative of correlations between clusters and its denotation as a "cluster peak" is misleading and incorrect. Rather, this low-$q$ feature in the scattering arises from a complex combination of correlations of monomers and particles in clusters as well as their cross-correlations. In the following sections, the ability to manipulate $r_c$ in MC simulations is utilized to further distinguish structural states before exploring the influence of these microstructures on the relative contributions to the IRO peak.

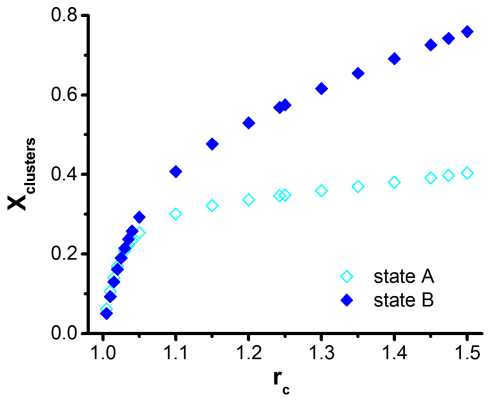


**Figure 3.7:** The dependence of the fraction of particles contained in clusters $X_{clusters}$ on $r_c$ for state A (open diamonds) and state B (filled diamonds).

## 3.6 Cut-off Distance as a Probe of Solution Structure

### 3.6.1 Monomer Dominated IRO Peak

The extent of clustering, represented by the fraction of particles in clusters $X_{clusters} = 1 - N(1)$, in states A and B are shown in Fig. 3.7 for comparison. Both states remain dispersed fluids despite the fraction of particles in clusters increasing steadily with increasing $r_c$.

However, state B has up to twice as many particles (75%) in clusters at the largest cut-off distance ($r_c > 1.47$) compared to state A, which has roughly the same number of particles in clusters at all values of $r_c > 1.1$. This is reflected in the cluster size distribution, which spans to much larger sizes for state B while state A is almost unchanged. Thus, as more particles are in clusters they populate larger sizes relatively evenly while smaller sizes are slightly less likely. States A and B have nearly identical cluster size distributions at a cut-off distance of 1.035 and also have the same fraction of particles in clusters, which provides a basis for comparing the microstructure of two states with an IRO peak under different conditions ($\phi$, $T^*$).

While the sensitivity of $S(q)$ to $N(s)$ will be addressed in the next section, it is essential to emphasize the additional sensitivity of IRO peak formation on the relative

orientation of particles and clusters. Uncertainty as to the physical significance of the IRO peak arises from the non-trivial convolution of the real space orientation, represented by $g(r)$, upon its Fourier transformation into the $S(q)$ according to Eq. 3.7. As an example, a cut-off distance of 1.035 is used to compare states A and B because they have similar contents of monomers and clusters, but produce IRO peaks with different magnitudes. The microstructures of these two states are represented by their respective decomposed structure factors in Fig. 3.8. It is important to note that altering $r_c$ from 1.2424 does not change the structure or state of each state point, but provides a unique method of probing the lengthscale dependence of connectivity and the corresponding relationship between $N(s)$ and $S(q)$.

While $S_{CC}(q)$ is nearly identical for both states across the entire $q$-range, shown in Fig. 3.8a, $S(q)$ of state A has a larger IRO peak. In the same figure, the magnitude of $S_{MM}(q)$ appears to differ most significantly in the low-$q$ region between states A and B. Further, both $S_{MM}(q)$ and $S_{MC}(q)$ of state A exhibit a small IRO peak. By plotting the magnitude of $S_{MM}(q)$ and $S_{CC}(q)$ for state A relative to state B in Fig. 3.8b, the larger magnitude of monomer correlations almost perfectly overlaps the relative magnitude of $S(q)$ over the full $q$-range. At the $q$-values of the IRO peak, the relative magnitude of monomer correlations drops slightly below that of $S(q)$ and cluster correlations become slightly more significant. Thus, an enhanced correlation of monomers, rather than clusters, is the most significant factor contributing to the more pronounced low-$q$ peak at lower volume fraction and reduced temperature. However, it is a combination of both monomer and cluster correlations that produces the exact magnitude of the IRO peak in $S(q)$. These features demonstrate that the magnitude and position of IRO peaks cannot, in general, be simply interpreted in terms of cluster size and spacing.

### 3.6.2 Analyzing Moments of the Cluster Size Distribution

From studying trends in the cluster size distribution with respect to cut-off distance, the clustered state can easily be distinguished from dispersed fluid and percolated states. In particular, clustered fluids display a distinguishing (and therefore

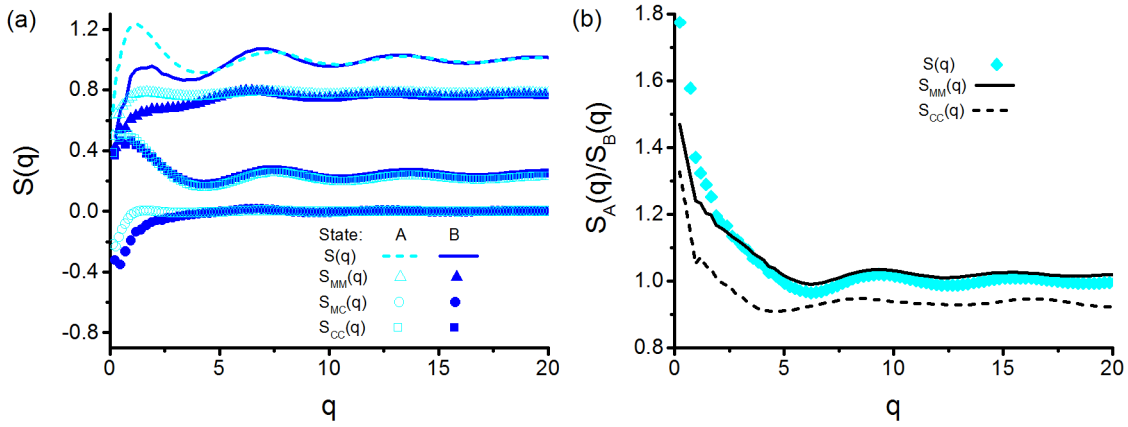


**Figure 3.8:** (a) Comparison of $S(q)$ for state A (dotted line) and state B (solid line) and their corresponding partial structure factor contributions (triangles and circles, respectively) for connectivity defined by $r_c = 1.035$. (b) The magnitude of $S(q)$, $S_{MM}(q)$, and $S_{CC}(q)$ for state A relative to state B as a function of $q$-value.

possibly characteristic) trend in the product of the average and skewness (i.e., the first and third moments), or ASK factor, of the cluster size distribution. The skewness is a measure of an excess of values to one side of the distribution relative to the mean (normalized by the variance). As an example, the skewness approaches zero when the distribution becomes evenly distributed about the average. Figure 3.9 demonstrates the change in ASK with $r_c$ for a HS fluid at three volume fractions (a) and all six HSDY states (b).

Every state in the HS fluid and HSDY system except the clustered state displays some divergence in the ASK factor. Clustered states maintain a steady value of ASK throughout the range of cut-off distances due to a steady average and skewness. For state C, these moments of $N(s)$ balance to a value of about one, but it is unclear whether this is by chance or not. In general, this is a distinguishing characteristic of states with a preferred cluster size in systems with SALR interactions.

In contrast, dispersed states diverge at small $r_c$ while percolated states diverge at both extremes of $r_c$. The same trends in the ASK factor are observed for HS systems

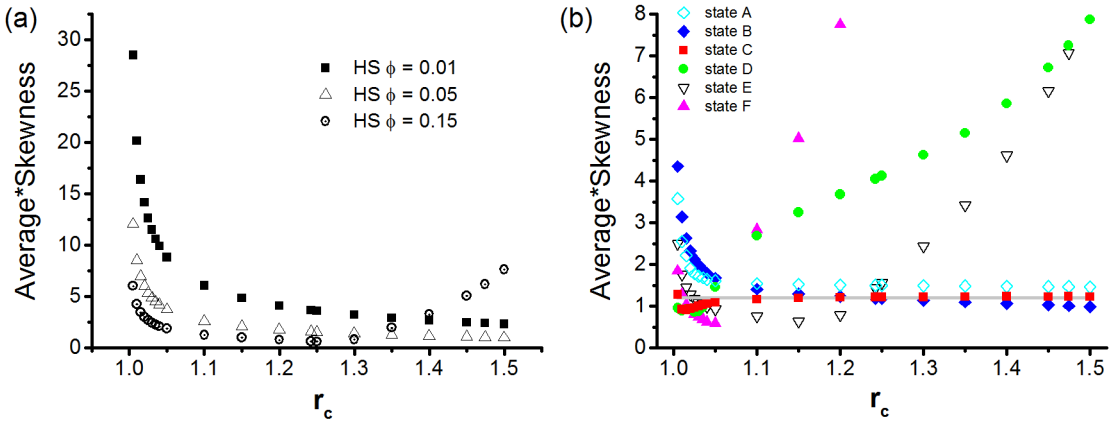


**Figure 3.9:** The product of the average and skewness of the cluster size distribution are plotted as a function of cut-off distance for (a) HS fluids at three volume fractions and (b) each of the six HSDY state points studied here. The trend in this parameter with $r_c$ appears to be a distinguishing feature of clustered states.

at small $\phi$ and large $\phi$, respectively. Due to the cluster size distribution being purely positive, the skewness arises mainly from the extent of the tail away from the average size. Therefore, dispersed fluid states (and low $\phi$ HS fluids) have a large positive skewness in conjunction with a small average cluster size. Consequently, the small probability of larger clusters creates a large skewness that causes a large ASK factor. For a percolated state, the average cluster size is so large that a small cluster size "tail" forms. Thus, both the skewness and average cause the ASK factor to diverge at small $r_c$ while at large $r_c$ the average cluster size accentuates even a small skewness value, causing large values of ASK.

### 3.6.3 Distinguishing Percolated States

The difference between a random percolated state and a cluster percolated state can be further illustrated by varying the cut-off distance, which highlights the proximity of particles. Systematically increasing the cut-off distance probes the lengthscale dependence of local order and provides insight into the microstructure and particle correlations. Note that the actual microstructure does not vary, just the definition of

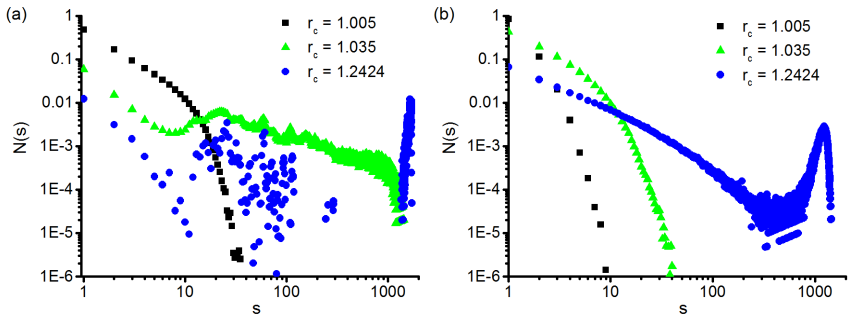


**Figure 3.10:** The cluster size distribution for three values of $r_c$ ( 1.005, 1.035, and 1.2424) for (a) state D and (b) state E.

cluster membership. Cluster size distributions for states D and E are shown in the Fig. 3.10 for three cut-off distances ($r_c$ = 1.005, 1.035, and 1.2424). State D evolves from a monotonically decreasing $N(s)$, to a preferred size with a peak at roughly 23 particles per cluster, and finally to a percolated cluster near the system size. This transition indicates the presence of clusters of a preferred size prior to percolation, which become integrated into the resulting percolated cluster structure. State E appears to transition directly from a monotonically decreasing $N(s)$ to a percolated $N(s)$ associated with a random dynamic percolation transition.

Figures 3.11 and 3.12 illustrate the trends in $g_{CC}(r)$ and characteristic particle configurations with cut-off distance for the cluster percolated and random percolated states (state D and state E, respectively). A single configuration with a representative cluster size distribution of the average for each percolated state is selected for the analysis. Configuration snapshots show only particles that are part of clusters and each cluster is labeled with a different color. When comparing the microstructure of states D and E (Fig. 3.11f and 3.12f), the cluster percolated state D appears to have a more ordered network that is similar to states found previously in experiment[26] and simulation.[46] Quantitatively, this order is evident by a pronounced doublet near $r$ = 1.8 and a smaller peak at $r$ = 2.6 in $g_{CC}(r)$ (Fig. 3.11c and 3.12c). These peaks help to distinguish state D from the other two percolated state as a cluster percolated

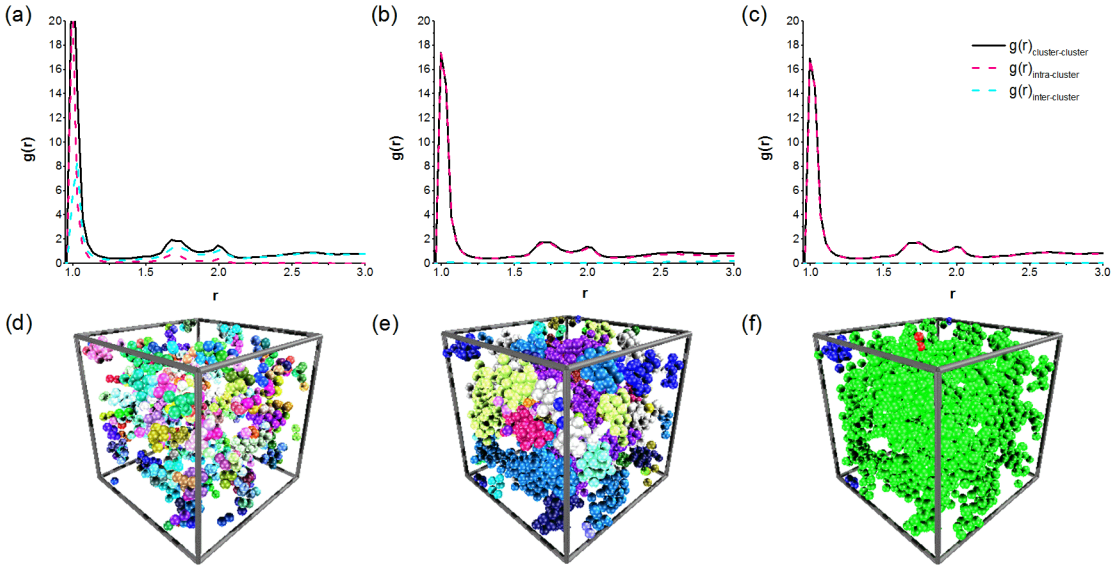


**Figure 3.11:** The $g_{CC}(r)$ as well as the intra-cluster and inter-cluster components are shown for cut-off distances of (a) 1.005, (b) 1.035, and (c) 1.2424 for state D. The snapshots (d-f) are of a characteristic configuration with the corresponding $r_c$ of the plot above and show particles within a given cluster as the same color.

state.

The intermediate range peaks in the $g_{CC}(r)$ of state D are present for all choices of cut-off distance. At a small cut-off distance of 1.005, the structure is already dominated by clusters. Further increase of the cut-off distance to 1.035 and 1.2424 shifts the preferred cluster size to larger sizes until a system spanning percolated cluster is evident. Interestingly, the location and magnitude of the peaks in $g(r)$ change little over this variation in cut-off distance indicating that the particle-level microstructure of state D is relatively homogeneous through the clustered fluid. This analysis supports a mechanism of percolation in state D, upon increasing $\phi$ from the clustered state, resulting from the merging of clusters. This is consistent with the stabilization of clusters at $T^* = 0.25$ by well-understood cluster-cluster repulsion.[39]

In contrast, the structure of state E in Fig. 3.12 exhibits a $g_{CC}(r)$ that contains a peak at contact and a weak, broad peak at $r = 2.0$ for all bond distances. At

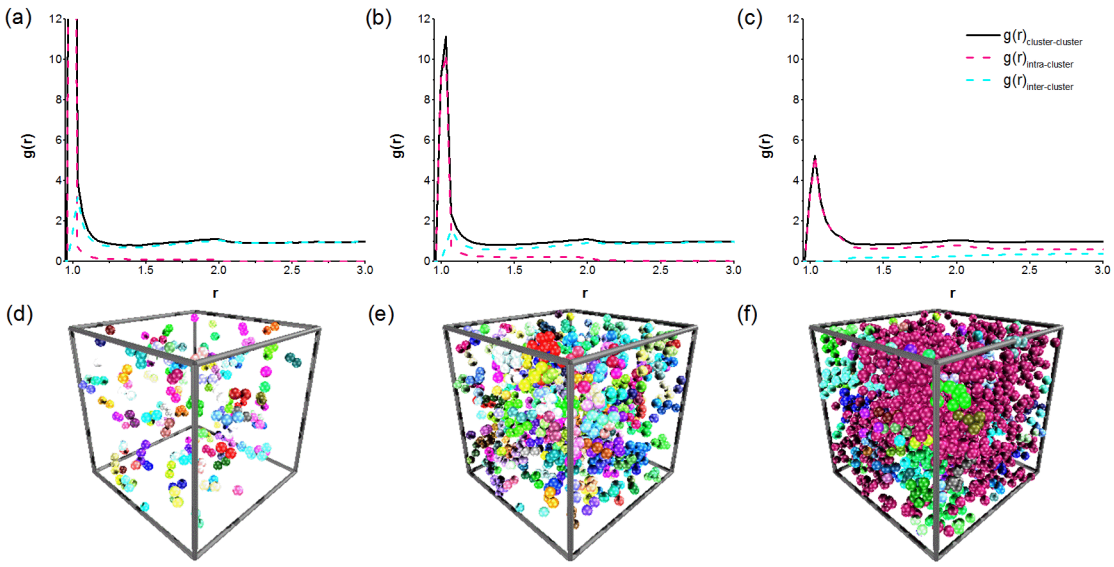


**Figure 3.12:** The same details as given in Fig. 3.11 for percolated state E.

the smallest cut-off distance of 1.005, the system is composed mainly of monomers and very small clusters. Upon increasing the cut-off distance to 1.035, more clusters appear with larger size and more polydispersity. Further increase of the cut-off distance to 1.2424 leads to percolation. For each choice of cut-off distance the $g_{CC}(r)$ is composed mainly of inter-cluster correlations with a small peak just above the bond distance value. Thus, clusters are randomly dispersed in the simulation box. Further, the dramatic drop in magnitude of the contact peak in the $g_{CC}(r)$ when increasing the cut-off distance is indicative of particle by particle growth of clusters. In contrast, in a percolated cluster state, aggregation of two clusters reduces the number of particles at cluster surfaces, which enhances the number of nearest neighbors and maintains a large contact peak. From this analysis we can conclude that the percolated structure of state E forms from the aggregation of monomers and small polydisperse clusters that eventually span the system. While the IRO peak indicates an inherent internal length scale, the correlations are weaker than those observed for the cluster-percolated state due to the size polydispersity of small clusters that comprise the percolated cluster.

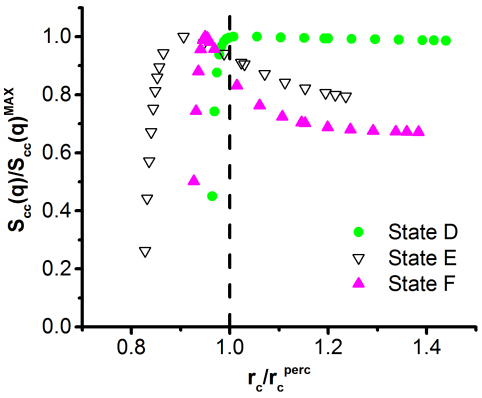


**Figure 3.13:** The relative magnitude of the IRO peak compared to its maximum value as a function of the cut-off distance. For comparison, the data are plotted relative to the cut-off distance at which 50% of the sampled configurations contain a percolated cluster.

Considering the large content of particles in percolated clusters in states D, E, and F (Fig. 3.4), as well as the large contribution to $S(q)$ from $S_{CC}(q)$ (Fig. 3.6) and $g(r)$ from $g_{CC}(r)$ (Fig. 3.11, Fig. 3.12), it is apparent that particle correlations and the IRO peak are mainly due to the intra-cluster correlations. By analyzing the height of the IRO peak in $S_{CC}(q)$, the cluster percolated state may also be distinguished from the other two percolated states. Figure 3.13 shows the magnitude of the peak in $S_{CC}(q)$ relative to its maximum value as a function of the cut-off distance relative to the value at which the system is percolated, $r_c^{perc}$ (i.e., the smallest cut-off distance where at least 50% of configurations have a percolated cluster). Immediately upon increasing the cut-off distance from a particle diameter, the $S_{CC}(q)$ peak magnitude increases dramatically before reaching a maximum for all three states, which is not necessarily at the percolation transition. States D, E, and F percolated at $r_c^{perc}$ values of 1.0422, 1.2141, and 1.0843, respectively. The cluster percolated state reaches the maximum at the onset of percolation then remains relatively constant. However, the IRO peak in $S_{CC}(q)$ of the two random percolated states reaches a maximum at a cut-off distance before the onset of percolation and slowly decreases until approaching its

own plateau. The relatively constant magnitude of the IRO peak with cut-off distance beyond percolation in state D indicates that the characteristic length scale separating clusters is maintained in the network, while randomly percolated states lack any such order.

### 3.7 Decomposing Contributions to the Solution Structure

Monomer-monomer, cluster-cluster, and cross-correlation contributions as well as the total system structure factor are presented in Fig. 3.14 for each of the six states studied. Each state has a unique combination of these features, which are compared in detail with respect to the structural features outlined in previous sections.

The three correlation components of the structure factor of the two monomer states (states A and B) are shown in Fig. 3.14a and 3.14b, respectively. As a reminder, these results are at the $r_c$ of 1.2424 as opposed to the earlier analysis comparing states A and B using an $r_c$ of 1.035. As shown in Fig. 3.7, monomers are the most abundant species in both monomer state solution structures at $r_c = 1.2424$, and similar to Fig. 3.8a both states have a structure with a pronounced IRO peak (at $q \approx 1$) relative to the monomer peak (at $q \approx 7.3$). The magnitude of the monomer correlations $S_{MM}(q)$, which are roughly 50% of the magnitude of the total structure factor over the full $q$-range, demonstrates the large content of monomers in both dispersed states. Although the magnitude of cluster correlations is smaller than monomer correlations, the presence of an IRO peak in $S_{CC}(q)$ in the low-$q$ region is more representative of the shape of $S(q)$. However, the location of the IRO peak in $S_{CC}(q)$ for both state A and state B are shifted from that of $S(q)$. This shift is caused by the drop in magnitude of $S_{MM}(q)$ and $S_{MC}(q)$ in the range of $q$-values around the IRO peak. Thus, the preferred length scale represented by the IRO peak in $S(q)$ is a complex combination of monomer and cluster correlations in solution. Interestingly, state B, which has roughly 50% more clusters in solution relative to state A, has a more significant peak in $S_{CC}(q)$ but a smaller total magnitude of the IRO peak in $S(q)$ relative to state A. These results suggest that

the weaker IRO correlations result from monomers and particles in clusters becoming significantly less correlated despite a larger extent of clustering.

Fig. 3.14c shows the partial structure factors for state C. Cluster-cluster correlations clearly dominate the structure factor at all $q$-values and are largely responsible for the IRO peak. The IRO peak has a magnitude of roughly 3.3, which is larger than the Hansen-Verlet criterion for crystallization of HS systems (2.85).[22, 27] However, these MC simulations and previous findings for SALR systems with short range attraction ($z_1 \geq 8$)[28] show no evidence of crystallization under conditions that produce IRO peaks above the Hansen-Verlet criterion. Although Ref. [22] has demonstrated that the Hansen-Verlet criterion is indeed applicable to SALR systems, crystallization is avoided with a short enough range of attraction. The delicate balance of short range attraction and long range repulsion produces sufficient polydispersity that prevents crystallization. Thus, the small "residual multi-particle entropy" described in Ref. [22] as the mechanism preventing crystallization is manifested in the intermediate range order correlations in SALR systems. In the case of a clustered state (state C), the polydispersity of the cluster size distribution prevents the formation of a Wigner crystal state of clusters.

The original hypothesis that an IRO peak can be used to quantify an average cluster size[45] can be shown to hold under conditions where the cluster size distribution has a defined, preferred size. The IRO peak position of these clustered states can be used as an estimate of the characteristic spacing between clusters, as previously reported in literature,[39] according to $r = 2\pi/q$. The $q$-value of the IRO peak for state C ($q = 1.2$) results in a cluster spacing estimate of $r \sim 5.2\sigma$. Assuming a monodisperse system of clusters of 12 particles, which is the preferred cluster size according to the maximum in $N(s)$, the average spacing ($d \approx {\rho_c}^{-1/3}$) between clusters is estimated as $5\sigma$. Thus, the preferred cluster size can be estimated from the location of the IRO peak for state points corresponding to a clustered fluid. However, this methodology will be misleading if applied more broadly to experimental results for dispersed fluids with an IRO peak. The broad polydispersity of clusters and a non-zero contribution from

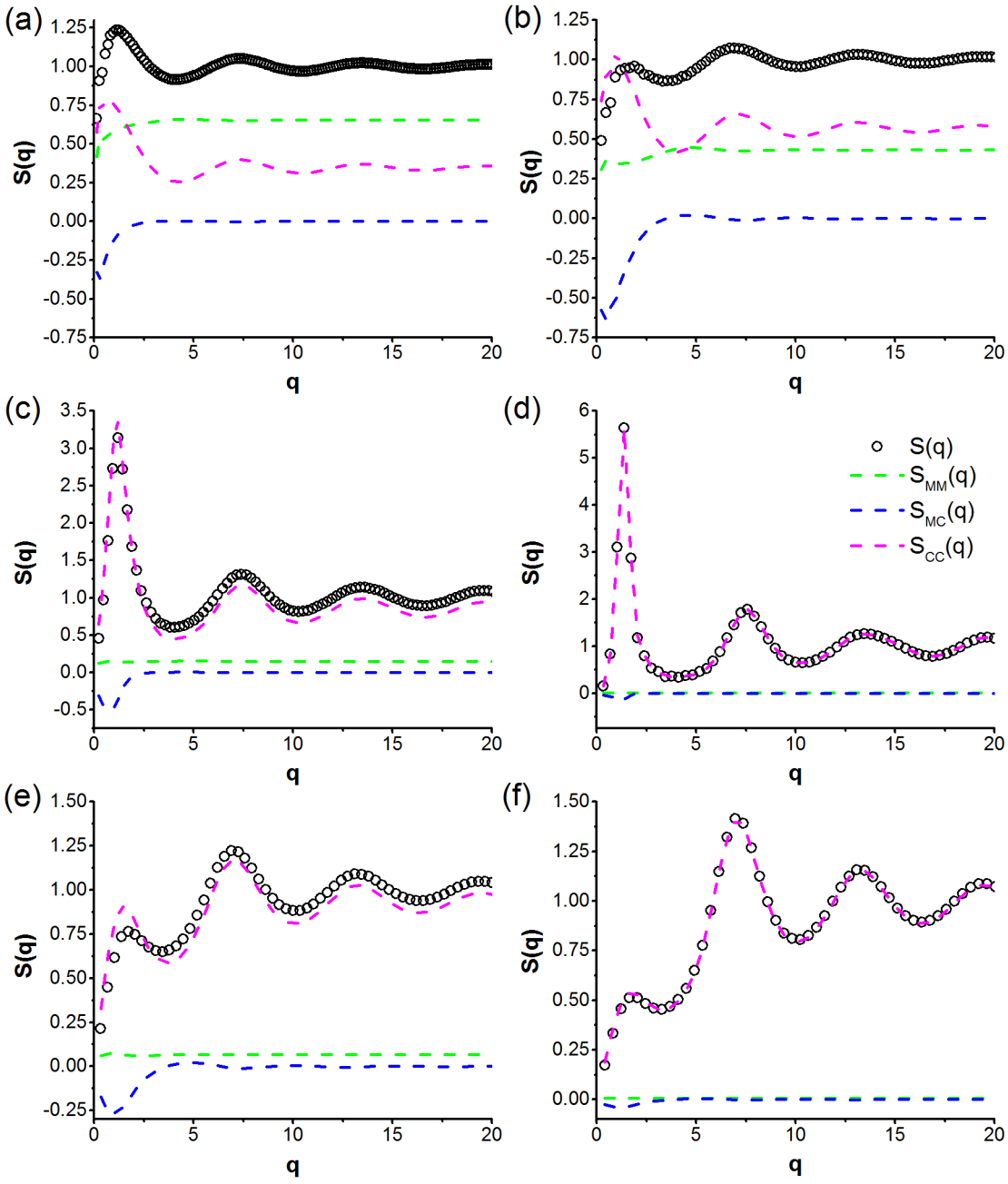


**Figure 3.14:** Structure factors and the three partial structure factor contributions are shown for (a) state A, (b) state B, (c) state C, (d) state D, (e) state E, and (f) state F. The diversity of microstructures that produce an IRO peak is direct evidence of the inaccuracy in using it as an indication of cluster formation.

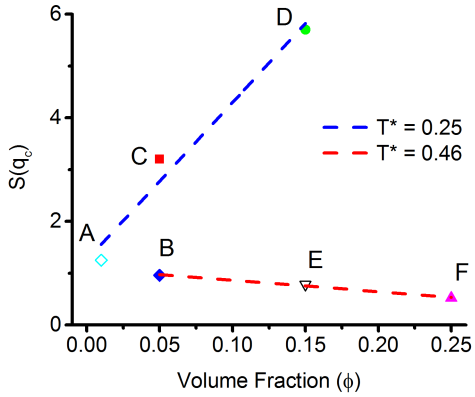


**Figure 3.15:** IRO peak magnitudes are shown for state points along the two isotherms studied. Trend in IRO peak height with volume fraction are distinctly different when below the critical reduced temperature ($T^* = 0.25$) compared to systems outside the two phase region of the reference attractive system ($T^* = 0.46$).

$S_{MM}(q)$ and $S_{MC}(q)$ are responsible for the general lack of correspondence between the location of the IRO peak in $S(q)$ and the physical microstructure of the fluid.

The percolated states have been analyzed in detail in previous sections, but the decomposition of $S(q)$ for states D, E and F are shown in Fig. 3.14d, 3.14e and 3.14f, respectively, to further demonstrate the generality of IRO peak formation. Clearly, cluster correlations are the main contribution to the structure factor. Although the IRO peaks formed by these states are in roughly the same position as in state C, they do not contain a preferred cluster size associated with its corresponding real space length scale. Depending on the type of percolated state, the magnitude of the IRO peak will differ significantly. This further indicates the danger in generalizing the presence of an IRO peak to cluster formation.

The magnitudes of each of the six states' IRO peak are summarized and provided in Fig. 3.15 as a function of volume fraction. The dotted lines display a possible distinguishing trend between the size of the IRO peak and volume fraction along the two isotherms studied here. Below the critical reduced temperature ($T^* = 0.25$), the

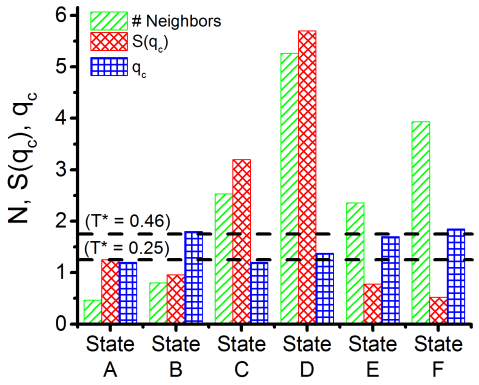


**Figure 3.16:** The average number of neighbors, IRO peak height $S(q_c)$ and IRO peak location $q_c$ are given for all six HSDY states studied.

magnitude of the IRO peak increases with volume fraction while above $T_c^*$ ($T^* = 0.46$) the magnitude decreases with increasing volume fraction. Thus, as clusters form and become more abundant with increasing volume fraction, they order or localize more significantly. In contrast, at higher temperatures, where a dominant cluster size does not form, increasing volume fraction produces an increasingly more disordered solution structure on the IRO lengthscale. These findings further support the distinction of cluster percolated and randomly percolated states. By systematically increasing $\phi$ during SANS experiments, the corresponding change in the IRO peak magnitude can be used to identify states with a preferred cluster size.

The large difference in the magnitude of the IRO peak between the clustered and dispersed/random states (both percolated and fluid) is highlighted in Fig. 3.16. Both the clustered state and the cluster percolated state have a distinctly larger IRO peak than the corresponding monomer states. Both state C and state D have an IRO peak magnitude greater than three. Previously, a large sharp IRO peak ($S(q) \geq 3$) has also only been observed in conjunction with the formation of a peak in the cluster size distribution (i.e., the formation of a cluster phase as defined in this work),[39, 40] although this trend was not emphasized. These literature results and the state points

studied in this chapter lead to the hypothesis that clustered states can be identified by an IRO peak greater than three in magnitude. This point will be expanded upon in the next chapter.

IRO peak magnitude can be understood in terms of its location ($q$-value) and the average number of neighbors of any given particle. These values are shown in Fig. 3.16 for each state point. The dotted lines distinguish the two reduced temperatures studied and highlight the effect of $T^*$ on the location of the IRO peak. States (A, C and D) at low temperature consistently formed IRO peaks at smaller $q$-values than at higher temperature (states B, E and F). The enhanced order at increasingly smaller $q$-values (larger lengthscales) for the lower temperature can be attributed to the larger strength of the repulsive barrier, which increases with decreasing $T^*$ in addition to the attractive well. However, the decomposition of correlations in $S(q)$ discussed earlier are sensitive to the balance of these two forces. Also, the average number of neighbors $N$ varies substantially between states. As expected, the clustered and percolated states have more neighbors compared to monomer states. The small value of $N$ for the monomer states indicates less widespread association compared to the random percolated states, yet the IRO peak magnitude of states A and B is actually larger than that of states E and F. Therefore, it is largely the localization of monomers over larger lengthscale that generates the observed IRO peak, which further demonstrates the lack of a direct relationship between cluster correlations and an IRO peak.

## 3.8 Conclusions

In this chapter, MC simulations were used to distinguish four distinctly different fluid microstructures that exhibit an IRO peak: dispersed, clustered, cluster percolated, and random percolated systems. These results support IRO peak formation as a general occurrence in dispersions with an SALR potential. The particle-level detail allows for the decomposition of an IRO peak into the contributions from both monomer and cluster correlations. The results indicate that the location of the IRO peak is not an accurate representation of inter-cluster spacing except in the specific scenario

of a preferred cluster size in solution. This study suggests that IRO peaks with a magnitude of roughly three or greater is a helpful "rule-of-thumb" to identify clustered and cluster percolated states. Further, under conditions conducive to cluster formation ($T^* < T_c^*$), increasing the volume fraction appears to enhance IRO in the system, while the opposite is true for states without distinct cluster formation. These trends may serve as experimentally useful criteria for identifying possible clustered states.

The clustered and cluster percolated states as defined in this chapter and Ref. [20] exist within the binodal of a reference attractive system. This relative location indicates cluster formation is driven by the short-range attraction that corresponds to phase separation for the reference state under identical conditions ($T^*$, $\phi$). The long-range repulsion suppresses the macroscopic phase separation, resulting in the formation of clusters with a preferred, finite size. The possible connections between the clustered fluid and the phase behavior of the reference attractive system are explored in more detail in the following chapter and documented in Ref. [21].

## REFERENCES


[1] Allen, M. P., and Tildesley, D. J. *Computer Simulation of Liquids*. Oxford University Press, 1987.

[2] Baxter, R. J. PercusYevick Equation for Hard Spheres with Surface Adhesion. *J. Chem. Phys. 49*, 6 (1968), 2770.

[3] Benavides, A. L., and Gil-villegas, A. The thermodynamics of molecules with discrete potentials. *Mol. Phys. 97*, 12 (1999), 1225–1232.

[4] Bomont, J.-M., Bretonnet, J.-L., and Costa, D. Temperature study of cluster formation in two-Yukawa fluids. *J. Chem. Phys. 132*, 18 (2010), 184508.

[5] Bomont, J.-M., Bretonnet, J.-L., Costa, D., and Hansen, J.-P. Communication: thermodynamic signatures of cluster formation in fluids with competing interactions. *J. Chem. Phys. 137*, 1 (July 2012), 011101.

[6] Broccio, M., Costa, D., Liu, Y., and Chen, S.-H. The structural properties of a two-Yukawa fluid: Simulation and analytical results. *J. Chem. Phys. 124*, 8 (Feb. 2006), 084501.

[7] Campbell, A., Anderson, V., van Duijneveldt, J. S., and Bartlett, P. Dynamical Arrest in Attractive Colloids: The Effect of Long-Range Repulsion. *Phys. Rev. Lett. 94*, 20 (May 2005), 1.

[8] Cardinaux, F., Gibaud, T., Stradner, A., and Schurtenberger, P. Interplay between Spinodal Decomposition and Glass Formation in Proteins Exhibiting Short-Range Attractions. *Phys. Rev. Lett. 99*, 11 (Sept. 2007), 1–4.

[9] Cardinaux, F., Stradner, A., Schurtenberger, P., Sciortino, F., and Zaccarelli, E. Modeling equilibrium clusters in lysozyme solutions. *Europhys. Lett. 77*, 4 (Feb. 2007), 48004.

[10] Cardinaux, F., Zaccarelli, E., Stradner, A., Bucciarelli, S., Farago, B., Egelhaaf, S. U., Sciortino, F., and Schurtenberger, P. Cluster-Driven Dynamical Arrest in Concentrated Lysozyme Solutions. *J. Phys. Chem. B 115*, 22 (June 2011), 7227.

[11] Chapela, G. A., del Río, F., Benavides, A. L., and Alejandre, J. Discrete perturbation theory applied to Lennard-Jones and Yukawa potentials. *J. Chem. Phys. 133*, 23 (Dec. 2010), 234107.

[12] Charbonneau, P., and Reichman, D. Phase behavior and far-from-equilibrium gelation in charged attractive colloids. *Phys. Rev. E 75*, 5 (May 2007), 1.

[13] Chen, S.-H., Broccio, M., Liu, Y., Fratini, E., and Baglioni, P. The two-Yukawa model and its applications: the cases of charged proteins and copolymer micellar solutions. *J. Appl. Crystallogr. 40*, s1 (Apr. 2007), s321–s326.

[14] Chen, S.-H., Rouch, J., Sciortino, F., and Tartaglia, P. Static and dynamic properties of water-in-oil microemulsions near the critical and percolation points. *J. Phys. Condens. Matter 6*, 50 (Dec. 1994), 10855–10883.

[15] Chiew, Y. C., and Glandt, E. D. Percolation behaviour of permeable and of adhesive spheres. *J. Phys. A. Math. Gen. 16*, 11 (1983), 2599–2608.

[16] Coniglio, A., Angelis, U. D., and Forlani, A. Pair connectedness and cluster size. *J. Phys. A. Math. Gen. 10*, 7 (1977), 1123.

[17] Costa, D., Caccamo, C., Bomont, J.-M., and Bretonnet, J.-L. Theoretical description of cluster formation in two-Yukawa competing fluids. *Mol. Phys. 109*, 23-24 (2011), 2845–2853.

[18] Cundy, C. S., and Cox, P. A. The hydrothermal synthesis of zeolites: Precursors, intermediates and reaction mechanism. *Microporous Mesoporous Mater. 82*, 1-2 (July 2005), 1.

[19] Frenkel, D., and Smit, B. *Understanding Molecular Simulations: From Algorithms to Applications*. Academic Press, 2002.

[20] Godfrin, P. D., Castañeda Priego, R., Liu, Y., and Wagner, N. J. Intermediate range order and structure in colloidal dispersions with competing interactions. *J. Chem. Phys. 139*, 15 (2013), 154904.

[21] Godfrin, P. D., Valadez-Pérez, N. E., Castañeda Priego, R., Wagner, N. J., and Liu, Y. Generalized phase behavior of cluster formation in colloidal dispersions with competing interactions. *Soft Matter 10* (2014), 5061.

[22] Hansen, J.-P., and Verlet, L. Phase transitions of the Lennard-Jones System. *Phys. Rev. 184*, 1 (1969), 151–161.

[23] Heyes, D. M., Cass, M., and Braka, A. C. Percolation threshold of hard-sphere fluids in between the soft-core and hard-core limits. *Mol. Phys. 104*, 20-21 (Oct. 2006), 3137.

[24] Jiang, T., and Wu, J. Cluster formation and bulk phase behavior of colloidal dispersions. *Phys. Rev. E 80*, 2 (Aug. 2009), 1–8.

[25] Kim, J. M., Castañeda Priego, R., Liu, Y., and Wagner, N. J. On the importance of thermodynamic self-consistency for calculating clusterlike pair correlations in hard-core double Yukawa fluids. *J. Chem. Phys. 134*, 6 (Feb. 2011), 064904.

[26] Klix, C. L., Royall, C. P., and Tanaka, H. Structural and Dynamical Features of Multiple Metastable Glassy States in a Colloidal System with Competing Interactions. *Phys. Rev. Lett. 104*, 16 (Apr. 2010), 165702.

[27] Kremer, K., Robbins, M. O., and Grest, G. S. Phase diagram of Yukawa systems: Model for charge-stabilized colloids. *Phys. Rev. Lett. 57*, 21 (1986), 2694.

[28] Lee, L. L., Hara, M. C., Simon, S. J., Ramos, F. S., Winkle, A. J., and Bomont, J.-M. Crystallization limits of the two-term Yukawa potentials based on the entropy criterion. *J. Chem. Phys. 132*, 7 (Feb. 2010), 074505.

[29] Liu, Y., Chen, W.-R., and Chen, S.-H. Cluster formation in two-Yukawa fluids. *J. Chem. Phys. 122*, 4 (Jan. 2005), 44507.

[30] Liu, Y., Porcar, L., Chen, J., Chen, W.-r., Falus, P., Faraone, A., Fratini, E., Hong, K., and Baglioni, P. Lysozyme protein solution with an intermediate range order structure. *J. Phys. Chem. B 115*, 22 (June 2011), 7238.

[31] Malins, A., Williams, S. R., Eggers, J., Tanaka, H., and Royall, C. P. The effect of inter-cluster interactions on the structure of colloidal clusters. *J. Non. Cryst. Solids 357*, 2 (Jan. 2011), 760.

[32] Martin, J. D., Goettler, S. J., Fossé, N., and Iton, L. Designing intermediate-range order in amorphous materials. *Nature 419*, 6905 (Sept. 2002), 381–4.

[33] Miller, M., and Frenkel, D. Phase diagram of the adhesive hard sphere fluid. *J. Chem. Phys. 121*, 1 (July 2004), 535.

[34] Mulheran, P., Pellenc, D., Bennett, R., Green, R., and Sperrin, M. Mechanisms and Dynamics of Protein Clustering on a Solid Surface. *Phys. Rev. Lett. 100*, 6 (Feb. 2008), 068102.

[35] Nagele, G. On the dynamics and structure of charge-stabilized suspensions. *Phys. Rep. 272*, 5-6 (1996), 215–372.

[36] Noro, M. G., and Frenkel, D. Extended corresponding-states behavior for particles with variable range attractions. *J. Chem. Phys. 113*, 8 (2000), 2941.

[37] Porcar, L., Falus, P., Chen, W.-R., Faraone, A., Fratini, E., Hong, K., Baglioni, P., and Liu, Y. Formation of the Dynamic Clusters in Concentrated Lysozyme Protein Solutions. *J. Phys. Chem. Lett. 1*, 1 (Jan. 2010), 126.

[38] Provis, J. L., and Vlachos, D. G. Silica nanoparticle formation in the TPAOH-TEOS-H2O system: a population balance model. *J. Phys. Chem. B 110*, 7 (Feb. 2006), 3098–108.

[39] Sciortino, F., Mossa, S., Zaccarelli, E., and Tartaglia, P. Equilibrium Cluster Phases and Low-Density Arrested Disordered States: The Role of Short-Range Attraction and Long-Range Repulsion. *Phys. Rev. Lett. 93*, 5 (July 2004), 5.

[40] Sciortino, F., Tartaglia, P., and Zaccarelli, E. One-dimensional cluster growth and branching gels in colloidal systems with short-range depletion attraction and screened electrostatic repulsion. *J. Phys. Chem. B 109*, 46 (2005), 21942.

[41] Seaton, N. A., and Glandt, E. D. Aggregation and percolation in a system of adhesive spheres. *J. Chem. Phys. 86*, 8 (1987), 4668.

[42] Sedgwick, H., Egelhaaf, S. U., and Poon, W. C. K. Clusters and gels in systems of sticky particles. *J. Phys. Condens. Matter 16*, 42 (Oct. 2004), S4913–S4922.

[43] Segrè, P., Prasad, V., Schofield, A., and Weitz, D. A. Glasslike Kinetic Arrest at the Colloidal-Gelation Transition. *Phys. Rev. Lett. 86*, 26 (June 2001), 6042.

[44] Stauffer, D. Scaling theory of percolation clusters. *Phys. Rep. 54*, 1 (1979), 1.

[45] Stradner, A., Sedgwick, H., Cardinaux, F., Poon, W. C. K., Egelhaaf, S. U., and Schurtenberger, P. Equilibrium cluster formation in concentrated protein solutions and colloids. *Nature 432*, 7016 (Nov. 2004), 492.

[46] Toledano, J. C. F., Sciortino, F., and Zaccarelli, E. Colloidal systems with competing interactions: from an arrested repulsive cluster phase to a gel. *Soft Matter 5*, 12 (2009), 2390.

[47] Torres-Arenas, J., Cervantes, L. A., Benavides, A. L., Chapela, G. A., and del Río, F. Discrete perturbation theory for the hard-core attractive and repulsive Yukawa potentials. *J. Chem. Phys. 132*, 3 (Jan. 2010), 034501.

[48] Valadez-Pérez, N. E., Benavides, A. L., Schöll-Paschinger, E., and Castañeda Priego, R. Phase behavior of colloids and proteins in aqueous suspensions: theory and computer simulations. *J. Chem. Phys. 137*, 8 (Aug. 2012), 084905.

[49] Vidales, A., Benavides, A. L., and Gil-villegas, A. Perturbation theory for mixtures of discrete potential fluids. *Mol. Phys. 99*, 9 (2001), 703–710.

[50] Woodcock, L. V. Percolation transitions in the hard-sphere fluid. *AIChE J. 58*, 5 (May 2012), 1610.

# Chapter 4

# GENERALIZED PHASE BEHAVIOR AND PROPERTIES OF CLUSTER FLUIDS

## 4.1 Introduction

Based on early scattering studies that associated the formation of a low-$q$ peak in the structure factor with cluster formation,[45, 47] several studies have explored the influence of competing interactions on the formation of a low-$q$ or IRO peak.[3, 6, 27] Relying on this definition of a cluster state, effective phase diagrams have been made of cluster fluids.[14] However, in the previous chapter, these interesting peaks that appear in the structure factor of solutions with competing interactions were shown to be a general consequence of intermediate range order (IRO)[18] rather than due to cluster formation as previously proposed. Therefore, identification of clustered fluid states in SALR systems based on this criterion of a low-$q$ peak are a misidentification and inaccurate.[18]

Clarification of the phase behavior of clustering solutions is of significant technological importance for biological materials of varying complexity, ranging from model globular proteins to therapeutic monoclonal antibodies (mAbs). Recent experimental work with high concentration solutions of mAbs[5, 11, 26, 35, 55, 56] and globular proteins, such as lysozyme,[9, 10, 13, 15, 30, 37, 47] suggest extensive formation of clusters in solution (though, not necessarily of a preferred size). In addition to stable clustered fluids, aggregation of such clusters have been reported as precursors or building blocks of gels.[7, 10, 18, 40, 42, 48] However, the fundamental issue of experimentally identifying clustered fluids in protein solutions is still debated in literature,[9, 28, 29, 30, 37, 43, 44, 46, 47] which further complicates the matter.

This chapter expands upon the link between the existence of clustered fluid states and the gas-liquid phase behavior of a reference potential fluid suggested in the previous chapter. Although clustered states were found to exist in the two-phase region of an appropriately defined reference fluid with excluded volume and a short range attraction, the transition boundary from random fluid states to clustered states was not precisely determined. In this chapter, by investigating a large number of state points and a wide range of potential parameters, this observation is conclusively demonstrated to be a general trend in SALR systems. A corresponding states diagram is found for the reference attractive potentials, which is used to create a generalized state diagram for clustered fluids. The resulting localization of state points is consistent with published results.[7, 39, 40, 48] Clustered states are also shown to consistently produce characteristically large IRO peaks and average coordination number of particles in the fluid, providing a new, semi-empirical method for identifying clustered fluids directly from scattering experiments. The majority of the work in this chapter has appeared as published research.[19]

## 4.2 Simulation and Analysis Methods

### 4.2.1 Simulation Protocol

Monte Carlo (MC) simulations[1, 17] are used as outlined in Chapter 2 to study the phase behavior of spherical particles by explicitly accounting for isotropic, two-body interactions including a short range attraction and longer range repulsion (SALR). Two representative SALR interaction potentials are shown in Fig. 4.1, which were described in detail in Chapter 2. The hard sphere double Yukawa (HSDY) and the Leonard-Jones-Yukawa (LJY) interaction potentials are used for their representation of experimentally relevant clustering materials[9, 10, 13, 30] and to allow for direct comparison between these MC simulation results and literature values.[7, 32, 40, 48]

The solution structure is represented by the pair distribution function $g(r)$ and structure factor $S(q)$ for each state, which are experimentally relevant functions obtained from scattering experiments. As a reminder, the pair distribution function is

calculated by averaging all particle configurations using direct summation according to:

$$g(r) = \frac{V^2}{N_p^2}\left\langle \sum_{i=1}^{N_p}\sum_{j=1}^{N_p} \frac{\delta(r_{ij}-r)}{V} \right\rangle, \tag{4.1}$$

using standard methods.[1, 17] Here, $r_{ij}$ is the separation of two particle centers, $N_p$ is the number of particles in the system, $V$ is the sample volume, and $\delta$ is the Dirac delta function. Restricting the calculation of Eq. 4.1 to include only particles contained in clusters, and explicitly accounting for each particle within the double summation, generates cluster-cluster correlations defined by $g_{cc}(r)$, the radial distribution function of clustered particles. This function represents the degree of order between clusters and helps in distinguishing between structural states formed by SALR systems as discussed in the previous chapter. The structure factor is calculated using the radial distribution function according to

$$S(q) = 1 + \rho \int_0^\infty \frac{\sin(qr)}{qr}[g(r)-1]4\pi r^2 \mathrm{d}r, \tag{4.2}$$

which is identical to Eq. 2.5 in Chapter 2 with $q$ defined as the scattering vector. Structure factors and radial distribution functions calculated from all simulations were found to quantitatively agree with numerical calculations using a thermodynamically self-consistent closure relation for the Ornstein-Zernike (OZ) equation.[18, 22]

### 4.2.2 Thermodynamics of a Reference Attractive System

A reference potential is defined for the HSDY and LJY potentials as the purely attractive portion of each potential. These are shown in Fig. 4.1 as dashed lines with their corresponding "full" potential. The HSDY reference potential is defined as:

$$\frac{U_{HSDY}^{ref}(r)}{kT} = \begin{cases} \infty & r < 1 \\ \frac{1}{T^*(1-\lambda)r}(-e^{-z_1(r-1)} + \lambda e^{-z_2(r-1)}) & 1 \le r \le r_c \\ 0 & r > r_c \end{cases} \tag{4.3}$$

and the LJY reference potential is:

$$\frac{U_{LJY}^{ref}(r)}{kT} = \begin{cases} \frac{1}{T^*}\left[4\left(r^{-2\alpha} - r^{-\alpha}\right) + A\left(\frac{\xi}{r}\right)\exp\left(\frac{-r}{\xi}\right)\right] & r \le r_c, \\ 0 & r > r_c \end{cases} \tag{4.4}$$

where $r$ is the separation distances normalized by the particle diameter $\sigma$ and $r_c$ is the cut-off distance defined as the separation at which the potential produces a zero interaction energy.[18, 19] For consistency, this cut-off distance is also used to determine connectivity as discussed in the previous chapter. The interaction parameters and corresponding cut-off distance of each of the potentials studied in this work, including those of previous studies used for comparison, are provided in Table 4.1. The choice of parameters is motivated by research that models physically meaningful systems observed in experiments and also overlap with potential parameters studied in literature. This range is extensive and covers many physically realizable systems of interest to the protein, biopharmaceutical, nanoparticle, and colloid communities.

Binodal lines representing liquid-liquid phase separation for the reference attractive potentials of each system in Table 4.1 are generated by discrete perturbation theory (DPT).[2, 12, 49, 53] DPT represents the interaction potential by numerous discrete square well-like steps and is known to calculate accurate gas-liquid binodals and critical points of purely attractive systems. The critical point obtained from DPT is compared with estimates for the reference attractive potentials using the law of

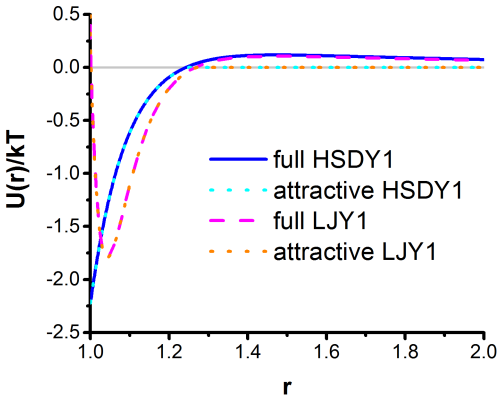


**Figure 4.1:** The HSDY1 (solid line) and LJY1 (dashed line) potentials from Table 4.1 are shown as representative of each function form of interaction potential. The attractive component of the potential (dotted lines) is used as a reference potential.

corresponding states.

The thermodynamic basis for a corresponding states representation of materials is well understood as a result of similar underlying interactions. This can readily be shown for different simple fluids interacting with an attractive potential, such as the classic Leonard-Jones fluid.[38] However, the phase behavior of systems with attractive interactions is sensitive to the range of attraction. Therefore, any two systems with a hard sphere excluded volume and attractive interactions will not necessarily represent each other within the construct of corresponding states.[16] In the particular case of sufficiently short range attraction, Noro and Frenkel demonstrated that these systems uphold such a relationship.[33] Though this original extended law of corresponding states (ELCS) restricted the range of (isotropic) attraction to less than $\sim 10\%$ of a particle diameter, recent work has shown ELCS to remain accurate for a range of attraction as large as $0.25\sigma$.[50] Therefore, the phase behavior of fluids interacting

**Table 4.1:** The inverse range of attraction, inverse range of repulsion, relative strength of repulsion to attraction, and cut-off distance are provided for all HSDY ($z_1$, $z_2$, $\lambda$, $r_c$) and LJY ($\alpha$, $1/\xi$, $A$, $r_c$) potentials used in this chapter.

| HSDY | $z_1$ | $z_2$ | $\lambda$ | $r_c$ |
|---|---|---|---|---|
| HSDY1 | 10.0 | 0.5 | 0.10 | 1.2424 |
| HSDY2 | 11.30 | 0.5 | 0.0945 | 1.2184 |
| HSDY3 | 11.93 | 0.5 | 0.0923 | 1.2085 |
| HSDY4 | 8.134 | 0.5 | 0.20 | 1.2108 |
| HSDY5 | 20.0 | 0.5 | 0.175 | 1.0894 |
| HSDY6 | 5.0 | 0.5 | 0.20 | 1.3577 |
| HSDY7[3] | 10.0 | 0.5 | 0.01 | 1.4847 |
| HSDY8[3] | 10.0 | 0.5 | 0.05 | 1.3153 |
| LJY | $\alpha$ | $1/\xi$ | $A$ | $r_c$ |
| LJY1 | 16.676 | 0.5 | 0.0910 | 1.2665 |
| LJY2 | 32.0 | 0.5 | 0.17 | 1.1005 |
| LJY3[48] | 100.0 | 0.5 | 0.20 | 1.0282 |
| LJY4[39] | 100.0 | 0.5 | 0.05 | 1.0433 |
| LJY5[40] | 18.0 | 2.0 | 8.0 | 1.1358 |

with the reference potentials defined in this chapter will also reduce to a common corresponding states diagram according to ELCS.

According to ELCS, the equilibrium phase behavior is less sensitive to the exact shape of the potential than the total effective strength of attraction. Therefore, the critical point can be recast in terms of a universal measure of total attractive strength such as the critical normalized second virial coefficient $B^*_{2c}$ calculated according to

$$B^*_{2c} = \frac{B_2(T^* = T^*_c)}{B_2(T^* = \infty)} = 1 + 3\int_1^{r_c} \left(1 - \exp\left[\frac{-U^{ref}(r, T^*_c)}{kT}\right]\right) r^2 \mathrm{d}r, \tag{4.5}$$

which is equivalent to Eq. 3.4 in the previous chapter, but specified at the critical point. Previous studies have then converted this measure to an effective range of attraction $\delta$ of an "equivalent" square well (SW) fluid (i.e., with the same $B^*_{2c}$ value) by

$$1 + \delta = \left(1 - \frac{1 - B^*_{2c}}{1 - \exp[1/T^*_c]}\right)^{1/3}, \tag{4.6}$$

where $T^*_c$ is the critical reduced temperature and $1/T^*_c$ is the well depth.[24, 33, 34] This mapping methodology is accurate for systems with short range attraction with either SW or Yukawa functional forms.[24, 34, 50] Normalizing the binodal of each reference potential by its corresponding critical point ($\phi_c$, $T^*_c$) produces nearly identical results for all systems in Table 4.1, consistent with the concept of corresponding states.

### 4.2.3 State Definitions

A particle is defined as part of a specific cluster when it is less than a distance $r_c$ from a neighboring particle. These calculations distinguishing particle "species" are summarized by the normalized cluster size distribution $N(s)$ represented by Eq. 3.1 in the previous chapter. The state of the fluid is determined by $N(s)$ at each set of conditions using definitions established in the previous chapter and in Ref.[18]. Figure 4.2 shows representative cluster size distributions of each of the four states found in SALR systems: dispersed fluid, clustered fluid, random percolated and cluster percolated states. Between 5 and 15 state points are chosen for each potential in Table 4.1 and associated with one of the four states.

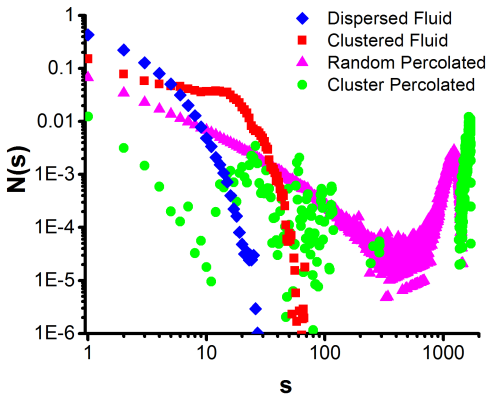


**Figure 4.2:** Characteristic cluster size distributions used to define each state point are shown for each of the four states identified in SALR systems (specifically for potential HSDY1): dispersed, clustered, random percolated and cluster percolated states.

A monotonically decreasing $N(s)$, which represents a state where monomers are the most abundant species in the system and clusters form without a preferred size, is used to identify a dispersed fluid. Several previous studies have defined clustered states by an average cluster size of 2 or greater[10, 31] or a large effective hydrodynamic radius,[37] which will fit the definition of a dispersed fluid used here. Although dispersed fluids are composed mainly of monomers, they will still contain some clusters that can influence material properties. In contrast, a clustered fluid state is defined by the formation of a local maximum in $N(s)$ for $s > 1$. Such a cluster size distribution indicates the ensemble average contains an energetically preferred range of cluster sizes. Therefore, unlike dispersed fluids, clustered fluid properties are expected to be governed predominantly by clusters around the preferred size. The combination of this particular state classification and definition of $r_c$ provides a self-consistent and physically significant solution structure and correlation with both the particle interactions and mechanical properties.

Percolation is defined as described in Chapter 2 when at least 50% of the sampled configurations contain a system-spanning cluster.[41] Both percolating states produce

a single peak in $N(s)$ near the system size. Clustered states will also percolate upon increasing the concentration and their $N(s)$ may exhibit a cluster peak in addition to the system-size peak, as shown in Fig. 4.2. This is a distinctly different structural state from a randomly percolated state due to the association of "building blocks" of a preferred size to form the cluster percolated network. As detailed in the previous chapter, these two percolated states can be distinguished by analyzing their structural order.

## 4.3 Results and Discussion

### 4.3.1 Corresponding States of the Reference Potentials

The diversity of interaction potentials used in this chapter is demonstrated by plotting them together in Fig. 4.3 with a value of $T^* = 0.5$. The range of repulsion is constant among all potentials (fixed at $2\sigma$) while the effective range of attraction varies from $1.0282\sigma$ to $1.4847\sigma$ and the relative strength of repulsion to attraction varies from 0.01 to 8.0. These parameters produce maximum repulsive interaction energy values ranging from $0.05kT$ to $3.0kT$ and energy well depths ranging from $-1.74kT$ to $-10.85kT$ (as a function of $T^*$ values used with each potential).

Although ELCS is anticipated to apply to the reference potentials studied in this chapter, it is explicitly tested and compared with literature results. The values of $T_c^*$ from previous studies are shown in Fig. 4.4a with simulation results of HSDY states and two representations of the LJY states. In the case of the LJY potential, the value of $\delta$ depends on the definition of the well depth, while the HSDY potential is normalized such that the well depth is always equal to $1/T_c^*$. Figure 4.4b compares the LJY2 potential to the SW potentials that result from defining the well depth as the same value as the HSDY potential $1/T_c^*$ (labeled $T_c^*$) or as the minimum in the potential at $T_c^*$ (labeled $U_{min}$). The effective square well potentials plotted in Fig. 4.4b produce the effective range of attraction of the circled stars in Fig. 4.4a. Despite having identical values of $B_{2c}^*$, the definition based on $U_{min}$ is significantly shifted from the $T_c^*$ definition and literature results. From Fig. 4.4a, this appears to be a

general failure of this methodology for LJY potentials. Therefore, $T_c^*$ is the more appropriate representation of an effective SW potential and also provides consistency with the estimates used for HSDY potentials. As such, the dependence of the critical temperature on the effective range of attraction for the reference attractive potentials (filled stars and *green* open stars) are consistent with literature results for square well[24] and attractive Yukawa[34] fluids. Only when approaching an effective range of about 1.1 do the reference potentials deviate from expected trends. However, these correspond with HSDY potentials whose $r_c$ is larger than even the longest reported range accurately represented by ELCS.[50]

According to the Noro-Frenkel ELCS,[33] the Baxter parameter $\tau_B = 0.25/(1 - B_2^*)$ should be about 0.1 at the critical point of any system with short range attraction. In Fig. 4.5, the $\tau_B$ for all potentials used in this work are compared to this expected value for the set of calculated effective ranges of attraction. The majority of the critical points calculated for the 13 potentials used in this chapter appear to follow the expected ELCS behavior. However, two potentials with large effective ranges have critical temperature values that are greater than expected. This is likely because

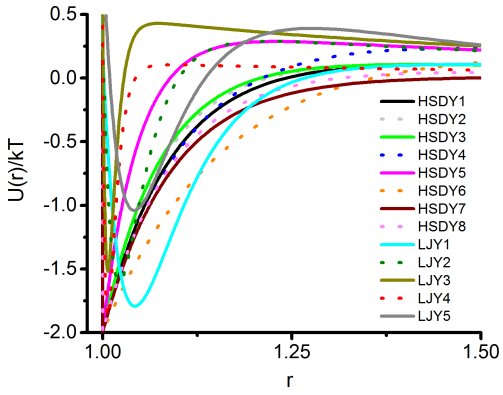


**Figure 4.3:** Interaction potentials are plotted for each condition in Table 4.1. Each has a different color and lines alternate between solid and dotted for clarity.

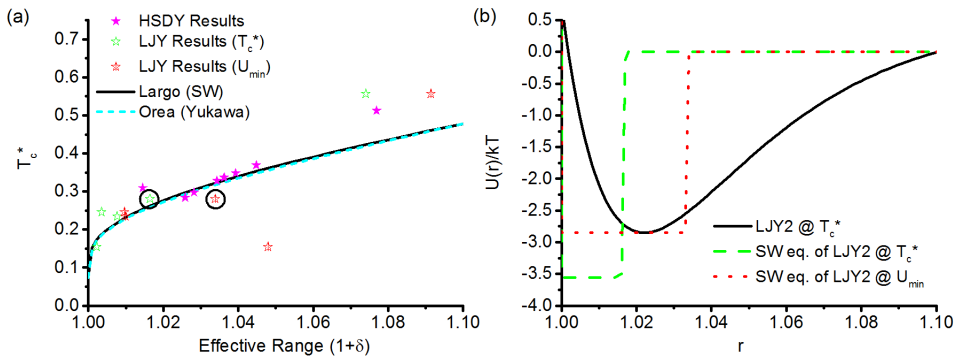


**Figure 4.4:** (a) The critical reduced temperature is plotted for HSDY (filled stars) and LJY (open stars) systems as a function of the effective range of attraction for a SW fluid with the same $\tau_B$ value $(1+\delta)$. Also plotted are literature results for SW[24] (solid line) and Yukawa[34] (dotted line) fluids. (b) Two definitions of the effective range of attraction (dashed lines) for SW potentials are shown compared to potential LJY2 (solid line). Open stars in (a) correspond to the definition of $\delta$ with the same color in (b).

the range of these potentials is near the upper limit of validity of ELCS. Further, three (circled) points deviate significantly from a $\tau_B$ of 0.1, which correspond to the potentials with the shortest ranges of attraction. The deviations most likely arise from inaccuracies in the DPT method used to estimate $T_c^*$ under these conditions.[50]

Normalization of effective strengths of attraction in HSDY systems may also provide a useful *universal* measure of intermediate range order in the solution structure factor. Figure 4.6 shows the location of the IRO peak $q_c$ formed in several systems studied in this chapter as well as results from two previous studies.[3, 40] This data set includes the location of IRO peaks for all four types of states defined in the previous section. Interestingly, when $q_c$ is plotted by a measure of the strength of attraction $T^*/T_c^*$ combined with a convoluted measure of the strength and range of attraction $(1-B_{2c}^*)$, the data appear to fall onto one single linear curve. One noticeable aspect of this normalization is that the peak locations are insensitive to variations in

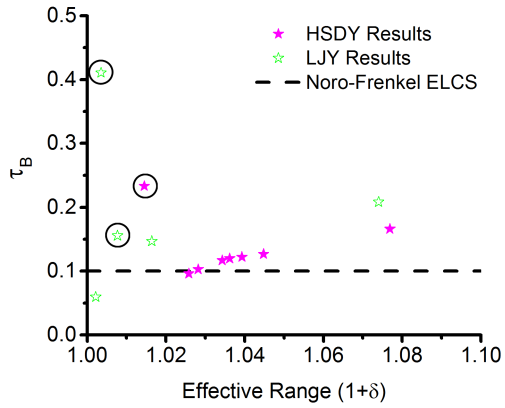


**Figure 4.5:** The Baxter parameters at the critical point of each HSDY (filled stars) and LJY (open stars) potential are plotted relative to the prediction from ELCS (dashed line)[33] as a function of the effective range of attraction.

volume fraction and repulsive interactions (that act to produce a larger effective volume fraction). Previous work has highlighted the fact that the location of the IRO peak is insensitive to volume fraction, but shifts when changing temperature or salt concentration (subsequently altering the effective interactions).[47]

Increasing values along the x-axis indicate stronger and possibly longer range attraction, which leads to smaller correlation lengths (larger $q_c$). As was shown in the last chapter and will be demonstrated more generally later this chapter, the location of clustered states (with large IRO peaks and therefore strong IRO correlations) below the binodal of a reference attractive system suggests that particle localization to any extent is driven largely by attractive interactions.[18] Regardless of volume fraction, if particles interact by some form of long range repulsion, the strength and range of attraction appear to dictate the lengthscale of spacing between different cluster species/sizes.

The empirical correlation shown in Fig. 4.6 is an additional representation of the general relationship between competing interactions and IRO. While clustered states have significantly larger IRO peaks relative to other states, the universality of this

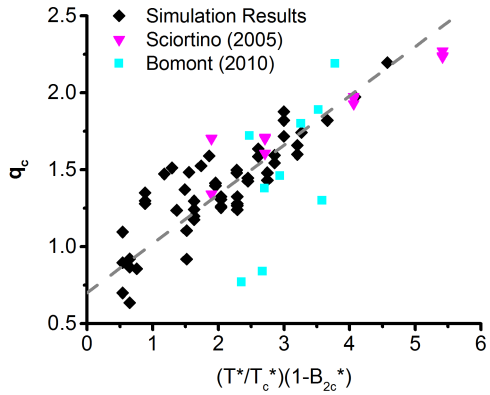


**Figure 4.6:** The location of the IRO peak $q_c$ appears to be a universal (linear) function of an effective strength of attraction represented by $(T^*/T_c^*)(1 - B_{2c}^*)$. Diamonds are simulation results of new states studied in this chapter, triangles are from Ref. [40] and squares are from Ref. [3].

trend in $q_c$ for all four types of state points suggests a common fundamental driving force for association on intermediate lenthscales. The consistency of the data with the given x-axis parameter (as a function of $B_2^*$) in Fig. 4.6 also further implicates using an $r_c$ determined from the point of zero energy in the potential as the most physically representative value as discussed in Chapter 3.

### 4.3.2 Generalized Cluster State Diagram

Binodal lines of all reference attractive potentials are plotted together in Fig. 4.7a. The critical points of these systems are found to vary in volume fraction from roughly 0.2 to 0.4 and critical temperatures vary from about 0.15 to 0.55. This diversity is reflected in the different location and shapes of the two-phase regions of each SALR system. Each of the binodals is then normalized by their corresponding critical points to reduce the diversity into a consistent set of lines encompassing the same region of phase space.

The reduced temperature $(T^*/T_c^*)$ is plotted as a function of reduced volume fraction $(\phi/\phi_c)$ in Fig. 4.7b, consistent with the law of corresponding states. When

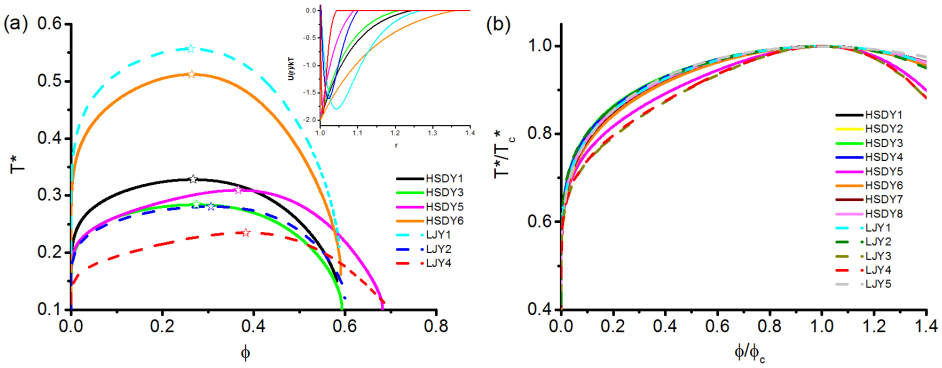


**Figure 4.7:** (a) Binodals corresponding to a subset of the potentials studied in this chapter are plotted together. The inset shows the associated reference attractive potential of each binodal with the same line color and style. (b) Binodal lines of all reference attractive potential are normalized by their respective critical points and shown to overlap (except for HSDY5, LJY3, and LJY4 that are discussed in the text).

plotted together, almost all systems overlap, displaying excellent congruence for all but three systems. Binodal calculations for potentials HSDY5, LJY3, and LJY4 produces the greatest inaccuracy when applying ELCS. These potentials show the largest deviations from the average behavior and were also circled as outliers in Fig. 4.5. However, DPT calculations become more difficult for potentials with ranges of attraction less than $1.1\sigma$, or less than 10%, and deviations from exact behavior have been reported to be as large as 15%.[49] Specifically, if the range of attraction is too short, DPT calculations have been shown previously to bias the liquid branch of the binodal,[50] as observed in Fig. 4.7a for these potentials. Therefore, the differences observed between the majority of normalized binodals and the three outliers is roughly within the uncertainty of DPT. In the previous section, the behavior of all critical points ($T_c^*$) was shown to be consistent with reported results for square well[24] and attractive Yukawa[34] fluids. Therefore, in general, the binodals show a universal behavior and potential HSDY1 is used to represent all SALR systems for the remainder of the chapter.

Several equilibrated state points for the potentials given in Table 4.1 are classified into one of four structural states, which are subsequently normalized by the corresponding critical point of their reference potential. These normalized state points are plotted in Fig. 4.8, which is a master corresponding states diagram within reduced phase space ($\phi/\phi_c$, $T^*/T_c^*$). The four types of states are observed to lie in defined regions of the state diagram (distinguished by color and pattern) relative to the reference attractive fluid binodal. Note that although the binodal of the HSDY1 potential is used here, the binodal of any other potential can be substituted without alteration of this interpretation (see Fig. 4.7b). As might be expected, dispersed fluids and random percolated states lie above the binodal of the reference attractive fluid at low and high volume fractions, respectively. Similarly, clustered fluids and cluster percolated states lie within the two-phase region of the reference attractive fluid. The overlap between the dispersed and clustered fluid regions highlights the uncertainty in the binodals calculated by DPT and the semi-quantitative nature of the relationship between a purely attractive system phase separation and cluster formation.

The results in Fig. 4.8 distinctly demonstrate that the two-phase region of a reference attractive system can be used to identify the behavior of clustered fluids and cluster percolated states of (isotropic) SALR systems. This confirms the hypothesis presented in Chapter 3 and extends it to a much broader range of potential parameters. Below the reference binodal, the fluid would phase separate due to the absence of repulsion. Therefore, cluster formation is similar to, but not literally, a frustrated phase separation. The long range repulsion balances the strong attractive driving force initiating aggregation, thereby preventing the unbounded growth of clusters. The result is clusters with a preferred size. As $\phi$ increases, more clusters of the preferred size form until they merge and span the system (i.e., percolate), producing a network-like structure with strong intermediate range order.

The observation of a corresponding states diagram for cluster fluids provides an efficient and robust method for identifying the presence of clusters of a preferred size for a diverse range of materials with (isotropic) SALR interactions. By extracting an

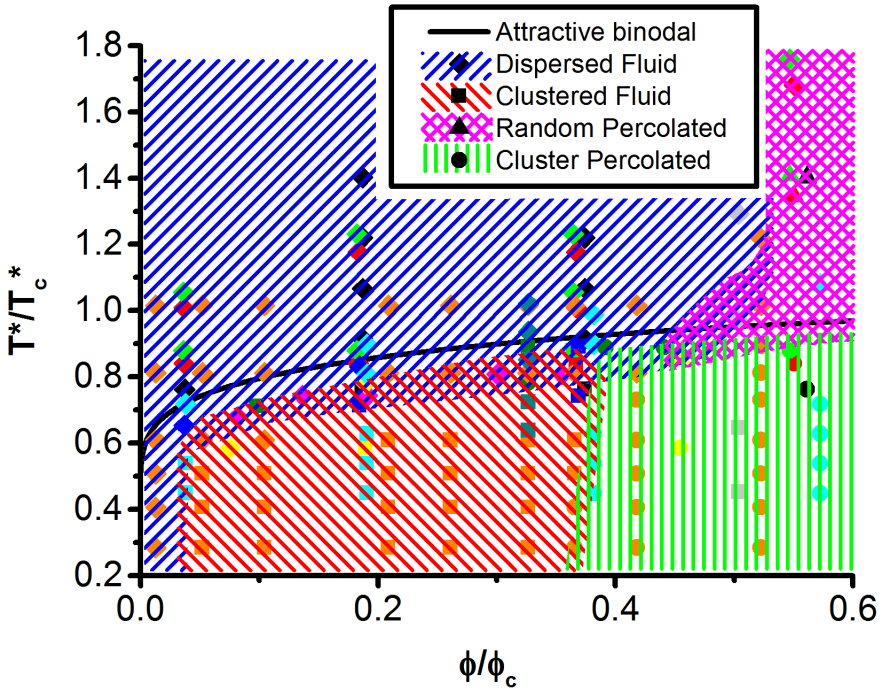


**Figure 4.8:** Normalizing several state diagrams according to ELCS,[33] a generalized phase diagram for clustered states is produced. New state points from this chapter are combined with literature results from Ref. [40], Ref. [32] and Ref. [7] (orange, dark cyan, and grey points, respectively). The color of each state point corresponds with the potential in Fig. 4.3 used in that simulation. Four distinct regions are found for dispersed (up-right), clustered (down-right), random percolated (criss-cross), and cluster percolated (vertical).

effective square well range of attraction ($\delta$) from any HSDY potential, as demonstrated in Fig. 4.4b, known empirical relationships between $\delta$ and $T_c^*$ (see Fig. 4.4a) and $\phi_c$ can be used to estimate the location of the critical point for the system of interest.[24, 34] Using this point, the region of phase space expected to contain cluster fluids can be easily estimated.

### 4.3.3 IRO Peaks in Clustered States

The previous chapter demonstrated that IRO peaks alone are insufficient to indicate the formation of clustered or cluster percolated states. However, the work in Chapter 3 as well as previous studies provide evidence of a possible correlation between the magnitude of IRO peaks and the formation of a peak in the cluster size distribution (i.e., clustered states as defined here).[39, 40] It is logical to hypothesize that a large peak magnitude, which indicates greater structure in the fluid, would correlate with the presence of a preferred cluster size in the solution structure. Fig. 4.9 shows the IRO peak magnitudes for all states explored in this work. Data from literature[39, 40] is also shown in Fig. 4.9 as open and half-filled systems. Both new simulation and previous literature results for clustered and cluster percolated states appear to form larger IRO peaks than dispersed fluid and random percolated states. In particular, an IRO peak magnitude of $\sim$ 2.7 distinguishes these two subsets of solution structures, with dispersed and clustered fluids at low volume fractions and the two types of percolated states at larger volume fractions. Experimental results from concentrated lysozyme protein solutions, an experimentally relevant material with similar SALR interactions as these simulations, also agree with these results. Lysozyme solutions do form IRO peaks in $S(q)$, but with a magnitude below 2.7,[8, 10] which consistently corresponds with a broad cluster size distribution (i.e., a dispersed fluid as defined here).

Figure 4.9 also indicates that clustered and cluster percolated states can form IRO peaks with a magnitude of 10 or greater. As mentioned in the previous chapter, a peak in $S(q)$ with a magnitude greater than 2.85 is indicative of a freezing

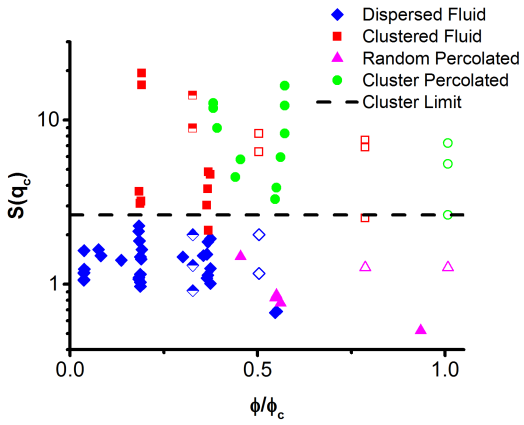


**Figure 4.9:** The magnitude of IRO peaks are plotted as a function of reduced volume fraction. All clustered and cluster percolated states lie above an apparent critical magnitude of $\sim 2.7$ (dashed line) separating them from monomer and monomer percolated states below this value. Filled symbols are from the new simulations performed here, open symbols are from Ref. [7], and half-filled symbols are from Ref. [32].

transition.[20, 23] Previous work has shown this empirical Hansen-Verlet criteria to accurately predict phase transitions for the HSDY interaction potential[25] and, in particular, the formation of Wigner crystals in cluster fluids.[39] However, short range attraction ($z_1 \geq 8$), as used in the current simulations, maintain a fluid state in SALR systems. In agreement with these expectations, there is no evidence of crystallization in the simulations reported here, despite the significantly larger peaks found in this chapter compared to Chapter 3. Most likely, non-ergodic behavior is prevented by the significant polydispersity of cluster sizes and shapes in cluster percolated and clustered states.[19]

### 4.3.4 Internal Cluster Structure in Clustered Fluids

In the presence of short-range attractive interactions, particles (or molecules) require at least 2.4 neighbors on average to produce what is known as "rigidity percolation"[21] as shown by theory and experimental studies of atomic glasses. Theoretically, the rigidity percolation transition assumes that a minimum number of neighbors or caging

elements is required to restrict the degrees of freedom available to particles in three dimensions.[36] A minimum of 2.4 nearest neighbors (or coordination number) has been reported as a criterion for dynamically arrested states in atomic systems[36] and, more recently, in colloidal systems.[52] Therefore, the ability to distinguish states according to the average particle coordination number $\langle N \rangle$ as a function of the average cluster size $\langle s \rangle$ is tested in Fig. 4.10. For systems that can be directly imaged by optical microscopy, this distinguishing feature will be more easily accessible than the magnitude of the IRO peak in scattering patterns.

Instead of defining states through the structure factor, as demonstrated in the previous section, the identification by coordination number shows that all four states appear to reside in distinct regions of Fig. 4.10. This plot includes all state points studied in this work as well as those from a previous study.[40] As expected, the two types of percolated states consistently have larger average cluster sizes than the dispersed and clustered fluids. Interestingly, both clustered fluid and cluster percolated states have distinctly larger coordination numbers than the other two states. Specifically, the transition from a dispersed fluid state to either a clustered state or random percolated state occurs at an average coordination number of $\sim 2.4$ (shown by the dashed line in Fig. 4.10), which is consistent with rigidity percolation. A random percolated state is distinguished from a cluster percolated state at a coordination number larger than 2.4, which is a function of $\langle s \rangle$ (shown by the solid line in Fig. 4.10). Due to the separation between these regions of state points, it appears that $\langle N \rangle$ can be used as a semi-empirical criterion for distinguishing between states.

As clusters grow in size, the relative amount of particles on the surface to those composing the "core" decreases. This is strictly true for spherical clusters, but holds for clusters whose fractal dimension $d_f$ is more spherical, $d_f \sim 3$, than linear, $d_f \sim 1$, which is true of the clusters formed by the SALR systems listed in Table 4.1 and in a previous work with similar potentials.[51] The internal particles have a higher number of neighbors as compared to those at the cluster surface or free in solution. Therefore, as the average cluster size increases, it is not surprising that the average

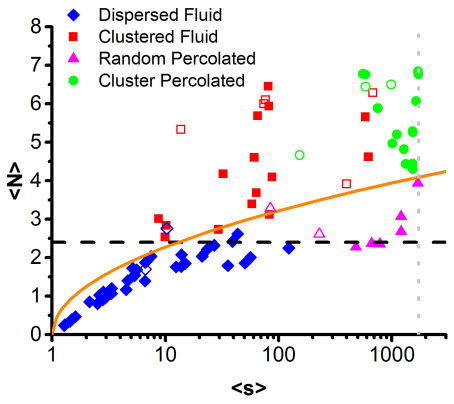


**Figure 4.10:** Average coordination number $\langle N \rangle$ is plotted as a function of average cluster size $\langle s \rangle$. The minimum value of $\langle N \rangle = 2.4$ (dashed line) for rigidity percolated[21] separates dispersed fluids from all other states. Clustered and cluster percolated states are further distinguished by Eqn. 4.7 (solid line). Open symbols are taken from Ref. [7].

coordination number does as well. This explains the general increase in the range of $\langle N \rangle$ values obtained with increasing $\langle s \rangle$ in Fig. 4.10. Interestingly, the minimum average coordination number required to form clustered states follows the empirical relationship between the average cluster size:

$$\langle N \rangle = 1.5(\ln\langle s \rangle)^{0.5}, \tag{4.7}$$

given by the solid line in Fig. 4.10. This minimum average coordination number is indicative of the local order necessary for cluster formation to be energetically preferred. A larger coordination number produces an enthalpic contribution to the free energy (from the short range attraction component of the potential) that compensates for the reduction in entropy in the compact structure. The net result is a lower free energy for cluster sizes around the average, making them preferential to other sized clusters.

As a measure of the local order necessary to form clusters represented by Eq. 4.7, these values of the average coordination number are compared with those calculated numerically for spherical clusters of $s$ particles with four cubic lattices: face-centered, body-centered, simple cubic and diamond cubic (FCC, BCC, SC and DC, respectively).

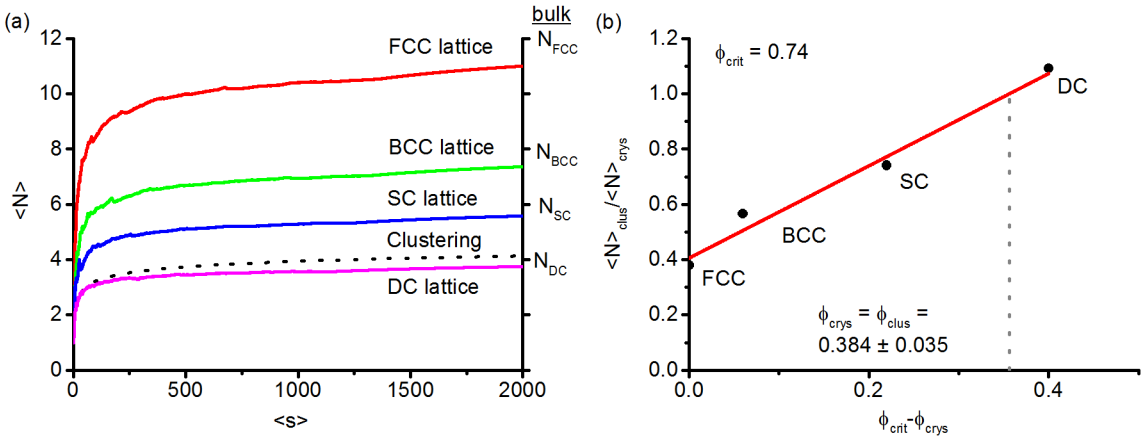


**Figure 4.11:** (a) The dependence of $\langle N \rangle$ on cluster size is plotted for spherical clusters with four different crystal lattices and Eq. 4.7. The bulk values of $\langle N \rangle$ for each crystal structure are also provided. (b) Normalizing $\langle N \rangle$ of the four crystal lattices by Eq. 4.7 produces constant values, which appear to increase linearly with the crystal volume fraction ($\phi_{crys}$) relative to the FCC lattice ($\phi_{crit}$). The equivalence point of the coordination numbers provides an estimate of the minimum volume fraction needed to form clustered states ($0.384 \pm 0.035$).

These structures have well-known packing fractions (0.74, 0.68, 0.52 and 0.34, respectively) and coordination numbers that are directly correlated. By comparing these non-linear relationships, the local volume fraction of clusters formed in clustered states can be estimated. Figure 4.11a shows the trends in coordination number with cluster size for all four crystal lattice based cluster structures and the empirical cluster line, Eq. 4.7. Remarkably, the empirical function is nearly identical to the trends in each of the four crystal structures, producing constant values when normalized by each other over the range of average cluster sizes. This indicates a consistent relationship between local packing fraction and coordination number regardless of cluster size. By taking the ratios of coordination number ($\langle N_{clus} \rangle / \langle N_{crys} \rangle$), a value of one would indicate the volume fraction of a well-defined crystal lattice that represents the local cluster structure in clustered states. Plotting these points as a function of the difference in volume fraction from the maximum possible packing ($\phi_{FCC} = 0.74$) in Fig. 4.11b results in a linear fit. The resulting equivalence point produces an estimate of the local volume fraction of cluster formation at $\phi = 0.38 \pm 0.04$. Previous experimental work in Ref. [7] estimated the cluster packing fraction to be $\sim 0.42$ at all bulk volume fractions in which clustering was observed, strikingly similar to that found here. These values may also serve as an upper limit of clustered fluid states, above which the bulk density makes individual clusters unable to be distinguished, likely leading to states being defined as cluster percolated.

While rigidity percolation theory predicts the average coordination number distinguishing dispersed fluid and random percolated states observed in Fig. 4.10, the applicability of this criterion to the formation of clustered fluids is unexpected. Interestingly, no cluster states form at $\langle s \rangle < 8$ or $\langle N \rangle < 2.4$. The value of 2.4 does not strictly demarcate dispersed and clustered fluids, but Eq. 4.7 consistently lies above this value at all average cluster sizes for which clustered states are found to exist. The significant IRO peak magnitudes shown in Fig. 4.9 can be used to extend the concept of restricted degrees of freedom to this empirical correlation. Strong intermediate range order indicates a large degree of localization, both within individual clusters and

correlations between monomers and clusters, as demonstrated in the last chapter. Apparently, when particles are localized to a density of about $\phi \sim 0.38$, the motion of particles and clusters is hindered in a similar fashion to the caging observed in glassy and percolated states of fluids interacting only with short range attraction. Further, the long-range repulsive forces between monomers and clusters make caging possible over the intermediate range lengthscale as well.

According to mode-coupling theory, a very large magnitude of the IRO peak indicates the formation of a cluster glass.[54] Within this physical picture, particles in a cluster are caged in the traditional sense by many neighbors. Therefore, despite the seemingly low local volume fraction inside a cluster from Fig. 4.11b, clusters likely have locally glassy structures that are sustained by a minimum average coordination number. Experimental observations of lysozyme diffusivity using neutron spin echo appear to agree with this hypothesis.[10, 15, 37] This SALR material has a collective diffusivity that is independent of lengthscale over small distances (large $q$-values), which suggests that local dynamics are slow and possibly glassy in nature (i.e., the dynamics are dominated by cluster diffusivity).

A possible signature of cluster formation was identified in Ref. [4] as a jump in the excess entropy $S^{ex}$ of systems interacting with an SALR potential. However, this jump was associated with the onset of an IRO peak in $S(q)$ as opposed to a peak in $N(s)$. Therefore, this feature is not necessarily associated with clustered states as defined here. Their work utilized the same parameters as potential HSDY1 in Table 4.1, which forms clustered states below the reference attractive binodal, where $T_c^* = 0.328$. The jump observed in $S^{ex}$ occurred at a $T^*$ of 0.688, far above the reference attractive binodal.[4] Therefore, this jump is likely a signature of the entropy change related to intermediate range order, not the formation of clustered states. However, further study of additional thermodynamic signatures of clustered fluids will progress current understanding of SALR systems.

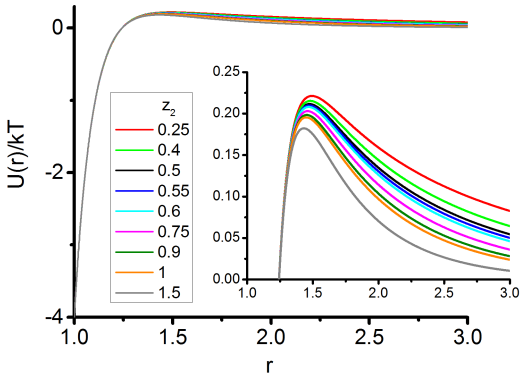


**Figure 4.12:** The HSDY1 potential is plotted with a variety of $z_2$ values with a fixed value of $B_{2c}^*$. The inset highlights the shift in the magnitude and position of maximum energy of $U(r)/kT$.

### 4.3.5 Role of Long-Range Repulsion

So far in this chapter, the range of the repulsion has been fixed to about $2\sigma$ ($z_2 = 0.5$), for which a corresponding states diagram of colloidal systems with an SALR potential has been shown conclusively to exist. The proposed corresponding states diagram is expected to remain valid over a wider range of conditions, but it is interesting to now identify the extent of repulsive interaction conditions for which this holds. SALR systems with longer range repulsion are still expected to favor the formation of finite size clusters, but cluster formation may not be energetically favorable when shortening the range of repulsion.[32] As a result, identifying states having clusters with a preferred size by the heuristic models described in the previous two sections may be limited to a specific set of interaction parameters.

One state point interacting with the HSDY1 potential (see Table 4.1 and Fig. 4.3) at $\phi = 0.05$ and $T^* = 0.25$ (a clustered state at $z_2 = 0.5$) is used to study the implications of altering the range of repulsion on representing clustered states by the binodal of a reference system. (However, a more complete study of all types of state points and several potentials is necessary to make more definitive conclusions.) The repulsion range is varied, both above and below the original value of 0.5, while

maintaining the reduced second virial coefficient of the reference potential and cut-off distance (i.e, the point of zero energy). As a result, the range of attraction $z_1$ and strength of repulsion $\lambda$ also must be varied, which consequently varies the maximum strength of repulsion $E_{max}$. Values of $z_1$ and the corresponding value of $E_{max}$ are shown in Fig. 4.13a as a function of $z_2$. Values of $\lambda$ needed to maintain $B_{2c}^*$ and $r_c$ values are plotted as a line in Fig. 4.13b over the same range of $z_2$ values. Clearly, as the range of repulsion decreases (increasing $z_2$) both $z_1$ and $E_{max}$ decrease while $\lambda$ increases. Despite an increase in the relative strength of repulsion to attraction, the range of attraction increases and the energy barrier decreases. The extreme case of this trend is the absence of a stabilizing repulsive force, which under any solution conditions would prevent stable clusters (of a preferred size) to be formed.

Requiring these new states to have identical values of $B_{2c}^*$ causes them to share the same reference binodal, which can be used to understand the limits of interaction conditions at which Fig. 4.8 is applicable to SALR systems. Each condition of $z_2$ tested using MC simulations are represented by symbols on the $\lambda$ line in Fig. 4.13b. The states at each value of $z_2$ are determined in the same manner as all previous simulations. Each state point is found to be either a dispersed or clustered fluid, with all remaining in the one phase region (i.e., the simulations converged) below a $z_2$ of roughly 2.5. Clustered states are found at long ranges of repulsion ($z_2 \leq 0.9$), which transition to dispersed fluid states as the range is reduced. According to the changes in $z_1$ and $E_{max}$ with increasing $z_2$, this transition is not unexpected.

To test whether the changes in the interaction potential are a dominant contribution to the transition from clustered to dispersed states at $z_2 \sim 0.9$ (for the HSDY1 potential at $\phi = 0.05$ and $T^* = 0.25$), a simple cluster model is used to estimate the configurational energy as a function of cluster size. Previous simulation studies have identified conditions of stable cluster formation as those with a particular cluster size that minimizes the configurational energy for a particular set of interaction parameters.[32, 39] This work observed a single cluster, making the results pertinent to the ground state (e.g., infinite dilution or zero temperature). As shown previously

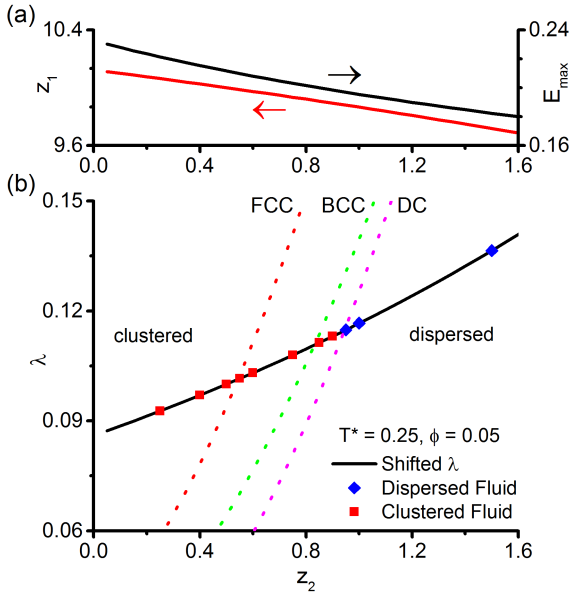


**Figure 4.13:** To maintain a constant value of $B_{2c}^*$ for HSDY1, the value of (a) $z_1$ and (b) $\lambda$ shift as a function $z_2$. The shift in the maximum energy is also plotted in (a). Clustered (squares) and dispersed (diamonds) states at ($T^* = 0.25$, $\phi = 0.05$) are plotted in (b) relative to the conditions at which spherical clusters with close packed structures can form clusters as described in the text (dashed lines).

for an LJY potential,[32] both increasing and decreasing the strength and range of repulsion too significantly will destabilize the formation of clusters of a preferred size. When the strength and range of repulsion are too small, unstable aggregation arises from an insufficient stabilizing force, while when too large, monomers are too stable to initiate aggregation.

While previous work used a modified basin-hopping algorithm in MC simulations,[32] this work simplifies the estimation using numerical calculations assuming a spherical close-packed structure of individual clusters. Each subsequent size cluster is constructing by adding one additional particle to the position in the crystal lattice that minimizes the average distance to every other particle in the cluster, thereby maintaining the most compact structure. These calculations using a face centered cubic (FCC) lattice were shown in Chapter 1 to quantitatively replicate the more time-consuming simulation

results.

Simulation state points are compared to the model representation of cluster stability as a function of these interaction parameters. The numerical model is used with face centered, body centered and diamond cubic lattice structures (FCC, BCC, DC, respectively), each with a different color dashed line and labeled and in Fig. 4.13b. The dotted lines demarcate the conditions where a minimum forms in the configurational energy as a function of cluster size, labeled "clustered" at small values of $z_2$, from "dispersed" conditions where the cluster energy continually decreases with increasing size. With a large enough strength and range of repulsion (large $E_{max}$ and small $z_2$, respectively), the balance of attraction and repulsion is sufficient to stabilize finite sized clusters. Conversely, above a $z_2$ of about 0.9, repulsion is not strong or long-range enough to make additional particles have a positive contribution to the cluster energy. Note that the value of $z_2$ distinguishing these two states will shift depending on the original set of interaction parameters before varying $z_2$.[32]

The transition from clustered states to dispersed fluid states corresponds with a packing fraction model between the BCC and DC lattices. Due to differences in the relative spacing of particles within a cluster, the transition point estimated by the model shifts as a function of the lattice used. This finding is consistent with the internal density of clusters determined in Fig. 4.11b according to the average number of neighbors separating dispersed and clustered fluids. Accounting only for internal cluster energetics suggests that enthalpic contributions to the system free energy are a major factor in forming clustered states. However, at finite temperatures and volume fractions, entropic contributions will only further destabilize cluster formation. Therefore, the simple numerical model provides an efficient and accurate method of identifying the (upper) limit of interaction parameters for which Fig. 4.8 can be used to identify clustered states. Interestingly, even when the range of repulsion is so short that a preferred cluster size cannot form, a unique phase will form in Fig. 4.8 between the binodal lines of the reference potential and the full SALR potential. Thus, there may be other interesting properties of SALR materials within this phase region, such

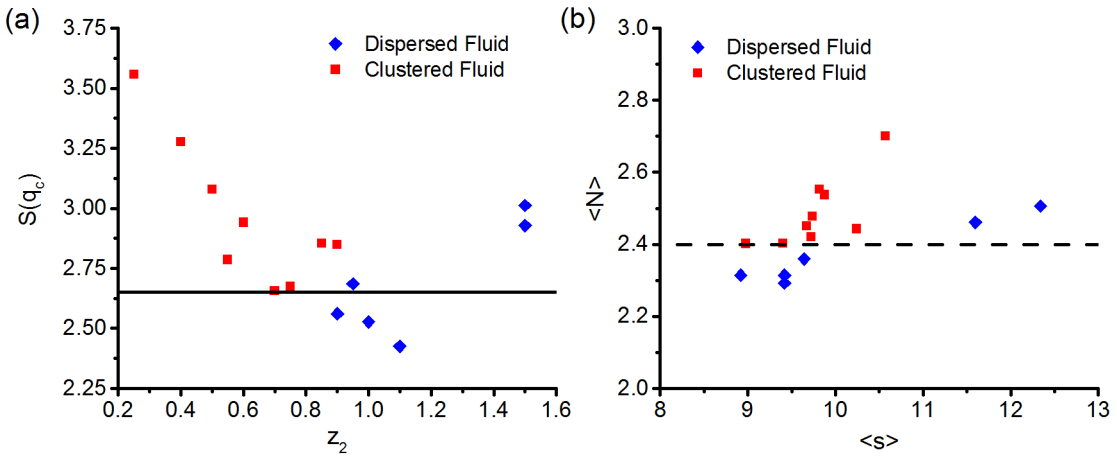


**Figure 4.14:** The (a) magnitude of the IRO peak and (b) average number of neighbors for clustered (squares) and dispersed (diamonds) fluids at varying values of $z_2$ (and $\langle s \rangle$) for the HSDY1 potential. Clustered and dispersed fluids are distinguished in (a) by $S(q_c) = 2.7$ (solid line) and in (b) by $\langle N \rangle = 2.4$ (dashed line).

as the generalized corresponding states behavior shown here.

New states with varying range of repulsion also exhibit the characteristic values found in the previous section to distinguish clustered and dispersed fluid states. Structure factors are calculated for each of the potentials shown in Fig. 4.12 corresponding to the state points in Fig. 4.13. Each of the states produces an IRO peak even though above a $z_2 \sim 0.9$ the states transition from clustered to dispersed fluids. This loss of a preferred cluster size at large $z_2$ corresponds with a drop in the magnitude of the IRO peak below a value of about 2.7, as shown in Fig. 4.14a. The dispersed fluid states at $z_2 = 1.5$ are above this limit. However, the peak position has shifted to smaller $q$-values and the magnitude of $S(0)$ has increased, suggesting a shift towards an attraction dominated microstructure approaching phase separation. The proposed limit of an average coordination number of 2.4 or greater for clustered states also appears to be applicable for these same states with varying range of repulsion, shown in Fig. 4.14b. Therefore, the semi-empirical observations of the IRO peak in the small angle scattering exceeding $\sim 2.7$ in magnitude and of the average coordination number

exceeding 2.4 seem to be very robust signatures of a clustered fluid.

## 4.4 Conclusions

This chapter highlights the existence of a generalized corresponding states phase diagram for a broad range of systems with physically meaningful SALR potentials. Four distinct types of states are distinguished as dispersed fluid, clustered fluid, random percolated, and cluster percolated states. The phase behavior of all SALR systems studied collapses onto a single state diagram when normalized by the critical point of an appropriately defined reference system, which interact by the excluded volume and short range attraction portion of the corresponding SALR potential. Importantly, the liquid state binodals for these reference potentials are nearly identical. Thus, this work extends the extended law of corresponding states as proposed for systems with excluded volume and short range attraction by Noro and Frenkel[33] to include this new and technologically important type of system.

Using the corresponding states normalization, all four types of states formed in SALR systems are found in distinct regions of the state diagram. Most importantly, clustered fluids are shown to consistently form within the binodal of the reference attractive system and in the one-phase region of the SALR system. This finding supports the notion that cluster fluids arise from the long-range repulsion frustrating what otherwise would be a phase separated fluid. As calculations of the binodal for fluids with attractive potentials are inexpensive, this corresponding state diagram is a very efficient method for estimating the conditions that produce cluster states. Preliminary evidence is also provided that this identification of clustered fluids is applicable to a broad range of physically meaningful ranges of repulsion.

Three semi-empirical characteristics of cluster formation in fluids with SALR interactions were identified by analyzing the solution structure. Expanding upon the hypothesis in the previous chapter, clustered fluids are shown to consistently have a large IRO peak magnitude $S(q_c) \geq 2.7$. Also, particles in a clustered state require an average number of neighbors greater than 2.4, consistent with rigidity percolation.

Finally, the local volume fraction of clusters in clustered fluid states is estimated to be $0.38 \pm 0.04$, similar to literature results. These results provide several methods to rapidly identify cluster formation by scattering and microscopy.

## REFERENCES


[1] Allen, M. P., and Tildesley, D. J. *Computer Simulation of Liquids*. Oxford University Press, 1987.

[2] Benavides, A. L., and Gil-villegas, A. The thermodynamics of molecules with discrete potentials. *Mol. Phys. 97*, 12 (1999), 1225–1232.

[3] Bomont, J.-M., Bretonnet, J.-L., and Costa, D. Temperature study of cluster formation in two-Yukawa fluids. *J. Chem. Phys. 132*, 18 (2010), 184508.

[4] Bomont, J.-M., Bretonnet, J.-L., Costa, D., and Hansen, J.-P. Communication: thermodynamic signatures of cluster formation in fluids with competing interactions. *J. Chem. Phys. 137*, 1 (July 2012), 011101.

[5] Borwankar, A. U., Dinin, A. K., Laber, J. R., Twu, A., Wilson, B. K., Maynard, J. a., Truskett, T. M., and Johnston, K. P. Tunable equilibrium nanocluster dispersions at high protein concentrations. *Soft Matter 9*, 6 (2013), 1766.

[6] Broccio, M., Costa, D., Liu, Y., and Chen, S.-H. The structural properties of a two-Yukawa fluid: Simulation and analytical results. *J. Chem. Phys. 124*, 8 (Feb. 2006), 084501.

[7] Campbell, A., Anderson, V., van Duijneveldt, J. S., and Bartlett, P. Dynamical Arrest in Attractive Colloids: The Effect of Long-Range Repulsion. *Phys. Rev. Lett. 94*, 20 (May 2005), 1.

[8] Cardinaux, F., Gibaud, T., Stradner, A., and Schurtenberger, P. Interplay between Spinodal Decomposition and Glass Formation in Proteins Exhibiting Short-Range Attractions. *Phys. Rev. Lett. 99*, 11 (Sept. 2007), 1–4.

[9] Cardinaux, F., Stradner, A., Schurtenberger, P., Sciortino, F., and Zaccarelli, E. Modeling equilibrium clusters in lysozyme solutions. *Europhys. Lett. 77*, 4 (Feb. 2007), 48004.

[10] Cardinaux, F., Zaccarelli, E., Stradner, A., Bucciarelli, S., Farago, B., Egelhaaf, S. U., Sciortino, F., and Schurtenberger, P. Cluster-Driven Dynamical Arrest in Concentrated Lysozyme Solutions. *J. Phys. Chem. B 115*, 22 (June 2011), 7227.

[11] Castellanos, M. M., Pathak, J. a., and Colby, R. H. Both protein adsorption and aggregation contribute to shear yielding and viscosity increase in protein solutions. *Soft Matter 10*, 1 (2014), 122.

[12] Chapela, G. A., del Río, F., Benavides, A. L., and Alejandre, J. Discrete perturbation theory applied to Lennard-Jones and Yukawa potentials. *J. Chem. Phys. 133*, 23 (Dec. 2010), 234107.

[13] Chen, S.-H., Broccio, M., Liu, Y., Fratini, E., and Baglioni, P. The two-Yukawa model and its applications: the cases of charged proteins and copolymer micellar solutions. *J. Appl. Crystallogr. 40*, s1 (Apr. 2007), s321–s326.

[14] Costa, D., Caccamo, C., Bomont, J.-M., and Bretonnet, J.-L. Theoretical description of cluster formation in two-Yukawa competing fluids. *Mol. Phys. 109*, 23-24 (2011), 2845–2853.

[15] Falus, P., Porcar, L., Fratini, E., Chen, W.-R., Faraone, A., Hong, K., Baglioni, P., and Liu, Y. Distinguishing the monomer to cluster phase transition in concentrated lysozyme solutions by studying the temperature dependence of the short-time dynamics. *J. Phys. Condens. Matter 24*, 6 (Feb. 2012), 064114.

[16] Foffi, G., McCullagh, G., Lawlor, A., Zaccarelli, E., Dawson, K., Sciortino, F., Tartaglia, P., Pini, D., and Stell, G. Phase equilibria

and glass transition in colloidal systems with short-ranged attractive interactions: Application to protein crystallization. *Phys. Rev. E 65*, 3 (Mar. 2002), 031407.

[17] Frenkel, D., and Smit, B. *Understanding Molecular Simulations: From Algorithms to Applications*. Academic Press, 2002.

[18] Godfrin, P. D., Castañeda Priego, R., Liu, Y., and Wagner, N. J. Intermediate range order and structure in colloidal dispersions with competing interactions. *J. Chem. Phys. 139*, 15 (2013), 154904.

[19] Godfrin, P. D., Valadez-Pérez, N. E., Castañeda Priego, R., Wagner, N. J., and Liu, Y. Generalized phase behavior of cluster formation in colloidal dispersions with competing interactions. *Soft Matter 10* (2014), 5061.

[20] Hansen, J.-P., and Verlet, L. Phase transitions of the Lennard-Jones System. *Phys. Rev. 184*, 1 (1969), 151–161.

[21] He, H., and Thorpe, M. Elastic Properties of Glasses. *Phys. Rev. Lett. 54*, 19 (1985), 2107–2110.

[22] Kim, J. M., Castañeda Priego, R., Liu, Y., and Wagner, N. J. On the importance of thermodynamic self-consistency for calculating clusterlike pair correlations in hard-core double Yukawa fluids. *J. Chem. Phys. 134*, 6 (Feb. 2011), 064904.

[23] Kremer, K., Robbins, M. O., and Grest, G. S. Phase diagram of Yukawa systems: Model for charge-stabilized colloids. *Phys. Rev. Lett. 57*, 21 (1986), 2694.

[24] Largo, J., Miller, M. A., and Sciortino, F. The vanishing limit of the square-well fluid: the adhesive hard-sphere model as a reference system. *J. Chem. Phys. 128*, 13 (Apr. 2008), 134513.

[25] Lee, L. L., Hara, M. C., Simon, S. J., Ramos, F. S., Winkle, A. J., and Bomont, J.-M. Crystallization limits of the two-term Yukawa potentials based on the entropy criterion. *J. Chem. Phys. 132*, 7 (Feb. 2010), 074505.

[26] Lilyestrom, W. G., Yadav, S., Shire, S. J., and Scherer, T. M. Monoclonal antibody self-association, cluster formation, and rheology at high concentrations. *J. Phys. Chem. B 117*, 21 (May 2013), 6373–84.

[27] Liu, Y., Chen, W.-R., and Chen, S.-H. Cluster formation in two-Yukawa fluids. *J. Chem. Phys. 122*, 4 (Jan. 2005), 44507.

[28] Liu, Y., Fratini, E., Baglioni, P., Chen, W.-R., and Chen, S.-H. Effective Long-Range Attraction between Protein Molecules in Solutions Studied by Small Angle Neutron Scattering. *Phys. Rev. Lett. 95*, 11 (Sept. 2005), 2–5.

[29] Liu, Y., Fratini, E., Baglioni, P., Chen, W.-R., Porcar, L., and Chen, S.-H. Liu et al. Reply. *Phys. Rev. Lett. 96*, 21 (June 2006), 219802.

[30] Liu, Y., Porcar, L., Chen, J., Chen, W.-r., Falus, P., Faraone, A., Fratini, E., Hong, K., and Baglioni, P. Lysozyme protein solution with an intermediate range order structure. *J. Phys. Chem. B 115*, 22 (June 2011), 7238.

[31] Malins, A., Williams, S. R., Eggers, J., Tanaka, H., and Royall, C. P. The effect of inter-cluster interactions on the structure of colloidal clusters. *J. Non. Cryst. Solids 357*, 2 (Jan. 2011), 760.

[32] Mossa, S., Sciortino, F., Tartaglia, P., and Zaccarelli, E. Ground-state clusters for short-range attractive and long-range repulsive potentials. *Langmuir 20*, 24 (2004), 10756–10763.

[33] Noro, M. G., and Frenkel, D. Extended corresponding-states behavior for particles with variable range attractions. *J. Chem. Phys. 113*, 8 (2000), 2941.

[34] Orea, P., Tapia-Medina, C., Pini, D., and Reiner, A. Thermodynamic properties of short-range attractive Yukawa fluid: simulation and theory. *J. Chem. Phys. 132*, 11 (Mar. 2010), 114108.

[35] Pathak, J. A., Sologuren, R. R., and Narwal, R. Do Clustering Monoclonal Antibody Solutions Really Have a Concentration Dependence of Viscosity ? *Biophys. J. 104* (2013), 1–11.

[36] Phillips, J. C. Topology of covalent non-crystalline solids I: short-range order in chalcogenide alloys. *J. Non. Cryst. Solids 34* (1979), 153–181.

[37] Porcar, L., Falus, P., Chen, W.-R., Faraone, A., Fratini, E., Hong, K., Baglioni, P., and Liu, Y. Formation of the Dynamic Clusters in Concentrated Lysozyme Protein Solutions. *J. Phys. Chem. Lett. 1*, 1 (Jan. 2010), 126.

[38] Sandler, S. I. *Chemical, Biochemical, and Engineering Thermodynamics*. 2006.

[39] Sciortino, F., Mossa, S., Zaccarelli, E., and Tartaglia, P. Equilibrium Cluster Phases and Low-Density Arrested Disordered States: The Role of Short-Range Attraction and Long-Range Repulsion. *Phys. Rev. Lett. 93*, 5 (July 2004), 5.

[40] Sciortino, F., Tartaglia, P., and Zaccarelli, E. One-dimensional cluster growth and branching gels in colloidal systems with short-range depletion attraction and screened electrostatic repulsion. *J. Phys. Chem. B 109*, 46 (2005), 21942.

[41] Seaton, N. A., and Glandt, E. D. Aggregation and percolation in a system of adhesive spheres. *J. Chem. Phys. 86*, 8 (1987), 4668.

[42] Sedgwick, H., Egelhaaf, S. U., and Poon, W. C. K. Clusters and gels in systems of sticky particles. *J. Phys. Condens. Matter 16*, 42 (Oct. 2004), S4913–S4922.

[43] Shukla, A., Mylonas, E., Di Cola, E., Finet, S., Timmins, P., Narayanan, T., and Svergun, D. I. Absence of equilibrium cluster phase in concentrated lysozyme solutions. *Proc. Natl. Acad. Sci. U. S. A. 105*, 13 (Apr. 2008), 5075–80.

[44] Stradner, A., Cardinaux, F., Egelhaaf, S. U., and Schurtenberger, P. Do equilibrium clusters exist in concentrated lysozyme solutions? *Proc. Natl. Acad. Sci. U. S. A. 105*, 44 (2008), E75.

[45] Stradner, A., Cardinaux, F., and Schurtenberger, P. A small-angle scattering study on equilibrium clusters in lysozyme solutions. *J. Phys. Chem. B 110*, 42 (Oct. 2006), 21222–31.

[46] Stradner, A., Cardinaux, F., and Schurtenberger, P. Comment on Effective Long-Range Attraction between Protein Molecules in Solution Studied by Small Angle Neutron Scattering. *Phys. Rev. Lett. 96*, 21 (June 2006), 219801.

[47] Stradner, A., Sedgwick, H., Cardinaux, F., Poon, W. C. K., Egelhaaf, S. U., and Schurtenberger, P. Equilibrium cluster formation in concentrated protein solutions and colloids. *Nature 432*, 7016 (Nov. 2004), 492.

[48] Toledano, J. C. F., Sciortino, F., and Zaccarelli, E. Colloidal systems with competing interactions: from an arrested repulsive cluster phase to a gel. *Soft Matter 5*, 12 (2009), 2390.

[49] Torres-Arenas, J., Cervantes, L. A., Benavides, A. L., Chapela, G. A., and del Río, F. Discrete perturbation theory for the hard-core attractive and repulsive Yukawa potentials. *J. Chem. Phys. 132*, 3 (Jan. 2010), 034501.

[50] Valadez-Pérez, N. E., Benavides, A. L., Schöll-Paschinger, E., and Castañeda Priego, R. Phase behavior of colloids and proteins in aqueous

suspensions: theory and computer simulations. *J. Chem. Phys. 137*, 8 (Aug. 2012), 084905.

[51] Valadez-Pérez, N. E., Castañeda Priego, R., and Liu, Y. Percolation in colloidal systems with competing interactions: the role of long-range repulsion. *RSC Adv. 3* (2013), 25110.

[52] Valadez-Pérez, N. E., Liu, Y., Eberle, A. P. R., Wagner, N. J., and Castañeda Priego, R. Dynamical arrest in adhesive hard-sphere dispersions driven by rigidity percolation. *Phys. Rev. E 88*, 6 (2013), 060302(R).

[53] Vidales, A., Benavides, A. L., and Gil-villegas, A. Perturbation theory for mixtures of discrete potential fluids. *Mol. Phys. 99*, 9 (2001), 703–710.

[54] Wu, J., Liu, Y., Chen, W.-R., Cao, J., and Chen, S.-H. Structural arrest transitions in fluids described by two Yukawa potentials. *Phys. Rev. E 70*, 5 (Nov. 2004), 3–6.

[55] Yearley, E. J., Godfrin, P. D., Perevozchikova, T., Zhang, H., Falus, P., Porcar, L., Nagao, M., Curtis, J., Gawande, P., Taing, R., Zarraga, I. E., Wagner, N. J., and Liu, Y. Observation of small cluster formation in concentrated monoclonal antibody solutions and its implications to solution viscosity. *Biophys. J. 106*, 8 (2014), 1763–1770.

[56] Zarraga, I. E., Taing, R., Zarzar, J., Luoma, J., Hsiung, J., and Patel, A. High Shear Rheology and Anisotropy in Concentrated Solutions of Monoclonal Antibodies. *J. Pharm. Sci. 102*, 8 (2013), 2538–2549.

# Chapter 5

# A MODEL PROTEIN WITH COMPETING INTERACTIONS TO STUDY THEIR EFFECT ON DYNAMICS AND VISCOSITY

## 5.1 Introduction

Colloidal theory and simulations provide a powerful framework for quantifying the thermodynamic and kinetic features of complex materials. Thus far, they have provided the means to gain a more fundamental understanding of intermediate range order (IRO) and cluster formation, as well as some experimentally identifiable signatures of cluster fluids. However, observing these features in experiments requires the use of a material with appropriate chemistry to produce the competing inter-particle potential. This connection between chemistry and interactions is portrayed in Fig. 1.1 as the foundation of engineering complex materials.

Developing a model system requires extensive characterization to identify materials that produce the desired effective interaction potential and can be manipulated by readily accessible parameters (e.g., temperature, pressure, pH). Creating such an experimental system will be discussed in Chapter 8 as a goal of future study, focused on identifying an ideal one-component system consisting of short-range attraction (SA) and long-range repulsion (LR) to further explore cluster fluid properties. Fortunately, and interestingly, SA and LR are common for protein solutions at low ionic strength. Previous studies have identified two readily available systems that interact by SALR interactions: micron sized colloidal particles with a non-adsorbing depletant[19, 47, 76, 77, 85] and the small globular protein lysozyme.[22, 23, 30, 53, 66, 83, 85] Clusters have also been observed in systems of nanoparticles in polymer composites[54] and solutions with polymer depletants[19, 76, 77, 85] as well as concentrated antibody protein

formulations,[49, 94] proteins on surfaces[58] and membrane proteins.[56, 80] Therefore, understanding the influence of clusters on solution properties will be beneficial to a wide range of engineered materials.

In this chapter, lysozyme is used as a model system due to its availability, stability and reproducible globular structure. Further, its natural chemical composition is similar to commercially relevant antibody proteins and produces an inherent combination of attractive and repulsive forces (under the right solution conditions) that are of particular interest in this work. Although heavily debated in early studies,[30, 53, 66, 79, 85] lysozyme has been conclusively shown to form clusters at high concentrations due to competing interactions at low ionic strength.[22, 53, 66] However, not all globular proteins form clusters. As an example, Bovine Serum Albumin (BSA) remains monomeric at low ionic strength, even at high concentrations, due to a balance of interactions that strongly favors the electrostatic repulsion.[68] In general, the use of globular proteins to study colloidal phase behavior has been successful due to their compact shape that, in addition to their interactions, can be modeled as spherically symmetric.[26, 53, 69, 89] As such, globular protein state diagrams can be accurately represented from estimates of the strength and range of an isotropic interaction potential.[1, 35, 39, 59, 69, 89]

Interestingly, solutions of lysozyme[23, 37] and monoclonal antibody (mAb) formulations[24, 49, 63, 94] at high concentrations have been shown to produce very large viscosities. For biopharmaceutical companies, the implications of such viscous products may significantly increase operating expenses during manufacturing and purification and can invalidate certain methods of delivery.[41] However, studying mAbs is difficult, in part, due to the convolution of their internal structural and dynamic features with the inter-protein correlations of interest (though these will be addressed in the following two chapters). As a result of its similarity in chemical composition to mAbs, lysozyme is expected to semi-quantitatively represent the influence of interactions on the properties of these proteins with more complex structures. The nearly spherical tertiary structure of lysozyme (more accurately, an oblate ellipsoid) allows the

use of colloidal models to distinguish the influence of its excluded volume, represented by hard sphere (HS) models, from the additional interactions on the phase behavior and material properties. Any deviations from well known theories for HS systems can then be attributed to the more complex interaction potential. Therefore, this chapter will focus on identifying structural states by comparing with the phase diagram presented in the previous chapter[38] and developing a semi-quantitative model of the macroscopic solution viscosity as a function of their interactions and corresponding microscopic properties (details of which are provided in the Appendix).

Despite using this nearly ideal experimental system, the ability to model the contributions of SALR interactions on the viscosity has several complications. As demonstrated in the previous chapter, cluster formation typically occurs at intermediate volume fractions and modest strengths of attraction where many existing viscosity models are inaccurate.[55] Further, the competing interactions can produce clusters that often have elongated structures and strongly interact through charge repulsion.[19, 74, 75] Therefore, the solution viscosity is expected to increase in excess of the contribution from competing interactions between monomers as a result of the clusters they may produce. Though the previous two chapters demonstrated that IRO is not a direct indication of a preferred cluster size, it is a sign of strong particle localization. In this chapter, this unique structure is shown to be responsible for the glassy behavior observed previously in lysozyme.[23] The impact of IRO structures on the viscosity can be captured by quantifying an effective cluster size representative of the locally dense regions. The viscosity can then be shown to correlate well with the extracted cluster size. A large portion of the work presented in this chapter is published research.[37]

## 5.2 Materials and Methods

### 5.2.1 Sample Preparation

Lysozyme samples ranging in concentration from 10 mg/mL ($\phi \approx 0.008$) to 480 mg/mL ($\phi \approx 0.345$) are prepared by dissolution of purified lyophilized protein in deuterium oxide without buffering agents. Lysozyme was purchased in the lyophilized state

and then carefully purified to remove ion impurities and minimize the residual counter-ion concentration. These efforts were necessary to enhance the resulting strength and range of long-range repulsion to a value sufficient to study cluster formation.

Samples with a concentration less than 300 mg/mL were filtered through $0.22\mu m$ filters, while higher concentrations required $0.45\mu$m filters as these samples were too viscous to filter through smaller pore sizes. High concentration samples (350 mg/mL) were prepared at $50°C$ to aid in dissolution during reconstitution due to their resulting high viscosities. These samples were returned to $25°C$ as soon as they were homogenized to minimize the rate of crystallization. Despite the purification process, the highest concentration samples (481 mg/mL) were observed to eventually form crystals after long incubation periods of about 12 hours. However, the repulsion sufficiently stabilized the protein such that all samples remained fluid during the time frame of all experiments and all experimental results were reproducible.

As a result of not incorporating buffering agents, the pH varies slightly as a function of protein concentration. However, all samples maintain a pH of roughly 5 due to self buffering, ensuring that the surface consistently contains between 9 and 10 charges over the range of conditions studied.[3, 15] Further, any changes in the effective protein interactions with solution conditions are explicitly accounted for by fitting small angle neutron scattering data with integral equation theory using the hard sphere double Yukawa (HSDY) potential,[51, 52] as described in Chapter 2 and discussed in the next section.

Protein content was initially determined by the mass fraction of purified lyophilized lysozyme in deuterium oxide, $X_L$. The "dry" definition of lysozyme volume fraction is calculated according to the specific volume, $\nu_0$, reported in literature ($\nu_0 = 0.717$ mL/g)[34] according to

$$\phi = \frac{X_L \nu_0}{X_L \nu_0 + (1 - X_L)/\rho_D)}, \tag{5.1}$$

where $\rho_D$ is the density of $D_2O$. For consistency with previous studies,[53, 66] all calculations of the protein volume fraction in this chapter will be completed using this definition unless explicitly noted otherwise. However, for comparison, recent work has

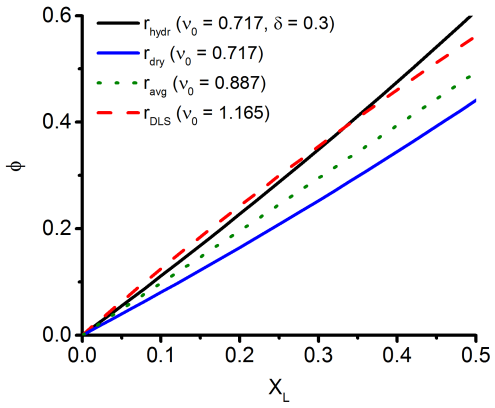


**Figure 5.1:** Estimates of protein volume fraction, $\phi$, as a function of lysozyme weight fraction, $X_L$, using definitions as discussed in the main text of a "hydrated" protein $r_{hydr}$ and "dry" protein with experimental intrinsic volume $r_{dry}$, average crystal size $r_{avg}$ and hydrodynamic DLS size $r_{DLS}$.

highlighted the sensitivity of including a hydration layer in the definition of volume fraction on fitting protein viscosity to colloidal hard sphere models.[72] The "hydrated" volume fraction, $\phi_{hydr}$, calculated according to

$$\phi_{hydr} = \frac{X_L(\nu_0 + \delta/\rho_D)}{X_L\nu_0 + (1 - X_L)/\rho_D} \tag{5.2}$$

includes an effective additional specific mass of bound water per mass of lysozyme, $\delta = 0.33$ g/g.[32, 33] The dependence of $\phi$ and $\phi_{hydr}$ on $X_L$ (i.e., the dry and hydrated definitions) are compared in Fig. 5.1. For perspective, two additional $X_L$–$\phi_L$ relations are also shown in Fig. 5.1 using values of $\nu_0 = (4\pi r^3)/(3M_w)$ ($r$ is the radius and $M_w = 14.4$ kDa). These two calculations of $\nu_0$ use the average lysozyme radius, $r_{avg} = (abb)^{1/3}$, where $a = 2.015$ nm and $b = 1.343$ nm, and the hydrodynamic radius obtained from DLS measurements, $r_{DLS}$, in Eq. 5.1 (the dry-$\phi$ definition). The similarity between the hydrated and DLS definitions suggests that bound water plays a role in the hydrodynamic mobility of the protein. It also provides an upper limit of protein volume fraction relative to the expectations from the average lysozyme size. Similarly, the dry volume fraction is a lower limit, assuming no hydration or significant conformation

change after dissolution. The influence of how $\phi$ is calculated on the accuracy of fitting protein viscosity with colloidal models will be discussed later in the chapter.

In addition to a hydration layer on the protein surface, protein volume fractions calculated according to the specific volume determined under dilute conditions can become inaccurate due to non-ideal mixing at high protein concentration. Specifically, if the partial specific volume of water or lysozyme deviates significantly from their respective molar volumes (the difference being the excess partial volume), then the actual volume would be different from the sum of both species' molar volumes. Under this scenario, the volume fraction of the protein solution calculated according to either Eq. 5.1 or Eq. 5.2 would incorrectly represent the solution. However, within the range of concentrations studied in this chapter, the excess partial volume of water is zero and that of lysozyme is -0.045 mL/g,[81] which amounts to a maximum relative error in the calculation of $\phi$ using Eq. 5.1 of about 6%. Therefore, this effect is minimal for this study and the resulting state points ($\phi$, $T$) can be quantitatively compared with the phase behavior determined in the previous chapter.

### 5.2.2 Small Angle Neutron and X-ray Scattering

Small angle neutron scattering (SANS) was performed to extract the effective protein-protein interactions as a function of lysozyme concentration and temperature. Though considered a model system, the interactions vary with temperature and concentration so they must be accounted for explicitly by fitting each state point. The scattering intensity is the ensemble average of all configurations, which may be simplified when particles and interactions are spherically symmetric (i.e., there is no orientational dependence on particle correlations). Under these circumstances, intra- and inter-particle spatial correlations can be separated, resulting in the function for scattering intensity $I(q) = \phi V(\Delta\rho)^2 P(q) S_{eff}(q)$, where the pre-factors are the volume fraction, $\phi$, particle volume, $V$, and scattering length density (SLD) difference, $\Delta\rho$.[97] The second to last term is the particle form factor, $P(q)$, which represents its shape,

and the last term is the inter-particle structure factor, $S_{eff}(q)$, which represents inter-particle correlations. However, the lysozyme form factor is accurately represented by an oblate ellipsoid,[87] which must be averaged over all angular orientations

$$P(q) = |F(q)|^2 = \int_0^1 \left[ \frac{3\big(sin[qR_{eff}(x)] - qR_{eff}(x)\cos[qR_{eff}(x)]\big)}{[qR_{eff}(x)]^3} \right]^2 \mathrm{d}x, \tag{5.3}$$

where $R_{eff}(x) = R_b\big[1 + x^2((R_a/R_b)^2 - 1)\big]^{1/2}$ and the major and minor axes of the oblate ellipsoid are represented by $R_b$ and $R_a$, respectively. As a result of lysozyme's non-spherical shape, the spherically symmetric representation of $I(q)$ by Eq. 2.11 must be corrected by implementing the decoupling approximation for the structure factor

$$S_{eff}(q) = 1 + \beta(q)[S(q) - 1], \tag{5.4}$$

where $\beta(q) = |\langle F(q)\rangle^2|/\langle|F(q)|^2\rangle$ and $S_{eff}(q)$ is the effective structure factor, which is averaged over all angular orientations, causing the features of $S(q)$ to be smeared.[25]

The same fundamental principles of scattering theory also apply to small angle X-ray scattering (SAXS) experiments. Treating SAXS data is therefore accomplished with the same functions discussed above with the only difference arising from the contrast term, $\Delta\rho$.[97] While the neutron SLD is a function of the atomic structure and isotope, the X-ray SLD is directly related to the electron cloud density. Therefore, while SANS is particularly sensitive to differences in hydrogen isotopes (i.e., $H_2O$ and $D_2O$), this difference will be minimal in SAXS experiments.

A low concentration sample ($1wt\%$) was used as an accurate representation of the protein form factor. SANS patterns were taken at $25°C$ and $5°C$ with little difference observed between the two. An ellipsoidal form factor, averaged over all angular orientations, was used to fit the data.[26, 53] The form factor was used to extract an effective scattering length density contrast value ($\Delta\rho$) used to represent the protein contrast in the dilute limit as well as the size of the major axis and the ratio of the length of minor to major axes. The extracted sizes closely resembled literature values for the ellipsoid axes (22.5 Åx 15.0 Åx 15.0 Å) representing the globular shape of the protein[14] and theoretical estimates of its neutron SLD[42] based on its

composition.[20] However, due to dissolution in $D_2O$, labile hydrogens within lysozyme will experience more significant H-D exchange at higher protein concentrations that will reduce the neutron SLD contrast.[42, 86] Therefore, $(\Delta\rho)^2$ is allowed to vary in fits to all SANS spectra, but remained within a range of values consistent with about 16% of hydrogens being labile in lysozyme.[64]

Protein interactions dictate its solution structure, captured by the structure factor as well as the resulting phase behavior. That protein interactions arise from an anisotropic distribution of surface charges makes modeling these thermodynamic features a significant challenge. Patchy colloidal models have been used to accurately represent the resulting phase behavior in certain proteins.[39] However, such models are impractical for understanding the effective interactions in protein solutions. Lysozyme protein has been extensively studied and its phase behavior and solution structure have been successfully modeled by effective isotropic interaction potentials.[17, 59, 89] More recently, a complex combination of short-range attraction and long-range repulsion has been demonstrated as the most accurate representation. While the most appropriate functional form is debated in literature,[52, 84] previous work has successfully used both a hard sphere double Yukawa (HSDY) potential[26, 53] and a $2\alpha - \alpha$ Leonard-Jones plus Yukawa (LJY) potential[1, 22, 23] in modeling lysozyme solutions.

In this chapter, lysozyme interactions are represented by the HSDY pair-wise potential. While fitting the data, $z_1$ is fixed at 10.0, which is calculated by fitting a Leonard-Jones interaction with an attractive Yukawa potential. This figure is close to those reported in literature from fits to SAXS[88] and SANS[23, 26] data, producing a range of attraction only slightly longer than these previous fits. The repulsive parameters, $K_2$ and $z_2$, are calculated using their relation to the ionic strength, $I_S$, and particle charge, $z_p$, through the generalized one component model for electrostatic interactions.[11] Due to effective purification during sample preparation, $I_S$ was directly attributed to protein counter-ions and therefore a function only of concentration. Each data set is fit allowing the parameters $\phi$, $\Delta\rho$, $K_1$, and $z_p$ to vary, while restricting the limits of $\phi$ and $\Delta\rho$ to well established values. The radial distribution function, $g(r)$, is

then calculated by its relationship with the structure factor, Eq. 2.2 in Chapter 2.

### 5.2.3 Simulation Protocol

Monte Carlo (MC) simulations[2, 31] are performed with HSDY interaction parameters extracted from SANS experiments as discussed above. Simulations are implemented by the procedure outlined in Chapter 2. Calculations of the thermodynamic structural functions $g(r)$ and $S(q)$ using MC trajectories in this chapter are identical to the previous two chapters. When using the parameters extracted from the two most concentrated samples (for which the IET fitting procedure to SANS data could converge) at $5°C$, the simulations showed a weak but continuous decrease in energy with increasing number of attempted MC moves. Therefore, these simulations never equilibrated, but the results are still provided to demonstrate the discrepancy with equilibrium experimental data.

### 5.2.4 Neutron Spin Echo

The dynamics of concentrated protein solutions are probed by neutron spin echo (NSE) experiments conducted on the IN-15 beam line at the Institute Laue-Langevin in Grenoble, France. NSE is particularly suitable to the study of protein dynamics by probing correlation times on the order of 100 ns over a range of lengthscales probed by SANS. While some studies have suggested that internal protein motion can be observed within these timescales, the dominant contribution to the intensity is diffusive motion for these lysozyme samples.[13, 18, 82]

As discussed in Chapter 1, colloidal dynamics (including proteins) can be considered independent of solvent motion due to their disparate sizes. The timescale at which colloidal motion becomes distinct from solvent fluctuations is specified by the Brownian regime $\tau \gg \tau_M$, where $\tau_M = (mD_0)/(k_BT)$ is the momentum relaxation time ($m$ is particle mass and $D_0$ is the bare diffusion coefficient). Over these relatively long times, the dynamics can be further separated into short and long time regimes. The

latter is typically associated with large scale structural rearrangement of the dispersion, referred to as structural relaxation $\tau_I = r^2/D_0$ where $r$ is the particle radius.[61] The short-time regime, on the other hand, is defined by $\tau_M \ll t \ll \tau_I$, to which NSE is acutely sensitive.[61] Within this regime, particles remain localized such that the equilibrium microstructure is relatively unperturbed. Data is obtained up to a 50 ns time window for all lysozyme samples.

For these short correlation times, the intermediate scattering function (ISF), $F_S(q,t)/F_S(q,0)$, probed directly by NSE is accurately represented by a single exponential decay function as discussed in Chapter 2. The $q$-dependent effective short-time collective diffusion coefficient, $D_C(q)$, is a reflection of the structure factor and the hydrodynamic function, $H(q)$, according to $D_C(q) = D_0 H(q)/S(q)$.[7, 61] In the limit of large $q$-values, $S(q) = 1$ and $D_0 H(q)$ is equal to the short-time self-diffusion coefficient, $D_S$. The high-$q$ limit is reached when $q > q_m$, where $q_m$ is the location of the monomer peak in $S(q)$. However, while $q_m \sim 0.2$ Å$^{-1}$ for lysozyme, NSE experiments were limited to $q < 0.16$ Å$^{-1}$ in order to maximize the range of solution conditions studied. Despite this apparent discrepancy, previous work has demonstrated that lysozyme short time collective diffusion remains constant for $q > 0.1$ Å$^{-1}$,[30, 66] allowing the high-$q$ limit of the data collected to remain an accurate representation of the self diffusion of lysozyme.

In order to qualitatively estimate an effective dynamic cluster radius, an average hydrodynamic radius, $R_h$, is estimated from $D_S$ as done previously[66] according to $R_h/R_0 = (D_0/D_S)(\mu/\eta'_\infty)C(\phi)$, where $D_0 = kT/(6R_0\pi\mu)$ is the bare diffusion coefficient, $R_0$ is the monomer radius, $\mu$ is the solvent viscosity, $\eta'_\infty$ is the high frequency limit of the dynamic viscosity, and $C(\phi)$ is a correction function. Due to its small size, experimentally obtaining the high frequency viscosity of lysozyme is impractical and is thus represented by the hard sphere relations $\eta'_\infty = 1 + 2.5\phi + 5.0023\phi^2 + 9.09\phi^3$ and $C(\phi) = 1 + 0.67\phi$.[6]

### 5.2.5 Microrheology

Viscosity values are obtained for a wide range of lysozyme concentrations and temperatures through pressure driven flow in a microcapillary. This technique minimizes the necessary sample volume (on the order of $20\mu L$ per measurement) and avoids air-water interfacial effects on rheological measurements that have been shown to have a strong impact on the bulk rheology of protein solutions.[78] Glass blown microcapillary tubes with a diameter of $25\mu m$ are used with measurements taken over a length of $5mm$, which is sufficiently far from the ends to avoid entrance and exit flow effects. The steady shear viscosity, $\eta$, is calculated according to its relationship with pressure drop, $\Delta P$, and volumetric flow rate, $Q$, via the Hagen-Poiseuille equation describing non-turbulent pressure driven flow in a tube by[28]

$$\eta = \frac{\pi R_t^4 \Delta P}{8QL}, \tag{5.5}$$

where $R_t$ and $L$ are the radius and length of the tube, respectively. Viscosities are obtained as a function of shear rate according to the Rabinowitsch equation, which accounts for possible non-Newtonian flow behavior:

$$\dot{\gamma} = \left(\frac{3x+1}{4x}\right)\left(\frac{4Q}{\pi R_t^3}\right), \tag{5.6}$$

where

$$x = \frac{\mathrm{d}\ln\left(\frac{R_t}{2}\left[\frac{-dP}{dz}\right]\right)}{\mathrm{d}\ln\left(\frac{4Q}{\pi R_t^3}\right)}. \tag{5.7}$$

A more detailed discussion of the device is provided elsewhere.[44] While the range of shear rates used for each sample is dictated by its viscosity at the given conditions, shear rates ranged from $1 - 10000s^{-1}$. Interestingly, all samples exhibited Newtonian behavior over the entire range of shear rates under all conditions. Thus, all data points remained within the low-shear plateau and the average value over all shear rates was used as the zero shear viscosity for each solution condition.

## 5.3 Low Concentration Structure and Dynamics

Gaining an accurate understanding of the fundamental structure of an individual lysozyme protein is imperative to the eventual study of effective interactions and their

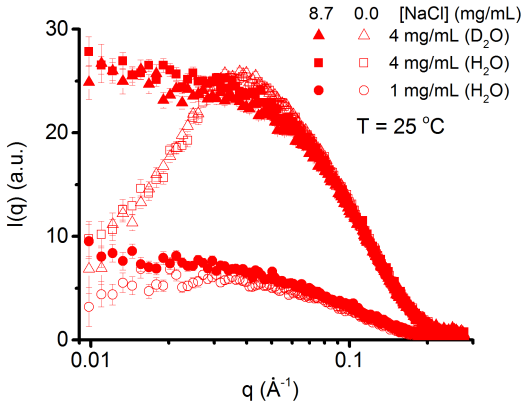


**Figure 5.2:** Scattering intensities (with arbitrary units, a.u.) obtained by SAXS are plotted for several lysozyme samples. The effect of solvent conditions are compared for samples with 0 mg/mL (open symbols) and 8.7 mg/mL (filled symbols) sodium chloride at a protein concentration of 4 mg/mL in $D_2O$ (triangles) and $H_2O$ (squares). A sample at 1 mg/mL (circles) in $H_2O$ is provided to represent the form factor.

subsequent implications to the dynamics, structure, and viscosity. For example, the bare diffusion, by which all self and collective diffusion coefficients at larger protein concentrations are normalized, is sensitive to the effective radius of the "particle". Thus, any inaccuracies in representing the fundamental shape are compounded in later analysis. To mitigate the influence of interactions and hydrodynamics on extracting effective lysozyme structure parameters, it is first studied in the dilute limit.

Low concentration lysozyme samples are studied using SAXS due to the significantly higher intensity compared to SANS. Further, due to the nearly identical contrast between $H_2O$ and $D_2O$ in SAXS experiments, the effect of altering the solvent on the tertiary structure of lysozyme (if any) in future SANS studies can be tested. A comparison of the 1-D SAXS scattering patterns is shown in Fig. 5.2 for several solution conditions. Although the remainder of this chapter will deal with salt free samples, the influence of very low concentrations of sodium chloride (NaCl) are presented to indicate the importance of purifying the stock protein material to minimize excess counter-ions.

An immediately observable trend in Fig. 5.2 is the increase in low-$q$ scattering

**Table 5.1:** Radii of gyration extracted from SAXS experiments at low lysozyme concentration without salt for both $H_2O$ and $D_2O$ as solvents.

| Solvent | [NaCl] (mg/mL) | $R_g$ (nm) |
|---|---|---|
| $H_2O$ (1 mg/mL) | 0.0 | $1.490 \pm 0.0467$ |
| $H_2O$ (1 mg/mL) | 8.7 | $1.700 \pm 0.0503$ |
| $H_2O$ (4 mg/mL) | 8.7 | $1.455 \pm 0.0103$ |
| $D_2O$ (4 mg/mL) | 8.7 | $1.435 \pm 0.0133$ |

by the addition of 8.7 mg/mL NaCl ($\sim$ 150 mM), even at protein concentrations as low as 1 mg/mL. This is a well known result of screening the electrostatic repulsion stabilizing the proteins, causing an overall increase in attractive strength. Interestingly, for the samples without salt the repulsive strength is sufficiently strong and long range to produce a peak in the scattering intensity at a protein concentration of only 4 mg/mL. From the low-$q$ regime of the scattering data, a Guinier analysis can be used to extract a radius of gyration, $R_g$, of the protein. The Guinier approximation simply expands the intra-particle density correlations as a McLaurin series, retaining only the first term, resulting in $R_g = [-3\frac{\mathrm{d}(\ln[I(q)])}{\mathrm{d}(q^2)}]^{1/2}$.[97] The Guinier analysis is only accurate for $q < 1.0/R_g$ and solutions free of interactions, which precludes the use of this method from estimating an effective $R_g$ from the samples at 4 mg/mL without salt. The resulting values of $R_g$ are provided in Table 5.1 for samples with salt.

While the crystal and fluid structures of lysozyme are not expected to be identical, they should be similar due to the compact and stable protein structure. For comparison with the extracted values of $R_g$ in Table 5.1, the effective radius from calculations of the dry volume (crystal structure) of lysozyme is 1.54 nm. The solution condition expected to provide the most representative results for an individual monomer is the 1 mg/mL sample without salt, for which the $R_g$ is within experimental uncertainty of the crystal structure size. Adding salt appears to have a noticeable effect on $R_g$ at 1 mg/mL. As with the 1 mg/mL and no salt sample, those with salt at 4 mg/mL have a similar radius of gyration to the crystal structure, though it may

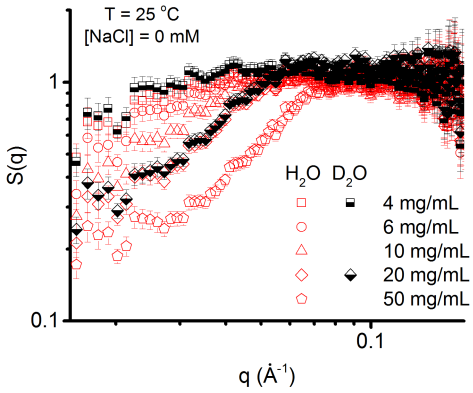


**Figure 5.3:** Structures factors of low concentration lysozyme samples in $H_2O$ (open symbols) and $D_2O$ (half-filled symbols) are compared at $25°C$ for several protein concentrations.

be slightly lower in magnitude as a result of protein interactions (due to screening of repulsion by the added salt). This suggests that lysozyme is quite stable and compact at low concentrations in both solvents.

Returning exclusively to samples without salt, the influence of solvent (either $H_2O$ or $D_2O$) on the effective lysozyme interactions can be explored by observing the subsequent changes in solution scattering. At increasingly larger protein concentration, effective interactions will contribute more significantly to the solution microstructure and therefore, are more likely to identify any differences between the two solvents. Structure factors are shown in Fig. 5.3 for lysozyme solutions at slightly elevated protein concentrations, from 4 mg/mL up to 50 mg/mL. Clearly, interactions become a more significant contribution to the scattering intensity with increasing protein concentration in both solvents, as indicated by the shift in $S(q)$ below a value of one. Interestingly, the $S(q)$ of samples in either solvent at 4 mg/mL and 20 mg/mL in Fig. 5.3 overlap nearly perfectly. Despite the fact that lysozyme solubility shifts by about $7°C$ in $D_2O$ relative to $H_2O$,[40] the similarity of the structure factors in both solvents at these low concentrations ($\leq$ 20 mg/mL) suggests that the effective interactions are relatively insensitive to the change in solvent.

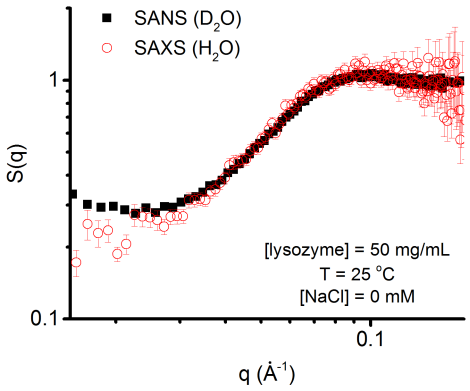


**Figure 5.4:** The structure factor of a 50 mg/mL lysozyme sample at $25°C$ in $H_2O$ and $D_2O$ obtained by SAXS and SANS, respectively, are plotted together to demonstrate the similarity of results in both solvents and by both experimental techniques.

In contrast, the different solvents are expected to produce differences in solution structure at even higher protein concentrations ($>$ 50 mg/mL) as suggested by solubility differences.[40] The decrease in low-$q$ intensity of $S(q)$ with increasing concentration in Fig. 5.3 signifies an increase in the effective magnitude of repulsive forces between proteins. This repulsion may be screening shorter range attractive forces that likely differ in strength between $H_2O$ and $D_2O$. As a result, at high concentrations, the average protein spacing will be small and proteins will sample different configurations leading to different scattering spectra.

For the remainder of this chapter, in which higher concentration samples will be of interest, structural functions will be obtained using SANS rather than SAXS. Therefore, the structure factors obtained from SAXS and SANS for an identical sample will be used to demonstrate differences in the $q$-dependence between techniques. (Theoretically, the scattering obtained by both techniques should have identical $q$-dependence, but will differ experimentally due to differences in contrast and resolution.) Shown in Fig. 5.4 are results of $S(q)$ for a 50 mg/mL lysozyme sample (without salt) obtained by SAXS and SANS. The sample used in SAXS is dissolved in $H_2O$ while $D_2O$ is used

for SANS, but it was just demonstrated that the results are independent of the solvent at these protein concentrations. Similarly, the structure factors determined using X-rays and neutrons are within experimental error of each other over the full $q$-range. However, the error bars in the low-$q$ and especially the high-$q$ limits are significantly smaller in the SANS data. This is due, in part, to the larger neutron SLD contrast by using $D_2O$ relative to the X-ray contrast using $H_2O$. This is most noticeable by the peak that forms in the SANS data in Fig. 5.4 at $q \sim 0.09$ Å$^{-1}$ that cannot be resolved in the SAXS data. Although longer exposure times using SAXS would reduce the error bars, proteins in solution are vulnerable to radiation damage, especially at high concentrations, which could produce results that are unrepresentative of equilibrium solution behavior. As a result, the remainder of the study will utilize the minimal influence from using $D_2O$ as a solvent and rely on SANS measurements to observe IRO and monomer peaks at intermediate to high $q$-values with sufficiently small error bars.

## 5.4 High Concentration Interactions, Structure and Dynamics

### 5.4.1 SANS Experiments and Analysis

The primary objective of this chapter is to extract a quantitative measure of the effective inter-protein interactions under the conditions of interest. All subsequent trends in the dynamics and viscosity as lysozyme solutions become more concentrated can be understood in terms of these fundamental forces. For this reason, interaction potentials will be quantified by means of SANS experiments. Specifically, integral equation theory will be used to extract the range and strength of interactions in an HSDY potential. A representative set of SANS data for lysozyme samples at three select volume fractions and temperatures are plotted together in Fig. 5.5. All data sets are reproducible upon changing temperature and dilution, indicating that all are in equilibrium. Each data set is provided with their corresponding best fits using the HSDY potential with a thermodynamically self-consistent closure[46] combined with the OZ equation. All extracted HSDY parameters are provided in Table 5.2, including

**Table 5.2:** A compilation of parameters determined from fits to the SANS data at several values of $\phi$ and $T$, including the fitted volume fraction ($\phi_{fit}$), strength of attraction and repulsion ($K_1$ and $K_2$, respectively), range of attraction and repulsion ($z_1$ and $z_2$, respectively), and neutron SLD contrast $(\Delta\rho)^2$. The Baxter parameter ($\tau_B$), representing the effective strength of attraction, calculated from each combination of potential parameters is provided for each solution condition (to be discussed later).

| $T = 5°C$ | | | | | | | | |
|---|---|---|---|---|---|---|---|---|
| $\phi$ | $\phi_{fit}$ | $K_1$ | $K_2$ | $z_1$ | $z_2$ | charge | $(\Delta\rho)^2$(x$10^6$) | $\tau_B$ |
| 0.0399 | 0.0398 | 6.1837 | -4.031 | 10 | 1.2238 | 6.6644 | 2.9888 | 0.7627 |
| 0.0801 | 0.0773 | 7.2 | -4.0715 | 10 | 1.9061 | 8 | 2.792 | 0.2454 |
| 0.1215 | 0.1263 | 6.5301 | -3.3148 | 10 | 2.5337 | 8.1884 | 2.6507 | 0.1901 |
| 0.1646 | 0.1432 | 6.4666 | -3.2868 | 10 | 2.7839 | 8.5537 | 2.8467 | 0.1918 |
| 0.2070 | 0.2017 | 6.3 | -3.0811 | 10 | 3.6117 | 9.523 | 2.855 | 0.1665 |
| 0.2509 | 0.2388 | 6.05 | -3.0033 | 10 | 4.1718 | 10.23 | 2.835 | 0.1842 |
| $T = 25°C$ | | | | | | | | |
| $\phi$ | $\phi_{fit}$ | $K_1$ | $K_2$ | $z_1$ | $z_2$ | charge | $(\Delta\rho)^2$(x$10^6$) | $\tau_B$ |
| 0.0399 | 0.0398 | 6.0291 | -4.2743 | 10 | 1.2473 | 6.9176 | 2.9971 | 1.3479 |
| 0.0800 | 0.0765 | 5.7 | -3.8857 | 10 | 1.8616 | 7.72 | 2.87 | 1.0865 |
| 0.1215 | 0.1286 | 5.8446 | -3.525 | 10 | 2.6287 | 8.6336 | 2.634 | 0.4994 |
| 0.1646 | 0.1472 | 5.8511 | -3.5588 | 10 | 2.9338 | 9.1983 | 2.8497 | 0.5030 |
| 0.2070 | 0.2099 | 5.743 | -3.3574 | 10 | 3.8785 | 10.441 | 2.887 | 0.3955 |
| 0.2509 | 0.24 | 5.587 | -3.3283 | 10 | 4.3792 | 11.2 | 2.82 | 0.4284 |
| $T = 50°C$ | | | | | | | | |
| $\phi$ | $\phi_{fit}$ | $K_1$ | $K_2$ | $z_1$ | $z_2$ | charge | $(\Delta\rho)^2$(x$10^6$) | $\tau_B$ |
| 0.0399 | 0.0401 | 6.0136 | -4.4161 | 10 | 1.2656 | 7.0734 | 2.9278 | 1.7420 |
| 0.0800 | 0.074 | 5.206 | -3.9707 | 10 | 1.8335 | 7.758 | 2.788 | 2.7741 |
| 0.1215 | 0.1262 | 5.4706 | -3.8298 | 10 | 2.6729 | 9.1199 | 2.5194 | 1.2629 |
| 0.1646 | 0.1551 | 6.1753 | -4.3252 | 10 | 3.3055 | 10.9763 | 2.7716 | 0.9561 |
| 0.2070 | 0.2091 | 5.2251 | -3.7215 | 10 | 4.0331 | 11.35 | 2.8166 | 1.2886 |
| 0.2509 | 0.2437 | 4.61 | -3.2208 | 10 | 4.3814 | 10.99 | 2.8 | 1.3278 |

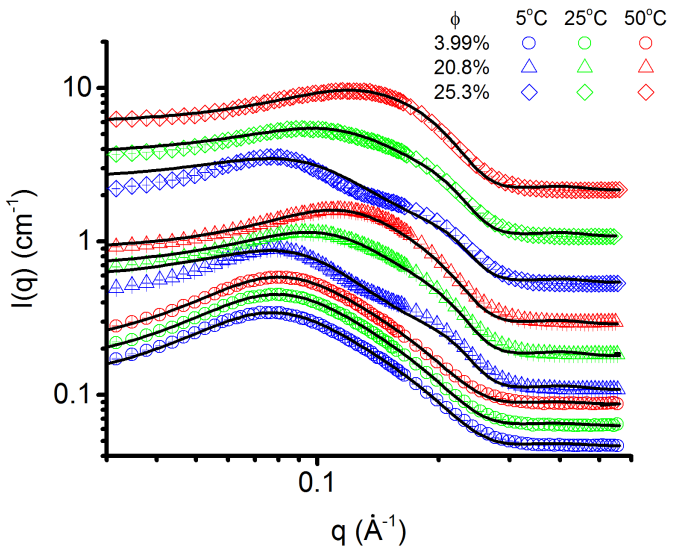


**Figure 5.5:** The absolute scattering intensity, $I(q)$, is plotted for several 1-D SANS profiles (symbols) relative to the best fits (lines) using the HSDY potential at $5°C$ (blue), $25°C$ (green) and $50°C$ (red). All data sets except that at ($\phi = 0.0399$, $T = 25°C$) are shifted for clarity.

the contrast terms, which shift due to the exchange of labile protons on the protein surface with deuterons (or "heavy protons") in equilibrium with $D_2O$ in the solvent.

All of the values of neutron SLD contrast between the solvent and lysozyme shown in Table 5.2 are plotted in Fig. 5.6 as a function of protein volume fraction. Combining theoretical values of the neutron SLD for amino acids[42] and the well known primary sequence of lysozyme[20] with experimental observation of the most easily exchanged protons in the lysozyme structure,[64] an estimate of the expected shift in the SLD contrast can be calculated as a function of the fraction of exchangeable protons. The result of this calculation is shown as the line in Fig. 5.6, which demonstrates that the values of $(\Delta\rho)^2$ corresponding to the expected extent of H-D ion exchange of 16% by lysozyme[64] corresponds well with the values extracted by fitting the SANS data. Although the calculation is not a perfect representation of the fitted values, the qualitative correspondence suggests that the exchange of labile protons on

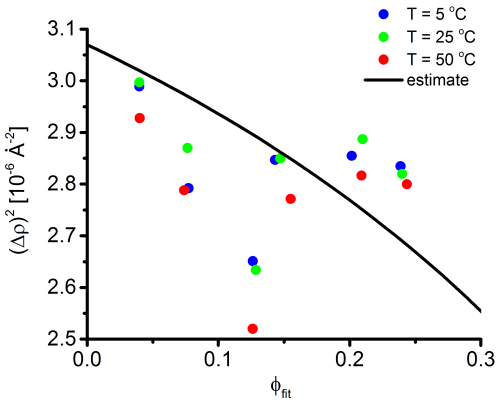


**Figure 5.6:** The neutron SLD contrast determined from fits to the SANS data is plotted as a function of fitted lysozyme volume fraction for $T = 5°C$ (blue), $T = 25°C$ (green) and $T = 50°C$ (red). Estimated values (line) assuming roughly 16% of hydrogen-deuterium exchange are provided for comparison.

lysozyme is accounted for in the fits to SANS data.

It is worth noting that, while IET calculations have converged for all the best fit lines provided in Fig. 5.5, the fits become slightly less accurate at $\phi = 0.2509$. At this large volume fraction, the accuracy of IET in representing the solution structure diminishes due to several assumptions built into the framework. In part, this is caused by neglecting multi-body interaction terms of higher order than the two-body potential considered here. Additionally, the non-spherical shape (and likely anisotropic interactions) will have a more significant influence on the solution structure as the density increases and proteins are more closely spaced. These effects are most noticeable for the two high-$\phi$ samples at $5°C$ in Fig. 5.5.

Normalizing the scattering patterns by the lysozyme form factor (and other pre-factors) allows the structure factors to be extracted, which are shown in Fig. 5.7. Also included with the data are calculations of $S(q)$ from IET and MC simulations using the parameters extracted from fitting $I(q)$. The inaccuracy of the IET fits to SANS intensity profiles at high volume fraction and low temperature is also apparent

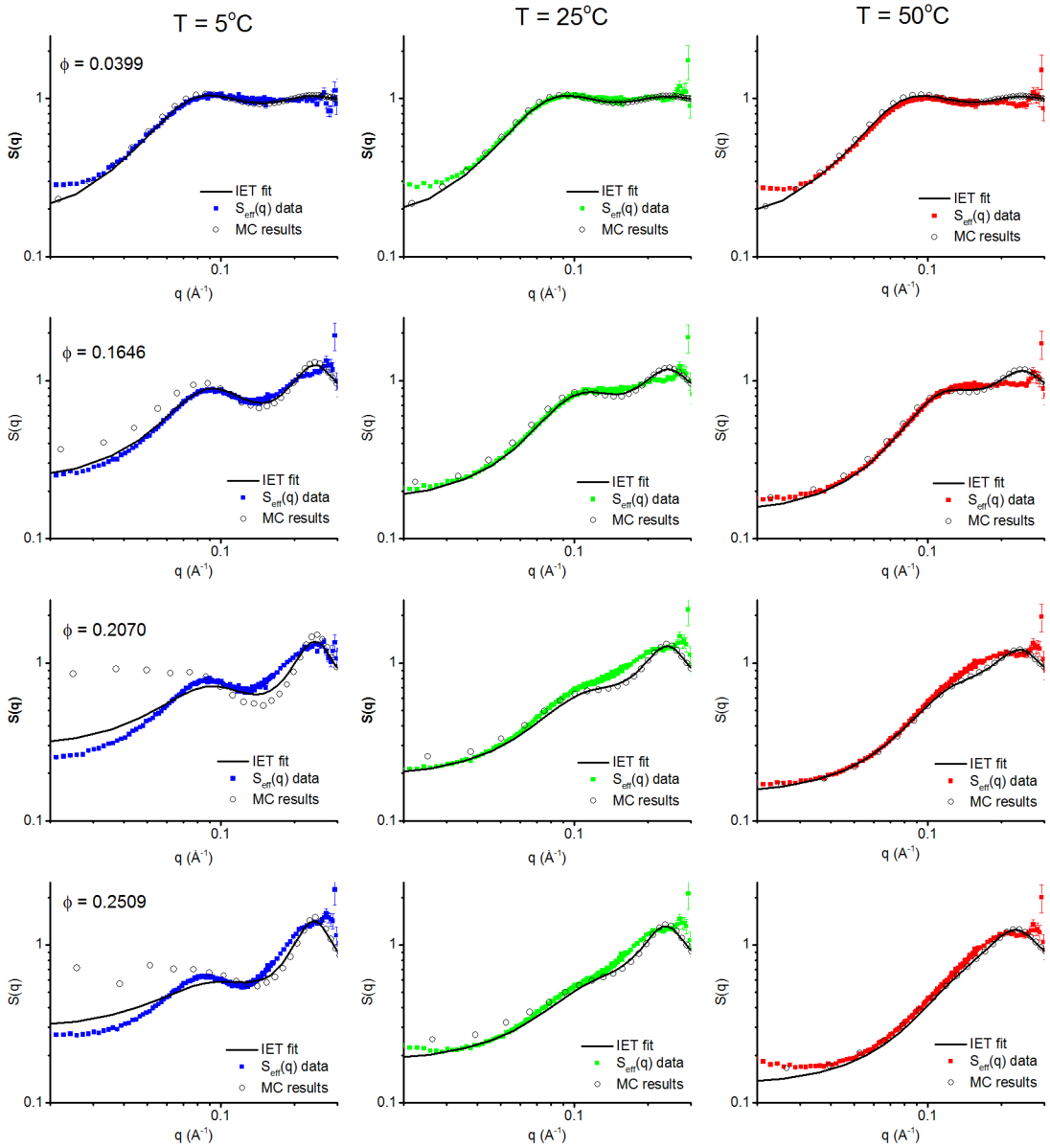


**Figure 5.7:** Structure factors, $S(q)$, obtained by normalizing experimental $I(q)$ data (filled symbols) are plotted relative to best fits (lines) and MC simulation results using the extracted potential parameters (open symbols) for protein volume fractions labeled at the left of each row at $5°C$ (left column), $25°C$ (middle column) and $50°C$ (right column).

when comparing the structure factor data and best fit lines in Fig. 5.7. Similarly, the simulation results show large differences under these same conditions at low-$q$ as a result of these simulations not converging. However, under all other conditions, the data and both analytical methods of estimating $S(q)$ are in excellent agreement. In particular, the IRO peak discussed in the previous two chapters is prevalent over a broad range of $T$ and $\phi$ and can be accurately captured by the HSDY potential. Although monomer peaks are noisy at $q \sim 0.25$ Å$^{-1}$ due to the anisotropic shape of lysozyme[26] and the large incoherent background in aqueous solution, the low-$q$ region is well resolved, allowing for the distinct trends in $S(q)$ with solution conditions to be explored.

The position and magnitude of an IRO peak, if present in $S(q)$, can be used to discern the extent of longer range order as a result of the competing interactions. Interestingly, lysozyme at $\phi = 0.0399$ produces an IRO peak at all temperatures. Further, an IRO peak is present at $5°C$ for samples of all volume fractions. At higher $\phi$, the magnitude of the peak weakens with increasing temperature, which in the extreme case becomes a shoulder at $25°C$ and eventually disappears at $50°C$. The higher the concentration, the more rapidly the samples lose their IRO peak with increasing temperature. However, the presence of these peaks is not a direct indication of a cluster fluid, though it suggests clusters are present to some extent.[36] Compared to previous simulations of HSDY systems, the magnitude of the IRO peaks here are too weak to suggest the presence of clusters of a preferred size.[38] Further, the decreasing IRO peak magnitude with volume fraction at $5°C$ indicates that these states remain outside of the generalized phase space of clustered fluids.[36] Still, these results suggest that clusters may be prevalent at these low temperatures across all volume fractions.

As shown in the previous two chapters, MC simulations are a powerful tool to extract detailed microstructural information for a given potential if the interaction parameters are known. Therefore, in addition to the qualitative features interpreted from trends in the experimental $S(q)$, the parameters determined from fitting these functions, provided in Table 5.2, can be used in MC simulations to explicitly extract

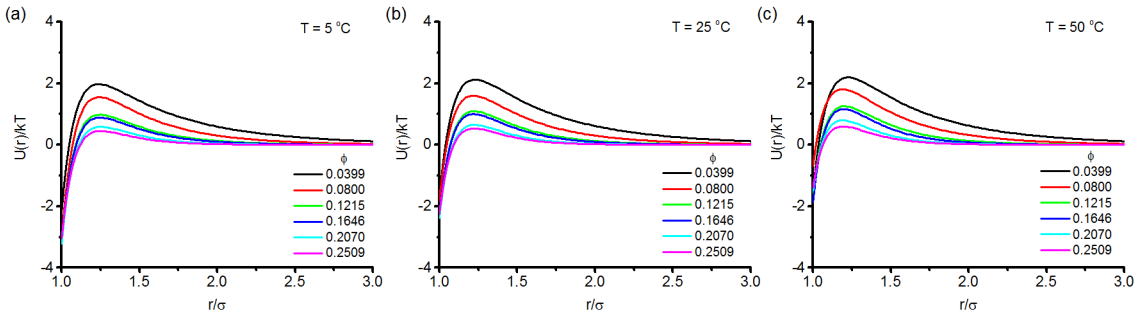


**Figure 5.8:** Interaction potentials extracted from best fits to SANS data at (a) $5°C$, (b) $25°C$ and (c) $50°C$ are plotted for a range of protein volume fractions.

a quantitative measure of the extent of clustering. The resulting potentials from each parameter sets are shown in Fig. 5.8 as a function of temperature and volume fraction. Trends in the potentials indicate that the strength and range of the repulsive component is independent of temperature, but the overall strength of repulsion decreases with increasing $\phi$. Simultaneously, the strength of attraction becomes significantly stronger with decreasing temperature and increasing concentration, though the attractive force at contact is nearly $\phi$-independent.

Using the corresponding simulation trajectories, the ensemble average cluster size distributions, $N(s)$, are calculated and plotted together in Fig. 5.9 for four protein volume fractions at three temperatures each. Samples at low concentration ($\phi = 0.0399$) have a small extent of cluster formation, which are present up to a size of about 6 particles at all three temperatures, yet the corresponding $S(q)$ show that these clusters have relatively strong correlations with each other and monomers on an IRO lengthscale. With an increase in volume fraction to $\phi = 0.1646$, cluster sizes approaching hundreds of particles become prevalent, albeit to a minimal extent. However, a strong temperature dependence can be seen as expected from the difference in the corresponding interaction potentials. Further increase of the volume fraction causes the microstructure to become percolated at low temperatures, as indicated by the peak at very large cluster sizes ($s \approx 2000$) for samples at $\phi = 0.2070$ and $\phi = 0.2509$. At

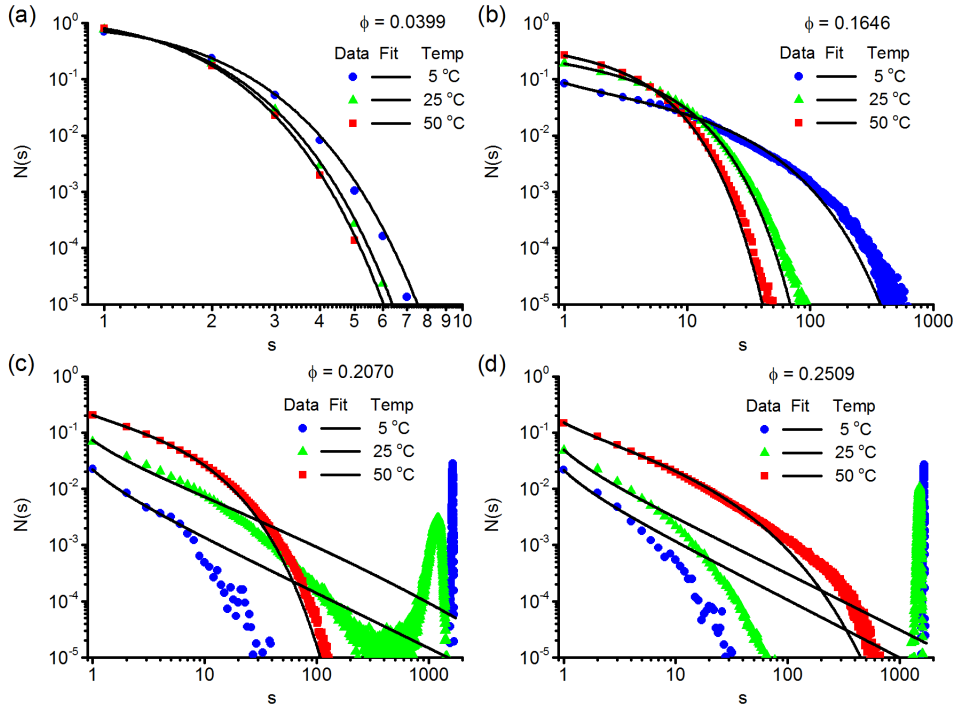


**Figure 5.9:** Cluster size distributions, $N(s)$, determined from MC simulations are plotted as a function of cluster size, $s$, at $5°C$ (blue circles), $25°C$ (green triangles) and $50°C$ (red squares) for four volume fractions labeled in each panel. The lines are best fits of $N(s)$ using a Weibull distribution function discussed in the text.

$T = 50°C$, the solution structure is not percolated, but the trend is continued in that the extent of cluster formation and the average size is enhanced at higher concentration.

The decrease in monomer content and large extent of cluster formation with increasing $\phi$ and decreasing $T$ is expected to have a large influence on the solution viscosity. Similarly, the association of clusters at even higher protein concentrations into large scale structures and even percolated clusters will also influence the viscosity.

All of the unpercolated cluster size distributions are found to be accurately represented by a Weibull distribution. By its statistical derivation, the Weibull function accounts for a random association of entities and has therefore previously been shown

to represent particle size distributions in particulate systems. The functional form is

$$p(s;k,\lambda) = \frac{k}{\lambda}\Big(\frac{s-s_0}{\lambda}\Big)^{k-1} \exp\Big[-\Big(\frac{s-s_0}{\lambda}\Big)^{k}\Big], \tag{5.8}$$

where $s_0$ is an offset term since the smallest cluster is a monomer ($s = 1$), $\lambda$ determines the magnitude of the distribution and can therefore be associated with a strength of association, and $k$ influences the shape of $p(s)$ that can physically be associated with a change in association rate between clusters. A global fit is performed on all distributions shown in Fig 5.9, resulting in a constant offset value of $s_0 = 0.463 \pm 0.005$ while the other two terms varied with $T$ and $\phi$ according to:

$$\begin{aligned} \lambda &= \exp\big[-0.552 + 7.65\phi + (88.34 - 1.52T)\phi^2\big] \\ k &= \frac{1.273}{1 + \exp\big[(83.05 - 1.35T)(\phi - 0.156 - 0.001T)\big]}, \end{aligned} \tag{5.9}$$

where $T$ is in units of $^\circ C$. Percolated states, shown in Fig. 5.9 for state points at $5^\circ C$ and $25^\circ C$ for $\phi = 0.2070$ and $\phi = 0.2509$, are poorly fit by Eq. 5.8 due to the formation of a system spanning network that can no longer be described as a random association of entities (on which the Weibull distribution is based). However, including these data sets in a global fit can provide qualitative trends in the corresponding parameters. The shift in $\lambda$ with $\phi$ and $T$ suggests that proteins associate more strongly with larger $\phi$ and lower $T$, in agreement with changes in the interaction potentials with these same parameters in Fig. 5.8. The decrease in $k$ with increasing $\phi$ suggests that the association of larger clusters becomes increasingly slower. Under these conditions the fits are poor, but the qualitative trend in $k$ corresponds well with the reduced mobility of extended networks expected with the onset of percolation, despite the inability to quantitatively capture the resulting cluster size distribution.

In an effort to generalize the behavior of lysozyme solutions over a broad range of solution conditions, empirical relationships can be used to identify trends in the fitted parameters extracted from Fig. 5.5. The significant set of state points as shown in Table 5.2 can be used to extract an accurate dependence on both $T$ and $\phi$. These will be useful for the purpose of estimating the protein dynamics and solution viscosity

later in the chapter. Each of the parameters provided in Table 5.2 explicitly captures the influence of temperature and protein concentration, which can be more readily visualized in Fig. 5.10 for the interaction parameters $K_1$, $K_2$ and $z_2$. Immediate features of each parameter with respect to $T$ and $\phi$ are noticeable. In particular, the magnitude and (linear) rate of change of $z_2$ with protein volume fraction is independent of temperature. However, the strengths of attraction and repulsion decrease with increasing protein concentration at each temperature (notice the sign of $K_2$). Further, while the magnitude of attraction increases with decreasing temperature, repulsion becomes weaker. Each of these variations with $\phi$ and $T$ is captured by fitting with the following empirical functions:

$$\begin{aligned}
K_1(5^\circ C) &= 7.48 - 5.91\phi \\
K_1(25^\circ C) &= 5.87 - 0.778\phi \\
K_1(50^\circ C) &= 5.90 - 3.40\phi \\
K_2(5^\circ C) &= -2.39\phi^{-0.174} \\
K_2(25^\circ C) &= -2.71\phi^{-0.140} \\
K_2(50^\circ C) &= -3.08\phi^{-0.113} \\
z_2 &= 0.708 + 14.62\phi,
\end{aligned} \tag{5.10}$$

which are shown by the lines in Fig. 5.10.

As discussed in Chapter 1, the protein chemistry is responsible for the resulting trends in interaction parameters shown in Fig. 5.10. A decrease in $K_1$ with increasing concentration correlates with an increase in ionic strength and a subsequent decrease in repulsive strength, which suggests a possible contribution from electrostatics. One explanation is a heterogeneous surface charge distribution that could produce dipoles. This type of interaction is inherently orientation dependent, but may still be captured by these spherically isotropic HSDY potentials. However, the difference in trends of $K_1$ and $K_2$ and the well known inclusion of non-polar residues on the lysozyme surface indicates that hydrophobic forces also contribute to the total attractive strength. Again, since hydrophobic residues exist in patches, these forces require specific orientations of

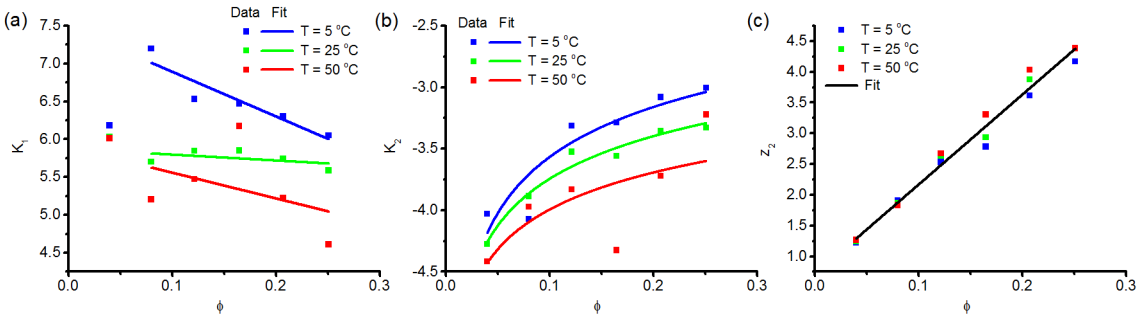


**Figure 5.10:** Empirical fits (lines) to the volume fraction dependence of the HSDY parameters (symbols) for (a) attraction strength, $K_1$, (b) repulsion strength, $K_2$ and (c) repulsion range, $z_2$ extracted from fits to SANS data.

two adjacent proteins.[45] As protein concentration increases, the ellipsoidal shape of lysozyme may restrict rearrangement to achieve the necessary two-body configuration. Thus, if the forces depend strongly on orientation, the net effective isotropic attractive strength would likely decrease with concentration.

An additional interesting observation is the difference in temperature dependence of $K_2$ and $z_2$, which both depend on the ionic strength. By implementing the generalized one-component model,[11] $K_2$ and $z_2$ can be used to calculate the corresponding ionic strength of lysozyme,[37] which increases from about 0.02 M at $\phi = 0.0399$ to about 0.2 M at $\phi = 0.2509$. Over the same conditions, the molarity of lysozyme is roughly an order of magnitude lower. Therefore, association of counter-ions with the protein surface will cause the ionic strength in solution to decrease very little, but could cause the surface charge to change significantly. Equilibrium concentrations of counter-ions can be used to estimate surface association in a similar fashion to the Henderson-Hasselbalch equation[43]

$$pC = pKa + \log\left(\frac{[R^-]}{[RC]}\right), \tag{5.11}$$

where $RC$ and $R^-$ represent a residue in the associated and dissociated state, respectively, $C^+$ represents a counter-ion ($pC = -\log\left([C^+]\right)$), and the brackets denote the

molar concentration. Thus, an increase in the concentration of counter-ions will drive re-association of counter-ions with surface residues on lysozyme. However, previous work using Debye-Huckel theory has demonstrated that the dissociation constants of several amino acids are quite sensitive within this regime of ionic strengths.[60] In particular, the $pKa$ values decrease with increasing ionic strength and temperature. The consequence is an increase in surface charge (i.e., repulsion strength, $K_2$) with increasing temperature as qualitatively observed in Fig. 5.10. In contrast, the $pKa$ values decrease by no more than 10% with increasing ionic strength (i.e., $pC$),[60] while $pC$ itself increases roughly an order of magnitude. Thus, $K_2$ still decreases with increasing protein volume fraction.

### 5.4.2 NSE Experiments and Analysis

In addition to the change in protein interactions and solution structure with sample conditions, the dynamics, which will also be intricately related to the interactions, will have a strong influence on the material properties. However, a complication in dealing with SALR systems is the significant polydispersity of aggregate species (i.e., cluster sizes) that may contribute to the average dynamic correlations. Such a system can be represented by a stretched exponential to represent the spectrum of relaxation times associated with each cluster size, which is well understood for polymers above the glass transition temperature[4] and colloidal solutions approaching the gel transition.[65, 95] Here, the mobility of lysozyme in solution is treated in two ways to physically represent the influence of $N(s)$ on the dynamics. The dynamic data obtained by NSE experiments are treated with the use of a single exponential to extract a single effective mobility representative of the total system and with a double exponential to quantify potentially two distinct timescales of motion – those of monomers and clusters.

A characteristic set of self-intermediate scattering functions obtained from NSE for a sample at $\phi = 0.2981$ and $T = 25°C$ are plotted in Fig. 5.11 with their corresponding fits to a single exponential decay function at five $q$-values. Fits are restricted

to the first 25 ns to remain within the short time limit, beyond which the data do appear to deviate slightly from the linear trend on the semi-log scale. Such a deviation is consistent with the presence of additional slower species, to be discussed later. From the single exponential fits, the collective diffusion coefficients are obtained, which are plotted in Fig. 5.12 as a function of $q$-value for most of the sample conditions studied. As outlined in previous work,[66] the high-$q$ limiting values of $D_C(q)$ are representative of the self-diffusion coefficients, which are obtained using a linear fit over an appropriate $q$-range. A sample at $\phi = 0.0077$, not shown in Fig. 5.12, is used to determine the bare diffusion coefficient by which the results at higher concentrations are normalized.

The normalized short-time self diffusion coefficients, $D_S/D_0$, are plotted in Fig. 5.13a as a function of volume fraction at $5°C$, $25°C$ and $50°C$. Also provided for comparison are trends determined by theoretical calculations of HS[50] and charged sphere (CS)[7, 9, 12] systems. A clear discrepancy arises at larger volume fractions between HS and CS predictions and the lysozyme data, as expected, due to the complex interactions between proteins. Note the log scale in Fig. 5.13a, as the decrease in protein diffusion with increasing concentration is significant. The data were fit to an

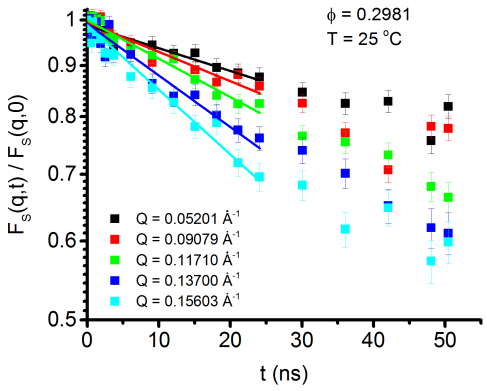


**Figure 5.11:** The ISF (symbols) at several $q$-values are shown for a lysozyme sample at $\phi = 0.2981$ and $T = 25°C$ with the best fits (lines) using a single exponential function up to only 25 ns to remain within the short-time limit.

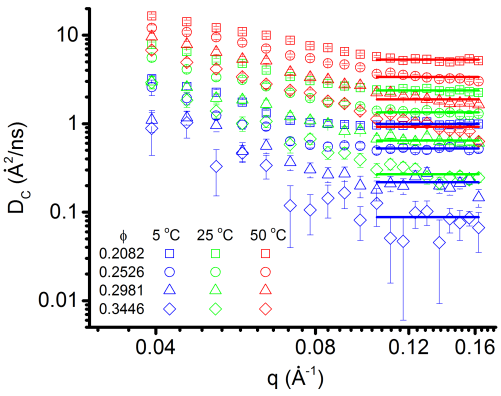


**Figure 5.12:** The $q$-dependence of the collective diffusion coefficient, extracted from fits to the ISF obtained by NSE, is plotted for several lysozyme samples at large volume fractions for $5°C$, $25°C$ and $50°C$. The lines represent the average value determined in the high-$q$ asymptotic limit to estimate $D_S/D_0$.

empirical model with the functional form of a sigmoidal shape logistic function

$$\frac{D_S}{D_0} = \frac{A}{1 + \exp\left[k(\phi - \phi_{crit})\right]}, \tag{5.12}$$

where $T$ is the temperature in $°C$, on which the remaining three parameters are linearly dependent: $A = 1.076 + 0.0022T$, $k = 19.39 - 0.115T$, $\phi_{crit} = 0.129 - 0.0001T$. The parameter $\phi_{crit}$ indicates the volume fraction at which diffusion begins to decline significantly, which may be used as an approximate indicator of the onset of cluster formation. Similarly, $k$ dictates the decrease in mobility with increasing volume fraction. By analogy with the Fermi-Dirac distribution, $k$ can be related to the energy state of the cluster size/structure associated with the diffusion coefficient produced at a particular volume fraction. For example, the larger value of $k$ at lower temperature could be directly related to a larger cluster size or a larger energy barrier that confines individual particles within a cluster longer. However, future work is required to uncover a more rigorous relation between these parameters and cluster properties.

The manifestation of the competing interactions is more clearly demonstrated by the calculated effective hydrodynamic radius, plotted in Fig. 5.13b. With increasing

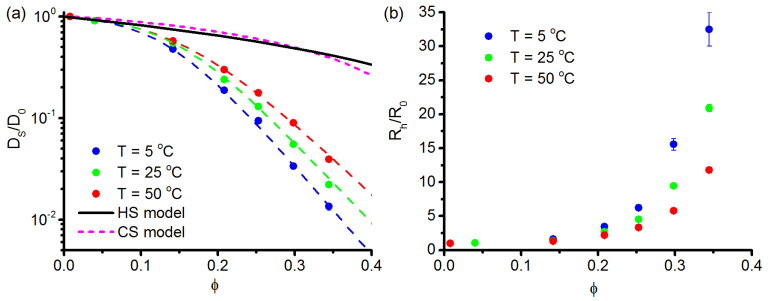


**Figure 5.13:** (a) Short-time self diffusion coefficients (symbols) extracted from the high-$q$ asymptotic limit shown in Fig. 5.12 are plotted relative to HS (solid line) and CS (dotted line) estimates as well as empirical fits (dashed lines). (b) Effective hydrodynamic radii, $R_h/R_0$, estimated from values of $D_S/D_0$ are plotted as a function of $\phi$ for each of the three temperatures studied.

volume fraction, the size of aggregates increases rapidly and even appears to diverge at $5°C$. While this calculation assumes clusters are spheres and ignores the effect of viscosity on diffusion, it indicates that clusters become dominating features in the solution microstructure above a volume fraction of about 0.2. Therefore, the reduced dynamics from cluster formation and their corresponding interactions are also expected to have an impact on the viscosity.

Considering that SANS results and corresponding MC simulations suggest significant clustering in these samples, especially at low temperature and high volume fraction, the dynamic corollary may provide additional information regarding the mobility of said clusters. Rather than restricting the fits of the ISF to the first 25 ns, the use of a double exponential fit over the entire 50 ns obtained from NSE experiments may yield insight into the extent of clusters and their average hydrodynamic size. The functional form of the ISF is therefore represented as

$$\frac{F_S(q,t)}{F_S(q,0)} = (1 - X_C)\exp[-D_C^{mon}(q)tq^2] + X_C\exp[-D_C^{clus}(q)tq^2], \tag{5.13}$$

where $X_C$ is the weighting function of clusters discussed in more detail in the Appendix, and $D_C^{mon}(q)$ and $D_C^{clus}(q)$ are the effective $q$-dependent monomer and cluster

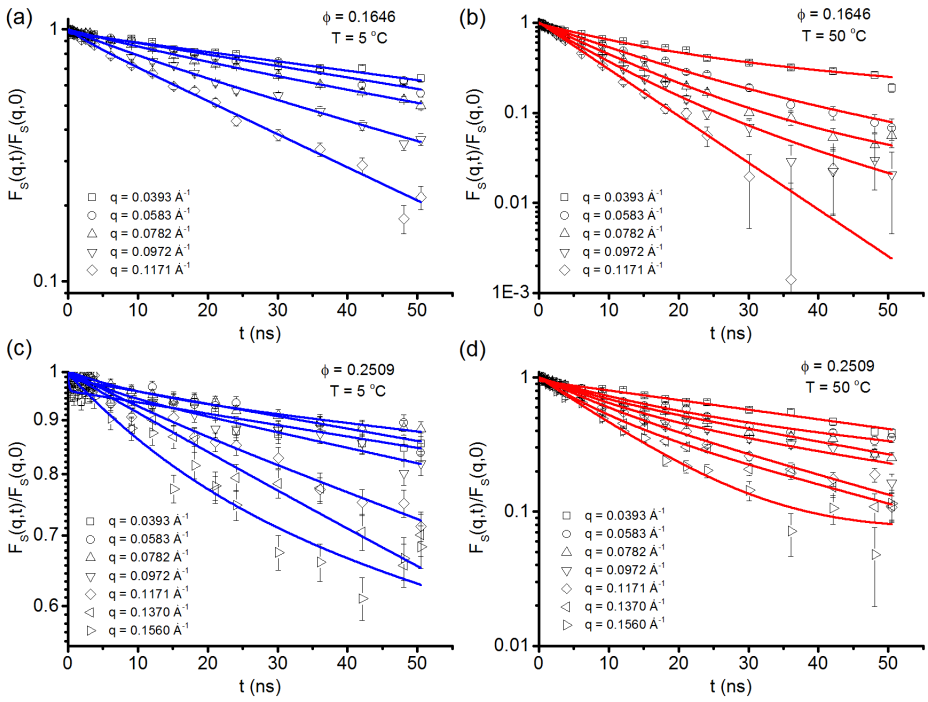


**Figure 5.14:** The experimental ISF (symbols) of lysozyme samples at several conditions and $q$-values are plotted with best fits (lines) using a double exponential function over the full correlation time range up to 50 ns.

collective diffusion coefficients, respectively. The short-time self diffusion coefficients corresponding to $D_C^{mon}(q)$ and $D_C^{clus}(q)$ will be determined from the high-$q$ asymptotic limit, in an identical fashion to the single exponential fits, and will be represented by $D_{mon}$ and $D_{clus}$, respectively, shown in Fig. 5.15.

If rescaled appropriately, the drop in diffusivity can provide an estimate of the effective cluster size as a function of volume fraction.[66] Considering the short time limit of a lysozyme monomer is about 25 ns, fits of the full 50 ns in the ISF will yield a second set of $q$-dependent diffusion coefficients that represent larger structures with slower relaxation times. However, cluster size distributions in SALR systems are known to be highly polydisperse, with each cluster size likely having a different diffusion coefficient. As a result, the extracted "cluster" diffusivity by a double exponential will be

a number average value from the full distribution of cluster sizes in solution, assuming the lifetime of clusters is sufficiently longer than the time window. Therefore, the reduced short-time diffusivity with increasing concentration and reduced temperature corresponds to an increase in the number average cluster size in solution. Though these clusters maintain a lifetime of at least 50 ns, they are expected to remain dynamic in nature over longer timescales.

All three parameters determined from the double exponential fits are provided in Fig. 5.15, where $D_{mon}$ and $D_{clus}$ are normalized by the bare diffusion coefficient. The results are plotted as a function of protein volume fraction at each of the three temperatures studied. Interestingly, the monomer diffusivity at $25°C$ and $50°C$ appears to decrease drastically at $\phi \sim 0.15$ before apparently reaching a high-$\phi$ plateau. However, whether the apparent plateau in $D_{mon}/D_0$ at each temperature is real or an artifact of the fitting is uncertain due to the small population of monomers ($X_C \approx 1$) at these large volume fractions. The increasingly dominant contribution from cluster mobility to the NSE data is expected when compared with SANS and MC simulation results. The short-time cluster diffusion coefficient decreases drastically with $\phi$ and in general decreases at all volume fractions with decreasing temperature, which corresponds with the stronger attractive interactions extracted from SANS data.

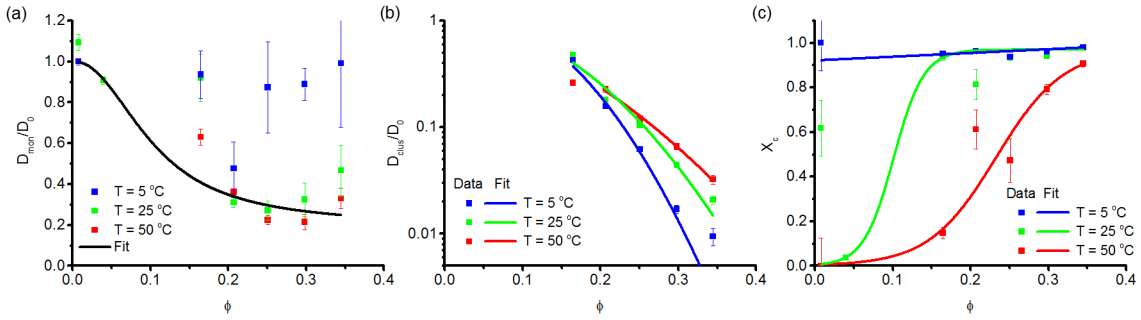


**Figure 5.15:** Empirical fits (lines) to the volume fraction dependence of the normalized (a) monomer and (b) cluster diffusion coefficients and (c) the scaling factor of clusters (symbols) determined from the high-$q$ asymptotic limit of each parameter extracted from fits to NSE data.

In order to capture the general trends observed in Fig. 5.15 for future estimates of solution viscosity, much as the interaction parameters were in Fig. 5.10, the dynamic parameters are fit with empirical relations. The resulting functional form(s) for $D_{mon}/D_0$ is

$$D_{mon}/D_0 = 0.196 + (1 - 0.196)/(1 + [\phi/0.103]^{2.21}), \tag{5.14}$$

for $D_{clus}/D_0$ at each temperature are

$$\begin{aligned} D_{clus}/D_0(5°C) &= \exp[-3.38\phi - 19.26\phi^2] \\ D_{clus}/D_0(25°C) &= \exp[0.611\phi - 37.21\phi^2] \\ D_{clus}/D_0(50°C) &= \exp[4.32\phi - 62.41\phi^2] \end{aligned} \tag{5.15}$$

and finally for $X_C$ at each temperature are

$$\begin{aligned} X_C(5°C) &= 0.974/(1 + \exp[-23.08(\phi - 0.233)]) \\ X_C(25°C) &= 0.969/(1 + \exp[-51.78(\phi - 0.101)]) \\ X_C(50°C) &= 5.357/(1 + \exp[-0.21(\phi - 7.33)]). \end{aligned} \tag{5.16}$$

Considering the experimental sensitivity of the monomer diffusion coefficient at large volume fractions is small due to their almost non-existent population, the values of $D_{mon}/D_0$ at $5°C$ were ignored when globally fitting the results to a single function. Upon ignoring this data set, the trend is followed by the remainder of the data points. Similarly, a cluster diffusion coefficient could not be fit at $\phi < 0.15$ due to the low population of clusters. However, the functional form of the empirical relation fit to $D_{clus}/D_0$ was forced to approach a value of one at low volume fractions to remain physically meaningful.

Finally, to test the monomer and cluster dynamics of fitting the NSE data with a double exponential function, an effective diffusion coefficient can be estimated by calculating the weighted average of $D_{mon}$ and $D_{clus}$. The resulting effective diffusion coefficient is plotted in Fig. 5.16 as $D_{2ex}$ compared with the diffusion coefficient from the single exponential fit $D_{1ex}$. The similarity of both estimates of the average diffusivity at all three temperatures (within the uncertainty) suggests that both representations are equivalent. Estimates of $D_{2ex}$ produce such large error bars due to the

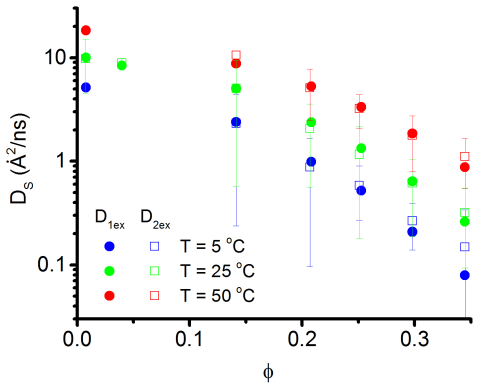


**Figure 5.16:** Comparison of effective, normalized short-time self diffusion coefficients determined from fits to the ISF using a single exponential, $D_{1ex}$, and a double exponential, $D_{2ex}$. Both methods of fitting show great agreement, but the weighted combination of two coefficients in the double exponential method produces large uncertainties (error bars).

large number of parameters needed for the fitting, the individual errors of which are compounded. However, as a result a more extensive set of information regarding the system dynamics can be extracted.

## 5.5 IRO Structure and Glassy Dynamics at High Concentration

Lysozyme viscosity was studied over a range of temperatures from $5°C$ to $50°C$ and volume fractions ranging between 0.0077 and 0.345 (11481 mg/mL). The zero shear viscosity, $\eta_0$, is calculated as the asymptotic value approached in the low shear limit. The dependence on shear rate and temperature for the three largest volume fractions tested ($\phi = 0.2070$, $\phi = 0.2509$, and $\phi = 0.3448$) are provided in Fig. 5.17a, 5.17b, and 5.17c, respectively. Even with such large viscosities as found for these samples at low temperatures, the behavior is completely Newtonian. Therefore, all data points are within the low shear plateau regime and $\eta_0$ of each sample is calculated as the average over the entire range of shear rates studied. Viscosity values are normalized by $D_2O$ viscosity at each respective temperature to obtain the relative zero-shear viscosities, $\eta_{r0}$, plotted in Fig. 5.17d. For comparison, the data are plotted along with two models

of the HS zero shear viscosity, the RWM-MCT model[71] and the Brady model,[16] both of which are discussed in more detail in the Appendix. The HS results include hydrodynamic and Brownian contributions to the viscosity.[16]

The range of shear rates ($10s^{-1} < \dot{\gamma} < 10^5 s^{-1}$) varied for each sample, but the data are well within the zero shear limit of $Pe = 6\pi\eta_s\sigma^3\dot{\gamma}/8k_BT << 1$, where $\eta_s$ is the solvent viscosity and $\sigma$ is the particle diameter. The highest $Pe$ number (at low concentrations) only approached $Pe \approx 2\text{x}10^{-3}$. Comparing an inverse measure of the relative time of viscous relaxation, $\dot{\gamma}^{-1}$, and diffusive relaxation,[47]

$$\tau = \frac{3\pi\eta_s\sigma^3}{4k_BT}, \tag{5.17}$$

which varies with temperature for lysozyme but is roughly 25 ns, indicates that viscosity measurements are about 5 orders of magnitude beyond the time for protein diffusion. Therefore, the large specific viscosities in Fig. 5.17d and corresponding Newtonian behavior are representative of long-time structural rearrangement.

Protein interaction effects (i.e., the difference between lysozyme data and HS results) are minimal at low volume fractions. Note the log scale as the magnitude of viscosity becomes significant above a volume fraction of about 0.20, especially for lower temperatures. At these elevated concentrations, the viscosity at $50°C$ is almost an order of magnitude above a HS fluid with an equivalent volume fraction. Remarkably, decreasing the temperature from $50°C$ to $5°C$ at $\phi = 0.3448$ causes the already high viscosity to increase an additional two orders of magnitude. Therefore, the zero shear viscosity is acutely sensitive to inter-protein interactions and the potentially large scale structures they produce.

Micromechanical viscosity models suggest that the relevant timescale is set by the short-time self diffusion coefficient of individual particles at a given set of solution conditions.[16] However, these same models also indicate that interactions contribute directly and indirectly by the corresponding radial distribution function (i.e., solution microstructure).[16] Therefore, as a way of inspecting the relative contribution of reduced mobility on the increase in viscosity, the product of the reduced viscosity and

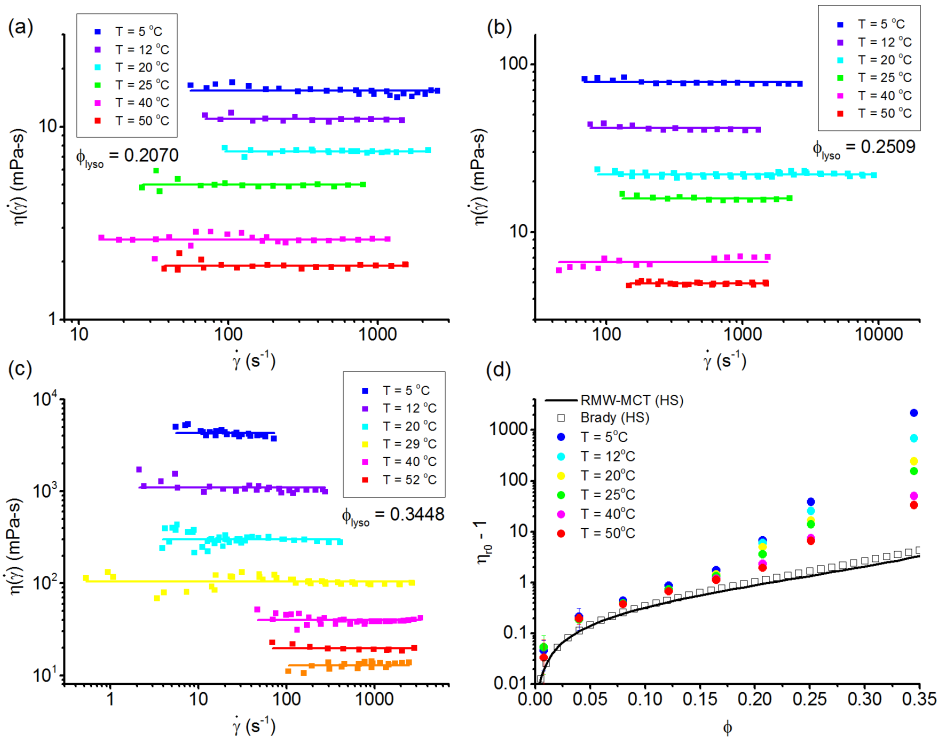


**Figure 5.17:** Viscosities (symbols) are plotted as a function of shear rate at several temperatures for (a) $\phi = 0.2070$, (b) $\phi = 0.2509$ and (c) $\phi = 0.3448$ along with fits of the zero shear viscosity (lines). (d) Specific viscosities in the zero shear limit (filled circles) are plotted as a function of protein volume fraction at several temperatures relative to HS estimates according to the Brady model (open squares) and RMW-MCT model (line).

self-diffusion coefficient is plotted in Fig. 5.18, in a similar fashion to a generalized Stokes-Einstein (GSE) plot.[55] Interestingly, lysozyme data maintain a nearly constant value at low to intermediate volume fractions ($\phi < 0.2$) for all temperatures, consistent with HS predictions. However, due to the lack of interactions in HS fluids, reduced dynamics are dictated by hydrodynamics. Here, values of lysozyme $D_S$ and $\eta_{r0}$ deviate from HS results due to the presence of competing interactions. Thus, in this volume fraction regime these interactions affect the viscosity indirectly via their influence on the reduced short-time self diffusivity.

At elevated concentrations ($\phi > 0.2$) and low temperatures ($T = 5 - 25°C$), lysozyme solution viscosity begins to increase significantly faster than the reduction in diffusivity (compare Fig. 5.17d and Fig. 5.13a, respectively) as shown by the large rise in magnitude in Fig. 5.18. Therefore, the viscosity is enhanced by additional direct contributions from the competing interactions in excess of the drastic drop in short-time mobility. In part, the influence of SALR interactions on the viscosity can be physically interpreted as the formation of clusters, but the cause of the quantitative difference found in Fig. 5.18 between lysozyme and HS systems at high-$\phi$ remains unclear.

For comparison, the excluded volume in HS fluids lead to a randomly dispersed, homogeneous microstructure that significantly hinders the relative motion of particles at large enough volume fractions. Experiments demonstrated that HS systems become kinetically arrested at $\phi = 0.58$,[67, 93] known as the repulsive glass transition at which long-time motion is suppressed by caging. Correspondingly, HS viscosity models such as the RWM-MCT model capture this transition by forcing $\eta_{r0}$ to diverge when approaching this $\phi$ from below. While the cages hinder long-time diffusion, particles within a glass remain mobile in the short-time limit as they "rattle" within their cage of nearest neighbors. Therefore, the predicted trend of HS systems in Fig. 5.18 will diverge, despite having a finite short-time self diffusion when approaching the glass transition (i.e., $\lim_{\phi \to 0.58} D_S/D_0 > 0$).

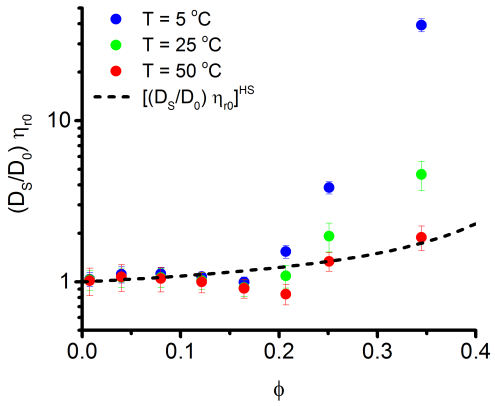


**Figure 5.18:** The product of relative viscosity and short time self diffusion (symbols) is plotted similar to a Generalized Stokes-Einstein-Sutherland relation as a function of volume fraction relative to HS expectations (dashed line).

As in HS systems, the long-time dynamics of SALR systems must also be explored to fully understand the resulting viscosity behavior. Calculations of $\tau$ in Eq. 5.17 for lysozyme show that the values of $D_S/D_0$ determined by NSE probe structural rearrangement on timescales that are many orders of magnitude smaller than that probed by rheology. Therefore, it will be useful to explore the correlation between long-time self diffusion and $\eta_{r0}$ to understand not only differences in the mobility on these two time scales, but also if structural relaxation on long times is a dominant contribution to the viscosity or if interactions must be explicitly accounted for in addition to their indirect influence on the dynamics.

Typically, GSE relations relate the long time viscous dissipation, $\eta_{r0}$, with long-time self diffusion, $D_L/D_0$, (i.e., diffusive relaxation) as they represent microscopic properties on the same timescale. A GSE relationship suggests that slow particle mobility is the dominant contribution to enhanced resistance to shear flow. For hard sphere systems, a GSE relation has been debated but generally shown to hold true with a weak volume fraction dependence.[8, 50] Although above $\phi = 0.58$, the HS viscosity diverges since particles are effectively frozen, a viscosity can still be measured

at $\phi < 0.58$ since the systems remains fluid. In order words, particles can still flow relative to each other. Therefore, cages restricting particle motion will eventually rearrange if observed over a long enough period. The eventual relaxation of a cage (i.e., escape of a particle) is quantified by the decay of a long timescale plateau in the ISF, known as $\alpha$-relaxation. This structural relaxation mechanism is what $D_L$ captures in HS fluids and will likely be a similar large scale structural rearrangement in SALR systems.

The long-time self diffusion, $D_L$, of lysozyme is difficult to determine experimentally due to its size and limitations of experimental techniques. However, $D_L$ can be approximately estimated from both the zero-shear viscosity and a normalization of short-time self diffusion. Using mode coupling theory (MCT), the experimental values of $D_S$ can be used to estimate $D_L$ according to

$$\frac{D_L}{D_0} \approx \left(\frac{D_S}{D_0}\right) D_L^{MCT}, \tag{5.18}$$

where $D_L^{MCT}$ is a volume fraction dependent ratio of $D_L/D_S$ determined by MCT.[5, 9] Further, the viscosity can be used to estimate the long-time diffusion according to a generalized Stokes-Einstein-Sutherland equation[28, 55]

$$\frac{D_L}{D_0} \approx \frac{1}{\eta_{r0}}. \tag{5.19}$$

Values of $D_L/D_0$ estimated by Eq. 5.18 and Eq. 5.19 are shown in Fig. 5.19 and are found to be in relatively good agreement for all states points except the most viscous sample condition.

Distinguishing the disparate short and long time scales in concentrated lysozyme samples ($\phi > 0.3$) was also accomplished using DLS. Two distinct relaxation times were observed at all temperatures, which were fully reversible over three temperature sweeps between $5°C$ and $50°C$, and thus not a result of irreversible aggregation on the time scale of the experiments. By analyzing the correlation functions in a similar manner to NSE data, but using a double exponential function, both time scales can be extracted to represent short, $D_{short}$, and long, $D_{long}$, time collective motion. From these two time

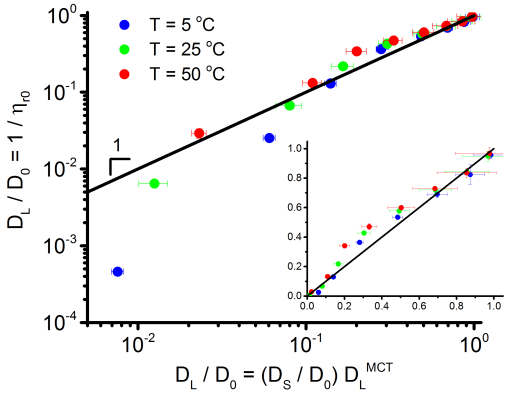


**Figure 5.19:** Comparison of long-time self diffusion estimated by the reciprocal of the experimentally determined zero-shear viscosity (y-axis) and MCT scaling of experimental $D_S/D_0$ from NSE (x-axis). The black line is the equivalence point. The inset shows the same plot on a linear scale to clarify the correlation at low $\phi$ (high $D_L/D_0$).

scales, an effective value of $D_{short}/D_{long}$ and shear rate at the onset of shear thinning $\dot{\gamma} \approx D_{long}/(2R_{short})^2$, where $R_{short} = kT/(6\pi\mu D_{short})$, are estimated and summarized in Table 5.3. The temperature dependence of $D_{short}/D_{long}$ shows an increase in the effective structural size by roughly an order of magnitude when decreasing $T$ from $50°C$ to $5°C$. This shift corresponds well with the change in $\eta_{r0}$ in Fig. 5.17d at these volume fractions. The correlation between $D_{short}/D_{long}$ and the viscosity is a strong indication that the DLS is probing the $\alpha$-relaxation time scale as opposed to large aggregates to which DLS is sensitive/susceptible. Viscosity is a measure of stress relaxation within the complete microstructure and as such is much less sensitive to individual aggregates compared to DLS. Further, the shear rate at the onset of shear thinning agrees well with estimates of the Péclet number indicating that the rheology data are well within the low shear regime. Although the viscosity measurements conducted here were unable to reach the shear thinning regime, the estimates of $\dot{\gamma}$ in Table 5.3 suggest that a sufficiently large pressure drop should also be able to generate shear rates necessary to probe the $\alpha$-relaxation.

**Table 5.3:** Estimates of $D_{short}/D_{long}$ and shear thinning shear rate from DLS results.

| $D_{short}/D_{long}$ | | | |
|---|---|---|---|
| $\phi$ | $T = 5°C$ | $T = 25°C$ | $T = 50°C$ |
| 0.283 | 611 | 337 | 283 |
| 0.335 | 750 | 403 | 218 |
| $\dot{\gamma} \approx D_{long}/(2R_{short})^2$ | | | |
| $\phi$ | $T = 5°C$ | $T = 25°C$ | $T = 50°C$ |
| 0.283 | 1657 | 11943 | 24395 |
| 0.335 | 664 | 5313 | 41801 |

Interestingly, the short-time dynamics of lysozyme under concentrated conditions display sub-diffusive behavior. For systems of colloidal particles with purely attractive interactions in either a gel or glass state, the sub-diffusive behavior persists for long times. A practical limit of $100s$ is typically used for most colloidal systems to determine dynamic arrest.[95] However, while this criterion is satisfactory for studies of relatively large colloidal particles, the dependence $\tau \propto 1/\sigma^3$ would exclude protein solutions from dynamic arrest by this standard. In contrast, the associated mean square displacement (MSD) of particles also becomes very small at $t \sim \tau$.[95] These criteria have been used to identify gelation or glass transitions.[47, 73, 95, 96] NSE can measure the ISF at relatively large $q$-values such that NSE can also probe the MSD, similar to the method used in dynamic light scattering.[92] As a result, NSE is used to estimate the MSD of concentrated lysozyme solutions. By rearranging the exponential dependence of the ISF with respect to the diffusion coefficient, the MSD, $\langle R^2 \rangle$, at a given $q$-value can be described as

$$\langle R^2 \rangle = 6D_C(q)t = -\frac{6}{q^2} \ln[F_S(q,t)/F_S(q,0)]. \tag{5.20}$$

The MSDs calculated using the ISF for $q > 0.1$ Å$^{-1}$ are provided in Fig. 5.20 as filled symbols with respect to lines representative of fluid, cluster, glassy, and gel states that are reported previously for samples with 1.95 $\mu$m diameter PMMA particles with SALR interactions.[47] Despite the large differences in the particle size and the

time scale of the measurement techniques, the normalized time ranges are similar for both lysozyme and PMMA particles.[47] At times $t/\tau < 1$, which represents the short-time limit,[7] all samples follow a power law expected for diffusive motion. At sufficiently low volume fractions ($\phi = 0.1646$), the data remain diffusive for times beyond $\tau$ at all temperatures. However, for $\phi \geq 0.2$, the power law exponent drops below one for $t/\tau > 1$, becoming sub-diffusive with decreasing temperature. These conditions correspond to the regime in Fig. 5.17d where the specific viscosity increases significantly. The normalized MSDs of lysozyme samples at high-$\phi$ and low-$T$ are well below the MSDs of glassy and gel samples reported previously for colloidal systems with SALR interactions.[47] This indicates that at the local length scale, lysozyme proteins in these samples have glassy behavior. In fact, for the highest concentration

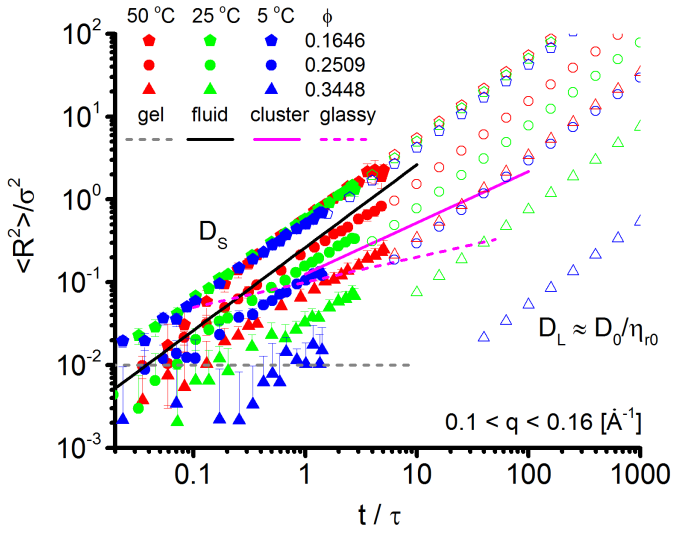


**Figure 5.20:** The mean squared displacement of all lysozyme solutions at short times determined from NSE (filled symbols) and long times determined from viscosity measurements (open symbols) are plotted on a normalized time scale relative to trends expected for four types of dynamic states determined previously.[47] Lysozyme in all solution conditions appears diffusive at $t < \tau$, but deviates from fluid-like behavior at $t > \tau$ at elevated $\phi$ and low $T$.

sample at $5°C$, the MSD is about the same as values reported for one glassy colloidal system with depletion attraction,[70] and is even smaller than that of one hard sphere system in a glass state measured by DLS.[92] Estimation of the MSD at the long time limit further supports the above observations.

The deviation of short-time and long-time mobility is also directly demonstrated by plotting the corresponding MSDs together in Fig. 5.20. The long time MSD is approximated by $6t/\eta_{r0}$, where $D_L$ is approximated using Eq. 5.19. As shown in Fig. 5.20, the short and long time displacements overlap almost perfectly in the limit of low $\phi$ and high $T$. In the other extreme of high $\phi$ and low $T$, the long time MSD is cut-off at the magnitude of the short time limit to represent the most extreme scenario of a plateau (i.e., a gel or glass). In general, the comparison indicates the disparity of these two time scales and thus, at some time $t > \tau$, the onset of sub-diffusive behavior. Here, SALR interactions cause an early onset of glassy behavior at $\phi \approx 0.3$ that varies slightly with temperature and therefore attraction strength.

Now, the quantitative disparity in short-time and long-time diffusivity can be leveraged to distinguish their correlations with the resulting solution viscosity. The ambiguity in Fig. 5.18 is removed by directly plotting $\eta_{r0}$ as a function of both diffusion coefficients in Fig. 5.21. Estimates of $D_L/D_0$ are calculated according to Eq. 5.19, though the use of Eq. 5.18 would provide similar results. By plotting the data in this manner, the implicit volume fraction dependence is removed allowing for direct comparison of HS and SALR systems. The well-known structure of HS fluids, and its corresponding influence on diffusivity and viscosity, can be used to rationalize the trends in lysozyme data.

In the case of HS fluids, homogeneous caging of individual particles (repulsive glasses) has relatively little influence on short-time mobility for relatively low concentrations, as particles are allowed to locally diffuse within their cages. However, the cages themselves are unable to rearrange and therefore long-time motion is restricted and zero shear viscosity diverges. As a result, the HS correlation $\eta_{r0}$–$D_S$ diverges at a relatively large value of $D_S/D_0$ while the correlation $\eta_{r0}$–$D_L$ follows a power law of

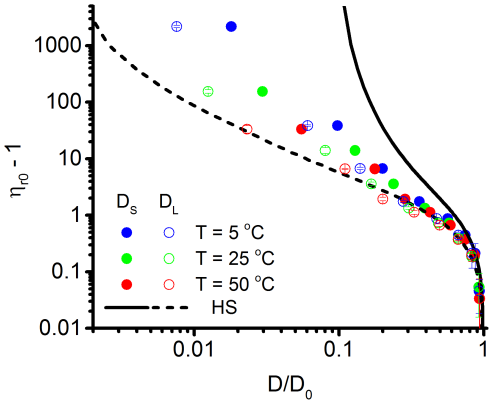


**Figure 5.21:** (a) The specific viscosity of lysozyme is plotted as a function of short-time (filled symbols) and long-time (open symbols) self diffusivity, relative to calculations for HS fluids (solid and dotted lines, respectively). The inset provides examples of fits to the ISF. (b) Structure factors are plotted for several state points, indicating the formation of IRO peaks.

order $\sim 1$ before appearing to diverge at very small $D_L/D_0$.

Most notable from Fig. 5.21 may be the lack of a divergence in the lysozyme zero shear viscosity with respect to diffusivity. For nearly all solution conditions, lysozyme $D_S/D_0$ is slower than that of a HS fluid with an equivalent viscosity. Interestingly, high temperature and most low volume fraction lysozyme data appear to follow the HS expectations of viscosity as a function of $D_L$. However, the long-time mobility in the highly viscous lysozyme states is actually faster than that of a HS system with an equivalent viscosity. This indicates that the microstructure resulting from SALR interactions is more conducive to large scale structural rearrangement. Recalling from Fig. 5.7 the structure factors of these state points, the same solution conditions at which lysozyme $D_S$ is slower than a HS fluid and $D_L$ is faster are those that have the most prominent IRO peaks in $S(q)$.

A physical interpretation of these results is that the balance of competing interactions localizes particles into clusters that then diffuse collectively with reduced mobility (ignoring possible IRO and inter-cluster interactions). Though these clusters

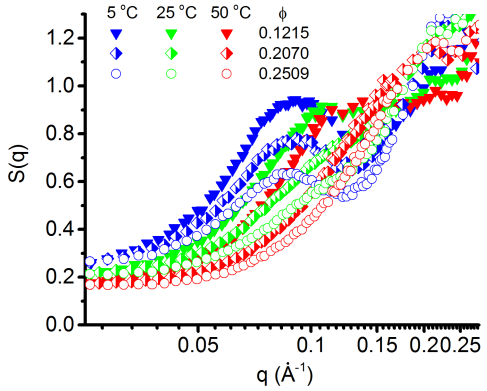


**Figure 5.22:** Structure factors are plotted for samples with volume fractions $\phi = 0.1215$ (triangles), $\phi = 0.2070$ (diamonds) and $\phi = 0.2509$ (circles) at $T = 5°C$ (blue), $T = 25°C$ (green) and $T = 50°C$ (red) to highlight shifts in the IRO peak magnitude.

maintain a lifetime of at least 50 ns, they are expected to remain dynamic in nature over longer timescales. Thus, it is hypothesized that the lower resistance to shear flow in SALR systems relative to HS fluids with an equivalent short-time self diffusivity arises from heterogeneous particle localization that opens sufficient free volume for clusters to rearrange or fragment. Such a microstructure contains a diverse landscape of local environments that will influence the mobility of individual particles and clusters in a non-trivial way.

This heterogeneous local density distribution was examined through the solution structure factor. The formation of IRO peaks in $S(q)$, shown in Fig. 5.22, indicates a unique localization of proteins that can be used to rationalize the dynamics observed in Fig. 5.21. While the length scale of the IRO peak is usually associated with distances between locally dense regions, this is conceptually consistent with an excluded region separating them. An IRO peak is observed at $5°C$ for all volume fractions studied, which is consistent with the increased viscosity at this temperature. A decrease in the IRO peak intensity at high temperatures indicates the loss of intermediate range order, causing the system to become more uniformly distributed over this length scale and

resulting in the decrease of the viscosity. Eventually at high enough temperature, the system becomes dominated by the long range repulsion and attractive forces are insufficient to induce intermediate range particle localization, represented by the transition from a peak to a weak shoulder that then disappears. Therefore, for a given volume fraction, the evolution of a peak with decreasing temperature demonstrates a preference for strong particle localization that significantly reduces the short-time mobility. Simultaneously, IRO introduces void space available to proteins, making the exchange between the local environments of a cluster with reduced short-time mobility and a monomer in an excluded region with enhanced long-time diffusivity.

Interestingly, as clusters become more abundant with increasing volume fraction their structural arrangement appears to become weaker. Though the distribution of cluster sizes shifts to larger clusters with increasing volume fraction, they will eventually merge and form large dynamic networks as shown in Fig. 5.9. As a result, individual clusters are no longer distinguishable. Therefore, a weaker peak can be interpreted as a reduction in the presence of voids in the microstructure, which remain roughly constant in size according to the constant position of the IRO peak. The resulting viscosity could possibly be explained by the dynamic nature of the stress bearing network structure and inter-cluster interactions.

To provide further context for the observed viscosity, all lysozyme states are plotted relative to the adhesive hard sphere (AHS) phase behavior in Fig. 5.23. The previous chapter demonstrated the relation between a system with SALR interaction and a reference system with only the attractive portion of the interaction.[38] Hence, the lysozyme interaction potentials are used to locate the state points within the generalized state diagram. Effective strengths of attraction are represented by the Baxter paremeter $\tau_B = 1/4(1 - B_2)$, where $B_2$ is the second virial coefficient.[10] Values of $\tau_B$ are determined from the attractive portion of the full HSDY potential extracted from fits to the SANS data. Using a potential with $2\alpha - \alpha$ Leonard-Jones attraction and Yukawa repulsion as done previously[21, 23, 84] would provide nearly identical results according to the Noro-Frenkel extended law of corresponding states.[62] Also note that

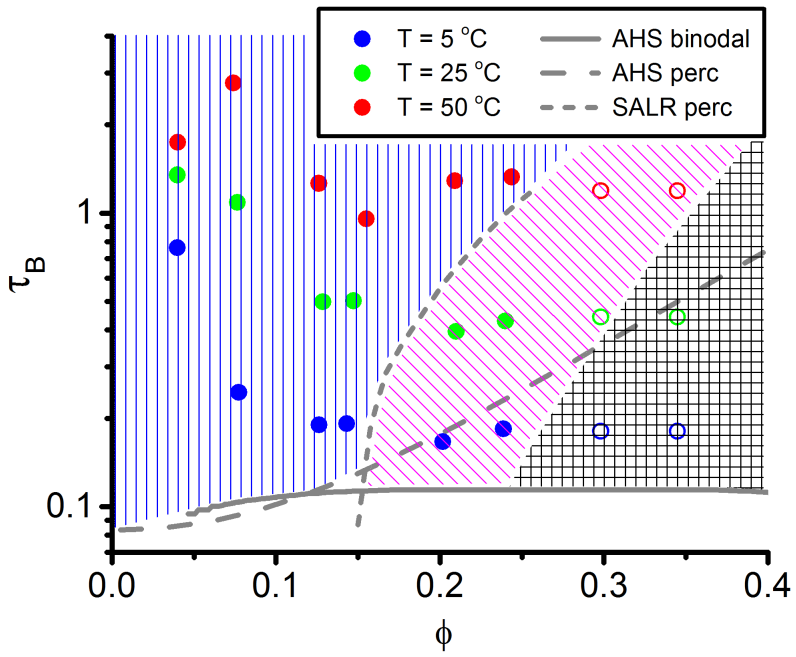


**Figure 5.23:** Lysozyme state points are plotted on the AHS phase diagram (open symbols represent estimates of $\tau_B$ for state points that could not be fit by IET) along with the percolation transition of an SALR system with repulsion representative of lysozyme interactions (gray dotted line). Shaded regions represent dispersed fluids (blue vertical), random percolated (magenta diagonal) and a new local glassy state determined from MSD data (black criss-cross).

due to the inability of IET to converge when fitting the SANS spectra of the two most concentrated samples, represented by open symbols in Fig. 5.23, the $\tau_B$ values of these states are calculated as the average of those at $0.1 < \phi < 0.25$, which appear to have reached an asymptotic value at each temperature.

Every lysozyme state point in Fig. 5.23 lies above the reference binodal, indicating from previous simulation studies that under no condition does a preferred cluster size form in this SALR system.[38] However, state points at high volume fractions are in the random percolated region,[38] which agrees very well with the percolation transition determined by previous simulation studies.[90] In addition to the thermodynamic SALR phase diagram, an additional region of localized glassy dynamics is added, which was determined from the lysozyme states with MSDs below previously reported glassy behavior[47]

While certain attractive systems gel at the estimated percolation line,[29, 91] lysozyme surpasses this transition with no noticeable divergence in the viscosity as a function of diffusivity or volume fraction. In fact, the viscosity of these states remains Newtonian. In contrast, the glassy region in Fig. 5.23 exists at larger volume fractions than the percolation transition. However, in all likelihood, the dynamic nature of individual clusters persists when large percolated networks form. Depending on the structure of the network, a large fraction of particles may sit on the surface, which would accommodate easier particle exchange. However, if the percolated network becomes more robust, particles could become trapped within the interior of the percolated cluster, which could be one possible physical mechanism for the sub-diffusive motion observed in the MSD of high volume fraction solutions at low temperature.

## 5.6 Testing the Representation of Lysozyme Viscosity by Colloidal Models

Previous work using BSA suggests that colloidal viscosity models are unable to accurately capture the dependence of globular protein viscosity on various solution conditions such as temperature and volume fraction.[72] However, by a colloidal model this work was referring only to HS representations, which ignored the influence of

protein interactions. The experiments discussed thus far in this chapter provide strong evidence that complex inter-protein interactions are prevalent at all solution conditions and therefore must be accounted for to accurately represent the subsequent viscosity of these materials. Therefore, the lysozyme viscosity is tested in this section against viscosity models of HS fluids as well as weakly attractive systems to demonstrate the general applicability of colloidal models and that the incorporation of interactions more appropriately represents trends in the solution viscosity. However, the functional form of these specific models are still shown to be quantitatively inaccurate.

Figure 5.24 below compares the trends in zero shear viscosity for the (a) dry and (b) hydrated definitions of protein volume fraction. The data shift along the x-axis depending on the definition. Multiple functional forms of HS viscosity are used to try and reproduce both representations of the lysozyme viscosity. In particular, the Eilers equation,

$$\eta_{r0} = \left(1 + \frac{1.5\phi}{1 - \phi/\phi_{max}}\right)^2, \tag{5.21}$$

the Maron-Pierce equation,

$$\eta_{r0} = (1 - \phi/\phi_{max})^{-2}, \tag{5.22}$$

and the Mooney equation,

$$\eta_{r0} = \exp\left(\frac{[\eta]\phi}{1 - \phi/\phi_{max}}\right), \tag{5.23}$$

where $[\eta]$ is the intrinsic viscosity and $\phi_{max}$ is the volume fraction where the viscosity diverges,[55] are fit to the lysozyme data by allowing $\phi_{max}$ to vary.

Every function failed to capture the trends in viscosity with both temperature and volume fraction. Only the volume fraction dependence of the $50°C$ data using the dry volume fraction definition was relatively accurately represented, which was accomplished using the Eilers equation. All other data sets were poorly fit by significantly overestimating the low to intermediate volume fraction regime. The cause of the poor fits stem from the derivation of each of these models, which were designed to accurately represent the divergent behavior at high-$\phi$. A common feature of each

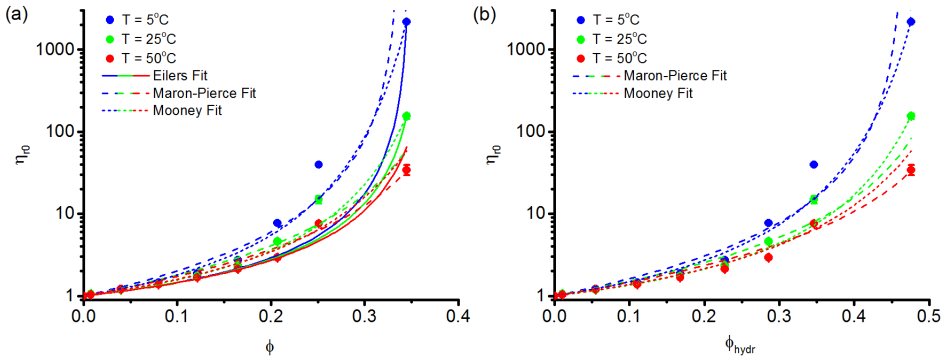


**Figure 5.24:** Lysozyme zero-shear vicsosity (symbols) is plotted for three temperatures as a function of volume fraction according to (a) the dry definition and (b) the hydrated definition. Best fits of HS estimates using the Eilers (solid line), Maron-Pierce (dashed line) and Mooney (dotted lines) equations are also provided.

function is a reciprocal dependence on $\phi/\phi_{max}$, which is an empirical representation of the viscosity divergence due to caging. Practically, this lumps all contributions to the viscosity into one parameter. However, Fig. 5.18 indicated that interactions are a significant influence on lysozyme viscosity and Fig. 5.21 suggests that its viscosity is not a result of jamming due to the lack of divergence with diffusivity. Therefore, the poor representation of lysozyme solution viscosity by these HS models is to be expected.

That the lysozyme viscosity at high temperature, where inter-protein interactions are the weakest, could be represented by a HS model with a shifted value of $\phi_{max}$ suggests that colloidal models possess some practical value. As a first order approximation of the influence of the interactions extracted from the SANS data, the viscosity at lower temperatures could be fit with a perturbation to these HS estimates. Unfortunately, no viscosity models of SALR systems have been previously developed, so for now a model accounting for weak attractive interactions is tested in Fig. 5.25. The so called KW model has a functional dependence on $\phi$ and $\tau_B$ according to[48]

$$\eta_{r0}^{KW} = \eta_{r0}^{HS}\left(1 + \frac{1.9\phi^2}{\tau_B}\right), \tag{5.24}$$

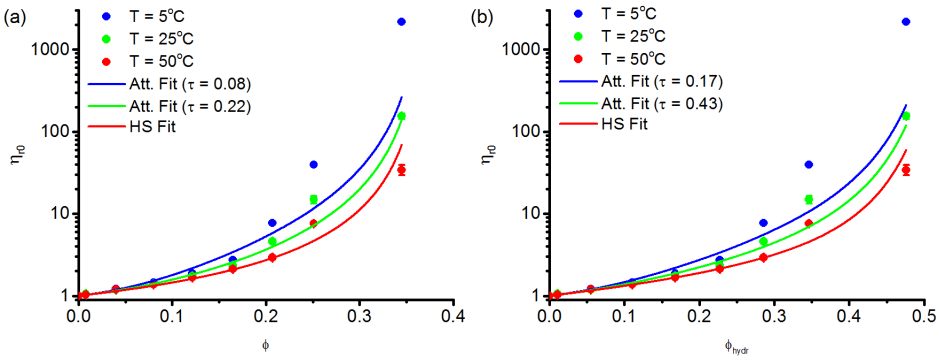


**Figure 5.25:** Lysozyme zero-shear vicsosity (symbols) is plotted for three temperatures as a function of volume fraction according to (a) the dry definition and (b) the hydrated definition. Best fits using the KW attractive model (lines) are provided using a single value of $\tau_B$ for a given temperature provided in the legend, where HS indicates $\tau_B = \infty$.

where the HS viscosity, $\eta_{r0}^{HS}$, represents the data at $50°C$ using the $\phi_{dry}$ definition by the Eilers equation with a $\phi_{max}$ of 0.391 and the data at $50°C$ using the $\phi_{hydr}$ definition by the RWM-MCT model with a $\phi_{max}$ of 0.531. According to both volume fraction definitions, the attractive term captures the low to intermediate volume fraction trend at $25°C$ quite well. Under these conditions, the attractive forces are still relatively weak, so cluster formation is not prevalent. However, for samples at high-$\phi$ and $5°C$ where this is no longer true, accounting for attraction alone is insufficient to reproduce the lysozyme viscosity. Still, the ability of colloidal viscosity models to qualitatively and in some cases quantitatively reproduce the experimental data further supports their utility, even for globular protein solutions.

While Fig. 5.25 demonstrates that an effective attraction strength can be extracted from fitting the viscosity, interaction parameters have already been quantified from SANS experiments. Since the lysozyme viscosity is a result of competing forces, the relative contribution from the attractive component can be estimated using values of $\tau_B$ calculated from the extracted interaction potentials. In fact, this procedure can be performed for both the reduction in short-time self diffusion as well as the increase

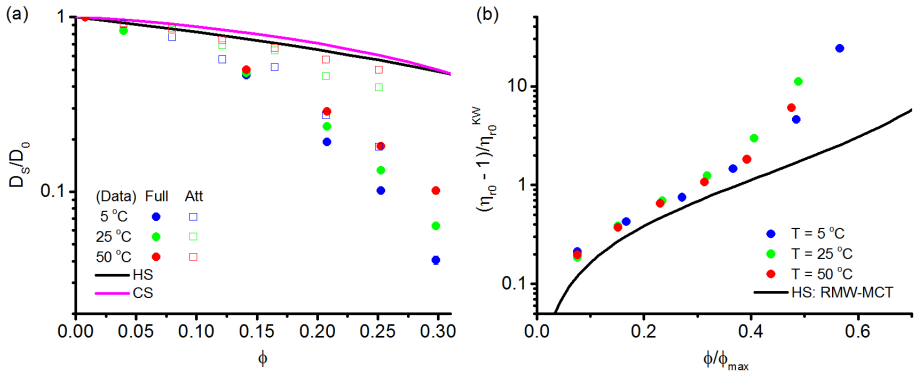


**Figure 5.26:** (a) Experimental lysozyme diffusivity ("Full") is plotted relative to HS (black line) and CS (pink line) trends and estimates using the KW attractive model ("Att") with values of $\tau_B$ extracted from fits to SANS data. (b) Lysozyme viscosity data are normalized according to a weakly attractive model (symbols) and plotted relative to HS expectations (line), which should be identical if the viscosity was driven purely by attractive forces.

in zero-shear viscosity. The short-time self diffusivity in weakly attractive systems has been modeled by[27]

$$\frac{D_S}{D_0} = 1 - \left(1.8315 + \frac{0.295}{\tau_B}\right)\phi. \tag{5.25}$$

Further, the viscosity will be estimated using the KW model with the HS component represented by the RWM-MCT model with $\phi_{max} = 0.57$ as the model was originally developed. Values of $\tau_B$ will be taken from Table 5.2.

In Fig. 5.26 lysozyme data are plotted relative to estimates of the diffusion[27] and viscosity[48] if only the attractive portion of the full HSDY potential were present in solution. The attractive diffusion model provides the correct qualitative trend in both volume fraction and temperature observed for lysozyme. The similarity of the data and the model suggest that the attractive component of the interactions might be the dominant contribution to particle mobility and viscosity. However, as may be expected, the mobility in SALR systems is not an average of the estimated individual contributions from attraction and repulsion and therefore the lysozyme diffusion falls below the model estimates in Fig. 5.26a. Rather, the competing interactions have a

synergistic effect, which structurally is manifested as the formation of dynamic clusters under certain conditions. At low temperature, where clusters are qualitatively more abundant, the estimated diffusion arising from attractions alone becomes close in magnitude to experimental observations of an SALR system. The similarity suggests that attraction is a strong driving force to the formation of clusters, but particle localization and structural heterogeneity in the form of cluster formation is necessary to produce the significant reduction in mobility found in lysozyme. Further, normalizing the viscosity by the expected effect of attractive interactions in Fig. 5.26b does not reduce the experimental data to HS estimates. The magnitude of the residual difference between the data and HS line is a direct result of the additional repulsive forces. The significant increase at elevated volume fraction is then an indication of enhanced contributions due to cooperative effects of the competing interactions.

The influence of competing interactions on the viscosity appears to grow with increasing volume fraction in Fig. 5.26. Interestingly, the temperature dependence of the viscosity disappears when explicitly accounting for the different strengths of attraction. Therefore, a stronger repulsive contribution should account for the growth in viscosity. However, Fig. 5.8 indicates that monomer-monomer repulsion decreases at each temperature with increasing protein concentration. Therefore, additional repulsive forces, or some synergistic effect of the competing interactions that is not being considered, may account for the discrepancy in Fig. 5.26. By normalizing the experimental data according to the viscosity model developed in the Appendix, the dominant contribution to the lysozyme viscosity can be distinguished as a function of solution conditions.

The relative contribution of attractive and repulsive forces can be quantified by normalizing the experimental viscosity by theoretical hydrodynamic contributions and experimentally determined values of the structure and dynamics. As a result, the remaining contributions arise solely from the interaction potential according to $\eta_{eff}^{B+P} = (4/3)\big[1 - 2\int_1^\infty dU(r)/dr g(r)/g(2)dr\big]$, where the term in square brackets is simply one for a HS fluid. The sign of the derivative of the potential will indicate the

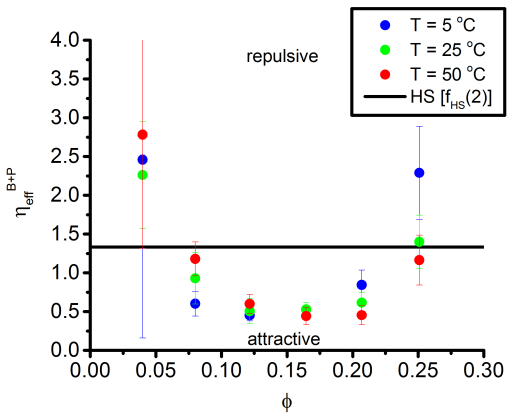


**Figure 5.27:** Combined contributions to the viscosity from the Brownian and Interaction terms determined from experimental results (symbols) are plotted relative to the HS estimate (line). Deviations above the HS line are indicative of predominantly repulsive contributions to increases in viscosity while points below the HS line represent attractive driven enhancements to the viscosity.

dominant form of interaction. Accordingly, attraction dominated solution conditions should lie below the HS value, while repulsion dominated states are above. Lysozyme state points are plotted in Fig. 5.27 for three temperatures, which interestingly show a similar but more dramatic transition as observed in Fig. 5.18.

Clearly, the dominant contribution to the solution viscosity shifts from attraction at small volume fractions to repulsion at large volume fractions. Such a transition from attractive to repulsive behavior is characteristic of clustering systems, which rely on attraction to drive aggregation until sufficient repulsion exists between clusters to prevent further growth.[74] Theoretically, the resulting clusters should become more abundant and increase in size with increasing volume fraction. Given that clusters interact with each other in a purely repulsive manner,[57, 75] they will introduce an additional contribution to the viscosity. This trend serves as a strong motivation for including effective inter-cluster interactions in estimating the solution viscosity of SALR systems.

Models of colloidal viscosity, including that developed here, indicate that the

additional contributions will arise from inter-particle interactions. SALR interactions have been demonstrated to localize particles, which in the extreme case results in IRO and clustered fluids. Lysozyme states far above HS estimates in Fig. 5.17d have significant IRO peaks that indicate sufficient void space exists between locally dense regions.[37] Therefore, as opposed to a jamming transition observed in HS systems, lysozyme viscosity is likely a result of cluster interactions and dynamics. Such a microstructure contains a diverse landscape of local environments that will influence the mobility of individual particles and clusters in a non-trivial way. Therefore, the structural and dynamic information in hand from SANS and NSE experiments will be used to rationalize representing this microstructure with effective cluster forces in order to semi-quantitatively estimate their contributions to the viscosity.

## 5.7 Viscosity Predictions

At this point in the chapter, several key signatures of cluster formation in lysozyme solutions have been observed using techniques that probe both structural and dynamic properties. Therefore, it is well established that clusters can be formed by lysozyme proteins and, under the appropriate conditions, will play a dominating role in the resulting solution viscosity. As a means of quantifying those contributions, a model accounting for contributions from cluster formations and interactions to the diffusivity and viscosity has been developed in the Appendix.

The first test of this model will utilize the trends in interaction and diffusion parameters with temperature and volume fraction shown in Fig. 5.10 and Fig. 5.15, respectively, to extract an effective experimental measure of the average cluster size in equilibrium with monomers. Specifically, from the three dynamic parameters in Fig. 5.15, three properties of clusters can be calculated at each $T$ and $\phi$: the fraction of particles in clusters, $X_{clus}$, the average fractal dimension of the clusters formed, $d_f$, and the average cluster size, $N$. As described in the Appendix, $X_C$ in Fig. 5.15 is a weighted function of the extent of cluster formation and therefore $X_C \neq X_{clus}$. Further, the hydrodynamic radius of a cluster of size $N$ is sensitive to the fractal dimension, which

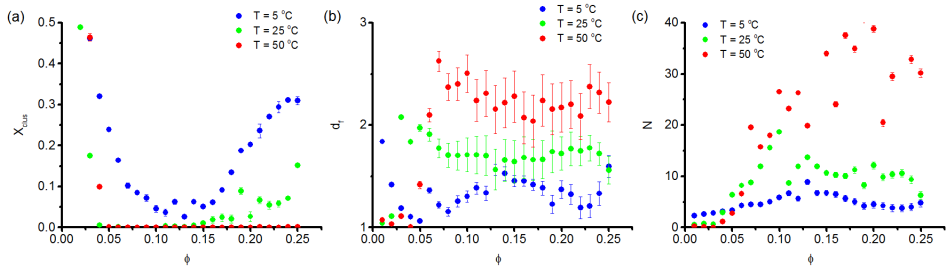


**Figure 5.28:** Values of (a) $X_{clus}$, (b) $D_{mon}$ and (c) $D_{clus}$ determined from simultaneously fitting the diffusivity parameters using the double exponential model fits to NSE data (discussed in the main text) are plotted for $T = 5°C$ (blue), $T = 25°C$ (green) and $T = 50°C$ (red).

makes it necessary to determine its value. Subsequent calculations of the viscosity due to these clusters require each of these parameters since the abundance and size of clusters dictates the relative contribution of monomer-monomer, monomer-cluster, and cluster-cluster interactions.

The results of fitting the NSE parameters extracted from a double exponential fit to the ISF with the cluster dynamics model in the Appendix are shown in Fig. 5.28. One of the first observations is a distinct temperature dependence of the population of clusters at large volume fractions. At $5°C$, clusters start to form at lower volume fractions and grow larger in size at the same $\phi$ compared to higher temperatures. Although the fraction of particles in clusters appears large at small $\phi$, the experimental values of $X_C$ are very small here and thus the extracted values of $X_{clus}$ are expected to be unreliable. Regardless, the average cluster size determined at low volume fractions is essentially zero. In contrast to $X_{clus}$, $N$ is larger with higher temperature. However, this is again a manifestation of the statistical uncertainty of these inter-related parameters. At $50°C$, no clusters appear to form and therefore the cluster size extracted from the model is irrelevant. Clusters do appear to be present at the highest volume fractions at both $5°C$ and $25°C$, and become more abundant with decreasing temperature. Interestingly, effective cluster radii, where $R \propto N^{d_f}$, are similar at each temperature, but have a more compact configuration of more particles (larger $d_f$ and

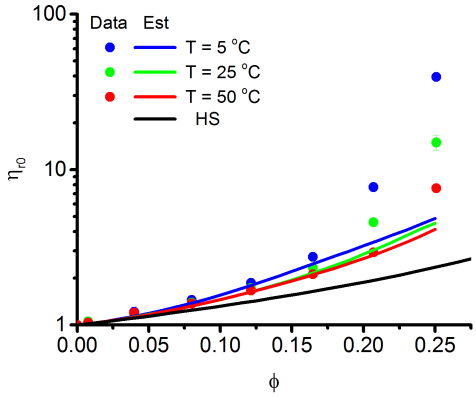


**Figure 5.29:** Lysozyme viscosity data (symbols) are compared to estimates using the viscosity model (colored lines) developed in the Appendix by estimating cluster sizes using diffusion data as well as HS estimates (black line).

$N$, respectively) at higher temperature. Only by implementing these values in the cluster interaction model can their synergistic influence on the viscosity be quantified.

By obtaining an estimate of the effective cluster size in solution from dynamic experiments, the viscosity model of SALR systems with additional cluster contributions can be utilized in a completely predictive manner. Shown in Fig. 5.29 are the estimates using the novel model developed in the Appendix (lines) compared with the lysozyme viscosity determined from capillary viscometry (symbols). The model clearly underestimates the lysozyme viscosity at higher volume fractions, but are actually quite accurate for $\phi < 0.15$ at all three temperatures. Further, in defense of this model, the point at which it becomes inaccurate corresponds with the percolation transition of lysozyme states, as determined from the cluster size distributions obtained by MC simulations in Fig. 5.9 and shown in the phase diagram in Fig. 5.23. Thus, under the conditions at which individual clusters can be distinguished, the SALR viscosity model appears to capture, at least semi-quantitatively, the contribution of SALR interactions and subsequent cluster formation on the viscosity in lysozyme solutions.

If additional contributions to the stress dissipation by propagation through the

dynamic network could be accounted for, the viscosity may be more accurately reproduced at higher volume fractions (above the percolation transition). Interestingly, as discussed previously, despite lysozyme samples becoming percolated they remain fluid and Newtonian. Therefore, the stochastic cluster size distribution obtained by MC simulations may not be the most representative measure of the clusters responsible for the increase in viscosity. Rather, quantifying a so-called "dynamic" cluster size distribution may be worth the attention of future work. In the next and final section, a first order attempt at identifying the dominant dynamic cluster size at all volume fractions will simultaneously fit the dynamics and the viscosity as a means of comprehensively capturing the underlying stresses producing the viscosity in lysozyme samples.

## 5.8 Effective Cluster Properties from a New SALR Viscosity Model

The full cluster diffusion/viscosity model developed in the Appendix is fit simultaneously to the diffusion and viscosity data over a range of concentrations at three temperatures. A powerful aspect of this model is that the fitting parameters are constrained by two sets of data, which are uniquely sensitive to cluster formation, ensuring that the extracted values are robust. The two fit parameters are the fraction of particles in clusters and the average cluster size, as used in the previous section, while the fractal dimension is held constant. However, $d_f$ can be used to tailor the model's accuracy. As part of the fitting, a monomer and cluster diffusion coefficient are weighted to calculate an effective diffusion coefficient to be fit to the values of $D_S/D_0$ in Fig. 5.13a. The diffusivity obtained from the single exponential fits to the ISF is used rather than $D_{mon}$ and $D_{clus}$ from the double exponential fit for two reasons. One, fitting two parameters instead of three was found to greatly enhance the statistics of the resulting fit parameters and, two, it was less restrictive of the possible cluster sizes extracted from the model.

The fits to the experimental data at each temperature were optimized by using a $d_f$ of 1.6, which agrees well with the results determined in the previous section at $5°C$ and $25°C$ in Fig. 5.29. This result is also consistent with previous simulation

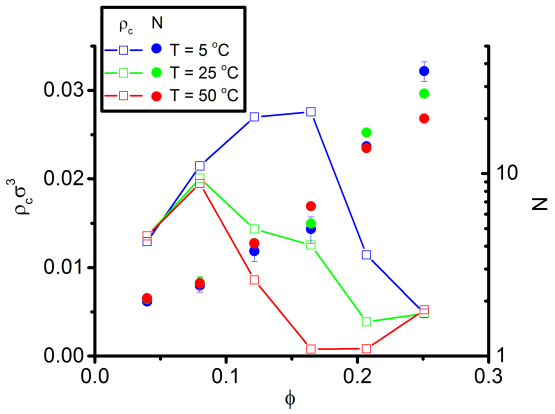


**Figure 5.30:** Values extracted from simultaneous fits to effective diffusion coefficients and viscosities of lysozyme are plotted as a function of $\phi$ for the density of clusters (lines and open squares), $\rho_c$, and cluster size (filled circles), $N$.

studies of SALR systems.[90] Further, while both the monomer and cluster diffusion contribute to the resulting effective short-time diffusion coefficient, the fitted value is nearly entirely weighted by the cluster diffusion over most of the solution conditions.

Extracted cluster properties are plotted in Fig. 5.30 as a function of protein volume fraction and temperature. Rather than comparing the fraction of particles in clusters with the average cluster size, the number density of clusters, $\rho_c$, is calculated according to $\rho_c\sigma^3 = 6X_{clus}\phi/(\pi N)$, which is the relevant parameter representing the density of interacting units within the microstructure. In contrast to the analysis in the previous section, the diffusion–viscosity model indicates that the average cluster size increases relatively significantly with volume fraction. Further, the average size is essentially independent of temperature for all volume fractions until the largest concentration studied, at which point the size is inversely proportional to temperature. At low volume fractions, cluster sizes are only roughly the size of a dimer and thus cluster formation is negligible at all temperatures. However, at intermediate volume fractions, the relative population of clusters is sensitive to the temperature. Lower temperature states have a larger concentration of clusters in solution. These clusters

and the remaining monomers then localize on intermediate lengthscales, as suggested by Fig. 5.22, which further contributes to larger viscosities. At the highest volume fractions, the cluster density becomes identical for all temperatures, but this is compensated for by an increase in the average cluster size at lower temperatures. These two parameters in conjunction produce the resulting reduced diffusion and enhanced viscosity.

It is important to keep in mind that at elevated volume fractions ($\phi \geq 0.15$), these state points are percolated. Therefore, the values of $N$ in Fig. 5.30 can be associated with an average size of clusters of which the transient networks are composed under these conditions. If the shear thinning regime estimated in Table 5.3 could be reached, it would be very interesting to compare the extracted structural lengthscale with the cluster size determined from these fitting results. However, for the time being, it is hypothesized that the fluid-like rheological response to shear by lysozyme solutions with percolated structures is predominantly caused by this transient network structure fragmenting into dynamic clusters of size $N$ (as defined here) that subsequently interact, both repulsively due to their stable size and attractively due to SALR interactions that lead to re-association into the transient network.

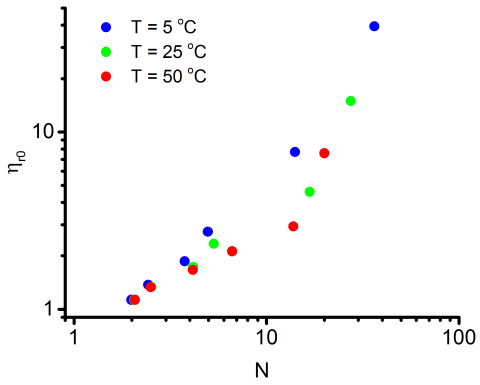


**Figure 5.31:** Zero-shear viscosity is plotted as a function of the estimated cluster size for three temperatures, indicating an apparent lack of universal relationship between these two parameters.

An additional useful result of this model is the evident lack of a universal correlation between cluster formation and viscosity. Figure 5.31 demonstrates the relationship between viscosity and the average cluster size for each solution condition studied. Although the strength of repulsive interactions at lower temperatures is weaker, the fact that clusters are larger and/or more abundant produces more significant contributions to the viscosity form inter-cluster interactions. As a result, the low temperature states have a larger viscosity at a given average cluster size. The main cause for the differences in temperature likely arises from the implicit cluster density shown in Fig. 5.30. Although clusters are less abundant at higher temperatures, their relatively strong inter-cluster repulsions are capable of more significantly reducing diffusivity at an equivalent cluster size and producing drastically increased viscosities. Therefore, the solution viscosity is very sensitive to the balance of competing interactions in SALR systems.

## 5.9 Conclusions

In conclusion, the work presented here has made significant progress in providing accurate measurements of viscosity and short-time self diffusivity over a large range of concentrations and temperatures, as well as its phase transitions to localized glassy states. The significant set of results presented in this chapter provides a cohesive representation of the impact of intermediate range order on the dynamics and viscosity in systems with short-range attraction and long-range repulsion. The existence of IRO introduces localized heterogeneous density distributions at the length scale comparable to that extracted from the IRO peak position. While the system is relatively uniform over longer length scales, the locally large packing fraction of proteins leads to glassy localized motion on the scale of the protein. Despite the significantly slow local motion, the void space associated with the IRO enables diffusive motion at long time scales that keep the samples in a fluid state. This heterogeneity is a unique distinguishing feature of kinetic arrest in SALR systems relative to purely attractive driven arrested states. The experimental evidence shown here highlights the importance of both structure

and dynamics in understanding the properties of these complex fluids with competing potential features. Specifically, models for the macroscopic transport properties of such protein solutions will need to explicitly consider the dynamics and structure corresponding to the intermediate range order evident in the scattering patterns.

This chapter also presented a colloidal model to capture the diffusion and viscosity of systems with SALR interactions. While this model is applicable to any SALR system, it is particularly useful for its adaptability to include the additional interactions present in states with significant cluster formation. The results presented here are the first to demonstrate a semi-quantitative relationship between clustering and viscosity in systems with competing interactions, highlighting the importance of cluster dynamics and cluster-cluster interactions. By decomposing the various contributions, the relative importance of each form of interaction on the resulting solution viscosity can be quantified. This methodology provides a framework for using viscosity measurements as a sensitive tool to determine the presence of clusters in solution. The remaining chapters will be dedicated to applying the framework developed here to industrially relevant monoclonal antibody solutions and making necessary alterations to capture the additional complexities associated with their anisotropic shape and interactions.

## REFERENCES


[1] Abramo, M. C., Caccamo, C., Costa, D., Pellicane, G., Ruberto, R., and Wanderlingh, U. Effective interactions in lysozyme aqueous solutions: a small-angle neutron scattering and computer simulation study. *J. Chem. Phys. 136*, 3 (Jan. 2012), 035103.

[2] Allen, M. P., and Tildesley, D. J. *Computer Simulation of Liquids*. Oxford University Press, 1987.

[3] Allison, S. A., and Tran, V. T. Modeling the electrophoresis of rigid polyions: application to lysozyme. *Biophys. J. 68*, 6 (June 1995), 2261–70.

[4] Bahar, I., Erman, B., Fytas, G., and Steffen, W. Intramolecular Contributions to Stretched-Exponential Relaxation Behavior in Polymers. *Macromolecules 27*, 18 (1994), 5200–5205.

[5] Banchio, A. J., Bergenholtz, J., and Nägele, G. Rheology and Dynamics of Colloidal Suspensions. *Phys. Rev. Lett. 82*, 8 (Feb. 1999), 1792–1795.

[6] Banchio, A. J., McPhie, M. G., and Nägele, G. Hydrodynamic and electrokinetic effects on the dynamics of charged colloids and macromolecules. *J. Phys. Condens. Matter 20*, 40 (Oct. 2008), 404213.

[7] Banchio, A. J., and Nägele, G. Short-time transport properties in dense suspensions: from neutral to charge-stabilized colloidal spheres. *J. Chem. Phys. 128*, 10 (Mar. 2008), 104903.

[8] Banchio, A. J., Nagele, G., and Bergenholtz, J. Viscoelasticity and generalized StokesEinstein relations of colloidal dispersions. *J. Chem. Phys. 111*, 18 (1999), 8721.

[9] Banchio, A. J., Nagele, G., and Bergenholtz, J. Collective diffusion, self-diffusion and freezing criteria of colloidal suspensions. *J. Chem. Phys. 113*, 8 (2000), 3381.

[10] Baxter, R. J. PercusYevick Equation for Hard Spheres with Surface Adhesion. *J. Chem. Phys. 49*, 6 (1968), 2770.

[11] Belloni, L. Colloidal interactions. *J. Phys. Condens. Matter 12*, 46 (2000), R549.

[12] Bergenholtz, J., and Wagner, N. J. Self-diffusion in dispersions of charged colloidal spheres by generalized hydrodynamics. *Physica A 235*, 1-2 (Jan. 1997), 34–47.

[13] Biehl, R., Monkenbusch, M., and Richter, D. Exploring internal protein dynamics by neutron spin echo spectroscopy. *Soft Matter 7* (2011), 1299.

[14] Blake, C. C. F., Mair, G. A., North, A. C. T., Phillips, D. C., and Sarma, V. R. On the Conformation of the Hen Egg-White Lysozyme Molecule. *Proc. R. Soc. London, Ser. B, Biol. Sci. 167*, 1009 (1967), 365.

[15] Boncina, M., Rescic, J., and Vlachy, V. Solubility of lysozyme in polyethylene glycol-electrolyte mixtures: the depletion interaction and ion-specific effects. *Biophys. J. 95*, 3 (Aug. 2008), 1285–94.

[16] Brady, J. F. The rheological behavior of concentrated colloidal dispersions. *J. Chem. Phys. 99*, 1 (1993), 567.

[17] Broide, M. L., Tominc, T. M., and Saxowsky, M. D. Using phase transitions to investigate the effect of salts on protein interactions. *Phys. Rev. E 53*, 6 (June 1996), 6325.

[18] Bu, Z., Biehl, R., Monkenbusch, M., Richter, D., and Callaway, D. J. E. Coupled protein domain motion in Taq polymerase revealed by neutron spin-echo spectroscopy. *Proc. Natl. Acad. Sci. U. S. A. 102* (2005), 17646–17651.

[19] Campbell, A., Anderson, V., van Duijneveldt, J. S., and Bartlett, P. Dynamical Arrest in Attractive Colloids: The Effect of Long-Range Repulsion. *Phys. Rev. Lett. 94*, 20 (May 2005), 1.

[20] Canfield, R. E. the Amino Acid Sequence of Egg White Lysozyme. *J. Biol. Chem. 238*, 8 (Aug. 1963), 2698–2707.

[21] Cardinaux, F., Gibaud, T., Stradner, A., and Schurtenberger, P. Interplay between Spinodal Decomposition and Glass Formation in Proteins Exhibiting Short-Range Attractions. *Phys. Rev. Lett. 99*, 11 (Sept. 2007), 1–4.

[22] Cardinaux, F., Stradner, A., Schurtenberger, P., Sciortino, F., and Zaccarelli, E. Modeling equilibrium clusters in lysozyme solutions. *Europhys. Lett. 77*, 4 (Feb. 2007), 48004.

[23] Cardinaux, F., Zaccarelli, E., Stradner, A., Bucciarelli, S., Farago, B., Egelhaaf, S. U., Sciortino, F., and Schurtenberger, P. Cluster-Driven Dynamical Arrest in Concentrated Lysozyme Solutions. *J. Phys. Chem. B 115*, 22 (June 2011), 7227.

[24] Castellanos, M. M., Pathak, J. a., and Colby, R. H. Both protein adsorption and aggregation contribute to shear yielding and viscosity increase in protein solutions. *Soft Matter 10*, 1 (2014), 122.

[25] Chen, S.-H. Small angle neutron scattering studies of the structure and interaction in micellar and microemulsion systems. *Annu. Rev. Phys. Chem. 37* (1986), 351–399.

[26] Chen, S.-H., Broccio, M., Liu, Y., Fratini, E., and Baglioni, P. The two-Yukawa model and its applications: the cases of charged proteins and copolymer micellar solutions. *J. Appl. Crystallogr. 40*, s1 (Apr. 2007), s321–s326.

[27] Cichocki, B., and Felderhof, B. U. Diffusion coefficients and effective viscosity of suspensions of sticky hard spheres with hydrodynamic interactions. *J. Chem. Phys. 93*, September (1990), 4427.

[28] Deen, W. M. *Analysis of Transport Phenomena*. Oxford University Press, New York, 1998.

[29] Eberle, A. P. R., Wagner, N. J., and Castañeda Priego, R. Dynamical Arrest Transition in Nanoparticle Dispersions with Short-Range Interactions. *Phys. Rev. Lett. 106*, 10 (Mar. 2011), 1.

[30] Falus, P., Porcar, L., Fratini, E., Chen, W.-R., Faraone, A., Hong, K., Baglioni, P., and Liu, Y. Distinguishing the monomer to cluster phase transition in concentrated lysozyme solutions by studying the temperature dependence of the short-time dynamics. *J. Phys. Condens. Matter 24*, 6 (Feb. 2012), 064114.

[31] Frenkel, D., and Smit, B. *Understanding Molecular Simulations: From Algorithms to Applications*. Academic Press, 2002.

[32] García de la Torre, J. Hydration from hydrodynamics. General considerations and applications of bead modelling to globular proteins. *Biophys. Chem. 93*, 2-3 (Nov. 2001), 159–70.

[33] García de la Torre, J., Huertas, M. L., and Carrasco, B. Calculation of hydrodynamic properties of globular proteins from their atomic-level structure. *Biophys. J. 78*, 2 (Feb. 2000), 719–30.

[34] Gekko, K., and Noguchi, H. Compressibility of globular proteins in water at 25 degree C. *J. Phys. Chem. 83*, 21 (Oct. 1979), 2706.

[35] Gibaud, T., Cardinaux, F., Bergenholtz, J., Stradner, A., and Schurtenberger, P. Phase separation and dynamical arrest for particles interacting with mixed potentialsthe case of globular proteins revisited. *Soft Matter 7*, 3 (2011), 857.

[36] Godfrin, P. D., Castañeda Priego, R., Liu, Y., and Wagner, N. J. Intermediate range order and structure in colloidal dispersions with competing interactions. *J. Chem. Phys. 139*, 15 (2013), 154904.

[37] Godfrin, P. D., Hudson, S. D., Hong, K., Porcar, L., Falus, P., Wagner, N. J., and Liu, Y. Excess viscous response from intrinsic structural heterogeneity caused by competing potential features. *Submitt. to Phys. Rev. Lett.* (2015).

[38] Godfrin, P. D., Valadez-Pérez, N. E., Castañeda Priego, R., Wagner, N. J., and Liu, Y. Generalized phase behavior of cluster formation in colloidal dispersions with competing interactions. *Soft Matter 10* (2014), 5061.

[39] Gögelein, C., Nägele, G., Tuinier, R., Gibaud, T., Stradner, A., and Schurtenberger, P. A simple patchy colloid model for the phase behavior of lysozyme dispersions. *J. Chem. Phys. 129*, 8 (Aug. 2008), 085102.

[40] Gripon, C., Legrand, L., Rosenman, I., Vidal, O., Robert, M., and Boue, F. Lysozyme solubility in H2O and D2O solutions : a simple relationship. *J. Cryst. Growth 177* (1997), 238.

[41] Harris, R. J., Shire, S. J., and Winter, C. Commercial manufacturing scale formulation and analytical characterization of therapeutic recombinant antibodies. *Drug Dev. Res. 61*, 3 (Mar. 2004), 137–154.

[42] Harroun, T., Wignall, G., and Katsaras, J. Neutron Scattering for Biology. In *Neutron Scatt. Biol. Tech. Appl.*, J. Fitter, T. Gutberlet, and J. Katsaras, Eds. Springer, 2006, pp. 1–18.

[43] Hiemenz, P. C., and Rajagopalan, R. *Principles of Colloid and Surface Chemistry*, 3rd editio ed. Taylor & Francis Group, 1997.

[44] Hudson, S. D., Sarangapani, P., Pathak, J. A., and Migler, K. B. A Microliter Capillary Rheometer for Characterization of Protein Solutions. *J. Pharm. Sci.* (2014).

[45] Israelachvili, J. N. *Intermolecular and Surface Forces*, 3rd editio ed. Elsevier, 2011.

[46] Kim, J. M., Castañeda Priego, R., Liu, Y., and Wagner, N. J. On the importance of thermodynamic self-consistency for calculating clusterlike pair correlations in hard-core double Yukawa fluids. *J. Chem. Phys. 134*, 6 (Feb. 2011), 064904.

[47] Klix, C. L., Royall, C. P., and Tanaka, H. Structural and Dynamical Features of Multiple Metastable Glassy States in a Colloidal System with Competing Interactions. *Phys. Rev. Lett. 104*, 16 (Apr. 2010), 165702.

[48] Krishnamurthy, L.-N., and Wagner, N. J. The influence of weak attractive forces on the microstructure and rheology of colloidal dispersions. *J. Rheol. (N. Y. N. Y). 49*, 2 (2005), 475.

[49] Lilyestrom, W. G., Yadav, S., Shire, S. J., and Scherer, T. M. Monoclonal antibody self-association, cluster formation, and rheology at high concentrations. *J. Phys. Chem. B 117*, 21 (May 2013), 6373–84.

[50] Lionberger, R. A., and Russel, W. B. A Smoluchowski theory with simple approximations for hydrodynamic interactions in concentrated dispersions. *J. Rheol. (N. Y. N. Y). 41*, 2 (Mar. 1997), 399.

[51] Liu, Y., Chen, W.-R., and Chen, S.-H. Cluster formation in two-Yukawa fluids. *J. Chem. Phys. 122*, 4 (Jan. 2005), 44507.

[52] Liu, Y., Fratini, E., Baglioni, P., Chen, W.-R., Porcar, L., and Chen, S.-H. Liu et al. Reply. *Phys. Rev. Lett. 96*, 21 (June 2006), 219802.

[53] Liu, Y., Porcar, L., Chen, J., Chen, W.-r., Falus, P., Faraone, A., Fratini, E., Hong, K., and Baglioni, P. Lysozyme protein solution with an intermediate range order structure. *J. Phys. Chem. B 115*, 22 (June 2011), 7238.

[54] Meth, J. S., Zane, S. G., Chi, C., Londono, J. D., Wood, B. A., Cotts, P., Keating, M., Guise, W., and Weigand, S. Development of Filler Structure in Colloidal Silica-Polymer Nanocomposites. *Macromolecules 44* (2011), 8301–8313.

[55] Mewis, J., and Wagner, N. J. *Colloidal Suspension Rheology.* Cambridge University Press, New York, 2012.

[56] Morozova, D., Weiss, M., and Guigas, G. Shape as a determinant of membrane protein cluster formation. *Soft Matter* (2012), 11905–11910.

[57] Mossa, S., Sciortino, F., Tartaglia, P., and Zaccarelli, E. Ground-state clusters for short-range attractive and long-range repulsive potentials. *Langmuir 20*, 24 (2004), 10756–10763.

[58] Mulheran, P., Pellenc, D., Bennett, R., Green, R., and Sperrin, M. Mechanisms and Dynamics of Protein Clustering on a Solid Surface. *Phys. Rev. Lett. 100*, 6 (Feb. 2008), 068102.

[59] Muschol, M., and Rosenberger, F. Liquid  liquid phase separation in supersaturated lysozyme solutions and associated precipitate formation / crystallization. *J. Chem. Phys. 107*, 6 (1997), 1953.

[60] Nagai, H., Kuwabara, K., Carta, G., and Way, E. Temperature Dependence of the Dissociation Constants of Several Amino Acids. *J. Chem. Eng. Data 53* (2008), 619–627.

[61] Nagele, G. On the dynamics and structure of charge-stabilized suspensions. *Phys. Rep. 272*, 5-6 (1996), 215–372.

[62] Noro, M. G., and Frenkel, D. Extended corresponding-states behavior for particles with variable range attractions. *J. Chem. Phys. 113*, 8 (2000), 2941.

[63] Pathak, J. A., Sologuren, R. R., and Narwal, R. Do Clustering Monoclonal Antibody Solutions Really Have a Concentration Dependence of Viscosity ? *Biophys. J. 104* (2013), 1–11.

[64] Pedersen, T. G., Rhomsen, N. K., Andersen, K. V., Madsen, J. C., and Poulsen, F. M. Determination of the rate constants k1 and k2 of the Linderstrom-Lang model for protein amide hydrogen exchange. *J. Mol. Biol. 230* (1993), 651–660.

[65] Pontoni, D., Narayanan, T., Petit, J., Grübel, G., and Beysens, D. Microstructure and Dynamics near an Attractive Colloidal Glass Transition. *Phys. Rev. Lett. 90*, 18 (May 2003), 188301.

[66] Porcar, L., Falus, P., Chen, W.-R., Faraone, A., Fratini, E., Hong, K., Baglioni, P., and Liu, Y. Formation of the Dynamic Clusters in Concentrated Lysozyme Protein Solutions. *J. Phys. Chem. Lett. 1*, 1 (Jan. 2010), 126.

[67] Pusey, P. N., and van Megen, W. Phase behaviour of concentrated suspensions of nearly hard colloidal spheres. *Nature 320* (1986), 340–342.

[68] Roosen-Runge, F., Hennig, M., Zhang, F., Jacobs, R. M. J., Sztucki, M., Schober, H., Seydel, T., and Schreiber, F. Protein self-diffusion in crowded solutions. *Proc. Natl. Acad. Sci. U. S. A. 108*, 29 (2011), 11815–11820.

[69] Rosenbaum, D., Zamora, P., and Zukoski, C. Phase behavior of small attractive colloidal particles. *Phys. Rev. Lett. 76*, 1 (Jan. 1996), 150.

[70] Royall, C. P., Williams, S. R., Ohtsuka, T., and Tanaka, H. Direct observation of a local structural mechanism for dynamic arrest. *Nat. Mater. 7*, July (2008), 556–561.

[71] Russel, W. B., Wagner, N. J., and Mewis, J. Divergence in the low shear viscosity for Brownian hard-sphere dispersions: At random close packing or the glass transition? *J. Rheol. (N. Y. N. Y). 57*, 6 (2013), 1555.

[72] Sarangapani, P. S., Hudson, S. D., Migler, K. B., and Pathak, J. a. The limitations of an exclusively colloidal view of protein solution hydrodynamics and rheology. *Biophys. J. 105*, 10 (Nov. 2013), 2418–26.

[73] Sciortino, F. Disordered materials: One liquid, two glasses. *Nat. Mater. 1* (2002), 145–146.

[74] Sciortino, F., Mossa, S., Zaccarelli, E., and Tartaglia, P. Equilibrium Cluster Phases and Low-Density Arrested Disordered States: The Role of Short-Range Attraction and Long-Range Repulsion. *Phys. Rev. Lett. 93*, 5 (July 2004), 5.

[75] Sciortino, F., Tartaglia, P., and Zaccarelli, E. One-dimensional cluster growth and branching gels in colloidal systems with short-range depletion attraction and screened electrostatic repulsion. *J. Phys. Chem. B 109*, 46 (2005), 21942.

[76] Sedgwick, H., Egelhaaf, S. U., and Poon, W. C. K. Clusters and gels in systems of sticky particles. *J. Phys. Condens. Matter 16*, 42 (Oct. 2004), S4913–S4922.

[77] Segrè, P., Prasad, V., Schofield, A., and Weitz, D. A. Glasslike Kinetic Arrest at the Colloidal-Gelation Transition. *Phys. Rev. Lett. 86*, 26 (June 2001), 6042.

[78] Sharma, V., Jaishankar, A., Wang, Y.-C., and McKinley, G. H. Rheology of globular proteins: apparent yield stress, high shear rate viscosity and

interfacial viscoelasticity of bovine serum albumin solutions. *Soft Matter 7*, 11 (2011), 5150.

[79] Shukla, A., Mylonas, E., Di Cola, E., Finet, S., Timmins, P., Narayanan, T., and Svergun, D. I. Absence of equilibrium cluster phase in concentrated lysozyme solutions. *Proc. Natl. Acad. Sci. U. S. A. 105*, 13 (Apr. 2008), 5075–80.

[80] Sieber, J. J., Willig, K. I., Kutzner, C., Gerding-reimers, C., Donnert, G., Rammner, B., Eggeling, C., Hell, S. W., Lang, T., Kutzner, C., Gerding-reimers, C., Hell, S. W., Grubm, H., and Lang, T. Anatomy and Dynamics of a Supramolecular Membrane Protein Cluster. *Science (80-. ). 317*, 5841 (2007), 1072–1076.

[81] Sirotkin, V. a., Komissarov, I. a., and Khadiullina, A. V. Hydration of proteins: Excess partial volumes of water and proteins. *J. Phys. Chem. B 116*, 13 (2012), 4098–4105.

[82] Smolin, N., Biehl, R., Kneller, G. R., Richter, D., and Smith, J. C. Functional domain motions in proteins on the ˜ 1-100 ns timescale: Comparison of neutron spin-echo spectroscopy of phosphoglycerate kinase with molecular-dynamics simulation. *Biophys. J. 102*, 5 (2012), 1108–1117.

[83] Stradner, A., Cardinaux, F., and Schurtenberger, P. A small-angle scattering study on equilibrium clusters in lysozyme solutions. *J. Phys. Chem. B 110*, 42 (Oct. 2006), 21222–31.

[84] Stradner, A., Cardinaux, F., and Schurtenberger, P. Comment on Effective Long-Range Attraction between Protein Molecules in Solution Studied by Small Angle Neutron Scattering. *Phys. Rev. Lett. 96*, 21 (June 2006), 219801.

[85] Stradner, A., Sedgwick, H., Cardinaux, F., Poon, W. C. K., Egelhaaf, S. U., and Schurtenberger, P. Equilibrium cluster formation in concentrated protein solutions and colloids. *Nature 432*, 7016 (Nov. 2004), 492.

[86] Stuhrmann, H. B. Neutron Small-Angle Scattering of Biological Macromolecules in Solution. *J. Appl. Crystallogr. 7*, 6 (1974), 173.

[87] Stuhrmann, H. B., and Fuess, H. A Neutron Small-Angle Scattering Study of Hen Egg-White Lysozyme. *Acta Crystallogr. A32*, 5 (1976), 67.

[88] Tardieu, A., Le Verge, A., Malfois, M., Bonnete, F., Finet, S., Ries-Kautt, M., and Belloni, L. Proteins in solution: from X-ray scattering intensities to interaction potentials. *J. Cryst. Growth 196*, 2-4 (1999), 193–203.

[89] Valadez-Pérez, N. E., Benavides, A. L., Schöll-Paschinger, E., and Castañeda Priego, R. Phase behavior of colloids and proteins in aqueous suspensions: theory and computer simulations. *J. Chem. Phys. 137*, 8 (Aug. 2012), 084905.

[90] Valadez-Pérez, N. E., Castañeda Priego, R., and Liu, Y. Percolation in colloidal systems with competing interactions: the role of long-range repulsion. *RSC Adv. 3* (2013), 25110.

[91] Valadez-Pérez, N. E., Liu, Y., Eberle, A. P. R., Wagner, N. J., and Castañeda Priego, R. Dynamical arrest in adhesive hard-sphere dispersions driven by rigidity percolation. *Phys. Rev. E 88*, 6 (2013), 060302(R).

[92] van Megen, W., Mortensen, T., Williams, S., and Müller, J. Measurement of the self-intermediate scattering function of suspensions of hard spherical particles near the glass transition. *Phys. Rev. E 58*, 5 (1998), 6073–6085.

[93] van Megen, W., and Underwood, S. M. Change in Crystallization Mechanism at the Glass-Transition of Colloidal Spheres. *Nature 362* (1993), 616–618.

[94] Yearley, E. J., Godfrin, P. D., Perevozchikova, T., Zhang, H., Falus, P., Porcar, L., Nagao, M., Curtis, J., Gawande, P., Taing, R., Zarraga, I. E., Wagner, N. J., and Liu, Y. Observation of small cluster formation in concentrated monoclonal antibody solutions and its implications to solution viscosity. *Biophys. J. 106*, 8 (2014), 1763–1770.

[95] Zaccarelli, E. Colloidal gels: equilibrium and non-equilibrium routes. *J. Phys. Condens. Matter 19*, 32 (Aug. 2007), 1–61.

[96] Zaccarelli, E., Buldyrev, S. V., La Nave, E., Moreno, A. J., Saika-Voivod, I., Sciortino, F., and Tartaglia, P. Model for Reversible Colloidal Gelation. *Phys. Rev. Lett. 94*, 21 (June 2005), 218301.

[97] Zemb, T., and Lindner, P. *Neutrons, X-rays and Light: Scattering Methods Applied to Soft Condensed Matter*. Elsevier B.V., Amsterdam, 2002.

# Chapter 6

# EFFECT OF SMALL LONG-LIVED CLUSTERS ON THE VISCOSITY OF CONCENTRATED MONOCLONAL ANTIBODY FORMULATIONS

## 6.1 Introduction

The fastest growing sector of the pharmaceutical market is comprised of products derived from biological sources, referred to as "biologics," which consist of blood, gene and cell therapy techniques, vaccines and recombinant therapeutic proteins. Of this broad category, monoclonal antibodies (mAbs) have quickly become the largest and most successful. The rapid growth over the past few decades in the biologics market for mAb based therapeutics is due to their reproducibility, high binding specificity and relatively minimal side effects.[12] This success has placed a significant emphasis on gaining a fundamental understanding of their solution properties.[6, 12] In particular, the ability to manufacture on the commercial scale, then purify and deliver these materials requires that formulations have sufficiently low viscosities.[12] Additionally, a current goal of many biopharmaceutical companies is to transition antibody therapeutics from intravenous (IV) infusion to subcutaneous (SC) injection delivery. Such a shift would provide a more enjoyable experience for patients by reducing their inconvenience through minimizing the time commitment and providing more freedom in the administering location. However, SC delivery requires mAb therapeutics to have a very low solution viscosity, which places a significant restriction on their formulation composition.

The SC delivery method requires small sample volumes, which require high protein concentrations on the order of $100 - 200$ mg/mL for a dose with sufficient potency. A possible repercussion of concentrated mAb formulations are larger viscosities that, if in excess of $\sim 50$ mPa-s, make it difficult to deliver drugs via SC injection.[6, 12] As

demonstrated previously, lysozyme protein solutions can become highly viscous when sufficiently concentrated.[3, 10] The large viscosity was directly shown as a response to intermediate range order (IRO) caused by a combination of short-range attraction and long-range repulsion (SALR), but could also be interpreted as a result of dynamic cluster formation.[10] Both attractive and repulsive interactions, as well as anisotropic particle shape, can increase the solution viscosity.[20] Therefore, clusters in mAb based solutions are hypothesized to further increase the viscosity, which is expected to depend on their number, size, shape, charge, and possibly their lifetime.[10] Similarly, the large viscosity of some mAb formulations is hypothesized to result from their reversible self-association into dynamic clusters.[4, 12]

Given the concentrated conditions at which clusters form, it has been difficult to directly observe mAb clusters and quantify their characteristic structural and dynamic properties. Although mAbs and other proteins have similar chemical composition, their interactions can vary significantly due to the wide variety of secondary and tertiary structures in solution. Thus, it is plausible that reversible antibody association at high concentration could be driven by highly directional forces. However, clusters can be identified by dynamic signatures when the interactions responsible for their formation are unknown.[8, 17, 23] Using neutron scattering, the structure and mobility of individual "moving units" can be distinguished over a range of lengthscales,[36] even under concentrated conditions. Specifically, neutron spin echo can identify the larger effective hydrodynamic radius of clusters (before they reversibly dissociate) relative to monomers. This is a novel approach in which structural and dynamic techniques are used to conclusively identify reversible cluster formation.

In this chapter, the solution properties of two immunoglobulin type-G1 (IgG1) based antibodies are compared to demonstrate a direct correlation between dynamic cluster formation and increased viscosity in concentrated mAb formulations. Both proteins have nearly identical primary sequences and tertiary structure, but display significantly different solution behavior.[30, 32, 33] One produces a prohibitively large viscosity at concentrations relevant to SC injection formulations, while the viscosity

of the other remains consistent with expected excluded volume effects. Neutron scattering results will demonstrate that the mAb with larger viscosity readily forms small dynamic clusters at low concentration that then become more populous at higher concentration. Thus, the larger excluded volume and effective interactions of clusters are correlated with the increase in viscosity for this particular mAb, but this technique can readily identify a similar relationship in other antibody formulations. The body of work presented in this chapter is largely comprised of published research.[33]

## 6.2 Materials and Methods

Two humanized mAbs with markedly different solution viscosities, denoted as mAb1 and mAb2, are used as model systems. Both mAbs are constructed with the same human IgG1 framework, and thus, have nearly the same molecular mass ($\approx$ 150 kDa) and primary structure, with small sequence differences confined in the complementarity determining region.[34, 35] The samples are purified so that the amount of irreversible dimers is about 1% for each mAb.[35] Both mAbs are stored in their lyophilized form and subsequently reconstituted into $D_2O$ based buffers, which reduces the incoherent background during neutron scattering experiments. The buffer composition used for all samples is composed of 32 mM Histidine/Histidine-HCl, 360 mM sucrose and 0.6 mg/mL polysorbate-20 at pD $\approx$ 6.4. Despite the structural and chemical similarity, the theoretical net charge is +17 for mAb1 and +27 for mAb2.[34]

Solutions of these mAbs are studied using a combination of rheology, small angle X-ray and neutron scattering (SAXS and SANS, respectively), neutron spin echo (NSE) and dynamic light scattering (DLS) techniques. All samples were stable and the experiments were reversible on the timescale of each experiment at all conditions tested. Rheological experiments were performed on a stress-rate controlled rheometer (Anton Paar Physica MCR 501) using a 50 mm 0.490° anodized aluminum cone geometry. A flow sweep, ascending and descending, from 1 $s^{-1}$ to 2000 $s^{-1}$ was performed to check for hysteresis and sample degradation, which were never observed.

SANS, NSE and DLS measurements were conducted at the NIST Center for Neutron Research in Gaithersburg, MD and the Institut Laue-Langevin (ILL) in Grenoble, France. SAXS experiments were performed on the F2 beamline of the Cornell High Energy Synchrotron Source.

Antibody dynamics were determined using DLS under dilute conditions and NSE at high concentrations. Collective diffusion coefficients, $D_c$, are determined by fitting intermediate scattering functions with a single exponential functional form as outlined in Chapter 2. Hydrodynamic radii, $R_h$, of mAb solutions at low concentration are calculated using the generalized Stokes-Einstein-Sutherland equation: $R_h = k_B T/(6\pi\eta_s D_c)$, where $\eta_s$ is the solvent viscosity. The short-time self diffusion coefficient, $D_s$, is determined from the high-$q$ asymptotic limit of $D_c$ determined from NSE.

Raw SANS and SAXS data were analyzed following standard methods outlined in Chapter 2 using software provided by NCNR.[15] SAXS intensity as a function of $q$-value follows the same functional form as SANS data, but the contrast depends on the electron density rather than neutron scattering length density. A 5 mg/mL sample of mAb2 without salt is used as the form factor, $P(q)$, to normalize high concentration SANS results to determine the effective structure factor, $S_{eff}(q)$. Both SANS and SAXS data at low $q$-values are analyzed using the Guinier approximation to estimate radii of gyration, $R_g$, and apparent molecular weight, $M_{w,app}$. The Guinier approximation relates $R_g$ and the slope of the natural log of the scattering intensity by expanding the Fourier transform of intra-particle density correlations with the first term in the McLaurin series in the limit of small $q$-values, resulting in

$$\ln[I(q)] = \ln[I(0)] - (qR_g)^2/3, \tag{6.1}$$

where $I(0)$ is the extrapolated zero-$q$ intensity. The Guinier analysis is applicable within a $q$-range of $q < 1.0/R_g$ and is limited to solutions of non-interacting scattering entities (i.e., $S(q) \sim 1$). Once $I(0)$ is determined, the apparent molecular weight can

be calculated by

$$M_{w,app} = I(0)\left(\frac{\rho_m^2 N_A}{C V_p (\Delta\rho)^2}\right), \tag{6.2}$$

assuming $S_{eff}(0) \approx 1$, where $C$ is the protein concentration, $\rho_m$ and $V_p$ are the mass density and volume of a mAb protein, respectively, $\Delta\rho$ is the neutron scattering length density contrast and $N_A$ is the Avogadro constant. The $M_{w,app}$ of mAb2 is taken to be 150 kDa at low concentrations because both DLS and NSE measurements indicate it remains dispersed as single mAbs in solution, even at high protein concentration.

## 6.3 Influence of mAb Association on Solution Viscosity

### 6.3.1 Solution Viscosity

The effects of protein concentration, salt concentration, and temperature on the solution viscosity, $\eta$, are presented in Fig. 6.1 for both mAb1 and mAb2. Comparing both mAbs in the absence of salt at $25°C$ in Fig. 6.1a indicates that mAb1 solutions become significantly more viscous at elevated concentrations, approaching an anomalously large value of 310 mPa-s at 150 mg/mL as compared to a viscosity of only 18 mPa-s at 150 mg/mL for mAb2. Even though the viscosity of mAb1 is not overly viscous as compared to other soft materials such as colloidal gels,[7] these viscosity levels are capable of limiting the protein concentration in formulations for bulk manufacturing and SC delivery.

The addition of sodium chloride (NaCl) to concentrated (150 mg/mL) mAb formulations, shown in Fig. 6.1b, has different effects on the viscosity for solutions of mAb1 as compared to solutions of mAb2. While the addition of NaCl does not significantly alter the viscosity of mAb2 solutions, the viscosity of mAb1 solutions decreases significantly with increasing salt content. For example, the addition of 150 mM NaCl reduces the viscosity of mAb1 solutions by approximately a factor of five. This trend holds for both temperatures examined. This difference in the effect of salt on the viscosity of these two mAb solutions indicates that there is a difference in the interactions that lead to the viscosity between these two systems. In particular, the salt sensitivity observed for mAb1 suggests electrostatic interactions are significant

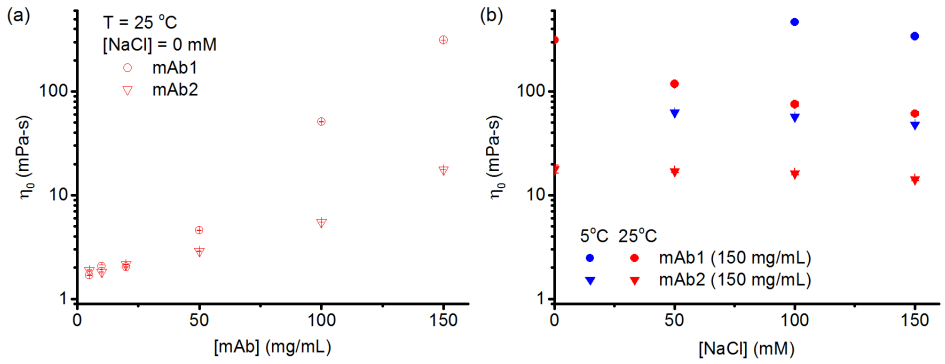


**Figure 6.1:** The viscosity of mAb1 (circles) and mAb2 (triangles) is plotted (a) as a function of protein concentration without added NaCl and (b) at 150 mg/mL antibody concentration as a function of added salt concentration. Measurements conducted at 5 $°C$ and 25 $°C$ are represented by blue and red symbols, respectively.

in determining the solution viscosity, while the insensitivity for mAb2 suggests other forces dominate.

Normalizing the solution viscosities by that of the solvent under each corresponding salt concentration and temperature results in a reduced zero shear viscosity, $\eta_{r0}$. By comparing values of $\eta_{r0}$, the influence of protein concentration and buffer formulation on the viscosity can be directly compared. In particular, Fig. 6.2 compares reduced viscosities of mAb1 and mAb2 without salt at $25°C$ with theoretical predictions for a hard sphere (HS) colloidal suspension in which the particles have an excluded volume, but no additional interactions. To conform to the HS viscosity model dependence on volume fraction, the protein concentration is converted according to $\phi = (C/M_w)(4/3)\pi R_h^3$, using the $M_w$ and $R_h$ of the fundamental mAb2 moving unit determined from SANS and DLS, respectively. The distinctly larger relative viscosity of mAb1 formulations indicates that interactions between mAb1 antibodies are significantly stronger than mAb2. Values of reduced viscosity at lower temperature, though not available or shown in Fig. 6.2, can be estimated from the available data in Fig. 6.1b. Reducing temperature from $25°C$ to $5°C$ increases the viscosity of the

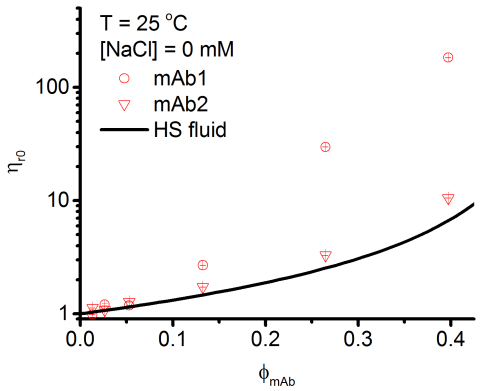


**Figure 6.2:** The reduced zero-shear viscosity of mAb1 (circles) and mAb2 (triangles) is plotted relative to hard sphere expectations (solid line) as a function of protein concentration without added NaCl (at $T = 25°C$).

solvent and mAb2 solutions by a factor of two, while that of mAb1 solutions increases by roughly a factor of five. This more significant increase in mAb1 solution viscosity suggests that mAb1 interactions become stronger with reducing temperature, which has been previously noted for proteins.[19, 21, 24] The influence of salt and temperature on the interactions as suggested by the viscosity data can be more quantitatively analyzed through SANS and SAXS measurements.

### 6.3.2 Small Angle Neutron Scattering

Comparing the SANS results for the most concentrated mAb solutions can provide insight into the interactions that, in part, cause the correspondingly large or small viscosities. The 1-D SANS spectra for mAb1 and mAb2 solutions at 150 mg/mL at $25°C$ are shown in Fig. 6.3a with a representative data set for an IgG1 antibody form factor, $P(q)$. Normalizing each set of $I(q)$ curves by $P(q)$ and other pre-factors discussed in Chapter 2 produces an effective structure factor, $S_{eff}(q)$, shown in Fig. 6.3b. Importantly, previous work has demonstrated that the structure of a mAb1 and mAb2 monomer are nearly identical and that each of the solution conditions studied in this chapter do not cause the tertiary structure to change significantly.[34] Thus,

normalizing all $I(q)$ curves by the same $P(q)$ function will provide accurate effective structure factor functions. Once $I(q)$ is normalized by $P(q)$ to remove the influence of protein shape and concentration, the $q$-dependence of $S_{eff}(q)$ is representative of the interactions alone.

The scattering intensity for mAb2 in solution without added salt exhibits a prominent correlation peak that is typical of systems with strong electrostatic repulsion. However, with the addition of 150 mM NaCl the peak reduces to a weak shoulder and a slight increase in intensity at low $q$-values also appears in the spectra. This trend suggests that the added salt weakens the effective repulsive force acting between antibodies in solution by screening the repulsion. The corresponding $S_{eff}(q)$ functions shown in figure 6.3b confirm that the interaction peak at a $q$-value of about 0.05 $\text{Å}^{-1}$ disappears with the addition of salt. Under the same conditions, the magnitude at low-$q$ becomes larger, but remains much less than one. Thus, while the addition of NaCl weakens the repulsion by screening the surface charge, repulsive forces remain a significant contribution to mAb2 interactions.

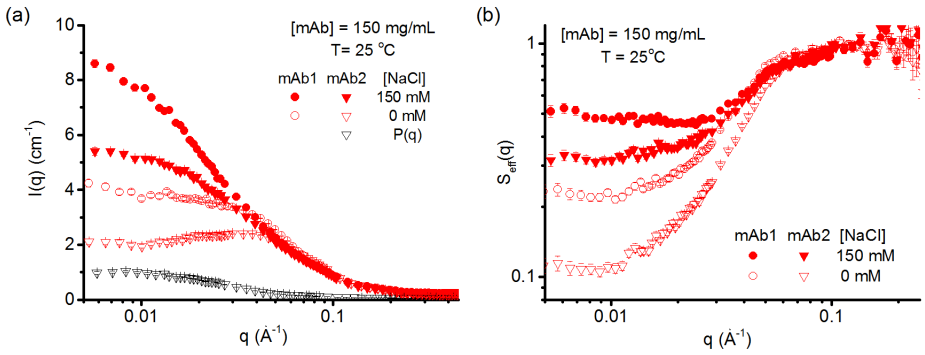


**Figure 6.3:** (a) Absolute scattering intensity and (b) effective structure factors from SANS of mAb1 (circles) and mab2 (triangles) samples at 150 mg/mL with 0 mM (open symbols) and 150 mM (filled symbols) added NaCl. The form factor (open black triangles) in (a) is a 5 mg/mL sample. All data sets were studied at 25 $°C$. Only a fraction of all points in each data set are included for clarity.

The SANS spectra for solutions of mAb1 exhibit a continual increase in intensity with decreasing $q$-value and at neither salt condition do these samples show a correlation peak indicative of structural order as observed for mAb2 solutions. Without added salt, solutions of mAb1 produce a SANS spectra with a shoulder in $I(q)$ at roughly the same $q$-value of the correlation peak produced by mAb2 solutions, which transitions to a weak increase in intensity at lower $q$-values. Adding 150 mM NaCl to mAb1 formulations increases the low-$q$ intensity, which suggests that initially attractive inter-protein interactions become more strongly attractive. The addition of 150 mM NaCl also causes the magnitude of $S_{eff}(q)$ at low-$q$ to increase as well as the slope to become slightly negative. These features indicate the prominence of attractive forces. However, Fig. 6.3b indicates that the magnitude of the effective structure factors under both salt conditions remains below one. This suggests that effective interactions between mAb1 antibodies also have a repulsive component.

While the qualitative analysis of the SANS spectra in Fig. 6.3 suggests that repulsive interactions dominate for mAb2 in solution while attractive forces play an important role in mAb1 solutions, mAb1 may interact both attractively and repulsively. Studying the concentration and temperature dependence of the SANS scattering profiles indicates a more distinct difference in the effective interactions between mAb1 and mAb2. The SANS intensities for mAb1 and mAb2 solutions without added salt are shown in Fig. 6.4a and 6.4b, respectively, and the corresponding $S_{eff}(q)$ are shown in Fig. 6.4c and 6.4d, respectively, for three protein concentrations at $5°C$ and $25°C$. The SANS spectra for solutions of mAb2 are consistent across the range of protein concentrations studied. Scattering intensities in Fig. 6.4b are all nearly identical at low-$q$ for a given temperature and differ only slightly at intermediate $q$-values as a result of their different concentrations. The corresponding effective structure factors decrease in magnitude at low-$q$ with increasing protein concentration, demonstrating that mAb2 becomes more repulsive under these conditions. Previous work has shown that this trend quantitatively agrees with estimates of $S(0)$ according to the surface charge of

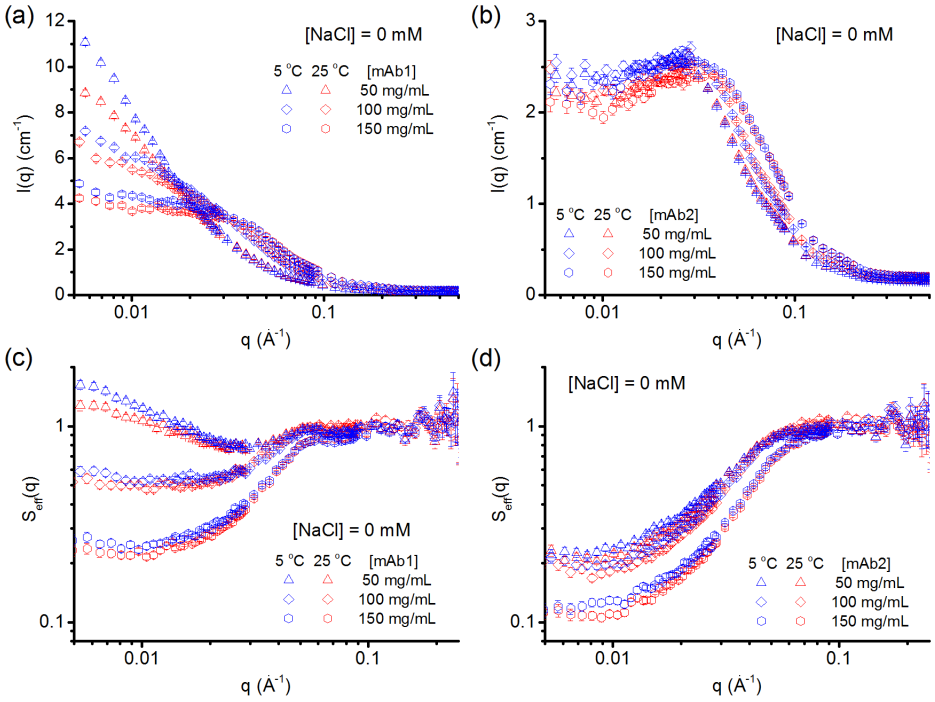


**Figure 6.4:** SANS 1-D scattering profiles of (a) mAb1 and (b) mAb2 at 5 $°C$ and 25 $°C$ for three concentrations. Corresponding effective structure factors are plotted for (c) mAb1 and (d) mAb2. All samples studied have 0 mM sodium chloride. Only a fraction of all points in each data set are included for clarity.

mAb2.[34] Furthermore, the interactions and associated $S_{eff}(q)$ are relatively insensitive to temperature, which agrees with theories of screened Coulomb repulsion.[25]

The most distinct feature of Fig. 6.4 is the large and systematic variation in $S_{eff}(q)$ for mAb1 solutions at small $q$-values with increasing protein concentration. Interestingly, the effective structure factor of the 50 mg/mL mAb1 sample without added salt (Fig. 6.4c) has a magnitude above one at low-$q$ and a strong negative slope. This profile bears a similar resemblance to the 150 mg/mL mAb1 sample with added 150 mM NaCl (Fig. 6.3b), despite the different electrolyte conditions. Presumably, in both cases the resulting features are representative of strong attractive interactions. Increasing the protein concentration leads to a dramatic decrease in low-$q$ magnitude of

$S_{eff}(q)$ for mAb1 solutions. The decrease of $S(0)$ with increasing protein concentration indicates that excluded volume effects become increasingly important such that the values approach those expected for a HS fluid at equivalent concentrations.[34] Samples at $5°C$ show the same trend, but with consistently larger magnitudes of $S_{eff}(q)$ at low-$q$ indicating stronger attractive interactions.

Previous research shows that the SANS spectra for mAb1 solutions can be modeled semi-quantitatively using an effective isotropic potential of interaction comprised of a short range attraction and long range repulsion.[34] Most forces responsible for protein association, such as hydrophobic interactions, van der Waals forces or hydrogen bonding, are well known to have a short range of interaction.[13] A possible source of the apparent extended range of this attraction is an anisotropic electric-dipole.[34] However, consideration of the surface charge on mAb1 suggests that the short-range interactions may be highly orientation dependent such that a spherically averaged potential may fail to accurately represent the interactions in solution. This is supported by the significant heterogeneity of its surface charge relative to mAb2[30] and coarse-grained simulation studies of charge-anisotropy induced mAb1 association.[4] Therefore, while the interactions between mAb2 in solution is anticipated to be weakly repulsive for all protein concentrations, mAb1 interacts by both a weak long range repulsion and an anisotropic, shorter range attraction.

### 6.3.3 Low Concentration Structure and Dynamics

The presence of a short range attraction combined with screened Coulomb repulsion leads to the possibility of forming dynamic clusters in solution.[27, 28] Although equilibrium clusters typically form at slightly elevated densities,[11] the competing forces found for mAb1 appear to induce small dynamic cluster formation even at very low protein concentrations. Cluster formation at low mAb concentrations can be identified by analyzing SAXS patterns using a Guinier analysis to estimate a radius of gyration, $R_g$, (Fig. 6.5a) and normalizing DLS results to estimate an effective hydrodynamic radius, $R_h$, (Fig. 6.5b).

Comparing the influence of protein concentration on $R_g$ and $R_h$ for solutions of mAb1 and mAb2 can distinguish the extent of association by each of these antibodies. The apparent $R_g$ at 1 mg/mL with both 0 mM and 150 mM added NaCl is identical for both mAbs ($\sim$ 5 nm) and corresponds to the size of an individual monomer in solution. However, the apparent $R_g$s for these two protein solutions have different behavior with increasing protein concentration, where (without added salt) the apparent size of mAb2 decreases and mAb1 increases. The decrease in *apparent* $R_g$ for mAb2 is a result of repulsive forces and reflects the influence of $S_{eff}(q)$ on the low-$q$ region of the scattering profile. When this structural effect is properly accounted for, the size of mAb2 in solution actually remains unchanged up to 10 mg/mL. The same is true when 150 mM NaCl is added to mAb2 solutions, as shown in Fig. 6.5a. On the other hand, the increase in apparent $R_g$ for mAb1 reflects the influence of competing interactions leading to association into larger aggregates. At 10 mg/mL, the size of mAb1 increases to $R_g \approx 6.9$ nm, which is reversible when diluted, indicating the formation of equilibrium clusters. The addition of 150 mM sodium chloride reduces the apparent size compared to samples without salt, which suggests that the association into dynamic clusters is weaker. This finding supports the hypothesis that anisotropic short-range attraction arises due to direct electrostatic interactions in this system that

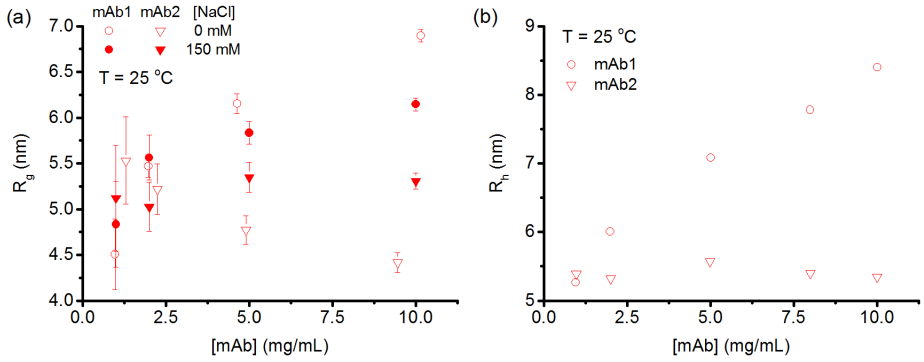


**Figure 6.5:** (a) The radius of gyration determined from a Guinier analysis of SAXS data and (b) the hydrodynamic radius estimated from DLS results at 25 $^{\circ}C$ are plotted for low mAb concentrations.

additional salt would screen and therefore make weaker.

DLS measurements further confirm the transition of mAb1 in solution from dispersed monomers to small clusters with increasing mAb1 concentration and in the absence of added salt. Similar to the SAXS analysis, the effective $R_h$ shown in Fig. 6.5b at 1 mg/mL without salt is about 5.4 nm for both mAbs. This value remains constant for mAb2 up to 10 mg/mL, but increases to about 8.5 nm at the same concentration for mAb1. The larger size of $R_h$ from DLS compared to $R_g$ from SAXS suggests that the clusters may be elongated. While $R_g$ reflects the moment of inertia of the protein itself, $R_h$ reflects the hydrodynamic resistance, which reflects the largest lengthscale of the anisotropic mAb in solution and is typically much larger than $R_g$ for compact objects.[20]

### 6.3.4 Structure at High Concentration

The apparent size of the clusters can be determined according to their apparent molecular mass, $M_{w,app}$, estimated using $I(0)$ from SAXS scattering profiles. Although the results in Fig. 6.5 indicate that mAb1 reversibly associates into equilibrium clusters, without additional information about the internal cluster configuration, knowledge of the radius alone is insufficient to conclusively determine the aggregation number. Estimated values of mAb1 cluster mass, shown in Fig. 6.6, are calculated using a pre-factor Eq. 6.2 based on the well dispersed solutions of mAb2 ($M_w \approx 150$ kDa) at low protein concentration. Also shown in Fig. 6.6 is the apparent weight of mAb2, which unlike mAb1 consistently decreases with increasing concentration in both salt conditions of the buffer. Similar to the apparent decrease of $R_g$ for mAb2 in Fig. 6.5, the decrease in $M_{w,app}$ does not suggest fragmentation of the mAb, but rather reflects the effect of $S_{eff}(0)$ at higher mAb2 concentrations. Physically, this trend is more intuitively understood as a reduction in the free volume available for each antibody with increasing concentration, where stronger repulsive interactions (causing the magnitude of $S_{eff}(0)$ to decrease) prevent adjacent mAbs from "sharing" space. The addition of 150 mM NaCl partially screens the repulsion and increases the $M_{w,app}$

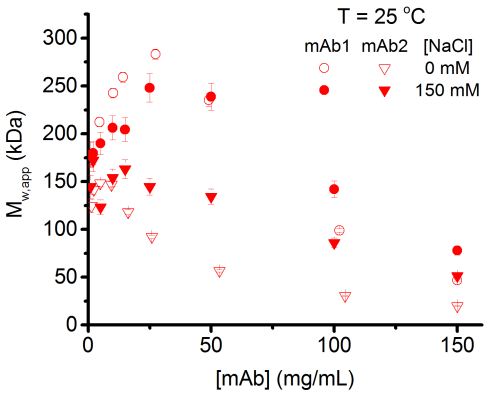


**Figure 6.6:** Apparent molecular weights determined from SAXS results are plotted as a function of protein concentration for mAb1 (circles) and mAb2 (triangles) both with 0 mM NaCl (open symobls) and 150 mM added NaCl (filled symbols) at 25 $°C$.

of mAb2 at higher concentrations by decreasing the compressibility. These results, together with the viscosity dependence and coarse-grained computer simulations,[4] suggest that mAb2 remains monomeric over these protein and salt concentrations.

Changes in $M_{w,app}$ of mAb1 in solution as a function of protein and salt concentration are distinctly different from mAb2. The results in Fig. 6.6 show that the apparent molecular mass of mAb1 is about 250 kDa with no salt and about 200 kDa with 150 mM NaCl at a low protein concentration of 10 mg/mL. These values, which are consistent with previous static light scattering measurements at low concentrations,[26] continue to increase up to mAb1 concentrations of about 30 mg/mL, after which they decrease rapidly. At a protein concentration of 150 mg/mL, values of $M_{w,app}$ for mAb1 approach those of mAb2. The maximum values of $M_{w,app}$ for mAb1 are similar to the mass of a dimer ($M_{w,app} \approx 300$ kDa). This suggests that solution microstructures of mAb1 are monomeric at very low protein concentrations ($C < 1$ mg/mL) and become dominated by clusters at about 10 mg/mL. The smaller value of $M_{w,app}$ for samples with 150 mM salt suggest that clusters form, but are less prevalent.

The decrease in apparent molecular mass at higher concentrations results from

a similar influence of $I(0)$ discussed for mAb2 solutions and does not necessarily reflect that small clusters no longer form under these conditions. While SAXS and DLS have clearly demonstrated that mAb1 associates into small clusters at low protein concentration, these techniques are unable to clarify their behavior at high protein concentration where mAb1 solution viscosities, shown in Fig. 6.1, becomes significant. Thus, further work identifying the presence of clusters and their size at higher concentrations is necessary to quantify their influence on the viscosity.

### 6.3.5 Dynamics at High Concentration

Measurements of the short-time mobility by NSE can be used to determine an effective cluster size in concentrated protein solutions. Specifically, an effective hydrodynamic radius (comparable to that obtained by DLS, but highly accurate at high concentration) can be determined by normalization of the short-time self diffusion coefficient, $D_s$. However, quantifying $D_s$ relies on first extracting $q$-dependent short-time collective diffusion coefficients, $D_c(q)$, by fitting the normalized intermediate scattering function, $F_s(q,t)/F_s(q,0)$, with an exponential function as discussed in Chapter 2. Examples of such a fitting can be found for lysozyme samples in Chapter 5. Here, a single exponential function is used for correlation times up to 50 ns due to the linearity of the data on a semi-log plot.

A variety of data sets over a range of protein concentrations, salt content and temperatures are plotted in Fig. 6.7 that explicitly demonstrate the $q$-dependence of the short-time collective diffusivity. As discussed in earlier chapters and outlined in previous research,[1, 8, 17, 22, 23] estimates of $D_s$ are determined by the value of $D_c(q)$ in the limit of large $q$-values. Interestingly, the values of $D_c(q)$ for mAb1 and mAb2 in Fig. 6.7 are nearly $q$-independent (over the range of $q$-values studied) under all solution conditions. Therefore, to enhance the statistics, the average value of all data points is used to determine values of $D_s$.

Given the flexibility and dynamic nature of protein structure, it is important to distinguish the contributions of translational motion from those of internal and

rotational motion on the NSE results. Therefore, it is worth noting that over the length ($q$-values) and time scales probed by NSE, the contribution of the latter two dynamic modes on the extracted values of $D_c(q)$ is negligible. If significant, internal and rotational dynamics would enhance $D_c(q)$ at $q$-values corresponding to the length scale of their motion.[2] Given the size of mAb domains, these motions would appear on length scales less than about 1 nm (i.e., $Q > 0.1$ Å$^{-1}$). However, values of $D_c(q)$ in Fig. 6.7 remain constant within this $q$-range. Further, the relaxation time for translation is much longer than that for internal motion at large $q$-values. Previous work has demonstrated that even proteins with significant internal motion have an effective $D_c(q)$ identified by NSE that is dominated by contributions from translational motion at high-$q$.[29] Thus, differences in mAb1 and mAb2 diffusive motion can be confidently determined by identifying differences in their $D_c(q)$.

A complete summary of all short-time self diffusion coefficients extracted from NSE data are provided in Fig. 6.8, including absolute values (a, b) and normalized values of $D_s/D_0$ (c,d), where the bare diffusion coefficient, $D_0$, was calculated as the infinitely dilute limit of the low concentration DLS results. Without salt, the $D_s$ of mAb2 is always larger than that of mAb1. Adding 150 mM NaCl actually increases $D_s$ for mAb1, while it slightly decreases that of mAb2, such that they become nearly identical. The decrease of temperature from $25°C$ to $5°C$ causes the mobility of both mAbs under both salt conditions to decrease. However, this reduction results from the corresponding increase in solvent viscosity, reduced thermal energy, and changes in inter-protein interactions. Normalization by $D_0$ removes the influence of the former two variables, thus leaving changes in interactions as the cause of changes in $D_s/D_0$ values.

The values of $D_s/D_0$ in Fig. 6.8 demonstrate changes with antibody type, concentration and the salt content of the buffer. Regardless of the protein or salt content, $D_s$ is equal to the free diffusion coefficient of a monomer at the lowest protein concentrations. However, with increasing mAb concentration, the behavior of mAb1 and mAb2 differ significantly. Interestingly, the value of $D_s/D_0$ for mAb2 solutions

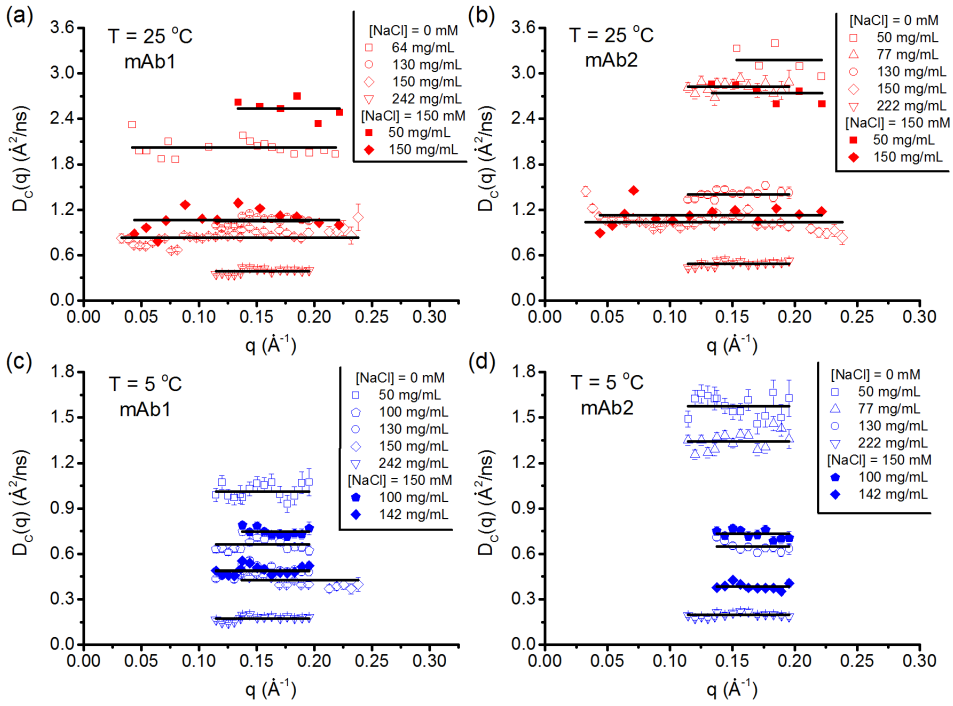


**Figure 6.7:** The short-time collective diffusion coefficients determined from NSE data are plotted as a function of $q$-value for solutions of mAb1 at (a) 5 $^{\circ}C$ and (c) 25 $^{\circ}C$ and for mAb2 at (b) 5 $^{\circ}C$ and (d) 25 $^{\circ}C$. Samples with 0 mM NaCl are open symbols and those with 150 mM NaCl added are filled symbols. The lines represent the average value used to determine the short-time self diffusion coefficient.

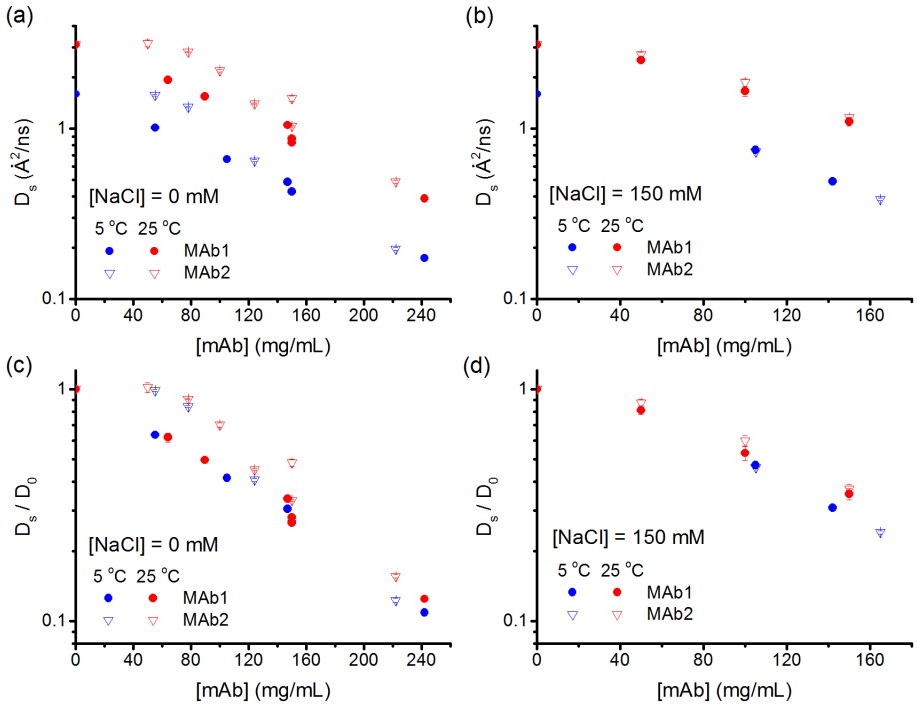


**Figure 6.8:** Short-time self diffusion coefficients are plotted as a function of protein concentration for formulations with salt concentrations of (a) 0 mM and (b) 150 mM at 5 $°C$ (blue symbols) and 25 $°C$ (red symbols). For clarity, filled circles and open triangles represent mAb1 and mAb2 samples, respectively, at both salt conditions. The same symbols are used for the normalized values $D_s/D_0$ with (c) 0 mM and (d) 150 mM added NaCl.

remains about one up to concentrations of 50 mg/mL despite the increasing strength of repulsive interactions reflected in Fig. 6.4d. Note that even in hard sphere systems, $D_s/D_0$ decreases at equivalent densities.[1, 16, 20] Therefore, the decrease of $D_s/D_0$ when increasing mAb2 concentration above 50 mg/mL is a result of hydrodynamic interaction effects at larger densities.[1, 23] This is consistent with previous simulations and experiments that indicate mAb2 remains dispersed as monomers up to at least 150 mg/mL without added salts.[4, 26, 34] Further, reducing the temperature has no significant impact on the normalized diffusivity, suggesting that mAb2 remains dispersed as single mAbs in solution at low temperatures as well.

The addition of 150 mM salt to mAb2 causes $D_s/D_0$ to shift to lower values at protein concentrations $\geq$ 50 mg/mL at both $5°C$ and $25°C$. The result is a consistent decrease in diffusivity with increasing concentration from the very dilute limit. Although mAb2 appears to become less mobile over short times with the addition of NaCl, mAb2 interactions become more HS-like with the addition of salt, as demonstrated in Fig. 6.3b. The correlation between the weaker repulsive forces and slower short-time self diffusion may be caused, in part, by more abundant association of neighboring mAb2 antibodies that enhances hydrodynamic interactions.

Increasing mAb1 concentration without added salt also results in a decrease in $D_s/D_0$, as shown in Fig. 6.8. This behavior is similar to that for solutions of mAb2 with 150 mM added salt, but with a more significant drop in magnitude over the same range of protein concentrations. Values of $D_s/D_0$ are comparatively small in mAb1 solutions without added salt due to strong anisotropic attraction combined with repulsion.[34] The significantly slower diffusion of mAb1 relative to mAb2 in solutions of 0 mM NaCl confirms that mAb1 cluster formation persists to very high protein concentrations. However, these clusters become unstable in the presence of 150 mM salt, as reflected by the nearly identical values of $D_s/D_0$ between mAb1 and mAb2 in Fig. 6.8d.

Similar to mAb2, changing the temperature from $25°C$ to $5°C$ has no apparent effect on the normalized diffusivity of mAb1, which shows the primary effect of temperature is to change the solvent viscosity.

Given the "ideality" of mAb2 solutions, in that they remain dispersed as monomers over the range of protein concentrations studied, mAb2 diffusivity can be used as a standard to estimate an effective size of clusters in mAb1 solutions with more significant inter-protein interactions. In particular, the proportionality $R_h \propto 1/D_s$ (the exact relationship is provided by Eq. 2.20 in Chapter 2) allows the ratio of $D_s/D_0$ values for mAb2 relative to mAb1 at the same concentration under the same solution conditions to quantitatively represent a mAb1 cluster size. The estimated size indicates the dominant moving unit in the short time limit. This effective hydrodynamic cluster size,

$R_h/R_0$, is shown in Fig. 6.9 as a function of mAb concentration, temperature, and salt content. Here, the bare size of a monomer, $R_0$, is determined by the value of $D_0$ in the infinitely dilute protein limit determined by DLS under each solution condition.

The effective radii of mAb1 in solution, as shown in Fig. 6.9, clearly differentiate the moving unit between solutions with 0 mM and 150 mM sodium chloride. Without added salt, mAb1 appears to form clusters with an effective radius of about 1.6 times larger than a monomer at a protein concentration of 50 mg/mL. This $R_h/R_0$ remains at about 1.6 up to about 100 mg/mL at $5°C$ and up to about 150 mg/mL at $25°C$ before decreasing slightly at higher concentrations (this will be discussed in more detail later). Interestingly, DLS (and SAXS) results for samples at low concentration and no added salt, shown in Fig. 6.5, indicate that dynamic clusters with an effective hydrodynamic size of about 1.6 also form at concentrations as low as 10 mg/mL. Interestingly, DLS values of $R_h$ even begin to increase above that of a monomer at a protein concentration of 2 mg/mL. Thus, the data suggest that mAb1 forms small dynamic clusters at very low concentration until about 10 mg/mL, when the system is nearly entirely composed of small clusters (whose average molecular mass is that of a dimer). These small dynamic clusters then remain constant in size up to about 150 mg/mL. Thereby, the number density of these small clusters increases with increasing protein concentration.

This behavior is qualitatively different from cluster formation in globular protein solutions, such as lysozyme, where clusters only form at relatively high concentrations ($>$ 100 mg/mL) due to isotropic short-range attraction and long-range repulsion[9, 11] and the average size increases with the increase of the volume fraction.[8, 23] The constant size of mAb1 clusters over the tested concentration ranges of protein and added salt can be attributed to the anisotropic (possibly site specific) attraction between mAb1 antibodies, as suggested/observed previously.[4, 34]

Computer simulations were used in previous work to identify representative morphologies of mAb1 dimers formed in solutions without salt.[33] Dimers were constructed by associating two mAbs together with various configurations using SASSIE.[5] The most representative dimer structures were those with the closest corresponding $R_g$ to

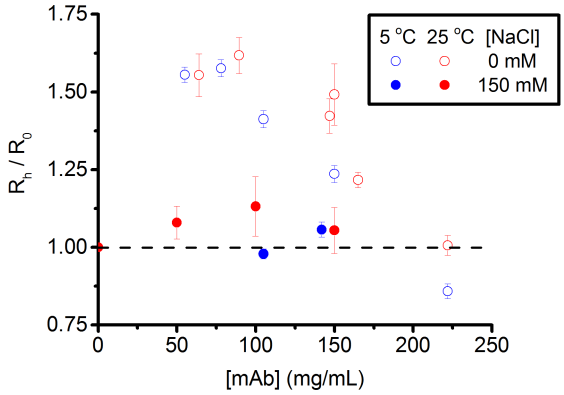


**Figure 6.9:** Effective hydrodynamic radii of mAb1 clusters are shown relative to protein concentration at 5 $^{\circ}C$ (blue symbols) and 25 $^{\circ}C$ (red symbols) for salt concentrations of 0 mM (open symbols) and 150 mM (filled symbols).

the experimental $R_g$ of mAb1 clusters ($\approx$ 6.9 nm at 10 mg/mL), as shown in Fig. 6.5. From about 23,000 configurations, the experimental $R_g$ could only be reproduced by those trial configurations with an extended structure.[33] Thus, mAb1 clusters likely have a similar configuration at high protein concentrations. Such a structure is qualitatively consistent with site specific interactions.

In contrast to mAb1 samples without added salt, values of $R_h/R_0$ in Fig. 6.9 for samples with added 150 mM NaCl remain about one at all concentrations. However, the increase in magnitude of $S_{eff}(q)$ at low-$q$ for mAb2 with salt in Fig. 6.3 suggests that the isotropically averaged repulsive (stabilizing) force is weaker. As a result, mAb2 with salt may not be a "model" monomeric system, which was used as an assumption in estimating an effective hydrodynamic size of mAb1 clusters in samples without salt. Removing this assumption reveals that $R_h/R_0 = D_s(mAb2)/D_s(mAb1) \approx 1$ simply suggests an equivalent short time mobility of mAb1 and mAb2 in the presence of 150 mM NaCl. Studying the trends in viscosity will help clarify the forces leading to this peculiar behavior of mAb1 and mAb2.

### 6.3.6 Cluster-Viscosity Correlation

The formation of dynamic clusters in mAb1 samples without added salt as demonstrated in Fig. 6.9 and the commensurate, dramatic increase of mAb1 solution viscosity shown in Fig. 6.1 over the same range of protein concentrations suggests a correlation between these two properties. This observation suggests that the solution viscosity can be controlled by the extent of cluster formation. In the absence of salt, the SANS and NSE evidence suggests that mAb2 is well dispersed and, as a result, its viscosity in Fig. 6.2 is similar to that of a HS fluid of comparable volume fraction in solution. Note that the determination of the effective hard sphere volume fraction is solely based on the density of the mAb and does not account for shape and interactions. The significantly larger viscosity of mAb1 in solution is consistent with the formation of small dynamic clusters with elongated structures, which will have a larger effective volume than two individual mAbs. Molecular dynamics simulations further suggest that Fab-Fab interactions are much more prevalent in mAb1 than that in mAb2.[4] Therefore, cluster shape and inter-cluster interactions are both expected to contribute to the greatly enhanced viscosity of mAb1 solutions.

The decrease in mAb1 solution viscosity with increasing salt content shown in Fig. 6.1 corresponds directly with the mitigation of dynamic cluster formation that occurs by adding salt, demonstrated in Fig. 6.9. This provides further evidence that the initial rise in viscosity with mAb1 concentration without added salt is caused by the formation of small reversible clusters. However, after the addition of 150 mM NaCl, the viscosity of mAb1 solutions remains larger than that of mAb2 solutions despite that the moving units of both are nearly identical in size.

By revisiting the SANS data, the strong increase in magnitude of $I(q)$ at low $q$-values with the addition of salt can be associated with the onset of a large length scale structure induced by transient mAb1 association. Scattering intensity, as well as the viscosity, of mAb1 solutions are larger than those of mAb2 solutions due to the slightly stronger interactions. Thus, while mAb1 attraction is weaker with added salt, it remains strong compared to mAb2, which was also observed in a previous study.[26]

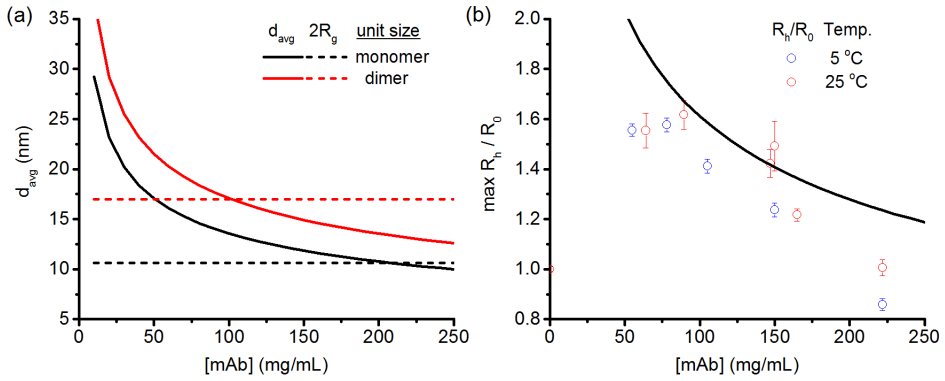


**Figure 6.10:** (a) The average separation distance between nearest mAbs (solid line), $d_{avg}$, is compared against the effective hydrodynamic diameter (dashed lines) of a mAb monomer and dimer as a function of protein concentration. (b) Maximum theoretical effective $R_h/R_0$ (solid line) as a function of concentration compared to estimates from NSE for mAb1 at $5°C$ and $25°C$.

This enhanced strength of attraction is expected to lead to a transient macromolecular network formed by weakly associated mAb1 monomers resulting in an enhancement of the viscosity relative to mAb2 solutions under similar conditions.

At very large concentrations, the large viscosities of mAb1 solutions without added salt also have significant contributions from inter-protein interactions, similar to the case of mAb1 solutions with added salt. The interactions in the former case are between dimers while in the latter are between monomers. Up to a protein concentration of about 100 mg/mL, the larger effective volume and steric hindrance of elongated dimers in mAb1 solution without added salt is correlated with the increase in viscosity. However, the apparent decrease in $R_h/R_0$ shown in Fig. 6.9 at higher concentrations is inconsistent with a direct correlation between cluster formation and enhanced solution viscosities. Therefore, while dimers are still present in mAb1 solutions without added salt ($R_h/R_0 > 1$), the continual increase in viscosity is proposed to result from dimer-dimer interactions. Modeling the trend in the effective hydrodynamic cluster size with protein concentration can provide insight into the onset of what appears to be stronger cluster interactions.

The decrease of the effective mAb1 cluster size in samples without salt above a concentration of about 100 mg/mL is a manifestation of the breakdown in assumptions inherent to the calculations of $R_h/R_0$. The high protein density in samples with a concentration above 100 mg/mL prevent a direct comparison of monomer and dimer (or larger cluster) mobility due to steric constraints. The short-time self diffusivity reflects the influence of protein interactions, microstructure and hydrodynamics on protein mobility. However, the soft, anisotropic and extended structure of mAb dimers suggests that the ensemble of configurations they can sample will be strongly influenced by the surrounding microstructure; much more so than monomers. This is readily demonstrated by considering a calculation shown in Fig. 6.10a by comparing the effective hydrodynamic diameter, $2R_h$, of monomers ($R_h \approx 5.3$ nm) and dimers (1.6 times the size of a monomer) with the average distance separating neighboring mAbs, $d_{avg} = (1/\rho)^{1/3}$, where $\rho$ is the protein number density. This comparison indicates that at about 100 mg/mL, dimers in an isotropically dispersed structure would have a smaller center-to-center separation than the hydrodynamic diameter of their "preferred" extended structure. Dividing $d_{avg}$ of a monodisperse solution of dimers by the $R_h$ of a monomer produces an estimate of the maximum possible apparent $R_h/R_0$ for mAb1 dimers. The result shows remarkably good agreement with the estimates of $R_h/R_0$ using NSE data at $25°C$ in Fig. 6.10b. Thus, rather than a reduction in the fraction of dimers (assuming a constant effective dimer size), the decrease in $R_h/R_0$ can be interpreted as a transition in cluster configuration to a more compact dimer structure due to crowding effects at higher concentrations. In another context, the same decrease in $R_h/R_0$ can be interpreted as a reduction in mAb1 cluster mobility due to enhanced hydrodynamic and/or inter-cluster interactions.

Changes in mAb2 solution viscosity with a change in temperature suggest that interactions can become important at high protein concentrations, even for a well dispersed protein. Although viscosity data for samples of both mAbs without added salt at $5°C$ is unavailable, the magnitude of a 150 mg/mL sample can be estimated by extrapolating the trend in the viscosity with varying amounts of salt in Fig. 6.1b to the

limit of 0 mM NaCl. Due to the negligible effect of NaCl on mAb2 solution viscosity, the influence of temperature will be consistent at all salt conditions. After normalization with the solvent viscosity at the corresponding temperature, mAb2 viscosities at $5°C$ are still roughly twice as large as those at $25°C$. This increase in reduced viscosity is a reflection of stronger interactions between mAb2 monomers dispersed in solution at lower temperature (regardless of salt content). While differences in $S_{eff}(q)$ at low-$q$ for mAb2 solutions in Fig. 6.4 appear negligible, even a marginal increase in interaction strength can produce larger viscosities and slower short time monomer diffusion due to the closer proximity of neighboring antibodies at high protein concentrations.

The temperature dependence of $R_h/R_0$ for mAb1 in solution without added salt, shown in Fig. 6.9 and Fig. 6.10b, suggests that the effective interactions influence the cluster mobility. The smaller apparent dimer size in mAb1 samples without added salt at $5°C$ does not necessarily indicate that dimers no longer form. Rather, the reduction in $R_h/R_0$ is an artifact of normalizing mAb1 diffusivity by a mobility of mAb2 monomers that have reduced mobility due to enhanced inter-protein interactions. Consequently, while densely packed dimers are believed to reduce the viscosity,[14] the close proximity of more compact dimers at higher protein concentrations leads to close-range interactions. Though a crowded environment may hinder the rearrangement of neighboring antibodies to become oriented in the lowest energy configuration, the small spacing allows very short range interactions to become significant contributions to the solution properties. Therefore, dimer interactions are expected to lead to a continual increase in viscosity in this high concentration regime with crowded local structures.

## 6.4 Influence of Solvent

By utilizing neutron scattering techniques to study the structure and dynamics of mAb formulations under concentrated conditions, the experimental signal-to-noise ratio was maximized by dissolution in heavy water. However, formulations of commercially available antibody-based therapeutics are dispersed in normal water. This difference may have a strong influence on the resulting solution properties, especially

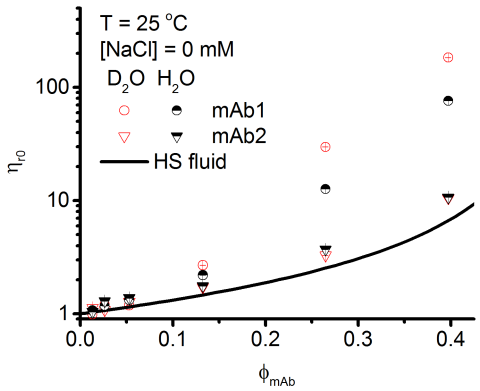


**Figure 6.11:** The reduced zero-shear viscosities of mAb1 (circles) and mAb2 (triangles) are compared between formulations of $D_2O$ (empty symbols) and $H_2O$ (half-filled symbols) at $25°C$ and 0 mM NaCl. These results are plotted relative to HS predictions (solid line).

if inter-protein interactions have a significant contribution from hydrogen bonding or hydrophobic forces. It is reported that the strength of hydrogen bonding of deuterium is stronger than that of hydrogen, [18] which would directly impact the solution structure in the case of hydrogen bonding mediated mAb-mAb interactions. If the mAb of interest has significant patches of hydrophobic surface residues, the stronger hydrogen bonding of deuterium would indirectly strengthen the hydrophobic force in heavy water due to a larger energetic "penalty" for deforming the surrounding water structure relative to normal water. Therefore, to test the influence of hydrogen-deuterium exchange on the viscosity and dynamics of mAb1 and mAb2 solutions, samples in buffers composed of both solvents are explicitly compared using DLS and SAXS, which is much less sensitive to isotope differences as compared to SANS.

The viscosity of mAb1 and mAb2 solutions with identical buffer compositions (with no added salt) suspended in $H_2O$ and $D_2O$ are compared in Fig. 6.11 relative to predictions for a HS fluid. To compare experimental data with the HS colloidal model, protein concentration is converted to an effective volume fraction as described earlier and demonstrated in Fig. 6.2. The relative viscosity of mAb2 solutions is independent

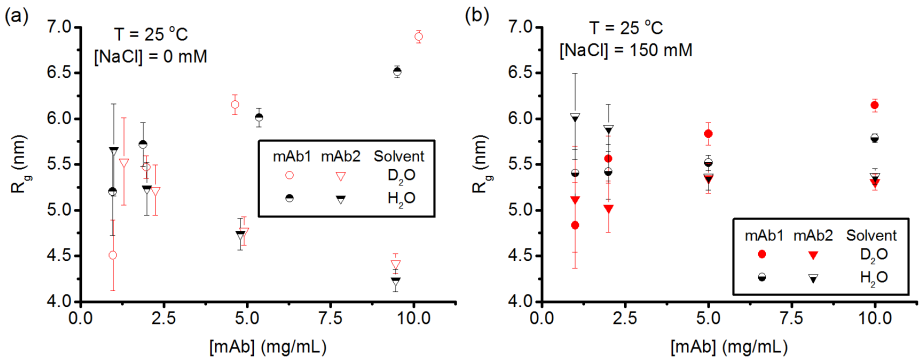


**Figure 6.12:** Values of $R_g$ determined from SAXS data are shown for mAb1 (circles) and mAb2 (triangles) samples with (a) 0 mM and (b) 150 mM added sodium chloride salt. Formulations in $H_2O$ are half-filled samples and in $D_2O$ are empty and filled symbols (0 mM and 150 mM NaCl, respectively).

of the solvent at all protein concentrations. In contrast to mAb2, the solvent influences the solution viscosity of mAb1 more significantly. At elevated protein concentrations, solutions composed of $H_2O$ are considerably less viscous than those in $D_2O$. Therefore, identifying the underlying influence of the solvent on inter-protein interactions requires further study of the resulting differences in the microstructure and dynamics.

Differences in mAb association when dissolved in $H_2O$ and $D_2O$ are compared through analysis of SAXS scattering profiles. Following an identical protocol to that described earlier in the chapter, an apparent radius of gyration and molecular mass can be estimated by a Guinier analysis of low-$q$ SAXS data. The effective $R_g$ of mAb1 and mAb2 in both solvents are compared in samples without salt (Fig. 6.12a) and with 150 mM NaCl (Fig. 6.12b). Furthermore, the apparent molecular weight is provided for an identical set of solution conditions in Fig. 6.13.

As was observed with the viscosity of mAb2 solutions, changing between $H_2O$ and $D_2O$ has no effect on the effective hydrodynamic size of mAb2 antibodies in solution. Additionally, the shift in apparent molecular mass with protein concentration is nearly identical in both solvents and at both salt conditions. Hence, mAb2 remains

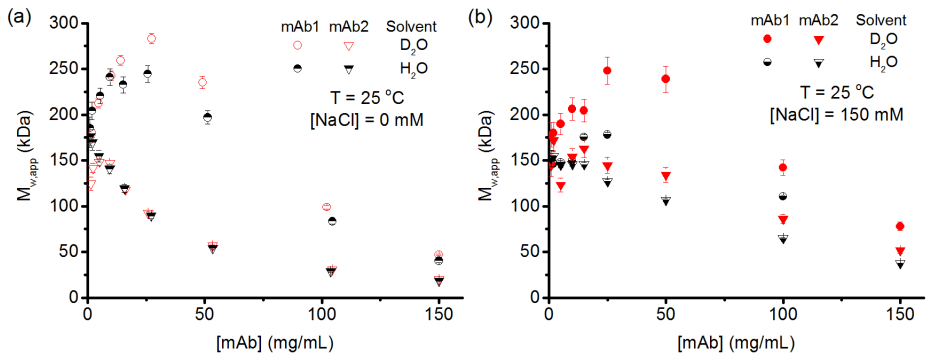


**Figure 6.13:** The same symbols as in Fig. 6.12 are used to distinguish the apparent molecular weight of formulations in $H_2O$ and $D_2O$.

well dispersed, regardless of the solvent used.

In contrast to mAb2, the solution behavior of mAb1 is quite sensitive to the solvent. For samples without salt, the effective cluster size in mAb1 solutions in $H_2O$ are smaller than those in $D_2O$. Interestingly, while the apparent molecular weight of mAb1 in $H_2O$ does not reach as large of a maximum as found in $D_2O$, they are relatively similar. This indicates that mAb1 associates into dimers without added salt in both solvents. Utilizing a lever rule, in which the effective $R_g$ indicates the relative amount of monomers and dimers, suggests that a smaller a fraction of dimers form in $H_2O$. The addition of NaCl has already been demonstrated to prevent association of mAb1 into small clusters, which is true for both deuterated and hydrogenated water. However, the maximum in mAb1 apparent molecular weight observed in $D_2O$ samples with 150 mM salt disappears when transitioned to buffers composed of $H_2O$.

Changes in viscosity with buffer composition can be interpreted physically by the changes in solution structure presented in Fig. 6.12 and Fig. 6.13. The viscosity of mAb2 solutions is independent of the solvent since mAb2 association is unchanged. This lack of sensitivity to the solvent suggests that hydrogen bonding has a minimal contribution to mAb2 interactions. By changing the solvent in mAb1 solutions from

$D_2O$ to $H_2O$, the extent of dimer formation is reduced, which corresponds with a decrease in solution viscosity by about a factor of two. This provides additional evidence that the formation of small dynamic clusters directly enhances the viscosity in concentrated mAb formulations. Further, the smaller $M_{w,app}$ values of mAb1 in $H_2O$ buffers with added salt reflects the smaller magnitude of $I(0)$ in the corresponding scattering patterns. Thus, the transient network-like association thought to maintain the larger viscosity of mAb1 relative to mAb2 in $D_2O$ with added salt is effectively destroyed when in $H_2O$. A weak peak in $M_{w,app}$ of mAb1 solutions with added salt can still be observed in Fig. 6.13, suggesting that a small amount of dimers may still form. While the corresponding viscosity data is unavailable, the results of this chapter would suggest that the viscosity of mAb1 and mAb2 in solutions of $H_2O$ with 150 mM NaCl will be similar, but slightly larger for mAb1 solutions due to the coexistence of dimers with monomers.

Two important conclusions can be made from examining the influence of solvent on the solution properties of these two antibodies. First, studying antibodies in heavy water is quantitatively representative of expected solution behavior in normal water. Hence, the conclusions made in earlier sections of this chapter are applicable to commercially relevant formulations. Further, explicitly comparing the structure and dynamics in each solvent can (at least qualitatively) identify whether hydrogen bonding or hydrophobic forces are a dominant contribution to the short range attractive interactions between mAbs. This methodology can thus be utilized to explicitly characterize their influence on solution properties, especially if the differences in hydrophobic and polar surface residues between two antibodies is known.

## 6.5 Conclusions

The formation of small dynamic clusters in mAb1 solutions has been shown to correlate directly with an increase in viscosity at elevated protein concentrations. Increases in viscosity are explicitly attributed to the formation of clusters with an extended conformation, which exclude a larger effective volume, and their resulting

interactions. An interesting observation is that mAb1 forms a preferred cluster size of a dimer at very low concentration ($\sim$ 10 mg/mL) that is maintained up to very high concentrations ($\sim$ 150 mg/mL), above which crowding effects seem to force cluster conformations to become more compact. These results agree with previous experiments[31, 34] and simulations,[4] which all support the idea that the small dynamic clusters arise from specific interactions due to the local electric dipole effect. Further, adding salt to these solutions decreases the average size of clusters, further supporting the hypothesis of charge-dipole induced attraction. Consequently, the viscosity is significantly reduced by reducing the cluster size. This suggests a unique method to control solution viscosity by strict control of protein cluster formation. Through the use of modern biomolecular engineering techniques (such as recombinant DNA), the primary sequence can be engineered to produce a preferred tertiary structure to mitigate protein interactions such as those found in mAb1 solutions to cause prohibitively large viscosities. The research presented in this chapter is a significant step towards the fundamental understanding of protein clustering as well as the development of mAb formulations with desired solution properties for commercial applications.

## REFERENCES


[1] Banchio, A. J., and Nägele, G. Short-time transport properties in dense suspensions: from neutral to charge-stabilized colloidal spheres. *J. Chem. Phys. 128*, 10 (Mar. 2008), 104903.

[2] Bu, Z., Biehl, R., Monkenbusch, M., Richter, D., and Callaway, D. J. E. Coupled protein domain motion in Taq polymerase revealed by neutron spin-echo spectroscopy. *Proc. Natl. Acad. Sci. U. S. A. 102* (2005), 17646–17651.

[3] Cardinaux, F., Zaccarelli, E., Stradner, A., Bucciarelli, S., Farago, B., Egelhaaf, S. U., Sciortino, F., and Schurtenberger, P. Cluster-Driven Dynamical Arrest in Concentrated Lysozyme Solutions. *J. Phys. Chem. B 115*, 22 (June 2011), 7227.

[4] Chaudhri, A., Zarraga, I. E., Kamerzell, T. J., Brandt, J. P., Patapoff, T. W., Shire, S. J., and Voth, G. A. Coarse-Grained Modeling of the Self-Association of Therapeutic Monoclonal Antibodies. *J. Phys. Chem. B 116* (July 2012), 8045.

[5] Curtis, J. E., Raghunandan, S., Nanda, H., and Krueger, S. SASSIE: A program to study intrinsically disordered biological molecules and macromolecular ensembles using experimental scattering restraints. *Comput. Phys. Commun. 183*, 2 (2012), 382–389.

[6] Daugherty, A. L., and Mrsny, R. J. Formulation and delivery issues for monoclonal antibody therapeutics. *Adv. Drug Deliv. Rev. 58*, 5-6 (Aug. 2006), 686–706.

[7] Eberle, A. P. R., Wagner, N. J., and Castañeda Priego, R. Dynamical Arrest Transition in Nanoparticle Dispersions with Short-Range Interactions. *Phys. Rev. Lett. 106*, 10 (Mar. 2011), 1.

[8] Falus, P., Porcar, L., Fratini, E., Chen, W.-R., Faraone, A., Hong, K., Baglioni, P., and Liu, Y. Distinguishing the monomer to cluster phase transition in concentrated lysozyme solutions by studying the temperature dependence of the short-time dynamics. *J. Phys. Condens. Matter 24*, 6 (Feb. 2012), 064114.

[9] Godfrin, P. D., Castañeda Priego, R., Liu, Y., and Wagner, N. J. Intermediate range order and structure in colloidal dispersions with competing interactions. *J. Chem. Phys. 139*, 15 (2013), 154904.

[10] Godfrin, P. D., Hudson, S. D., Hong, K., Porcar, L., Falus, P., Wagner, N. J., and Liu, Y. Excess viscous response from intrinsic structural heterogeneity caused by competing potential features. *Submitt. to Phys. Rev. Lett.* (2015).

[11] Godfrin, P. D., Valadez-Pérez, N. E., Castañeda Priego, R., Wagner, N. J., and Liu, Y. Generalized phase behavior of cluster formation in colloidal dispersions with competing interactions. *Soft Matter 10* (2014), 5061.

[12] Harris, R. J., Shire, S. J., and Winter, C. Commercial manufacturing scale formulation and analytical characterization of therapeutic recombinant antibodies. *Drug Dev. Res. 61*, 3 (Mar. 2004), 137–154.

[13] Israelachvili, J. N. *Intermolecular and Surface Forces*, 3rd editio ed. Elsevier, 2011.

[14] Johnston, K. P., Maynard, J. A., Truskett, T. M., Borwankar, A. U., Miller, M. A., Wilson, B. K., Dinin, A. K., Khan, T. A., and Kaczorowski, K. J. Concentrated Dispersions of Equilibrium Protein Nanoclusters That Reversibly Dissociate into Active Monomers. *ACS Nano 6*, 2 (Jan. 2012), 1357.

[15] Kline, S. R. Reduction and analysis of SANS and USANS data using IGOR Pro. *J. Appl. Crystallogr. 39* (2006), 895–900.

[16] Lionberger, R. A., and Russel, W. B. A Smoluchowski theory with simple approximations for hydrodynamic interactions in concentrated dispersions. *J. Rheol. (N. Y. N. Y). 41*, 2 (Mar. 1997), 399.

[17] Liu, Y., Porcar, L., Chen, J., Chen, W.-r., Falus, P., Faraone, A., Fratini, E., Hong, K., and Baglioni, P. Lysozyme protein solution with an intermediate range order structure. *J. Phys. Chem. B 115*, 22 (June 2011), 7238.

[18] López-Barrón, C. R., and Wagner, N. J. Solvent isotope effect on the microstructure and rheology of cationic worm-like micelles near the isotropic-nematic transition. *Soft Matter 7*, 22 (2011), 10856.

[19] Malfois, M., Bonnete, F., Belloni, L., and Tardieu, A. A model of attractive interactions to account for fluidfluid phase separation of protein solutions. *J. Chem. Phys. 105*, 8 (1996), 3290.

[20] Mewis, J., and Wagner, N. J. *Colloidal Suspension Rheology*. Cambridge University Press, New York, 2012.

[21] Muschol, M., and Rosenberger, F. Liquid  liquid phase separation in supersaturated lysozyme solutions and associated precipitate formation / crystallization. *J. Chem. Phys. 107*, 6 (1997), 1953.

[22] Nagele, G. On the dynamics and structure of charge-stabilized suspensions. *Phys. Rep. 272*, 5-6 (1996), 215–372.

[23] Porcar, L., Falus, P., Chen, W.-R., Faraone, A., Fratini, E., Hong, K., Baglioni, P., and Liu, Y. Formation of the Dynamic Clusters in Concentrated Lysozyme Protein Solutions. *J. Phys. Chem. Lett. 1*, 1 (Jan. 2010), 126.

[24] Rosenbaum, D., Zamora, P., and Zukoski, C. Phase behavior of small attractive colloidal particles. *Phys. Rev. Lett. 76*, 1 (Jan. 1996), 150.

[25] Sandler, S. *An Introduction to Applied Statistical Thermodynamics*. John Wiley and Sons, 2011.

[26] Scherer, T. M., Liu, J., Shire, S. J., and Minton, A. P. Intermolecular Interactions of IgG1 Monoclonal Antibodies at High Concentrations Characterized by Light Scattering. *J. Phys. Chem. B 114* (2010), 12948–12957.

[27] Sciortino, F., Mossa, S., Zaccarelli, E., and Tartaglia, P. Equilibrium Cluster Phases and Low-Density Arrested Disordered States: The Role of Short-Range Attraction and Long-Range Repulsion. *Phys. Rev. Lett. 93*, 5 (July 2004), 5.

[28] Sciortino, F., Tartaglia, P., and Zaccarelli, E. One-dimensional cluster growth and branching gels in colloidal systems with short-range depletion attraction and screened electrostatic repulsion. *J. Phys. Chem. B 109*, 46 (2005), 21942.

[29] Smolin, N., Biehl, R., Kneller, G. R., Richter, D., and Smith, J. C. Functional domain motions in proteins on the ˜ 1-100 ns timescale: Comparison of neutron spin-echo spectroscopy of phosphoglycerate kinase with molecular-dynamics simulation. *Biophys. J. 102*, 5 (2012), 1108–1117.

[30] Yadav, S., Laue, T. M., Kalonia, D. S., Singh, S. N., and Shire, S. J. The influence of charge distribution on self-association and viscosity behavior of monoclonal antibody solutions. *Mol. Pharm. 9*, 4 (Apr. 2012), 791–802.

[31] Yadav, S., Liu, J. U. N., Shire, S. J., and Kalonia, D. S. Specific Interactions in High Concentration Antibody Solutions Resulting in High Viscosity. *J. Pharm. Sci. 99*, 3 (2010), 1152–1168.

[32] Yadav, S., Sreedhara, A., Kanai, S., Liu, J., Lien, S., Lowman, H., Kalonia, D. S., and Shire, S. J. Establishing a link between amino acid sequences and self-associating and viscoelastic behavior of two closely related monoclonal antibodies. *Pharm. Res. 28*, 7 (July 2011), 1750–64.

[33] Yearley, E. J., Godfrin, P. D., Perevozchikova, T., Zhang, H., Falus, P., Porcar, L., Nagao, M., Curtis, J., Gawande, P., Taing, R., Zarraga, I. E., Wagner, N. J., and Liu, Y. Observation of small cluster formation in concentrated monoclonal antibody solutions and its implications to solution viscosity. *Biophys. J. 106*, 8 (2014), 1763–1770.

[34] Yearley, E. J., Zarraga, I. E., Shire, S. J., Scherer, T. M., Gokarn, Y., Wagner, N. J., and Liu, Y. Small-Angle Neutron Scattering Characterization of Monoclonal Antibody Conformations and Interactions at High Concentrations. *Biophys. J. 105* (2013), 720–731.

[35] Zarraga, I. E., Taing, R., Zarzar, J., Luoma, J., Hsiung, J., and Patel, A. High Shear Rheology and Anisotropy in Concentrated Solutions of Monoclonal Antibodies. *J. Pharm. Sci. 102*, 8 (2013), 2538–2549.

[36] Zemb, T., and Lindner, P. *Neutrons, X-rays and Light: Scattering Methods Applied to Soft Condensed Matter*. Elsevier B.V., Amsterdam, 2002.

# Chapter 7

# VISCOUS RESPONSE OF LARGE TRANSIENT CLUSTERS IN CONCENTRATED MONOCLONAL ANTIBODY FORMULATIONS

## 7.1 Introduction

The successful commercialization of biopharmaceutical therapeutic products is facilitated by understanding the relationship between protein structure and solution properties, such as stability or viscosity, in addition to the connection between structure and biological functionality. A significant challenge in product development is maintaining bioefficacy from production through storage and delivery, which can be described by an energy landscape formed from effective intra- and inter-protein interactions.[5, 11, 14, 30] Depending on the solution conditions (pH, temperature, ionic strength, salt valency, etc.) and protein composition/structure, proteins may partially unfold and irreversibly aggregate, or reversibly associate with each other while maintaining their native structure.[32] While the former renders therapeutics ineffective or even deadly,[35, 36] the latter can have strong effects on manufacturability and product delivery.[17, 42]

Both specific and nonspecific interactions contribute to protein association, while the nonspecific interactions are more common and sometimes the determining factor for certain complex protein structures.[33] It has been demonstrated in the previous chapter and other studies that some mAbs in solution under specific physiochemical conditions can form small reversible clusters and exhibit a dramatic increase in solution viscosity with increasing concentration and/or decreasing temperature.[22, 44, 46, 47, 48, 49] Relatively small deviations to the primary sequence can cause an order of magnitude difference in solution viscosity at elevated concentrations.[45, 46, 47, 50] As

a result, biologically unimportant deviations in protein primary sequence can significantly affect the ability to produce and deliver these mAbs as a therapeutic product.[42] This chapter explores the solution behavior of a mAb similar to, but more hydrophobic than, those explored in the previous chapter and is found to have equivalently large viscosities depending on the solution conditions.

Due to the highly non-spherical shape and heterogeneous charge distribution on its surface, mAbs are challenging to study, especially at high concentrations.[7, 44, 48, 49] The previous chapter and other recent work has extended the use of effective potentials to model mAb formulations and show that a type of reversible cluster formation is the underlying source of the anomalous transport properties observed at high protein concentrations.[48, 49] In these solutions, in the presence of very low salt concentration, the formation of long lived, small, elongated clusters is driven by an anisotropic electrostatic-driven attraction acting between mAbs. These clusters are the driving force of a significantly high solution viscosity.[48] Adding salt in large amounts weakens the anisotropic attraction, which reduces the number of clusters and results in a significant decrease of the viscosity.

This chapter presents an IgG1 monoclonal antibody that has been the subject of previous research showing a complex solution behavior as a function of protein concentration, ionic strength and temperature.[22] Of particular relevance here, Lilyestrom et al. showed that this mAb has both compact and elongated monomer structures at very low concentration.[21] Importantly, this previous research demonstrates that the tertiary conformation of mAb3 does not change with variations in temperature and added sodium sulfate concentration. In further work, this group demonstrated that a very slight increase in mAb concentration in the presence of $Na_2SO_4$ produces extended dimers as shown by small angle X-ray scattering.[22] Furthermore, reversible cluster formation is observed with increasing mAb concentration as derived from modeling of static light scattering results.[22, 38] The authors conclude that the dilute and semi-dilute mAb solution viscosity correlates linearly with the equilibrium cluster size.[22]

However, important questions remain about the structure of the clusters in concentrated solutions, the dynamic exchange of proteins in and out of these clusters, and the quantitative relationship between these dynamic clusters and the rheology.

Methods to address these questions on the nanoscale have been demonstrated so far in this dissertation and in prior work by combining neutron spin echo, small angle neutron scattering, dynamic light scattering and rheology. These methods have shown both similarities as well as differences in the behavior for concentrated solutions of several monoclonal antibodies. In particular, the behavior of this mAb with added salt is contrary to prior reports for a related mAb discussed in the previous chapter.[48, 49]

The work by Lilyestrom et al. is complimented in this chapter by investigating the motion of the same mAb on the nanosecond and nanometer time scales to identify the fundamental diffusing units over similar solution conditions. The combination of neutron techniques with DLS and viscosity measurements shows that the underlying physical mechanism driving the high viscosity in concentrated mAb solutions is similar for both mAb solutions. Namely, the increase of viscosity is due to the formation of reversible protein clusters. However, the inter-protein microstructure is found to be even more complex in the current study. Using neutron scattering techniques, the addition of salt is shown to promote the formation of small clusters that persist to high concentration. Importantly, the strongly bounded, small clusters interact with each other to form loosely bounded transient networks, probed by rheology. This hierarchical structuring of clusters is different from the observations reported in the previous chapter, and significantly increases the viscosity of the concentrated protein solutions. Therefore, this study builds upon previous work[22] by explicitly measuring the structure and dynamics over a range of conditions to identify the physical mechanism underlying the significant increase in solution viscosity with increasing mAb concentration. The body of work presented in this chapter is composed of published results.[16]

## 7.2 Materials and Experimental Techniques

### 7.2.1 Materials

The monoclonal antibody examined in this chapter is a humanized IgG1 protein produced by Genentech, Inc. referred to as mAb3 as the two mAbs in the previous chapter were labeled mAb1 and mAb2. However, mAb3 as it is labeled here is the same antibody referred to as mAb1 in two previous publications.[21, 22] The protein was expressed in Chinese hamster ovarian (CHO) cells and subsequently purified by multiple chromatographic methods including ion exchange chromatography. The antibody was then dialyzed into a buffer composed of 20 mM $_{\text{L}}$-histidine hydrochloride (His-Cl) in deuterium oxide ($D_2O$ or heavy water) at pH 6.0 with 0.02 wt% polysorbate-20 surfactant and two concentrations of sodium sulfate salt (0 mM and 50 mM). A stock solution with a mAb3 concentration of 150 mg/mL was obtained using tangential flow filtration and diluted for all concentrations studied. All samples were stored at 4 $^{\circ}C$ between production and experimentation. Samples with 50 mM $Na_2SO_4$ were fabricated by spiking the salt free stock solution with a 1 M $Na_2SO_4$ buffer solution.

### 7.2.2 Small Angle Neutron Scattering

Small angle neutron scattering (SANS) experiments were analyzed as discussed in Chapter 2 using previously reported protocols and methods.[31, 48, 49] The scattering intensity was obtained over scattering vectors or $q$-values ranging from 0.003 $\text{Å}^{-1}$ to 0.53 $\text{Å}^{-1}$. All samples were held in standard quartz Hellma cells at ILL and custom titanium cells with quartz windows at NCNR. Low concentration samples were studied using cells with a 2 mm path length to enhance intensity with minimal multiple scattering effects, while concentrated samples were studied in cells with a 1 mm path length. A range of mAb concentrations were studied at two temperatures, (5$^{\circ}C$ and 25$^{\circ}C$).

The scattering intensity from a solution of isotropic, monodisperse scatterers is a function of the particle volume fraction, $\phi$, the volume of one individual particle, $V$, and the scattering length density (SLD) difference between the particle and solvent, $\Delta\rho$,

as outlined in Chapter 2. Particle shape is represented by the normalized particle form factor, $P(q)$, that is the Fourier transformation of the intra-particle density correlations. Lastly, inter-particle correlations are represented by the solution structure factor, $S(q)$, which is related to the Fourier transformation of the pair distribution function, $g(r)$.[51]

The scattering intensity from a solution of (slightly) non-spherically symmetric particles such as mAbs, for which the intra- and inter- particle correlations cannot be decoupled, is represented by[8, 24]

$$I(q) = \phi V(\Delta\rho)^2 P(q)[1 + \beta(q)(S(q) - 1)] + B. \tag{7.1}$$

Here, all parameters have been defined previously in Chapter 2 except $\beta(q)$, the decoupling function, which is a $q$-dependent function of the protein shape. Practically, $\beta(q)$ is used to relate the experimentally accessible function $S_{eff}(q)$, defined previously as the term in square brackets in Eq. 7.1, to the theoretically predictable function $S(q)$, the structure factor of a spherically symmetric system. Thus, a coarse-grained 12 bead model of mAb structure, discussed in detail in the following section, is fit to the mAb form factor to calculate $\beta(q)$. Here, a 2 mg/mL sample under each solution condition studied is used to represent $P(q)$. By minimizing the residual between the data and model, the most representative protein conformation can be observed in real space coordinates. For the purposes of this study, the model is sufficiently sensitive enough to distinguish between compact and elongated structures.

Using integral equation theory, $S(q)$ can be directly related to the parameters of an effective interaction potential for a system with an isotropic interaction.[27] Even though mAb proteins have anisotropic interactions, the experimental data can be effectively fit using an isotropic interaction potential to approximately evaluate the potential parameters at different conditions. However, one must be cautious when interpreting these fitting results. Previous studies have successfully represented globular protein interactions by a combination of attractive and repulsive forces.[6, 9, 25] Therefore, the data are fit with the hard sphere double Yukawa (HSDY) potential, discussed in detail

in previous chapters. Estimates of the structure factor are generated by combining the HSDY potential with a thermodynamically self-consistent closure relation.[19]

The ensemble average radius of gyration, $R_g$, and molecular weight, $M_w$, can be calculated in the limit of very small $q$-values, and are used to quantify the effect of solution conditions on the extent of mAb clustering. Specifically, the Guinier analysis method described in the previous chapter can be used to calculate $R_g$ from the slope of Eq. 6.1 and $M_w$ by Eq. 6.2 using the extracted value of $I(0)$. However, as the concentration is increased, interactions will become a significant contribution to scattering at low $q$-values. Therefore, the molecular weight extracted from such an analysis will be an apparent molecular weight, $M_{w,app}$, similar to that obtained by static light scattering.[21, 22]

### 7.2.3 Form Factor Modeling

To quantify the effect of solution conditions on inter-protein interactions, SANS data are normalized according to Eq. 7.1 and fit using the Ornstein-Zernike equation and a closure relation (Eq. 2.7 and Eq. 2.9, respectively) with the HSDY potential (Eq. 2.1 in Chapter 2) to quantitatively extract interaction parameters. The conformation of a protein in solution is coupled to the structure factor such that using a spherically averaged protein conformation for the form factor, $P(q)$, leads to an effective structure factor, $S_{eff}(q)$, in Eq. 7.1. The $S_{eff}(q)$ function can be related to the actual structure factor, $S(q)$, through the decoupling function. A method is presented here to quantify the scattering contributions of the non-spherically symmetric mAb structure and their center of mass correlations in solution.

Equation 2.11 is a physically intuitive representation of the $q$-dependence of the scattering intensity that is derived from a more fundamental relationship for the particular scenario of a monodisperse suspension of isotropic scatterers. More generally, the scattering intensity, $I(q)$, is related to the correlation of the scattering length

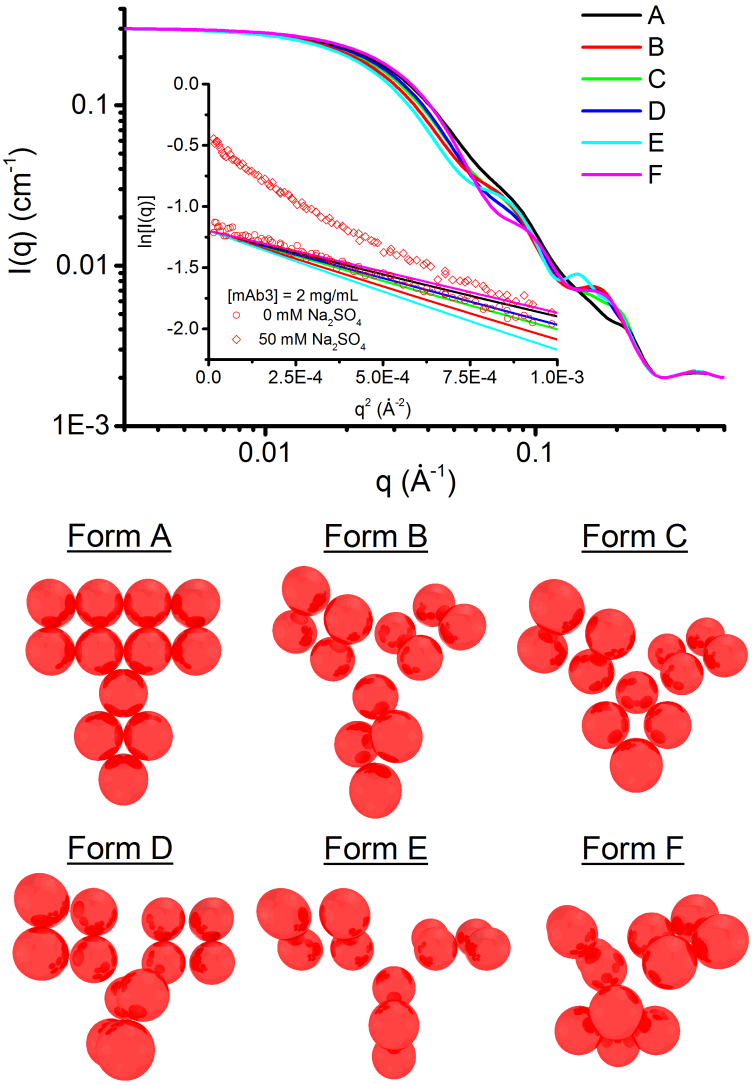


**Figure 7.1:** Scattering intensities are plotted as a function of $q$-value for six different mAb form factor structures represented by the 12 bead model, shown below (inset highlights the middle $q$-range).

densities in solution by

$$I(q) = \frac{1}{V}\left\langle \left[\int_V \rho(r)e^{iqr}\mathrm{d}r\right]\left[\int_V \rho(r')e^{-iqr'}\mathrm{d}r'\right]\right\rangle, \tag{7.2}$$

where $\rho$ is the neutron SLD at a given position, $r$, and the angled brackets indicate an average over all orientations. Introducing the center of mass location of a centralized particle, $r_i$, and a position relative to this particle as $x = r - r_i$, Eq. 7.2 can be further decomposed into the product of correlations within a particle and between particles as

$$I(q) = \frac{1}{V}\left\langle \sum_{i=1}^{N}\sum_{j=1}^{N} F_i(q)F_j^*(q)e^{-iq(r_i-r_j)}\right\rangle, \tag{7.3}$$

where $F(q)$ is the Fourier transformation of the spacial distribution of neutron scattering length densities defined as

$$F(q) = \left\langle \int_{V_p} \rho(x)e^{iqx}\mathrm{d}x\right\rangle \tag{7.4}$$

and $V_p$ indicates the integral is performed over the volume of a particle. In a system of spherically symmetric particles, the intra-particle and inter-particle correlations can be decoupled (i.e., $\langle AB\rangle = \langle A\rangle\langle B\rangle$), leading to a simplification of Eq. 7.3 to

$$I(q) = \frac{N}{V}\left\langle F_i(q)F_j^*(q)\right\rangle\left\langle \frac{1}{N}\sum_{i=1}^{N}\sum_{j=1}^{N} e^{-iq(r_i-r_j)}\right\rangle, \tag{7.5}$$

which is identical to Eq. 2.11, where the right bracket in Eq. 7.5 is the definition of $S(q)$. Since the system is composed of identical particles then $\langle F_i(q)F_j^*(q)\rangle = \langle|F(q)|^2\rangle = P(q)$, which is referred to as the particle form factor.

In the case of asymmetric particles, the orientational average of intra-particle density correlations can be decomposed, as demonstrated previously,[8] according to

$$\langle F_i(q)F_j^*(q)\rangle = \big(\langle|F(q)|^2\rangle - |\langle F(q)\rangle|^2\big)\delta_{ij} + |\langle F(q)\rangle|^2, \tag{7.6}$$

where $\delta_{ij}$ is the Kronecker delta function. The decoupling function, $\beta(q)$, is then defined as

$$\beta(q) = \frac{|\langle F(q)\rangle|^2}{\langle|F(q)|^2\rangle}, \tag{7.7}$$

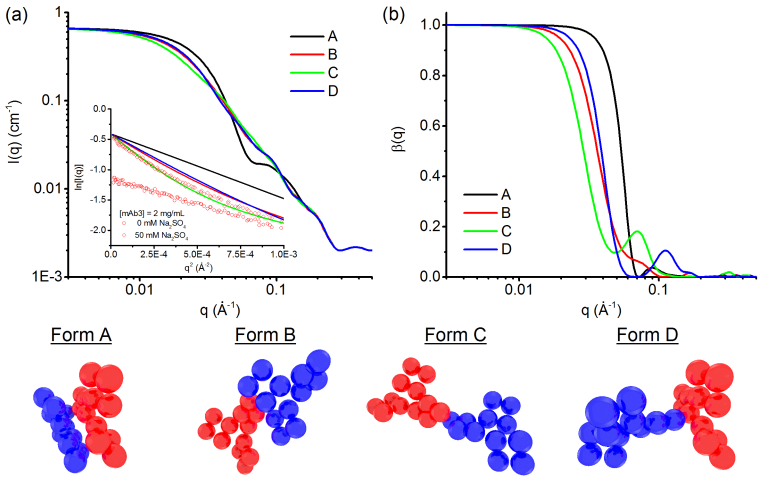


**Figure 7.2:** (a) Scattering intensities and (b) decoupling functions are plotted over a range of $q$-values for four dimer form factors constructed from the 12 bead model shown below.

which normalizes the orientation dependence of the scattering amplitude by the average scattering magnitude. Substitution of Eq. 7.7 and Eq. 7.6 into Eq. 7.5 results in

$$I(q) = \frac{N}{V}\langle|F(q)|^2\rangle\big(1 + \beta(q)[S(q) - 1]\big). \tag{7.8}$$

Once a suitable geometric form is chosen, the same functional form of $\beta(q)$ can be used to normalize the scattering intensity under all solution conditions as it is a function of shape only.

A representative shape is constructed to numerically calculate the decoupling function while imposing geometric and chemical constraints. For the former, the complex multi-domain structure of mAbs has been represented previously in coarse-grained dynamic simulation studies using spherical beads with particular orientations.[7] This shape is mimicked using 12 spheres arranged in three groups of four beads to approximate each of the three arms in a mAb, depleted for several configurations in Fig. 7.1. The size and orientation of all 12 spheres are allowed to vary to best fit the experimental data, requiring 13 parameters. The latter constraint of chemical similarity is imposed via the SLD difference. An estimate of mAb3 SLD is calculated using its

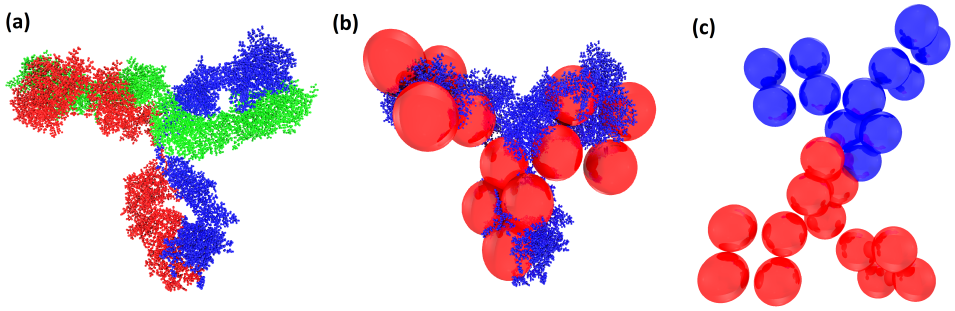


**Figure 7.3:** (a) The mAb3 crystal structure is shown, with each domain given a different color. The best fit structures from the 12-bead model of a 2 mg/mL mAb3 sample with (b) 0 mM and (c) 50 mM sodium sulfate salt. The monomeric structure is compared with the crystal structure in (b).

primary sequence and theoretical values for the intrinsic volume and neutron SLD of each amino acid.[18] Each sphere in the model has the same SLD, which is adjusted by a few percent of the calculated value to fit the data. Uncertainty in the density and hydration layer is allowed for by this slight adjustment in the SLD. The error between fitted and theoretical values was accounted for when the model sphere SLD was normalized by its volume relative to the protein such that the values of the pre-factor $\phi V(\Delta\rho)^2$ were nearly identical.

To demonstrate the sensitivity of the given model to different mAb conformations, a variety of orientations of the 12 spheres is constructed and their theoretical 1-D SANS profiles subsequently calculated. The results are provided in Fig. 7.1 with their corresponding structures. The most notable difference between scattering patterns of the six conformations is in the intensity at the slight peak and shoulder observed at $q$-values of roughly 0.2 $\text{Å}^{-1}$ and 0.1 $\text{Å}^{-1}$, respectively. The inset focuses on the slight differences in this $q$-range. A similar trend is observed in Fig. 7.2 for models of a mAb dimer composed of four different orientations of two identical monomer structures. The inset indicates that SANS intensities are less sensitive to changes in the configuration of dimers as compared to monomers. However, the second panel in Fig. 7.2 demonstrates a significant shift in the decoupling function intensity to higher $q$-values for

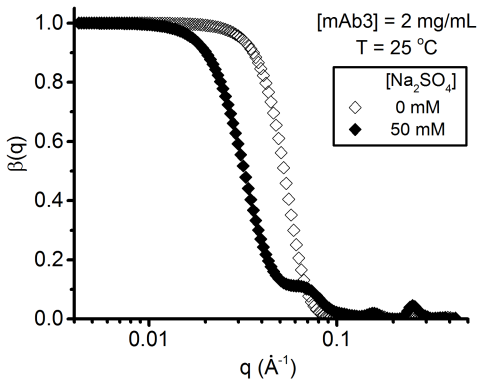


**Figure 7.4:** The decoupling functions corresponding to the best fit structures pictured in Fig. 7.3 are plotted as a function of $q$-value. The range of $q$-values over which smearing of protein interactions becomes significant, $\beta(q) < 0.1$, is shifted between the monomer and dimer structures.

more compact dimer structures. When normalizing the effective structure factor, such a shift could produce large deviations in the $q$-dependence of $S(q)$.

The most representative 12 bead model structures are shown in Fig. 7.3 by fitting a 2 mg/mL sample under each condition of sodium sulfate. In the case of no added electrolyte, the crystal structure of mAb3 is compared to the best fit coarse grained monomer structure. Both structures are remarkably similar, showing that configurations do not differ between the solid and fluid states. Fitting the form factor with 50 mM sodium sulfate required using a dimer structure composed of two monomers, each with a structure nearly identical to the configuration extracted from the sample without salt as the basic scattering unit. As seen from the image, the dimer appears elongated (that will be demonstrated later to agree with low concentration SANS and DLS data). The corresponding decoupling functions are plotted in Fig. 7.4 for these two model structures. Clearly, the larger and more elongated dimer leads to a decay in $\beta(q)$ intensity at smaller $q$-values. Normalized structure factors will therefore have a more significant smearing of mAb-mAb correlations in solutions with sodium sulfate.

### 7.2.4 Neutron Spin Echo

Samples were prepared for neutron spin echo (NSE) experiments on site, pipetted into 1 mm square quartz cells, and stored in a custom temperature controlled sample chamber. All samples were allowed 30 - 60 minutes to reach thermal equilibrium at each of the temperatures studied. Intermediate scattering functions (ISF), represented as $F_s(q,t)$, were obtained with the correlation time up to 50 ns at 30 - 35 $q$-value points ranging from 0.03 $\text{Å}^{-1}$ to 0.20 $\text{Å}^{-1}$ at each sample condition studied.

As a reminder, NSE is used to probe the short time dynamics over a range of lengthscales, defined as correlation times within the Brownian dynamics regime. This timescale is defined as $\tau_B \ll t \ll \tau_I$, where $\tau_B$ is the momentum relaxation time and $\tau_I = (R_g^2)/D_0$ is the structural relaxation or interaction time.[1] Based on the protein's size ($R_g \approx 5$ nm) and bare diffusion ($D_0 \approx 37\mu m^2/s$ at 25 $^\circ C$), the NSE correlation times explored here probe the short-time diffusion of mAb3.

In the short-time limit, the ISF is fit with a single exponential function to extract a $q$-dependent collective diffusion coefficient, $D_c(q)$, where $D_c(q) = D_0(H(q)/S(q))$ and $D_0$ is the free diffusion coefficient representing particle mobility in the infinitely dilute limit.[1, 29] The hydrodynamic function, $H(q)$, represents the effect of hydrodynamic interactions due to the flow of solvent molecules generated by particle motion. $H(q)$ can be decomposed into a $q$-independent term, $D_s/D_0$, the short-time self diffusion coefficient, and a distinct hydrodynamic function, $H_d(q; S(q))$, which is a function of the solution structure factor and therefore particle interactions. In the limit of large $q$-values, $S(q)$ approaches a value of 1 and $\lim_{q\to\infty} H(q) = D_s/D_0$, leading to $\lim_{q\to\infty} D_c(q) = D_s$.[12, 31] Therefore, the short-time self diffusion of mAb3 can be extracted from the high $q$-value limit of NSE data.

### 7.2.5 Dynamic Light Scattering

A DynaPro NanoStar instrument was used for dynamic light scattering (DLS) measurements of mAb formulations over a range of concentration and temperature conditions. All samples were allowed to thermally equilibrate at each temperature for

30 minutes before taking five independent measurements of the scattered intensity. The instrument was operated with a 663 nm wavelength laser at 90° scattering angle. The scattering wave vector was calculated according to $q = [4\pi/\lambda]\sin[\theta/2]$, where $n$ is the refractive index of the sample determined by $n = n_s + c_{mAb}(dn/dc)$. The solvent refractive index, $n_s$, was assumed equal to pure $D_2O$ (1.328) and the concentration dependence was captured by a value of $dn/dc = 0.185$ mL/g.

The output from the DLS experiments is a digital autocorrelation function that is analyzed as discussed in Chapter 2 in order to quantify the collective diffusion coefficient. In the limit of high protein concentration, multiple relaxation modes may exist in solution, which is revealed by a non-linear slope when plotting the ISF as a function of time on a semi-log plot. The dynamics in mAb solutions appears to transition from a single relaxation mode to two modes with increasing concentration. Therefore, the ISF is modeled using a double exponential decay, which extracts a primary, $D_{C,1}(q)$, and secondary, $D_{C,2}(q)$, relaxation mode according to:

$$\frac{F_s(q,t)}{F_s(q,0)} = A_1 \exp[-q^2 D_{c,1}(q)t] + A_2 \exp[-q^2 D_{c,2}(q)t]. \tag{7.9}$$

At low concentration, the effective hydrodynamic radius, $R_h$, can then be estimated according to the Stokes-Einstein-Sutherland relation

$$R_h = \frac{kT}{6\pi\eta_s D_{c,1}}, \tag{7.10}$$

where $\eta_s$ is the solvent viscosity and $k$ is the Boltzmann constant.

### 7.2.6 Rheology

The viscosity of each mAb sample was obtained using an Anton Paar MCR-301 rheometer with a titanium cone (50 mm, 0.3 degrees), which required a sample volume of 175 $\mu$L. Each sample was allowed to equilibrate at each temperature for 20 minutes, during which a solvent trap was used to minimize solvent evaporation. Steady shear measurements were made by ramping the shear rate, $\dot{\gamma}$, up from $10s^{-1}$ to $10,000s^{-1}$ and back down to check for reversibility. The viscosity at each shear rate was

determined from the average stress measured over a given time window, which followed the logarithmic shift in shear rate from $30s^{-1}$ to $5s^{-1}$. The zero shear viscosity was calculated as the average value of the data points within the plateau region at low shear rate. The upper limit of this region varied from $200s^{-1}$ at the highest concentrations to $1000s^{-1}$ at low concentrations.

Samples with 50 mM $Na_2SO_4$ at $5°C$ showed hysteresis during the ramp up and back down over the full range of shear rates. According to previous work,[41] this phenomenon is likely the result of association of protein at the air-water interface despite the presence of surfactant in the buffer. To resolve the issue, these samples required a short (3 minute) pre-shear step at $1000s^{-1}$ before performing the ramp from low to high shear rate. The shear rate dependence measured by this method was reproducible in both ramp directions.

### 7.3 Results

Measurements of the zero shear viscosity of mAb3 are summarized in Fig. 7.5a as a function of protein concentration for the four solution conditions studied. Not surprisingly, a distinctive, strong increase in viscosity is observed with increasing protein concentration for all formulation conditions. However, samples at higher ionic strength have consistently higher viscosities. The enhanced viscosities observed at $5°C$ for both salt conditions are due in part to the temperature dependence of the buffer viscosity, which is removed when normalizing the data by the buffer viscosity to yield the relative viscosities shown in Fig. 7.5b. This comparison shows that lowering the temperature results in an increase in the viscosity above that of the temperature dependence of the suspending medium.

It is of great interest to identify the underlying microscopic forces leading to the different macroscopic viscosities shown in Fig. 7.5. For example, the choice of buffer dictates which formulations meet the "syringeability" criteria at elevated protein concentrations, typically requiring viscosities much below 50 mPa-s.[17] The influence of temperature and salt on viscosity is apparent for protein concentrations as low as 35

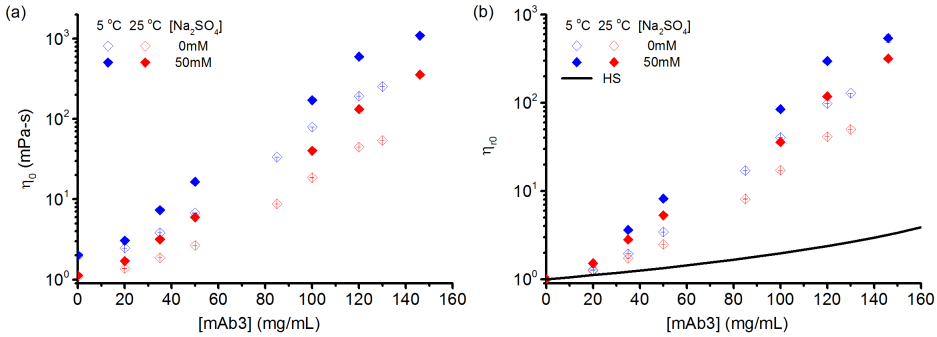


**Figure 7.5:** The (a) absolute magnitude and (b) reduced zero-shear viscosity is plotted for all conditions of mAb3 concentration, temperature, and salt content studied. The viscosity under all conditions increases significantly with protein concentration while reducing temperature and increasing salt content have similar effects on the magnitude of the relative viscosity.

mg/mL. By 120 mg/mL, the formulation with the lowest (0 mM $Na_2SO_4$ at 25°$C$) and highest (50 mM $Na_2SO_4$ at 5°$C$) viscosities differ by nearly an order of magnitude. The change in viscosity is influenced by both increasing ionic strength and reducing temperature, which are known to affect the net attractive strength between proteins.[26] Adding 50 mM sodium sulfate screens electrostatic repulsion between individual antibodies, potentially allowing attraction induced association to become more prevalent. Further, decreasing the temperature may enhance short-range attractive interactions as observed in lysozyme solutions.[34]

SANS experiments are performed on these solutions to gain some physical insight into the protein-protein interactions that mediate the solution microstructure and bulk properties such as viscosity. SANS scattering intensities of mAb3 formulations at several protein concentrations under the four solution conditions of interest are shown in Fig. 7.6.

For solutions without added electrolyte, increasing protein concentration leads to the development of a structure peak in the scattering evident as a maximum in the overall scattering intensity. The "correlation hole" at low-$q$ evident by the reduction in

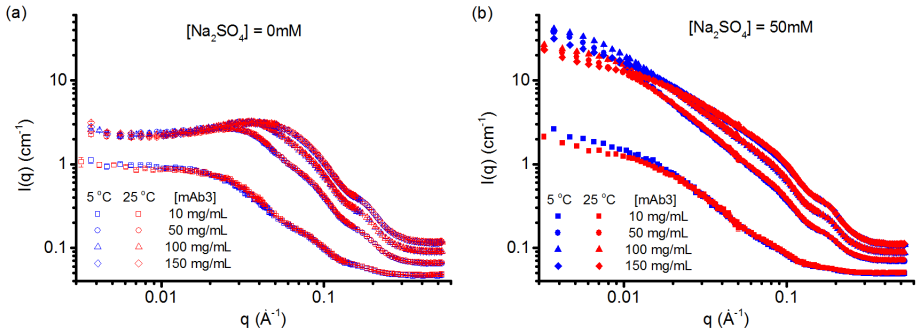


**Figure 7.6:** Reduced 1-D scattering profiles are plotted on the same scale for several mAb concentrations with (a) 0 mM and (b) 50 mM added sodium sulfate salt. The addition of salt leads to significantly higher intensities at low $q$-values, indicating the presence of larger scale structures.

forward scattering corresponds to a decrease in osmotic compressibility typical for concentrated systems with strong repulsive interactions.[37] Furthermore, the scattering patterns of samples without salt are nearly independent of temperature. These trends are consistent with screened electrostatic repulsion that is less temperature sensitive.

Comparing samples at 0 mM and 50 mM $Na_2SO_4$ at equivalent mAb concentration shows a strong increase in low-$q$ scattering upon salt addition, which signifies a change in mAb-mAb interactions. The addition of 50 mM sodium sulfate significantly enhances the low-$q$ scattering by roughly an order of magnitude at concentrations above 50 mg/mL. This large increase in intensity indicates the dominance of strong inter-protein attractions. The substantial magnitude in intensity observed in formulations with 50 mM sodium sulfate at small $q$-values suggests the presence of large scale structural features, which are expected to contribute to the higher viscosities seen in Fig. 7.5.

Unlike mAb3 solutions with no salt, changing temperature results in noticeable changes in the scattering pattern of mAb3 solutions with 50 mM sodium sulfate. At $5°C$, the scattering intensity for mAb3 samples with salt is nearly double that measured at $25°C$, indicating the attractions are stronger at lower temperature. The attractive

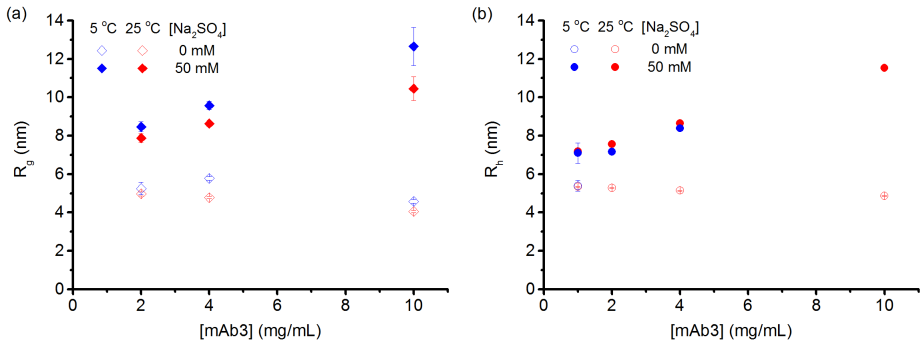


**Figure 7.7:** A comparison of (a) the $R_g$ extracted from Guinier analysis of low concentration SANS data and (b) the $R_h$ estimated from DLS data. While both methods agree quite well, mAb3 shows signatures of cluster formation in the presence of 50 mM sodium sulfate, even at low protein concentrations.

force acting between mAbs likely becomes stronger at lower temperatures with 0 mM $Na_2SO_4$ as well, but the long-range repulsive barrier is sufficient to prevent significant sampling of configurations within the attractive energy well. In the following, the underlying building blocks of such structures at low concentration are identified first to clarify the mechanism behind their assembly.

### 7.3.1 Low Concentration Behavior

Scattering patterns of mAb3 solutions at low protein concentrations (10 mg/mL) are noticeably different between those with 0 mM and 50 mM added sodium sulfate. In particular, the intensity at low $q$-values for samples with 50 mM salt in Fig. 7.6 are roughly twice that of mAb3 samples without salt. Surprisingly, this difference in low-$q$ intensity, and other parameters, between samples with 0 mM and 50 mM salt persists to even lower protein concentrations.

The radii of gyration, $R_g$, are determined from a Guinier analysis of SANS data that is model independent[51] and the hydrodynamic radii, $R_h$, are determined from independent DLS experiments according to Eq. 7.10 at small concentrations. These results are compared in Fig. 7.7. For samples with 0 mM sodium sulfate, both radii

values are almost independent of concentration and temperature. Without adding additional salt, $R_g$ and $R_h$ are roughly 5.0 nm and 5.3 nm, respectively, indicating that mAb3 exists as monomers with little change up to 10 mg/mL. However, adding 50 mM sodium sulfate to mAb3 solutions (at 2 mg/mL) causes the effective radius of mAb3 to increase by a factor of 1.4 relative to its size in solutions without salt, as indicated by measurements of both $R_g$ and $R_h$. This increase is nearly identical to that reported in a previous study of a dimerizing mAb.[48]

Apparent molecular weights, shown in Table 7.1, extracted from SANS data also indicate that the molecular mass is almost the same as that of a dimer in solution, even for samples as dilute as 2 mg/mL. This indicates that adding salt causes mAb3 to form dimers at very small concentrations, which are even smaller than observed previously for mAb systems.[22, 38, 48] These results are also consistent with previous studies of mAb3 in $H_2O$ based buffers in the presence of sodium sulfate.[21, 22]

A more detailed modeling of SANS data can reveal the structure of the mAb3 dimers in solutions with 50 mM $Na_2SO_4$. To estimate the real space conformation of mAb3, the coarse-grained mAb structure model described earlier is used to quantitatively determine the monomer and dimer structure and can replicate the theoretical estimate of the antibody's neutron SLD. Figure 7.8 displays the SANS data for a 2 mg/mL sample with 0 mM and 50 mM sodium sulfate along with the best fits using

**Table 7.1:** A compilation of apparent molecular weights and standard deviations ($\sigma$), determined from SANS data, at low mAb3 concentrations under each set of temperature and salt conditions studied.

| Temperature | | $25°C$ | | $5°C$ | |
|---|---|---|---|---|---|
| [mAb3] | [$Na_2SO_4$] | $M_{w,app}$ (kDa) | $\sigma$ (kDa) | $M_{w,app}$ (kDa) | $\sigma$ (kDa) |
| 2 mg/mL | 0 mM | 150.0 | 1.39 | 162.1 | 2.84 |
| 4 mg/mL | 0 mM | 134.1 | 0.71 | 161.1 | 1.40 |
| 2 mg/mL | 50 mM | 299.1 | 3.75 | 324.4 | 4.65 |
| 4 mg/mL | 50 mM | 355.0 | 2.74 | 393.6 | 4.23 |

the model. The 12-bead model fits the data remarkably well despite the fact that the scattering is a result of an ensemble average of antibody configurations.[10] The exact structures are displayed in Fig. 7.3 compared to the IgG1 crystal structure.

The 12-bead model provides insight into the antibody structure at low concentration. For samples with 0mM sodium sulfate, a model based on a single mAb as the fundamental scattering unit quantitatively fits the SANS spectra. The scattering profile for mAb3 solutions with 50 mM added $Na_2SO_4$ cannot be fit by any single monomer model. Rather, it is well described by scattering from a dimer comprised of two mAb3 proteins with a conformation similar to that observed for solutions with 0mM added salt. Comparison of the scattering intensities from experiment (Fig. 7.8) and several model monomer and dimer configurations demonstrates the inability of a monomer structure to reproduce the SANS data of samples with salt. The insets of Fig. 7.1 and Fig. 7.2 clearly distinguish $R_g$ between salt conditions (from the slope) and highlights the sensitivity of the 12-bead model to these differences. This sensitivity provides confidence in the elongated conformation of the dimer extracted from the model fit. Further, the relative sizes of the elongated dimer and monomer from the model quantitatively agree with the static SANS and DLS measurements and are consistent with a previously studied mAb known to form elongated dimers.[48]

Determination of mAb3 conformation also will be very important for understanding the effective interactions and dynamics at higher concentrations. From the known configuration of the monomer and dimer, the model can reproduce the form factor scattering intensity and calculate the corresponding decoupling function, $\beta(q)$, that is used to normalize the data at higher concentrations to extract interaction parameters. Because the dimer takes on an elongated configuration at low concentration, the development of large structures and high viscosities are observed at elevated protein concentrations. Already, the effective radii of samples with 50 mM $Na_2SO_4$ increase approximately linearly with mAb concentration up to 10 mg/mL, as shown in Fig. 7.7. These trends could be indicative of an increase in cluster size or conformation with concentration. However, in the low-$q$ range, the sensitivity of the 12-bead model to

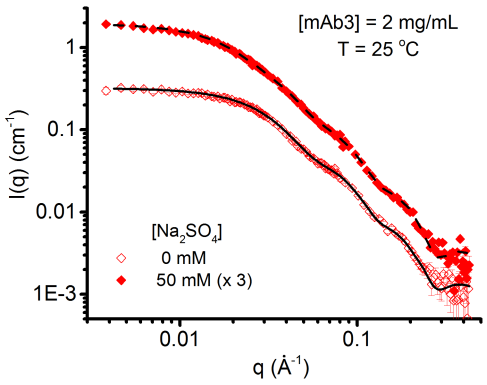


**Figure 7.8:** SANS profiles are plotted for two 2 mg/mL mAb3 samples representative of the form factor with best fits using the 12 bead model. Both sodium sulfate concentrations are plotted, with the sample at 50 mM sodium sulfate shifted by a factor of 3 for clarity.

dimer configuration is convoluted with changes to $S(q)$ due to mAb-mAb interactions at elevated concentrations. Therefore, in the following the short-time diffusivity is studied by NSE to better understand the moving units at higher concentrations.

### 7.3.2 High Concentration Behavior

Reversible cluster formation at high protein concentrations can be studied by focusing on the dynamics, as previously shown with other mAbs and globular proteins.[15, 48] Changes in either salt concentration or temperature directly influence mAb3 interactions and the equilibrium microstructure, both of which will have effects on protein mobility. Antibody diffusion is probed by both NSE and DLS, which cover significantly different lengthscales and timescales. Figure 7.9 shows the correlation functions obtained by both NSE and DLS with their corresponding best fits using a single and double exponential function, respectively, from which collective diffusion coefficients are extracted. Note the (orders of magnitude) difference in the scale of the x-axis to understand the difference in timescales of these two techniques.

NSE data are obtained for correlation times up to 50 ns, which is then fit

with a single exponential to measure the short-time collective diffusion coefficient. A range of $q$-values are studied using NSE, but Fig. 7.9 displays results only at 0.114 $\text{Å}^{-1}$ corresponding to sizes equivalent to that of a protein monomer. The $q$-dependent short-time collective diffusion coefficients obtained from fits to the NSE data are compiled in Fig. 7.10. The average value of $D_c$ in the limit of large $q$-values is calculated, as outlined already in previous work,[31] and used to estimate the short-time self diffusion coefficient, $D_s$. The decrease of short-time $D_c(q)$ at smaller $q$-values indicates an influence of structure and hydrodynamics.

DLS measures the long time collective diffusion coefficient in protein solutions. Here, the single $q$-value (0.0018 $\text{Å}^{-1}$) used in the DLS corresponds to a lengthscale of roughly 350 nm. A double exponential function is used to fit the DLS data to accommodate a possible slow mode in the data. At small concentrations the data only display a single relaxation mode, while a slow mode develops at higher concentrations and requires the double exponential for an accurate fit.

Fitting the correlation function obtained by DLS experiments with a double exponential function results in a weighting of the two contributions to the total intensity. Figure 7.11 plots the magnitude of the contribution of the fast mode ($X_1$)

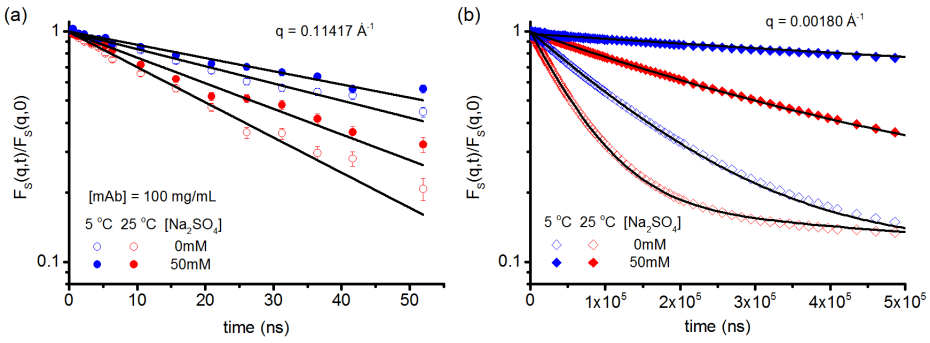


**Figure 7.9:** Characteristic correlation decay curves (symbols) from (a) neutron spin echo and (b) dynamic light scattering experiments are plotted with their corresponding exponential function fits (lines) for a 100 mg/mL mAb3 sample at $5°C$ and $25°C$ and with 0 mM and 50 mM sodium sulfate salt.

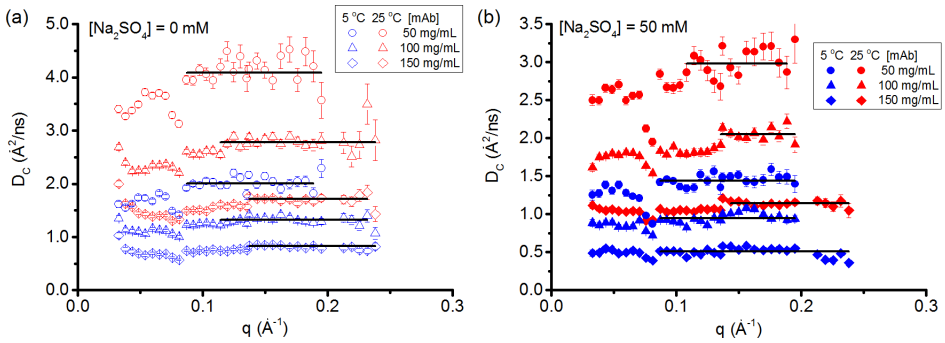


**Figure 7.10:** Collective diffusion coefficients (symbols) extracted from fits to the NSE data with (a) 0 mM and (b) 50 mM sodium sulfate salt are plotted as a function of $q$-value. The average value in the limit of high $q$-values (lines) indicates the short-time self diffusion coefficient under each set of conditions.

as a function of mAb3 concentration for each of the four solution conditions studied. Without added salt, the contribution of the fast mode is always at least 80% while with 50 mM sodium sulfate the relative magnitude of $X_1$ decreases with increasing protein concentration. As larger structures are expected to form at high concentrations with added salt, it is not unreasonable for the fast mode to become a less significant but it always remains the dominant contribution to the correlation function. The subsequent analysis focuses only on the fast mode of long-time collective diffusion, $D_{c,1}$, which is the dominant contribution at all solution conditions.

Figure 7.12 shows the values of $D_s$ from NSE and $D_{c,1}$ from DLS normalized by the bare diffusion of a mAb3 monomer, $D_0$, determined by extrapolating the DLS values of $D_{c,1}$ at low protein concentrations to the limit of zero concentration. Comparison of these results highlights the considerable discrepancy between short-time mobility of mAb3 and the long-time collective motion. In general, the collective diffusivity is a strong function of protein concentration and temperature. As shown in Fig. 7.12a, the mobility in samples without salt is observed to increase initially with increasing concentration. Although this appears counter-intuitive, this trend is consistent with the theoretical relationship between $D_{c,1}$ and $S(q)$. Eventually $D_{c,1}$ reaches a maximum

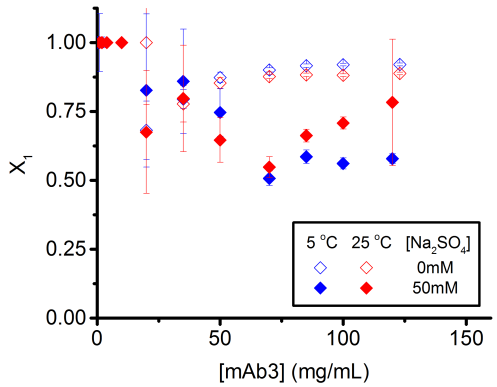


**Figure 7.11:** The magnitude of the contribution of the fast mode ($X_1$) is plotted as a function of mAb3 concentration for each of the four solution conditions studied.

and then decreases at sufficiently large concentrations. This is due to self-crowding and hydrodynamic effects that retard long-time dynamics more significantly than interactions reduce the magnitude of $S(q)$ at small $q$-values,[1] which originally caused the increase in $D_{c,1}$. In contrast, samples with added salt show a rapid decline in $D_{c,1}$ with increasing concentration. Under these conditions, $D_{c,1}$ decreases due to both an increase in low-$q$ scattering (see Fig. 7.6b), and therefore $S(q)$, and the subsequent reduction of long-time mAb mobility resulting from strong attractive interactions.

Under both salt conditions, decreasing temperature reduces protein diffusivity, which is likely a result of enhanced attractive interactions. This appears in SANS data as the relative increase in low-$q$ scattering intensity with decreasing temperature (Fig. 7.6b). The large absolute value of $I(q)$ in samples with 50 mM salt suggests that these stronger attractive forces drive the formation of large scale clusters. Despite the prevalence of repulsive interactions in samples without salt, the reduction in $D_{c,1}$ at high concentrations may indicate that mAb3 also associates into larger clusters under these conditions. These results are consistent with the rheological results that will be discussed in the Discussion section.

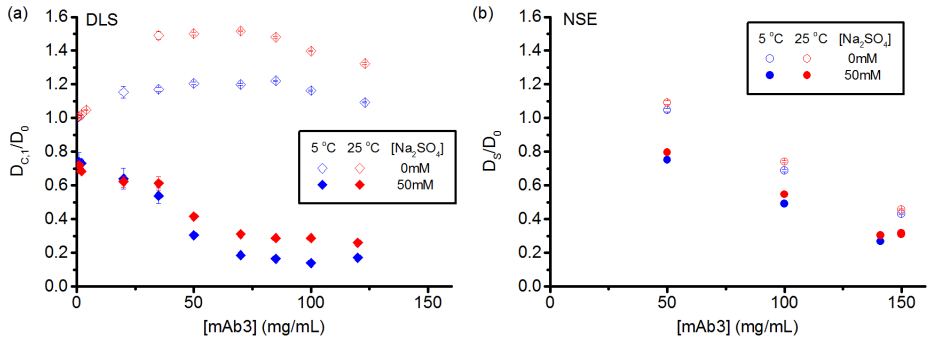


**Figure 7.12:** (a) Collective diffusion coefficients and (b) short-time self diffusion coefficients normalized by the bare diffusion of a mAb3 monomer, $D_0$, are plotted separately on the same scale. Deviations due to the presence of sodium sulfate are significant for long time collective motion (a), but relatively insignificant for the short-time mobility of individual moving units.

The short-time mobility as probed by NSE determines the fundamental "moving units" in solution by probing motion on the nanoscale on the timescale of up to $\approx$ 100 nanoseconds. Interestingly, $D_s$ is nearly identical at all concentrations below 50 mg/mL for samples at low ionic strength. This trend was recently observed for another antibody[48] and may be a generic feature of these macromolecules when there is strong repulsion between antibodies in solution. Previous work, discussed in the last chapter, demonstrated through the use of NSE that the short-time self diffusion of a charge stabilized mAb was significantly reduced at high concentrations by hydrodynamic interactions, despite remaining dispersed as monomers.[48] Hence, these prior results can be considered representative of the "standard" dynamic behavior of a mAb monomer.

The absolute values of $D_s$ for mAb3 are plotted along side these prior results in Fig. 7.13. The mobility of mAb3 with 0 mM $Na_2SO_4$ appears slightly faster on the short time scale as compared to the well-dispersed mAb2 at 25°$C$. When normalized by the ratio of buffer viscosity, which is larger for mAb2 due to the presence of sugars not included in the mAb3 buffer, the bare diffusion coefficients become nearly identical.

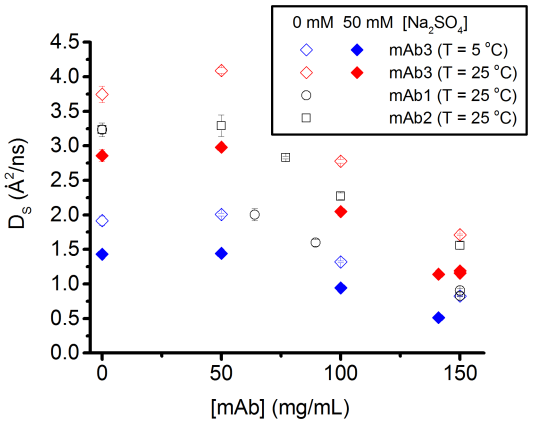


**Figure 7.13:** Absolute short-time self diffusion coefficients of mAb1 (circles), mAb2 (squares) and mAb3 (diamonds) in $D_2O$ buffers are compared as a function of protein concentration.

Therefore, from this comparison, mAb3 samples without salt can be considered mostly monomeric in the short-time limit at all mAb concentrations studied. Hydrodynamic effects will be discussed in more detail in the Discussion section.

The temperature dependence of $D_s$ and $D_{c,1}$ is consistent with a hierarchical association into structures with correlation lengths much larger than a single antibody. Lowering temperature reduces short-time self diffusivities at all concentrations, consistent with the associated increase in solvent viscosity, indicating the fundamental moving unit is itself unchanged with temperature for each salt concentration. However, temperature decreases lead to significant decreases in $D_{c,1}$ (as well increases in viscosity), which indicates a growing correlation length at the longer length and time scales probed by light scattering.

The most substantial impact on $D_s$ comes from the addition of 50 mM sodium sulfate. An effective hydrodynamic radius of mAb3 with salt can be estimated by taking the ratio of self diffusivities as $R_h/R_0 = D_s(0mM)/D_s(50mM)$. This ratio is indicative of the size of strongly bounded clusters in samples with salt relative to a mAb3 monomer. The resulting values of this ratio are presented in Fig. 7.14 for NSE results. The results indicate that the relative size of the "fundamental" moving

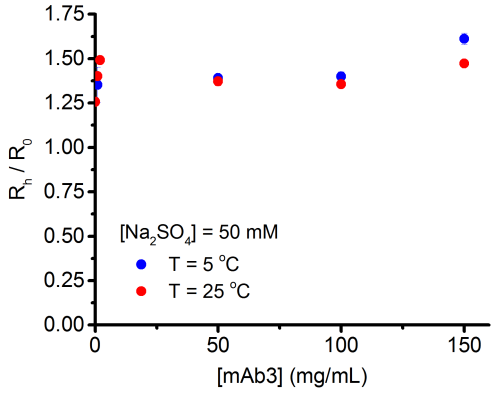


**Figure 7.14:** The effective hydrodynamic radius of the moving unit with 50 mM sodium sulfate is plotted as a function of temperature and protein concentration.

unit for solutions with 50 mM $Na_2SO_4$ remains almost unchanged at all concentrations studied. In other words, at this salt concentration the mAb always associates into elongated dimers that persist at higher mAb concentrations. The formation of dimers in formulations with 50 mM sodium sulfate also appears in Fig. 7.12a as $D_{c,1}/D_0$ values well below one at low concentrations.

Interestingly, the corresponding ratio of bare diffusion coefficients of monomers and dimers, $D_0(0mM)/D_0(50mM)$, is nearly identical to the values of $R_h/R_0$ in Fig. 7.14. The product of these ratios results in a measure of the short-time mobility of dimers relative to monomers after accounting for the influence of excluded volume. The resulting values of about one suggest that mAb3 monomers and dimers are capable of translating equally as easily in the short-time limit at higher concentrations.

## 7.4 Discussion

The combined results of NSE ($D_s$), DLS ($D_{c,1}$, $R_h$), and SANS ($P(q)$, $R_g$, $M_{w,app}$) show that, for short time and length scales, the diffusing species for samples without salt is a mAb monomer, while for samples with salt the diffusing species is an elongated mAb dimer at all mAb concentrations studied. Viscosity measurements

indicate a substantial increase in viscosity with increasing mAb3 concentration, added salt, and decreasing temperature. Importantly, the structure and long-time dynamics are markedly different depending on the amount of added sodium sulfate. The measurements presented indicate that mAb3 associates into elongated dimers that further associate into large, transient structures at high concentration in formulations with 50 mM $Na_2SO_4$. These structures retard mAb3 mobility over long times and strongly resist shear flow, leading to an increase in viscosity. Without added electrolyte, mAb3 appears dispersed as mostly monomers at all concentrations and moves as such on short timescales. These solutions also show a significant increase in viscosity at elevated concentrations, although less than the increase observed for solutions with added salt. This viscosity increase is consistent with increasing inter-protein repulsion due to crowding. In the following, a more quantitative assessment of the contributions to the viscosity is made based on colloidal micromechanics.

### 7.4.1 Hydrodynamic Effects

The hydrodynamic function, $H(q)$, provides more detailed information than is accessible from measurements of high shear viscosity, $\eta_\infty$ typically used to represent the hydrodynamic contribution to the viscosity. While $\eta_\infty$ is representative of large lengthscales, $H(q)$ presents a means by which multiple lengthscales of hydrodynamic effects can be explored in the short-time regime. Here, two experimentally accessible and physically meaningful characteristic lengthscales are of interest. Specifically, the distance separating monomers, represented at the $q$-value of $q_m$, and very long lengthscales, represented by the limit of zero $q$-value. Trends in $H(q_m)$ and $H(0)$ calculated using experimental results for mAb3 will be compared with predictions for hard sphere (HS) and charged sphere (CS) or electrostatically stabilized systems.

Values of $H(q_m)$ are determined from NSE data while $H(0)$ is derived from DLS data. While DLS captures the long-time behavior, previous work suggests that short-time and long-time limits of $H(0)$ should differ by less than 6% for concentrated HS suspensions.[1] This should be treated as a lower estimate of relative error between

short and long time dynamics because attraction will have a stronger influence on $H(q)$ than HS interactions.

Hydrodynamics of mAb3 over large lengthscales, represented by $H(0)$ in Fig. 7.15a, demonstrate behavior consistent with the physical picture developed thus far. Physically, the hydrodynamic function $H(0)$ can be associated with the resistance to particle sedimentation. Samples without sodium sulfate lie between predictions for HS and CS fluids, which is consistent with the long-range repulsion found in their corresponding effective potentials to be discussed later. However, samples with 50 mM sodium sulfate display unique behavior as a function of volume fraction.

The initial increase in $H(0)$ with increasing $\phi$ for mAb3 samples with added salt, shown in Fig. 7.15a, is interesting because it indicates that hydrodynamics promote faster collective mobility over short times and long lengthscales according to the relationship $D_c(q) = D_0'(H(q)/S(q))$. Here, $D_0'$ is the bare diffusion of a mAb3 dimer for samples with salt (and a mAb3 monomer for samples with no salt). To help rationalize this behavior, $H(q)$ can be decomposed into two contributions represented by the $q$-independent parameter $D_s/D_0'$ and a "distinct" hydrodynamic component, which is a weighted convolution of $D_s/D_0'$ and $S(q)$.[1] Interestingly, $D_s$ is constant over the range of concentrations where the peak in $H(0)$ is observed ([mAb3] $\leq$ 50 mg/mL or $\phi \leq 0.1$). Therefore, changes in $H(0)$ are a result of the convolution of structural and dynamic correlations. One possible interpretation is that fluctuations in the equilibrium solution configuration occur in sync with dynamically correlated bodies (e.g., clusters) in such a way that long-time collective motion is enhanced. While this hydrodynamic feature helps enhance mAb3 dimer mobility, Fig. 7.12 shows that $D_{c,1}/D_0'$ still decreases with increasing $\phi$ for mAb3 samples with 50 mM salt. At larger volume fractions, dimers aggregate into large structures, which leads to a reduction in the hydrodynamic function by hindering long-range motion and contributes to the drop in $D_{c,1}/D_0'$.

Short lengthscale hydrodynamics of mAb3 formulations, captured by $H(q_m)$ in Fig. 7.15b, appear nearly insensitive to solution conditions. However, values of $H(q_m)$

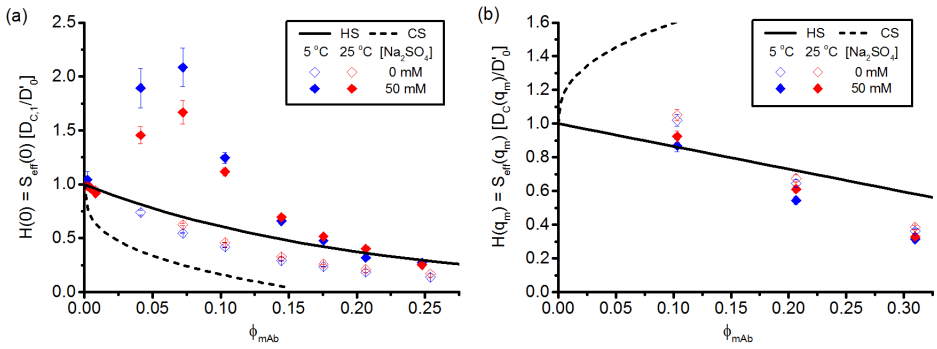


**Figure 7.15:** The effective hydrodynamic functions are plotted at (a) zero $q$-value, $H(0)$, and (b) the $q$-value of the monomer peak, $H(q_m)$ relative to HS (solid line) and CS (dashed line) fluids.

for solutions of mAb3 without salt are consistently larger than those for mAb3 with 50 mM $Na_2SO_4$. Under all solution conditions of mAb3 samples, the data qualitatively follow the trend predicted for HS fluids. At a protein concentration of 50 mg/mL, $H(q_m)$ for mAb3 samples without salt lie between predictions for HS and CS fluids, while $H(q_m)$ for mAb3 samples with salt are in nearly perfect agreement with HS predictions. The values of $H(q_m)$ for all mAb3 samples then decrease with increasing protein concentration at a rate slightly faster than predicted for a HS fluid.

The underlying forces producing the observed trends for HS and CS fluids can be used to understand the hydrodynamic features of mAb3. For CS systems, $H(q_m)$ increases with $\phi$ due to backflow of the suspending medium that causes enhanced frictional forces on a suspended particle.[2] Further, larger values of $H(q_m)$ for a CS fluid relative to a HS fluid are consistent with the well-known reduction in $\eta_\infty/\eta_0$ of CS fluids relative to HS systems.[28] Therefore, at low to intermediate protein concentrations ($c \sim 50$ mg/mL) mAb3 hydrodynamics in the presence of 50 mM salt are influenced by repulsive forces, but with no added salt they are more HS-like.

In the case of HS fluids, hydrodynamics are the dominant contribution to the viscosity in the zero shear and low volume fraction limit, represented by the hydrodynamic term, $\eta_H$.[13] Typically, this is captured by measuring the high shear limiting

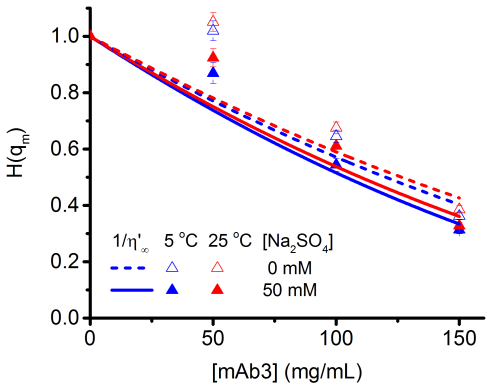


**Figure 7.16:** The hydrodynamic functions at $q_m$ determined from experimental results for samples with 0 mM (open symbols) and 50 mM (filled symbols) salt are fit with the inverse of the high frequency viscosity represented by Eq. 7.11 (dashed and solid lines, respectively).

viscosity, $\eta_\infty$.[28] However, this limit could not be reached for the mAb3 formulations studied here. Therefore, the influence of solution conditions on the hydrodynamic function, $H(q)$,[1] can be used to estimate $\eta_\infty$ for these mAb3 samples.

The similarity of mAb3 hydrodynamics to HS fluids at these volume fractions suggests that hydrodynamic interactions are not a dominant factor and the hydrodynamic contribution to the viscosity is relatively small compared to other contributions. Further, the behavior of HS and CS systems confirms that $\eta_\infty$ and $H(q)$ are approximately equal.[1, 2] Thus, by assuming $\eta_H \sim 1/H(q_m)$ the hydrodynamic contribution to the viscosity can be estimated. The inverse of an accurate model of hydrodynamic viscosity proposed by Lionberger and Russel[23]

$$\eta_\infty = \frac{1 + 1.5\phi(1 + \phi - 0.189\phi^2)}{1 - \phi(1 + \phi - 0.189\phi^2)} \tag{7.11}$$

is used to fit $H(q_m)$ values of mAb3 solutions, shown in Fig. 7.16, to estimate the hydrodynamic radius. The volume fraction is replaced by $\phi = Cv_0$, where $v_0$ is the intrinsic volume of the protein. The volume is subsequently used to estimate the hydrodynamic radius using the molecular weight extracted from $I(0)$ of SANS data. The

resulting radii of 4.8 nm and 6.4 nm for samples with 0 mM and 50 mM salt, respectively, compare quite well with the other measures of protein size discussed earlier.

### 7.4.2 Shear Thinning and Effective Structure Size

Rheological measurements are a sensitive probe of the formation of large scale structure in solution.[28] Thus, the presence of large lengthscale structures suggested by SANS measurements can be confirmed by studying the shear rate dependence of the viscosity at high concentration. The measurements of the shear rate dependent viscosities for all solution conditions studied here are presented in Fig. 7.17. The zero-shear viscosity plateau is observed for all conditions, but a shear thinning regime is found to arise at high concentrations. The shear rate at which shear thinning occurs appears to decrease with increasing concentration and decreasing temperature.

Deviations from Newtonian behavior indicate a timescale representative of structural deformation due to the shearing force. In particular, the onset of a shear thinning regime approximately corresponds with the point at which shear forces become comparable to Brownian forces. The balance of these forces is captured at high concentration by the rescaled Péclet number $Pe = (\dot{\gamma}L^2)/(2D_s)$, where $L$ is the characteristic lengthscale.[4] For these calculations, the shear rate can be replaced by the stress dependence of the viscosity, $\dot{\gamma} = \sigma/\eta(\sigma)$. In these mAb formulations, $L$ can approximately be considered a representative size of large scale, transient clusters. Shear thinning generally occurs at $Pe \geq 1$. Therefore, the transition point at $Pe \approx 1$ is indicative of an effective association structure lengthscale in solution.

Studies of colloidal particles with HS or CS interactions have demonstrated that shear thinning can be accurately modeled with respect to shear stress.[28] When the stress is normalized by a critical value (as a function of volume fraction), the behavior is universal across all systems.[28] The viscosity of all concentrated mAb3 formulations displaying shear thinning behavior are plotted in Fig. 7.18a, normalized according to the Cross model. Here, the solvent viscosity is used as an upper limiting representative value of the high frequency viscosity. Interestingly, normalized mAb3

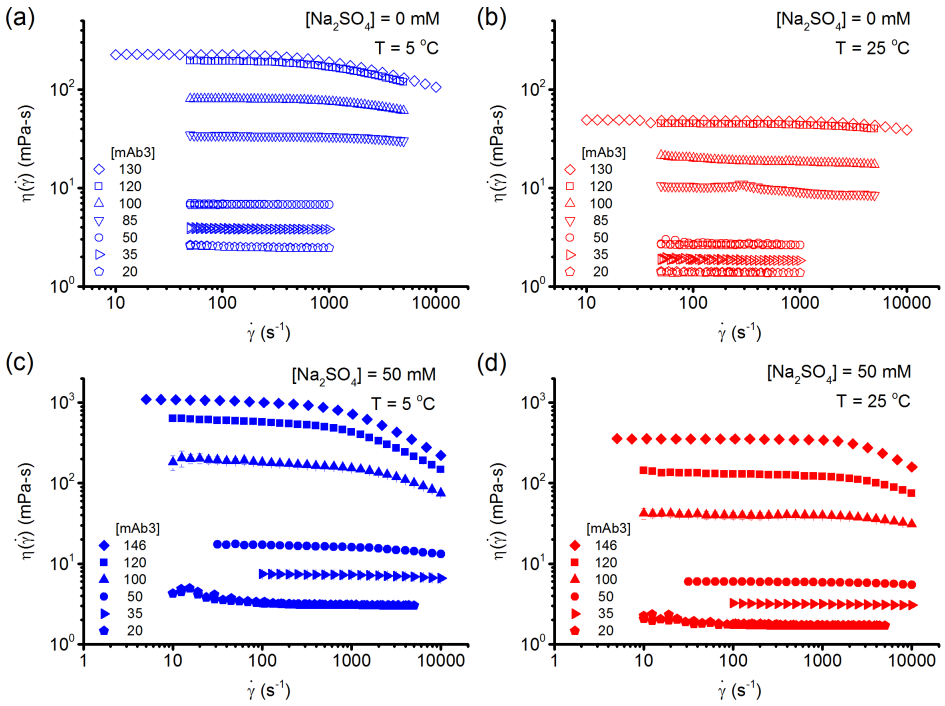


**Figure 7.17:** The shear rate dependence of the viscosity is plotted for a range of mAb3 concentrations (in mg/mL) for samples without added sodium sulfate at (a) $5°C$ and (b) $25°C$ and samples with 50 mM $Na_2SO_4$ at (c) $5°C$ and (d) $25°C$.

viscosities are nearly universal as a function of reduced shear stress. The similarity between all data sets indicates that shear effects on mAb3 solution microstructure are stress-dependent ($\sigma$) as opposed to rate-dependent ($\dot{\gamma}$). In Fig. 7.17, the onset of shear thinning is shown to differ significantly as a function of shear rate between conditions. A distinctive outlier is the most viscous solution at highest mAb concentration in salt solution at the lowest temperature.

While the critical shear stress is relatively insensitive to the buffer, the characteristic lengthscale varies significantly due to very different viscosities and short-time

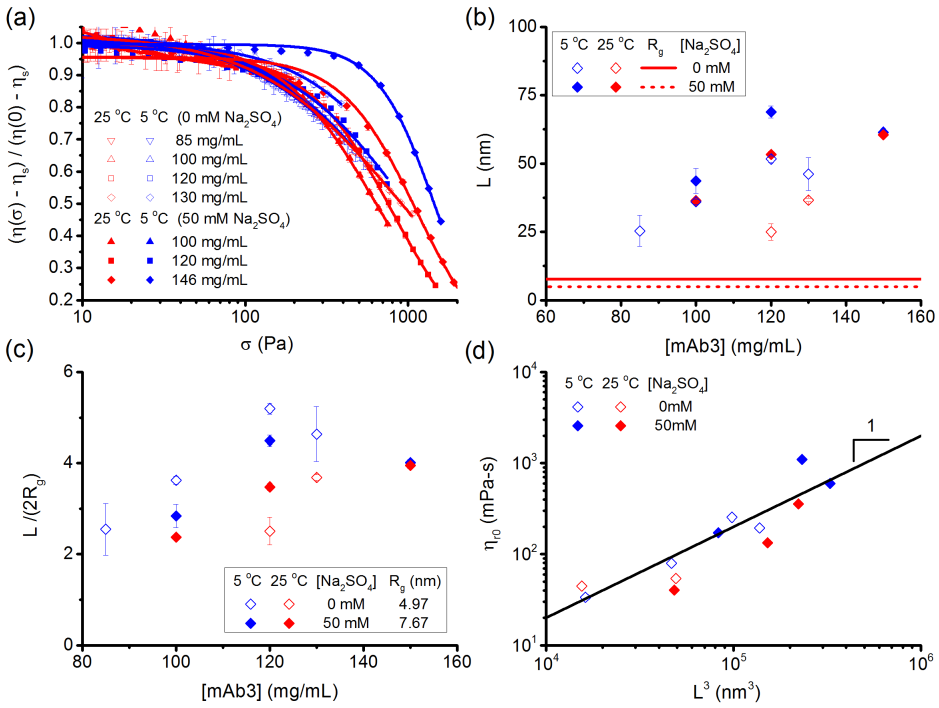


**Figure 7.18:** (a) A Cross model scaling of the viscosity is plotted as a function of stress for samples that display shear thinning behavior. All curves appear nearly identical, indicating that structural deformation is controlled by stress. Also plotted are (b) the characteristic structural lengthscale at the point of shear thinning and (c) values of $L$ normalized by the corresponding radius of gyration for each salt condition listed in the legend. (d) The zero shear viscosity scales well with the cube of the lengthscale.

self diffusivities (compare scales of Fig. 7.5b and Fig. 7.12b, respectively). The characteristic lengthscale $L$ is estimated by setting $Pe = 1$ and assuming the critical shear thinning point occurs at a 50% reduction in the low shear rate limiting value. These values of $L$ are plotted in Fig. 7.18b as a function of sample composition.

For all samples, the characteristic lengthscale is significantly larger than the protein size, which is also shown for reference in Fig. 7.18b. Samples with added electrolyte are found to have larger sizes than those without electrolyte at a given temperature and composition. This may be anticipated due to the presence of strongly bounded dimers as a larger fundamental moving unit in samples with added salt. When these lengthscales are normalized by the effective diameter (twice the radius of gyration) of the smallest moving unit under each set of conditions, plotted in Fig. 7.18c, the resulting value is an effective association size in solution at the conditions of interest. These sizes appear relatively insensitive to the solution conditions and increase slightly with increasing mAb concentration.

Note that this estimation depends on the choice of the critical shear thinning point. If the same calculation of $L$ is performed by using the point where $\eta$ is only 20% of $\eta_0$, then the lengthscales become roughly a factor of three larger. Nonetheless, these structural units of size $L$, which form from the interaction between fundamental moving units, associate hierarchically into larger dynamically correlated structures.

In the short-time limit, monomers in samples without salt and dimers in samples with added salt move freely on nanometer lengthscales. However, associations between proteins at higher concentrations lead to shear thinning behavior in the bulk solution. A strong correlation is observed between the solution zero shear viscosity and mAb3 association represented by $L^3$, as shown in Fig. 7.18d. This analysis indicates that the viscosity increases proportionally with the cube of the lengthscale, as expected for particulate suspensions,[28] as well as for semi-dilute polymer suspensions.[50] The lengthscales extracted from rheology can be understood with structural measurements using SANS as follows.

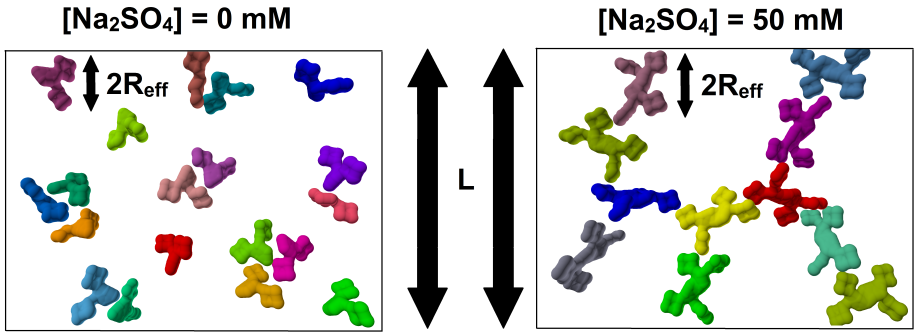


**Figure 7.19:** Proposed long time and length scale ($L$) solution microstructures and corresponding fundamental moving units over short time and length scales ($2R_{eff}$) are compared under both salt conditions. Without salt, structures contain a dispersion of monomers and dynamic clusters (composed of monomers). With 50 mM sodium sulfate, transient networks form due to weak association of long-lived dimers.

### 7.4.3 Effective mAb-mAb Interactions and Concentrated Solution Microstructure

Using the 12-bead model form factor fits derived from dilute solution, the SANS data reported in Fig. 7.6 are reduced to $S_{eff}(q)$ according to Eq. 7.1 and are shown in Fig. 7.20. Structure factors are calculated using integral equation theory with the model HSDY potential. The best fits shown in Fig. 7.20 as lines through the data. All resulting fit parameters, which include the four that define the interaction potential, an effective protein concentration and hydrodynamic radius, are tabulated in Table 7.1. From these last two parameters, the effective volume fraction is calculated to provide a comparison between salt conditions (since the concentrations vary slightly). The corresponding potentials derived from fitting the SANS data are shown in Fig. 7.21 and interpreted as follows.

For samples without added sodium sulfate, the data are fit very well using the monomer form factor with a combination of competing interactions of reasonable magnitude. Indeed, the potentials resulting from best fits to the SANS profiles contain a short-range attraction between mAb3 proteins in addition to long-range electrostatic

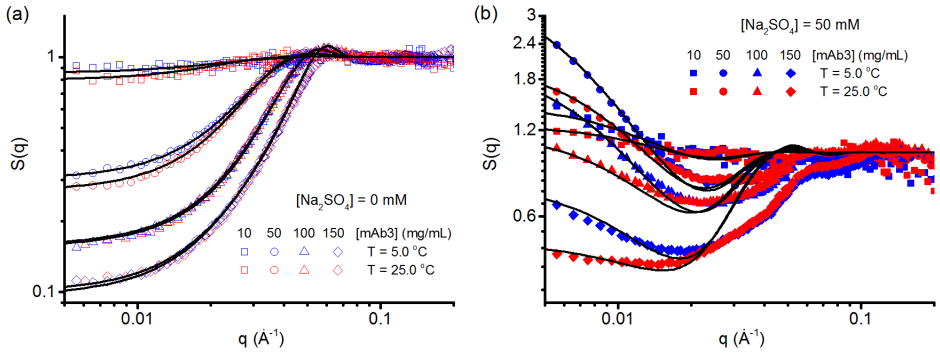


**Figure 7.20:** The structure factor (symbols) is plotted for samples with (a) 0 mM and (b) 50 mM sodium sulfate salt for several mAb3 concentrations at $5°C$ and $25°C$ with $S(q)$ fits (lines) using the HSDY potential and corresponding $\beta(q)$. Only a fraction of all points in each data set are included for clarity.

repulsion. The consistency of these potentials and parameters shown in Table 7.2 across the broad range of mAb3 concentrations studied is consistent with NSE results that indicate the fundamental moving unit is unchanging. The structure factors show the "correlation hole" typical of dispersions interacting with long range repulsions,[43] but without the characteristic structure peak.

The lack of a prominent nearest-neighbor structure peak is typical of mAbs[49] and is predicted for samples also having a short range attractive interactions.[19] One must be cautious of this interpretation, as it is based on a spherically symmetric potential acting between anisotropic mAb proteins that probably have anisotropic interactions. The small strength of attraction determined from these fits could result from an abundance of weakly interacting orientations, while a few specific configurations of two closely separated monomers could produce very strong attractive forces. This is supported by recent work on this antibody, which demonstrates an acute sensitivity of association to the inclusion of specific surface residues in the IgG1 structure.[45] An atomistic or coarse grained simulation[7] would be required to more accurately model these anisotropic interactions and is beyond the scope of this work, but the spherically

averaged potentially already yields valuable insight into the microscopic structure of these concentrated mAb solutions.

Structure factor fitting with a spherically symmetric potential is less satisfactory for samples with 50 mM $Na_2SO_4$. Figure 7.20 shows that the important long-range structure at low $q$-values can be accurately captured, while the intermediate $q$-range is poorly fit, especially at higher concentrations. Note that since dimers are the dominant moving unit at short times, the mAb structure model is implemented by taking a dimer as the form factor in the SANS fitting. Despite this inability to quantitatively model the intermediate $q$-range, the fitting results are still qualitatively useful as the well fit

**Table 7.2:** All fitting parameters extracted from fits to the SANS patterns in Fig. 7.20 are compiled together for each protein concentration (mg/mL) and temperature at both salt conditions. The table includes the strength and range of interactions, protein concentration, effective radius and extracted volume fraction.

| $[Na_2SO_4] = 0$ mM | | | | | | | | |
|---|---|---|---|---|---|---|---|---|
| [mAb3] | 10 | | 50 | | 100 | | 150 | |
| Temp ($°C$) | 5 | 25 | 5 | 25 | 5 | 25 | 5 | 25 |
| $K_1$ | 3.21 | 2.73 | 2.87 | 2.67 | 2.87 | 2.78 | 3.48 | 3.43 |
| $Z_1$ | 14.86 | 15.34 | 16.11 | 16.21 | 15.33 | 15.44 | 14.83 | 14.80 |
| $K_2$ | 1.19 | 1.42 | 1.42 | 1.53 | 1.36 | 1.33 | 1.43 | 1.33 |
| $Z_2$ | 4.45 | 4.31 | 4.31 | 4.21 | 4.34 | 4.41 | 3.24 | 3.21 |
| $[mAb3]_{fit}$ | 6.35 | 6.60 | 44.6 | 45.0 | 84.1 | 84.6 | 118.1 | 119.0 |
| $R_{fit}$ (nm) | 5.57 | 5.57 | 5.57 | 5.57 | 5.57 | 5.57 | 5.57 | 5.57 |
| $\phi_{fit}$ | 0.0185 | 0.0192 | 0.1297 | 0.1308 | 0.2445 | 0.2460 | 0.3434 | 0.3460 |
| $[Na_2SO_4] = 50$ mM | | | | | | | | |
| [mAb3] | 10 | | 50 | | 100 | | 150 | |
| Temp ($°C$) | 5 | 25 | 5 | 25 | 5 | 25 | 5 | 25 |
| $K_1$ | 2.05 | 2.05 | 2.38 | 2.01 | 2.17 | 1.92 | 2.27 | 1.86 |
| $Z_1$ | 5.02 | 5.02 | 6.02 | 6.02 | 7.22 | 7.22 | 7.53 | 7.73 |
| $K_2$ | -0.65 | 0.25 | | | | | | |
| $Z_2$ | -2.19 | 2.19 | | | | | | |
| $[mAb3]_{fit}$ | 4.4 | 4.4 | 39.4 | 41 | 73.4 | 73.4 | 118.4 | 118.4 |
| $R_{fit}$ (nm) | 6.491 | 6.491 | 6.491 | 6.491 | 6.491 | 6.491 | 6.491 | 6.491 |
| $\phi_{fit}$ | 0.0101 | 0.0101 | 0.0906 | 0.0943 | 0.1688 | 0.1688 | 0.2723 | 0.2723 |

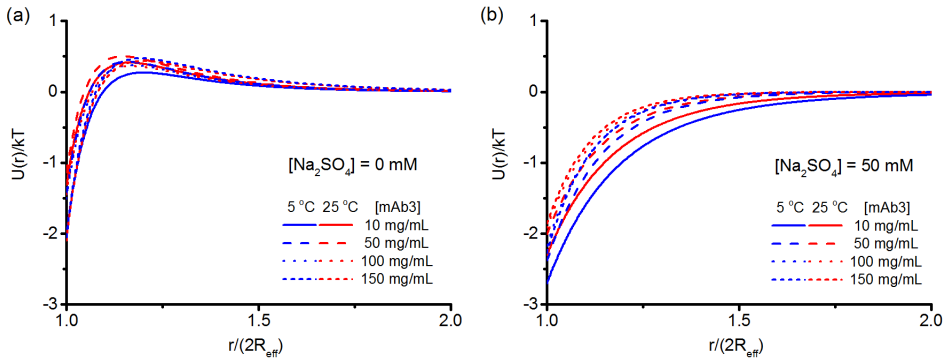


**Figure 7.21:** Potentials extracted from fits to the SANS data using the 12 bead model for samples with (a) 0 mM and (b) 50 mM sodium sulfate. Antibodies interact purely attractively in the presence of salt, which screens the weak, long-range repulsion found in samples without salt.

low-$q$ regime is the most sensitive to effective inter-protein interactions.

The fits yield a spherically symmetric potential of interaction with a significant primary attractive well and no stabilizing long-range repulsion, as shown in Fig. 7.21. This is consistent with the significant increase in scattering intensity observed in the SANS profiles for samples with salt shown in Fig. 7.6, as opposed to the correlation hole observed at low-$q$ for samples without added salt. The nearly identical potentials for all mAb3 concentrations again highlights the fact that dimers remain the fundamental moving and interacting unit.

The decoupling approximation is used in the fitting and so its limits must be carefully considered. As previously reported, the decoupling approximation assumes that the inter-particle distance is independent of the orientation/conformations of individual particles.[8, 24] When modeling particles with an extended structure, such as these mAb3 dimers in samples with added 50 mM $Na_2SO_4$, this assumption may not be valid when mAbs are in close proximity. Thus, it is possible, and even likely, that this average dimer association structure may depend on the solution concentration. More compact structures would cause a shift in the decay of the decoupling function to higher $q$-values (see Fig.7.2) and could potentially lead to more satisfactory fits.

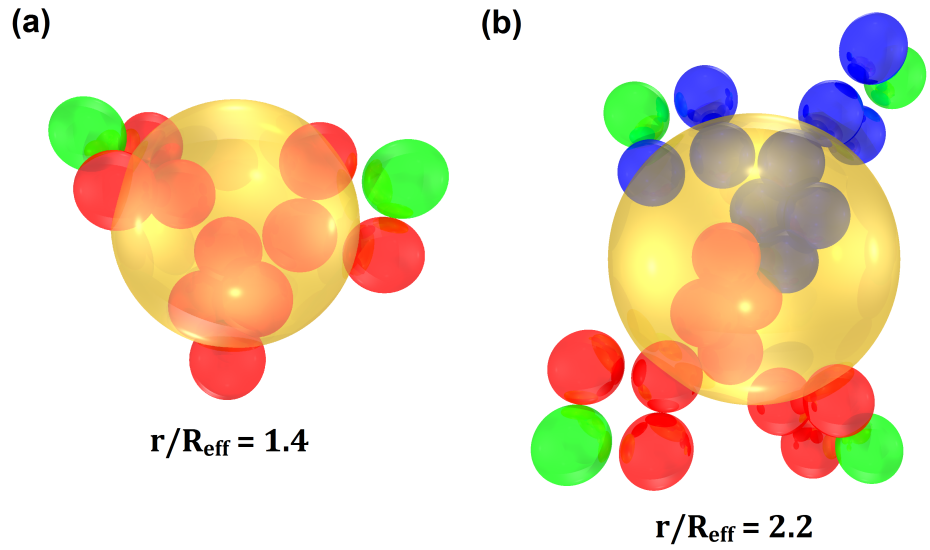


**Figure 7.22:** A pictorial representation of mAb3 (a) monomers without salt and (b) dimers with salt used to capture trends in protein interactions. The effective distances are those of the green spheres relative to the structure center of mass, which relate well with potential features in Fig. 7.21.

To better interpret the relationship between these spherically symmetric, average potentials and the mAb structure, Fig. 7.22 highlights particular lengthscales of the mAb3 monomer and dimer used to fit solution structure factors. The gold spheres represent the effective hard sphere excluded volume used to represent the antibodies as isotropically interacting particles. The green spheres are the components furthest from the center of mass for which the relative distance is labeled below each corresponding structure. For solutions without electrolyte, the spacing of these extremities could account in part for the long-range repulsion between mAbs due to steric hindrance. Similarly, the highlighted spheres of the dimer also agree with the location of the complimentarity determining region (CDR) in a full atomistic model of an antibody. Thus, due to the hydrophobic nature of mAb3,[21, 22] the relatively long range of attraction extracted for solutions with 50 mM salt could result from strong interactions caused by one (or several) specific orientation(s) between the CDR in the extremities of two mAb3

dimers averaged with all other orientations with weaker, shorter range attraction.

This detailed analysis of the SANS data provides additional evidence for the formation of larger association structures that increase the zero shear viscosity. The presence of competing forces in samples without salt demonstrates that mAb3 monomers can reversibly associate into dynamic clusters that are stabilized and interact strongly by long-range electrostatic repulsion. NSE shows that the proteins move as individual molecules on nanosecond and nanometer scales, whereas the bulk rheology and diffusion measurements suggest associations on longer length and timescales. Similarly, the interactions between dimers in the presence of 50 mM sodium sulfate indicate a strong driving force for the dimers to associate into large scale, loosely bounded clusters. If dimers do associate by their Fc domains leaving hydrophobic CDR regions exposed in extended structures, the presence of multiple physical interaction points on a single dimer would have the potential to form large network like structures in concentrated solutions.[7, 22] Again, the NSE data suggests that the fundamental unit for samples with added salt is a dimer. In the following section, several models are used to more quantitatively identify the relative importance of microscopic forces leading to the differences in zero shear viscosity as a function of solution conditions.

### 7.4.4 Microscopic Contributions to the Viscosity

Theoretical descriptions of the relative zero shear viscosity of colloidal suspensions include contributions from hydrodynamic ($\eta_H$), Brownian ($\eta_B$), and interaction ($\eta_I$) components.[3, 23] The hydrodynamic contribution is obtained experimentally and compared with the established relationship[23] discussed earlier in the Hydrodynamic Contributions section, where it was shown to be a relatively small component of the solution viscosity. The Brownian term is proportional to the extent of structure formation and the interaction contribution has a similar functional form that also accounts for the two-body potential. Both terms are inversely proportional to the short-time self diffusivity. Therefore, the focus of this analysis is to use the extensive data measured in

this work to isolate the contribution from the interparticle interactions to the viscosity and compare this with the structural analysis presented above.

By quantifying the individual viscosity contributions, the relative contribution of mAb associations to the solution viscosity can be estimated. The experimental viscosity can be compared with estimates according to $\eta_{r0} = \eta_H + \eta_B + \eta_P$. The hydrodynamic contribution is combined with the Brownian and Interaction terms, which are determined from theory for spherically symmetric interactions in the limit of hydrodynamic pre-averaging as:

$$\eta_{r0} = \left(\eta_H + \frac{12}{5}\frac{\phi^2 g(2)}{D_s/D_0}\right)\left(1 + 1.9\frac{\phi^2}{\tau_B}\right) - 2\int_{r_{max}}^{\infty} g(r')\frac{dU(r')}{dr}dr, \tag{7.12}$$

where the volume fraction $\phi = (C/M_w)(4/3)\pi R_h^3$ is calculated using the $M_w$ and $R_h$ determined from SANS and DLS, respectively, of the fundamental mAb3 moving unit. Note that the values of $R_g$ determined from SANS and $R_h$ determined from DLS and hydrodynamic modeling are all consistent and interchangeable with little difference in

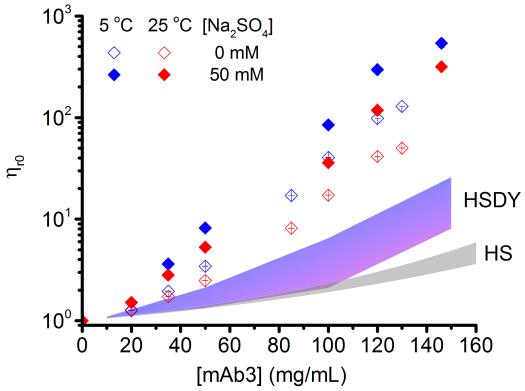


**Figure 7.23:** The experimental mAb3 viscosity (symbols) are compared with estimates of HS fluids (gray region) and interacting proteins calculated using parameters from NSE and SANS data (blue-red region). The ranges reflect differences in effective hydrodynamic radii and interaction parameters as a function of solution conditions. The upper (blue) portion of the HSDY range reflects low temperature samples while the lower (red) HSDY estimates represent higher temperatures.

the final value. All of the parameters in this equation are known from the analysis of the NSE data (yielding $D_s/D_0$ from Fig. 7.12b) and the effective spherically symmetric interaction potential, $U(r)$, shown in Fig. 7.21, and the corresponding pair distribution function, $g(r)$. The contribution of attractive interactions is captured by a previously developed relationship[20] with the Baxter parameter, $\tau_B = 0.25/(1 - B_2^*)$, where $B_2^*$ is the second virial coefficient normalized by a HS fluid at the same volume fraction. Here, $\tau_B$ is determined from only the attractive portion of each potential shown in Fig. 7.21.

Figure 7.23 shows the experimental solution viscosity relative to the range of estimated viscosities for a HS fluid (gray region) and the estimates using Eq. 7.12 from mAb structural and dynamic data (blue-red region). The wide range of values reflects the uncertainty in these calculations as well as the range of solution conditions represented. Within the HSDY region, the upper blue portion reflects estimates from samples at $5°C$ while the lower region is representative of samples at $25°C$. Regardless of solution conditions, the estimated magnitudes of $\eta_{r0}$ fall well below the experimental mAb3 viscosities. Again, the coarse-grained modeling used to extract the interaction parameters assumes spherical particles and isotropic interactions and are semi-quantitative in nature. Regardless, the two-body contribution underestimates the experimental value by roughly an order of magnitude at the highest concentrations. The substantial difference, especially for samples with 50 mM sodium sulfate, suggests that the large lengthscale structures formed at high concentration are the dominant mechanism of stress dissipation.

For comparison, a recent model is considered for the zero shear viscosity of associating mAb solutions based on polymer network theory.[39] The zero shear viscosity of mAb3 is plotted in Fig. 7.24a along with lines of best fit using the antibody network model,[39] which has the following functional form:

$$\eta_0 = Ac^{3/(3\nu-1)}\left[\frac{2kc}{\sqrt{1+4kc}-1}\right]^3, \tag{7.13}$$

where $A$ is a constant, $\nu \approx 0.6$, $C$ is the protein concentration in mg/mL and $k$ is the

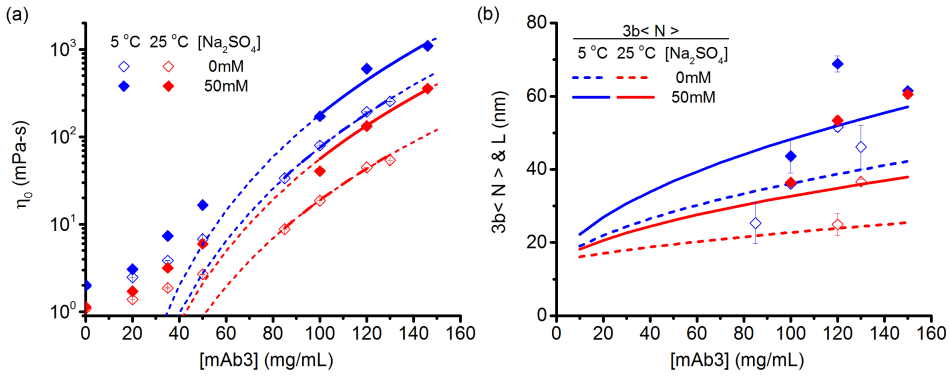


**Figure 7.24:** (a) The absolute zero-shear viscosity is plotted with fits (solid lines) using a polymer based entanglement model and their extrapolation over the full concentration range (dotted lines). (b) The estimates of effective aggregate size (solid lines) from the entanglement model fits are plotted relative to structural lengthscales (symbols) determined from shear thinning behavior.

partition function between all possible association states. The term in the square brackets in Eq. 7.13 is the aggregation number, $\langle N \rangle$. A linear chain length can be estimated by $3b\langle N \rangle$, where $3b$ is the size of an individual antibody that can be represented by its longest dimension, shown previously for mAb3 to be about 15 nm.[21] However, these derived parameters are *very* sensitive to the extent of data included in the fitting and correspondingly the pre-factor, $A$. Here, fits are inclusive of the highest three mAb3 concentrations and it can be seen that the model is unable to describe the data across the entire concentration series.

The effective aggregate lengths extracted from the fits are plotted in Fig. 7.24b at each solution condition studied. The values range from 20 nm to 50 nm in size, which increase with higher concentration and added salt and lower temperature. Note that the model does not fit the data well over the entire range of concentrations and fitting different ranges of the data can lead to variations in $\langle N \rangle$ by a factor of two. Nonetheless, these values are larger than the fundamental moving units of strongly bound dimers in samples with salt and monomers in samples without added salt. Fig. 7.24b also

compares these aggregate lengths with the effective lengthscales obtained from the shear thinning behavior of the viscosity. Here, the association numbers from the model fits correspond with those extracted from the shear thinning viscosity. However, the small size of the aggregates as extracted from the modeling is a point of concern, as pointed out in the original manuscript by the authors, because the model is based on long, entangled polymer-like aggregates.[39] Further, the fact that these intermediate sized aggregates are composed of dimers in mAb3 samples with 50 mM sodium sulfate cannot be deduced from this model fitting.

It is important to recognize the significance of the short-time dynamics in systems such as mAb3, where proteins are one component/species of a highly polydisperse dynamic microstructure. NSE data indicates that the fundamental mAb3 moving units remain mobile in the short-time limit, suggesting that small clusters are dynamic. However, the similarity of association sizes determined by the network model and shear thinning behavior suggests that the fundamental units do associate into larger transient clusters. Note that the morphology of the strongly bounded small clusters will have an effect on the formation of these large network-like clusters. How this hierarchical cluster formation affects the zero shear viscosity still requires further investigation.

Trends in the viscosity of concentrated mAb solutions have also been modeled by the modified Ross-Minton equation,[22] which represents the reduced zero shear viscosity with an exponential dependence on the protein concentration

$$\eta_{r0} = \exp\left[\frac{[\eta]c}{1-(k/\nu)[\eta]c}\right], \tag{7.14}$$

where $[\eta]$ is the intrinsic viscosity, $c$ is the protein concentration in g/mL, and $k/\nu$ is an association term composed of the Simha shape parameter, $\nu$, and a self-crowding factor, $k$.[22] The self-crowding factor is proportional to an interaction strength and inversely proportional to a maximum packing fraction. Similarly, the Simha shape factor can be regarded as an effective association structure size. The viscosity can be interpreted in the context of these terms to help elucidate effective cluster-cluster interactions.

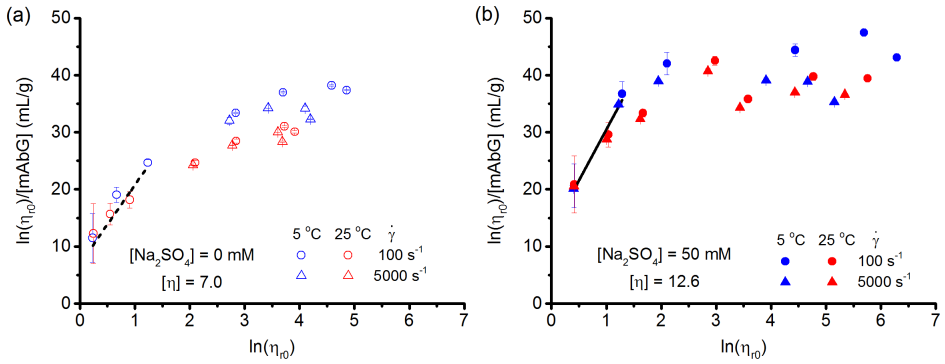


**Figure 7.25:** The viscosity is plotted according to the linearized Ross-Minton equation, where non-linearity indicates concentration dependent self-association, for (a) 0 mM and (b) 50 mM added sodium sulfate using viscosities at two different shear rates. The solid lines are used to estimate the intrinsic viscosity (provided in the corresponding pane).

An inherent assumption of the model is that $k/\nu$ is constant. However, the plot of $ln(\eta_{r0}))/c$ with respect to $ln(\eta_{r0})$ in Fig. 7.24 clearly demonstrates non-linearity, which suggests that the association factor is a function of concentration. The lines represent the linear region at low concentrations from which an intrinsic viscosity can be extracted. These values, shown in the legend of Fig. 7.25, agree with previous work, which estimates mAb monomers have intrinsic viscosities of about 7 mL/g and values approaching 12.6 mL/g are not uncommon for associating antibodies.[22, 46]

Differences in the association factor can be observed in Fig. 7.24 between all solution conditions and as a function of shear rate. The larger magnitude of $ln(\eta_{r0})/c$ for samples with added salt simply reflects the difference in $[\eta]$ between salt conditions, while the slope indicates differences in the association factor. Comparing Fig. 7.24a and Fig. 7.24b, the slope of the data is much flatter (i.e., smaller values of $k/\nu$) at high concentration for samples with added salt compared to samples without salt. Also, at each salt condition and shear rate $[\eta]$ is assumed to be constant, which indicates that reducing the temperature causes $k/\nu$ to increase. Therefore, the samples with 50 mM sodium sulfate appear to have a smaller association factor, indicative of either larger

aggregates, weaker association, or both.

Trends in the slope of $\ln(\eta_{r0})/c$ with increasing shear rate suggest that association strength between dimers in samples with 50 mM salt is weak enough to be disrupted by shear forces, while samples with 0 mM salt are largely unaltered by shear. While the aggregate size in samples with salt is larger (per the correlation between $\eta_{r0}$ and $L^3$ in Fig. 7.18d), they appear to be formed by weaker associations than found in samples without salt. Using Fig. 7.18c as an indication of the association size, the larger magnitude of $k/\nu$ for samples without salt suggests mAb3 has stronger interactions under these conditions despite having smaller viscosity. Note that this modified Ross-Minton model is unable to distinguish between attractive or repulsive interactions. From modeling of the SANS data and previous studies of cluster interactions,[40] the dynamic clusters in samples without salt interact via strong inter-protein repulsions leading to an increase in the viscosity with increasing concentration. Therefore, samples without salt form smaller aggregates that interact strongly repulsively while samples with added salt form large clusters that are transient due to weak association.

The same viscosity data can be fit using Eq. 7.14, shown in Fig. 7.26a for the lowest shear rate, to more quantitatively estimate the association factor as a function of protein concentration, which are plotted in Fig. 7.26b. The intrinsic viscosity values are held fixed at 7.0 and 12.6 for samples with 0 mM and 50 mM salt, respectively. These values were varied to optimize the fits and are in good agreement with values obtained in linear fits in Fig. 7.25. When treated as a fitting parameter, the values of $[\eta]$ are similar but the uncertainty in $k/\nu$ becomes significant. Changes in $[\eta]$ directly influence the low concentration regime and indirectly alter values of $k/\nu$ that predominantly dictate the magnitude in the high concentration regime. Distinct differences in the association factor can be observed in Fig. 7.26b between all solution conditions. The model is able to easily distinguish between salt conditions by the magnitude of $k/\nu$ values.

Quantitatively distinguishing the influence of formulation composition (specifically salt) on effective interactions provides additional insight into the mechanism causing the resulting solution viscosity behavior. Previously, large viscosities in mAb3

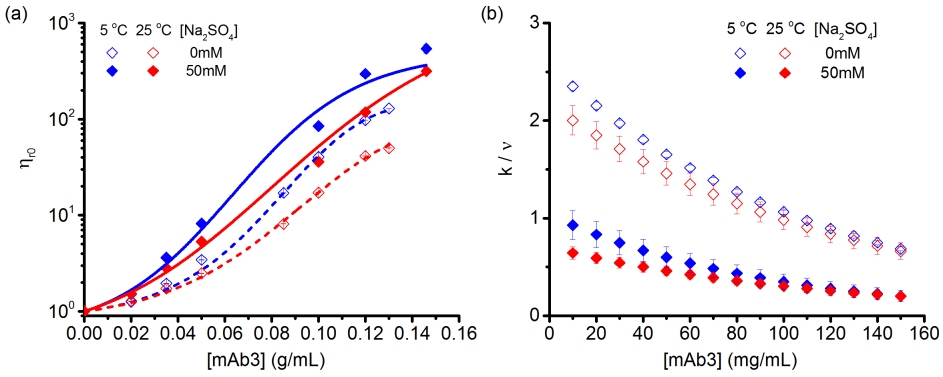


**Figure 7.26:** (a) The reduced zero-shear viscosity is plotted for each solution condition as a function of protein concentration with fits (solid lines) using the modified Ross-Minton equation while allowing $k/\nu$ to vary. (b) Corresponding values of $k/\nu$ extracted from the fits in (a) with each solution condition having identical symbols.

and other antibody solutions at high concentration have been qualitatively related with an effective cluster size.[22, 48, 50] However, cluster interactions have been discussed as an additional important contribution to the viscosity. The persistence of inter-protein interactions under shear, shown in Fig. 7.25 by non-linearity at multiple shear rates, is consistent with prior work on mAb3 by Lilyestrom, et al.[22] Therefore, this work compliments prior research by identifying the fundamental diffusing unit as being dimers in the presence of added salt, and by showing that the association of clusters forming at higher concentration arises from different inter-protein interactions depending on the salt concentration. Furthermore, this new knowledge helps to semi-quantitatively explain the significant rise in viscosity with increasing mAb concentration and salt and reduced temperature.

### 7.4.5 Comparison of mAb1, mAb2, and mAb3

Over the last two chapters, the structural and dynamic features of three monoclonal antibodies have been discussed in detail in order to rationalize the resulting solution viscosities. Here, they are explicitly compared to demonstrate the relative

influence of their distinct micromechanical properties on their corresponding solution properties. Figure 7.27 compares the reduced zero-shear viscosity of all three mAbs (to remove any influence of differences in buffer composition) under each of the solution conditions they were studied, as well as some literature results,[22] as a function of protein concentration.

In general, the results in Fig. 7.27 can be decomposed into small, medium and large viscosity groups. The smallest viscosities are found for solutions of mAb2 in $D_2O$ and mAb3 in $H_2O$ at $25°C$, which were shown previously to remain as a dispersed fluid phase of monomers with slightly repulsive interactions.[22, 48] Next, a larger intermediate viscosity is observed to result from formulations of mAb3 in $D_2O$ without salt and in $H_2O$ with 50 mM $Na_2SO_4$ at $25°C$. These two conditions are known to produce an equilibrium distribution of dynamic clusters with monomers.[16, 22] The presence of these clusters, and their subsequent effective interactions, thereby lead to the larger viscosities by analogy with more model globular proteins with similar cluster formation.[15]

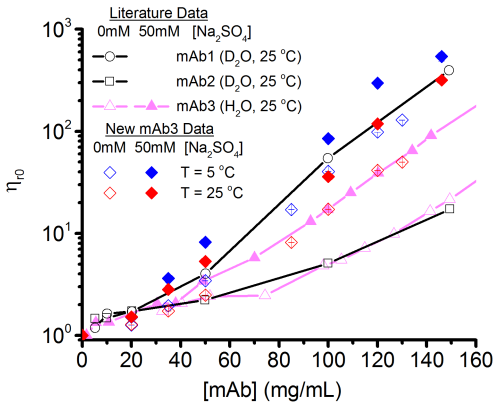


**Figure 7.27:** The concentration dependence of the zero-shear viscosity is compared for multiple antibodies and formulation conditions. Results are provided for mAb3 in $D_2O$ (diamonds) from this chapter[16] and literature results of mAb3 in $H_2O$ (triangles)[22] and mAb1 (circles) and mAb2 (squares) in $D_2O$.[48]

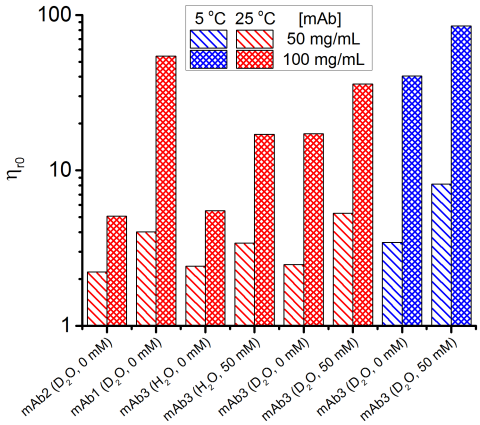


**Figure 7.28:** The viscosity of each of the mAbs and solution conditions presented in Fig. 7.27 at mAb concentrations of 50 mg/mL (diagonal bars) and 100 mg/mL (cris-cross bars).

The largest viscosities are found for samples of mAb1 in $D_2O$ without salt and mAb3 in $D_2O$ with 50 mM $Na_2SO_4$ at $25°C$, which is enhanced to even larger viscosities at lower temperature. Interestingly, the viscosity is nearly identical for mAb3 that forms large transient clusters in the presence of salt and mAb1 that was reported to form small long-lived clusters.[48] A common feature of the clusters formed by mAb1 without salt and by mAb3 with salt is that they both have elongated structures. Particles with larger aspect ratios are known to produce larger viscosities.[28] In the case of mAb1, these large effective radii, combined with electrostatic repulsion, was highlighted as the cause for the observed viscosity.[48] Here, the viscosity of mAb3 with added sodium sulfate appears to be driven primarily by attractive interactions. These forces cause protein dimers to associate into a distribution of cluster sizes that collectively resist shear flow. However, mAb3 dimers remain mobile and exchange between local environments to maintain fluidity.

The structure of the underlying fundamental moving unit and their effective interactions are explicitly shown to have a strong influence on the solution viscosity in Fig. 7.27. A summary of the differences between each mAb and solution condition are provided in Fig. 7.28 at two protein concentrations. Clearly, the differences become

more pronounced with increasing mAb concentration. However, the general connection between the antibodies and their propensity to associate with the viscosity is quite apparent. The existence of a universal correlation between average cluster size and viscosity is still questionable. Rather, the extent of cluster formation, cluster size/shape, and effective cluster-cluster interactions will dictate the viscosity. Consequently, these characteristics can lead to drastically different macromolecular structures, yet still produce similar macroscopic solution properties. In order to accurately engineer therapeutic formulations, a more quantitative relationship between the viscosity and each of these conditions will require additional development in the future.

## 7.5 Conclusions

The experimental evidence presented throughout this work in combination with previous studies[21, 22] indicates that mAb3, a relatively hydrophobic IgG1 antibody, can reversibly associate into small dynamic clusters. In the absence of salt these clusters are composed of monomers while in the presence of 50 mM sodium sulfate clusters consist of long-lived, elongated dimers that associate hierarchically into large, loosely bounded transient clusters at higher mAb concentrations. Both monomers and dimers remain mobile on short timescales at all mAb concentrations. Their effective interactions play a significant role in the resulting macromolecular microstructure in solution and viscosity. In formulations with salt, these small clusters associate into hierarchical, large scale structures that significantly increase the viscosity. Therefore, accurately modeling the viscosity of concentrated protein solutions requires more thorough characterization of cluster properties. Several existing viscosity models were shown to provide useful, semi-quantitative information concerning the underlying microstructure in viscous mAb solutions, especially when combined with structural and dynamic experiments. Although the existence of a universal relation between cluster formation and viscosity remains elusive, characterizing the appropriate properties can sufficiently guide the optimization of biopharmaceutical therapeutic formulation.

## REFERENCES


[1] Banchio, A. J., and Nägele, G. Short-time transport properties in dense suspensions: from neutral to charge-stabilized colloidal spheres. *J. Chem. Phys. 128*, 10 (Mar. 2008), 104903.

[2] Banchio, A. J., Nagele, G., and Bergenholtz, J. Viscoelasticity and generalized StokesEinstein relations of colloidal dispersions. *J. Chem. Phys. 111*, 18 (1999), 8721.

[3] Brady, J. F. The rheological behavior of concentrated colloidal dispersions. *J. Chem. Phys. 99*, 1 (1993), 567.

[4] Brady, J. F., and Morris, J. F. Microstructure of strongly sheared suspensions and its impact on rheology and diffusion. *J. Fluid Mech. 348* (Oct. 1997), 103.

[5] Bryngelson, J. D., Onuchic, J. N., Socci, N. D., and Wolynes, P. G. Funnels, pathways, and the energy landscape of protein folding: a synthesis. *Proteins 21*, 3 (Mar. 1995), 167–95.

[6] Cardinaux, F., Stradner, A., Schurtenberger, P., Sciortino, F., and Zaccarelli, E. Modeling equilibrium clusters in lysozyme solutions. *Europhys. Lett. 77*, 4 (Feb. 2007), 48004.

[7] Chaudhri, A., Zarraga, I. E., Kamerzell, T. J., Brandt, J. P., Patapoff, T. W., Shire, S. J., and Voth, G. A. Coarse-Grained Modeling of the Self-Association of Therapeutic Monoclonal Antibodies. *J. Phys. Chem. B 116* (July 2012), 8045.

[8] Chen, S.-H. Small angle neutron scattering studies of the structure and interaction in micellar and microemulsion systems. *Annu. Rev. Phys. Chem. 37* (1986), 351–399.

[9] Chen, S.-H., Broccio, M., Liu, Y., Fratini, E., and Baglioni, P. The two-Yukawa model and its applications: the cases of charged proteins and copolymer micellar solutions. *J. Appl. Crystallogr. 40*, s1 (Apr. 2007), s321–s326.

[10] Clark, N. J., Zhang, H., Krueger, S., Lee, H. J., Ketchem, R. R., Kerwin, B., Kanapuram, S. R., Treuheit, M. J., McAuley, A., and Curtis, J. E. Small-angle neutron scattering study of a monoclonal antibody using free-energy constraints. *J. Phys. Chem. B 117*, 45 (Nov. 2013), 14029–38.

[11] Dill, K. A., and Chan, H. S. From levinthal to pathways to funnels. *Nat. Struct. Biol. 4*, 1 (1997), 10–19.

[12] Falus, P., Porcar, L., Fratini, E., Chen, W.-R., Faraone, A., Hong, K., Baglioni, P., and Liu, Y. Distinguishing the monomer to cluster phase transition in concentrated lysozyme solutions by studying the temperature dependence of the short-time dynamics. *J. Phys. Condens. Matter 24*, 6 (Feb. 2012), 064114.

[13] Foss, D. R., and Brady, J. F. Structure, diffusion and rheology of Brownian suspensions by Stokesian Dynamics simulation. *J. Fluid Mech. 407* (2000), 167.

[14] Frauenfelder, H., Sligar, S. G., and Wolynes, P. G. The Energy Landscapes and Motions of Proteins. *Science (80-. ). 254*, 5038 (1991), 1598–1603.

[15] Godfrin, P. D., Hudson, S. D., Hong, K., Porcar, L., Falus, P., Wagner, N. J., and Liu, Y. Excess viscous response from intrinsic structural heterogeneity caused by competing potential features. *Submitt. to Phys. Rev. Lett.* (2015).

[16] Godfrin, P. D., Zarzar, J., Zarraga, I. E., Porcar, L., Falus, P., Wagner, N. J., and Liu, Y. Hierarchical cluster formation and its effect on the viscosity of concentrated monoclonal antibody formulations. *Submitt. to J. Phys. Chem. B* (2015).

[17] Harris, R. J., Shire, S. J., and Winter, C. Commercial manufacturing scale formulation and analytical characterization of therapeutic recombinant antibodies. *Drug Dev. Res. 61*, 3 (Mar. 2004), 137–154.

[18] Harroun, T., Wignall, G., and Katsaras, J. Neutron Scattering for Biology. In *Neutron Scatt. Biol. Tech. Appl.*, J. Fitter, T. Gutberlet, and J. Katsaras, Eds. Springer, 2006, pp. 1–18.

[19] Kim, J. M., Castañeda Priego, R., Liu, Y., and Wagner, N. J. On the importance of thermodynamic self-consistency for calculating clusterlike pair correlations in hard-core double Yukawa fluids. *J. Chem. Phys. 134*, 6 (Feb. 2011), 064904.

[20] Krishnamurthy, L.-N., and Wagner, N. J. The influence of weak attractive forces on the microstructure and rheology of colloidal dispersions. *J. Rheol. (N. Y. N. Y). 49*, 2 (2005), 475.

[21] Lilyestrom, W. G., Shire, S. J., and Scherer, T. M. Influence of the Cosolute Environment on IgG Solution Structure Analyzed by Small-Angle X-ray Scattering. *J. Phys. Chem. B 116* (2012), 9611–8.

[22] Lilyestrom, W. G., Yadav, S., Shire, S. J., and Scherer, T. M. Monoclonal antibody self-association, cluster formation, and rheology at high concentrations. *J. Phys. Chem. B 117*, 21 (May 2013), 6373–84.

[23] Lionberger, R. A., and Russel, W. B. A Smoluchowski theory with simple approximations for hydrodynamic interactions in concentrated dispersions. *J. Rheol. (N. Y. N. Y). 41*, 2 (Mar. 1997), 399.

[24] Liu, Y., Chen, W.-R., and Chen, S.-H. Cluster formation in two-Yukawa fluids. *J. Chem. Phys. 122*, 4 (Jan. 2005), 44507.

[25] Liu, Y., Porcar, L., Chen, J., Chen, W.-r., Falus, P., Faraone, A., Fratini, E., Hong, K., and Baglioni, P. Lysozyme protein solution with an intermediate range order structure. *J. Phys. Chem. B 115*, 22 (June 2011), 7238.

[26] Malfois, M., Bonnete, F., Belloni, L., and Tardieu, A. A model of attractive interactions to account for fluidfluid phase separation of protein solutions. *J. Chem. Phys. 105*, 8 (1996), 3290.

[27] McQuarrie, D. *Statistical Mechanics*. University Science Books, 2000.

[28] Mewis, J., and Wagner, N. J. *Colloidal Suspension Rheology*. Cambridge University Press, New York, 2012.

[29] Nagele, G. On the dynamics and structure of charge-stabilized suspensions. *Phys. Rep. 272*, 5-6 (1996), 215–372.

[30] Onuchic, J. N., Luthey-Schulten, Z., and Wolynes, P. G. Theory of protein folding: the energy landscape perspective. *Annu. Rev. Phys. Chem. 48*, 1 (Jan. 1997), 545–600.

[31] Porcar, L., Falus, P., Chen, W.-R., Faraone, A., Fratini, E., Hong, K., Baglioni, P., and Liu, Y. Formation of the Dynamic Clusters in Concentrated Lysozyme Protein Solutions. *J. Phys. Chem. Lett. 1*, 1 (Jan. 2010), 126.

[32] Roberts, C. J. Non-Native Protein Aggregation Kinetics. *Biotechnol. Bioeng. 98*, 5 (2007), 927–938.

[33] Roberts, C. J. Therapeutic protein aggregation: mechanisms, design, and control. *Trends Biotechnol. 32*, 7 (July 2014), 372–80.

[34] Rosenbaum, D., Zamora, P., and Zukoski, C. Phase behavior of small attractive colloidal particles. *Phys. Rev. Lett. 76*, 1 (Jan. 1996), 150.

[35] Rosenberg, A. S. Effects of Protein Aggregates : An Immunologic Perspective. *AAPS J. 8*, 3 (2006), 501–507.

[36] Ross, C. A., and Poirier, M. A. Protein aggregation and neurodegenerative disease. *Nat. Med. 10 Suppl*, July (July 2004), S10–7.

[37] Sandler, S. *An Introduction to Applied Statistical Thermodynamics*. John Wiley and Sons, 2011.

[38] Scherer, T. M., Liu, J., Shire, S. J., and Minton, A. P. Intermolecular Interactions of IgG1 Monoclonal Antibodies at High Concentrations Characterized by Light Scattering. *J. Phys. Chem. B 114* (2010), 12948–12957.

[39] Schmit, J. D., He, F., Mishra, S., Ketchem, R. R., Woods, C. E., and Kerwin, B. a. Entanglement model of antibody viscosity. *J. Phys. Chem. B 118*, 19 (May 2014), 5044–9.

[40] Sciortino, F., Mossa, S., Zaccarelli, E., and Tartaglia, P. Equilibrium Cluster Phases and Low-Density Arrested Disordered States: The Role of Short-Range Attraction and Long-Range Repulsion. *Phys. Rev. Lett. 93*, 5 (July 2004), 5.

[41] Sharma, V., Jaishankar, A., Wang, Y.-C., and McKinley, G. H. Rheology of globular proteins: apparent yield stress, high shear rate viscosity and interfacial viscoelasticity of bovine serum albumin solutions. *Soft Matter 7*, 11 (2011), 5150.

[42] Shire, S. J. Formulation and manufacturability of biologics. *Curr. Opin. Biotechnol. 20* (2009), 708–714.

[43] Wagner, N. J., Krause, R., Rennie, A. R., D'Aguanno, B., and Goodwin, J. The microstructure of polydisperse , charged colloidal suspensions by light and neutron scattering. *J. Chem. Phys. 95* (1991), 494.

[44] Yadav, S., Laue, T. M., Kalonia, D. S., Singh, S. N., and Shire, S. J. The influence of charge distribution on self-association and viscosity behavior of monoclonal antibody solutions. *Mol. Pharm. 9*, 4 (Apr. 2012), 791–802.

[45] Yadav, S., and Scherer, T. M. Solubility Challenges in High Concentration Monoclonal Antibody Formulations: Relationship with Amino Acid Sequence and Intermolecular Interactions. *submitted* (2015).

[46] Yadav, S., Shire, S. J., and Kalonia, D. S. Factors Affecting the Viscosity in High Concentration Solutions of Different Monoclonal Antibodies. *J. Pharm. Sci. 99*, 12 (2010), 4812–4829.

[47] Yadav, S., Sreedhara, A., Kanai, S., Liu, J., Lien, S., Lowman, H., Kalonia, D. S., and Shire, S. J. Establishing a link between amino acid sequences and self-associating and viscoelastic behavior of two closely related monoclonal antibodies. *Pharm. Res. 28*, 7 (July 2011), 1750–64.

[48] Yearley, E. J., Godfrin, P. D., Perevozchikova, T., Zhang, H., Falus, P., Porcar, L., Nagao, M., Curtis, J., Gawande, P., Taing, R., Zarraga, I. E., Wagner, N. J., and Liu, Y. Observation of small cluster formation in concentrated monoclonal antibody solutions and its implications to solution viscosity. *Biophys. J. 106*, 8 (2014), 1763–1770.

[49] Yearley, E. J., Zarraga, I. E., Shire, S. J., Scherer, T. M., Gokarn, Y., Wagner, N. J., and Liu, Y. Small-Angle Neutron Scattering Characterization of Monoclonal Antibody Conformations and Interactions at High Concentrations. *Biophys. J. 105* (2013), 720–731.

[50] Zarraga, I. E., Taing, R., Zarzar, J., Luoma, J., Hsiung, J., and Patel, A. High Shear Rheology and Anisotropy in Concentrated Solutions of Monoclonal Antibodies. *J. Pharm. Sci. 102*, 8 (2013), 2538–2549.

[51] Zemb, T., and Lindner, P. *Neutrons, X-rays and Light: Scattering Methods Applied to Soft Condensed Matter*. Elsevier B.V., Amsterdam, 2002.

# Chapter 8

# CONCLUSIONS AND FUTURE WORK

## 8.1 Conclusions

This dissertation advances the current understanding of cluster fluid fundamentals and associated material properties. In the context of the tiered representation of structure-property relationships introduced in Fig. 1.1, this work has solidified the link between the interaction potential (and parameters) and phase behavior of systems with SALR interactions by creating a generalized phase diagram of these materials. Due to the generality of SALR forces, this connection between the interactions and phase space bridges the gap between a wide range of chemistries and properties in materials susceptible to clustering. Within this broad set of properties, this dissertation successfully demonstrated that cluster formation directly contributes to significant increases in solution viscosity. The fundamental concepts garnered through studying model systems were applied to describe the solution viscosity behavior of commercially relevant biopharmaceutical therapeutics. Although still early in its development, the new relationship between cluster formation and solution viscosity has substantial potential to direct more optimized formulation of monoclonal antibody products. More generally, this dissertation has outlined a powerful framework to study the behavior of colloidal dispersions with competing interactions and their properties. While this work focused on the possible formation of cluster fluids, several structural states were identified and distinguished through simulations and a novel combination of experimental techniques. For example, the association of clusters into large percolated networks may lead to unique mechanical or electrical properties, such as the elastic modulus or conductivity, that may be particularly pertinent to various industries.

Each chapter of this dissertation addresses a fundamental issue of equilibrium cluster formation, the sum of which provides a hierarchy of knowledge ranging from the fundamental thermodynamics to some specific material properties of biopharmaceutical products. Specifically, this was accomplished by testing the two hypotheses proposed in Chapter 1. To start, a generalized phase diagram of clustered states due to SALR interactions was successfully created. This achievement helps resolve a current topical debate over the identification of cluster fluids. It also serves as an efficient method to determine cluster formation and the associated phase of a given material. Subsequently quantifying the extent of cluster formation (e.g., population and average size) and the resulting solution viscosity in protein dispersions confirmed that these two features are correlated. An accurate quantitative relationship remains to be developed, but a semi-quantitative model (incorporating cluster parameters) was developed.

Understanding the unique characteristics of cluster fluids first required a clear definition of the various states that may contain clusters. This includes structural and dynamic features. Therefore, a consistent and testable definition of states was constructed to unambiguously distinguish the variety of microstructures formed by particles with SALR interactions in solution (Chapter 3). Monte Carlo simulations were used to generate solution structures for a variety of state points to quantify cluster formation. Further, by testing a wide range of parameter sets, structural features of well-defined cluster fluids were identified that allow for accurate recognition of their formation experimentally without the need for additional simulations. In the course of this work it was discovered that small angle scattering experiments can distinguish cluster fluids as when the magnitude of the IRO peak rises above 2.7 or increases with increasing volume fraction (at a constant temperature). Further, using microscopy, clustered fluids can also be identified by an empirical logarithmic dependence of the average coordination number on the average cluster size or a local cluster volume fraction. Summarizing these state points on an appropriately normalized state diagram produced the generalized phase space of clustered fluids (Chapter 4).

Experimentally, a novel combination of techniques was necessary to accurately

account for both the structural and dynamic features of clusters. Interaction parameters obtained from fitting experimental results can be utilized in simulations to extract detailed microstructure information unavailable by the original technique itself. However, the equilibrium exchange of monomers between clusters and bulk solution sufficiently delineates dynamic correlations from structural properties, as measured by small angle scattering or calculated in simulations. Therefore, the explicit measurement of short time self diffusion was shown to be necessary to probe cluster formation. Estimates of the location of the protein samples on the idealized cluster phase diagram suggested they were not "true" clustered fluids as defined in the simulations, yet dynamic measurements indicated extensive cluster formation. In the case of lysozyme, semi-quantitative estimates of an average cluster size by both simulations and dynamics were shown to directly correlate with a significant increase in viscosity (Chapter 5). In fact, the clusters associated together at higher volume fractions leading to dynamic percolation (i.e., "random percolated" states in the general phase diagram), which likely contributed at least in part to the large viscosities. Similarly, mAb3 formed small clusters that subsequently associated into transient networks, also leading to very large viscosity at high concentration (Chapter 7). In contrast, mAb1 formed small, long-lived clusters with an extended structure that become more abundant but did not lead to a network-like structure. For this system the interactions between these clusters still produced an equivalently large viscosity increase as observed by mAb3 (Chapter 6). Thus, despite the differences in the interactions between mAb1 and mAb3, both have similar microstructures and yield significant viscosity increases in solution at higher protein concentration. Further, this relationship between interactions and viscosity can be understood semi-quantitatively using the framework developed by this dissertation.

## 8.2 Future Work

The work presented in this dissertation has enhanced the current understanding of the physical mechanisms of cluster formation in SALR systems, the characteristic

features of clusters that allow them to be observed experimentally, and the intricate relationship between the solution viscosity of clustering materials and the underlying competing interactions. These advancements provide a framework within which material properties of protein solutions and other systems with competing interactions can be understood. They also reveal new uncertainty in the applicability of the original simplifications made in earlier studies to gain this insight. The open ended questions that remain are a basis for further investigation. In what follows I present a few of the most promising research leads arising from the main content of this dissertation.

### 8.2.1 A Model One-Component Cluster Forming System

Several key conclusions regarding cluster formation were able to be made using lysozyme as a representative system with SALR interactions. Similar to other colloidal systems, the repulsion strength and range can be tuned by altering the pH (surface charge) and salt concentration, though these were not tuned in this study. However, the attraction strength is set by the composition (as discussed in Chapter 1 and demonstrated in Chapter 5) and thus, varies with concentration and temperature in a manner that is not completely controlled by the experimentalist.[6] While earlier work has also utilized a depletant to control the effective attraction strength,[2, 14, 15, 16] the addition of a second component may influence the resulting structural correlations of the colloidal particles due to its finite size (unlike counter-ions).

Further efforts to study a well defined and controlled connection between SALR interactions and associated properties would greatly benefit from developing a more "ideal" experimental system. The model SALR system proposed here is based on previous work studying the influence of purely attractive interactions. By grafting polar molecules (octadecyl chains) to the surface of spherical silica nanoparticles, the strength of attraction could be easily tuned by changing temperature.[4, 5] Physically, the attractive force is proposed to arise from inter-digitation of molecules in the grafted layers of two neighboring particles. These particles, which are suspended in a polar

medium (tetradecane), have no effective repulsive force due to the solvent's low relative permittivity combined with the nearly complete coverage of surface silanol groups.

In order to introduce additional long-range repulsion to the well-characterized short-range attraction in these systems, several possible alterations could be made to the surface chemistry. First, the surface graft density could be controlled to allow for an increase in the residual silanol groups capable of becoming exposed and subsequently charged. However, care must be taken to characterize the influence of reducing the chain graft density on the effective attraction strength as previous studies all utilized fully grafted particles. Another uncertainty is whether protons in surface silanol groups will dissociate in an organic solvent. To help induce dissociation, lipophilic salts could be added such as tetraphenylborate or hexafluorophosphate, which should be sufficiently soluble in tetradecane or similar organic solvents.

If an organic salt does not cause enough dissociation to induce an effective repulsive force between particles, a surfactant could be used that forms reverse micelles, such as sodium bis(2-ethylhexyl) sulfosuccinate or AOT. With a subtle amount of added water, reverse micelles could provide an environment for protons to sit and behave as large counter-ions in a manner similar to a Debye double layer. However, introducing micelles into the system could defeat the purposed of removing a second component to the system as is the concern with a depletion inducing polymer. Interestingly, depending on the size of the reverse AOT micelles, they could serve as a depletant themselves and, if they are able to extract a proton from the particle surface, could also serve as a large effective counter-ion that screens long-range repulsion.

Another approach is to change the graft chain chemistry. While this would require extensive characterization of the attractive force as was already accomplished for octadecyl chains, it would also allow for customization. In particular, silica particles could be covered in varying mixtures of polar and non-polar amino acids or polypeptides composed of several of the same amino acids. This would easily allow for these particles to be suspended in polar solvents rather than organic solvents. The polar groups (e.g., arginine, histidine, lysine, aspartic acid, glutamic acid) could provide

sufficient charge to induce repulsive forces while the non-polar groups (e.g., alanine, valine, leucine, phenylalanine, tyrosine, tryptophan) could induce short-range attractive hydrophobic forces.[7] By varying the relative content of hydrophilic and hydrophobic surface residues, the relative strength of attraction and repulsion could be tuned. Such surface chemistry is attractive as it may be comparable to "natural" protein surfaces (yet well controlled), especially if the surface becomes patchy due to preferential association of similar residues/chains.

### 8.2.2 Developing More Accurate Models of Cluster Interactions, Growth, and Viscosity

Although the development of a generalized phase diagram of SALR systems has progressed the understanding of cluster formation, the properties of clusters (including fractal dimension, local volume fraction, and lifetime) are still expected to vary as a function of solution conditions within the region of cluster fluids. In addition to the initial formation of clusters, their dynamics and growth will be dictated by their effective interactions. Therefore, quantifying intra- and inter-cluster forces is an important aspect of understanding cluster stability. In particular, the internal forces between particles in a given cluster and those between clusters may play an important role in quantifying cluster lifetime and dictate the fractal dimension.[2, 13]

Effective cluster forces can be quantified by building upon the fundamental interactions between individual monomers. The original identification of a sufficient stabilizing repulsion to halt aggregation to a preferred cluster size by competing interactions was founded on the inherent assumption that the cluster repulsive strength was an additive accumulation of the individual components.[11, 12] This assumption was also utilized in developing the viscosity model discussed in the Appendix.

As discussed in Chapter 1, early studies of SALR interactions demonstrated the interplay of the attraction and repulsion resulting in a preferred cluster size in the ground state (low concentration and temperature) limit.[12] Under these conditions, the influence of surrounding particles and clusters on the stability of an individual

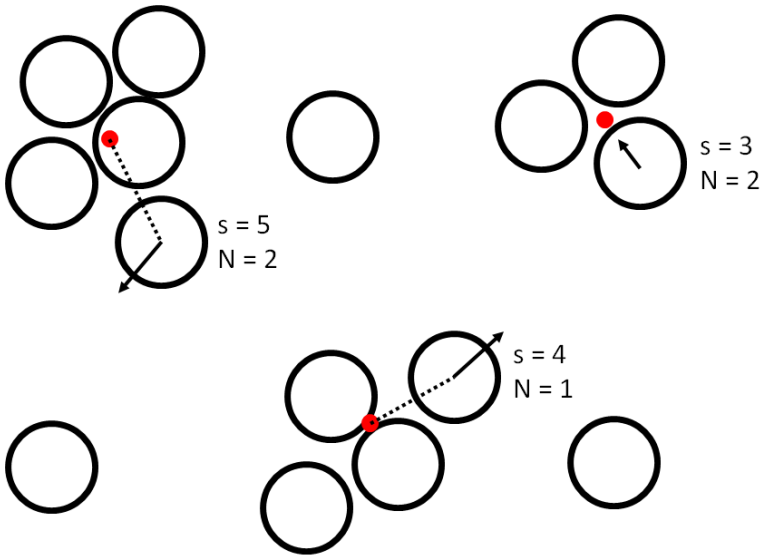


**Figure 8.1:** A hypothetical two dimensional microstructure is shown with three clusters. One particle in each cluster is shown with a dotted line connecting it to the cluster center of mass and an arrow depicting the directionality of the net force acting on it. Each particle is labeled as it would be distinguished, with a cluster size, $s$, and coordination number, $N$.

cluster is not accounted for. While simulations can indirectly account for the influence of the microstructure in determining the equilibrium distribution of cluster sizes, few studies have focused on the actual energy landscape within which a cluster exists. By doing so, the susceptibility of a single particle to leaving or joining a cluster may be deduced from stochastic simulations in addition to the ensemble average structural correlations. Otherwise, more time consuming dynamic simulations would be necessary to track the momentum of particles and quantify the dynamic correlations. Therefore, understanding cluster growth and dynamics will greatly benefit from developing a protocol to calculate the directionality of the forcefield acting on a particle as a function of (1) the cluster size within which it exists, (2) its location relative to the cluster center of mass, and (3) its coordination number. An example of such a calculation is depicted in Fig. 8.1. For comparison, recent work has actually demonstrated that particles of low coordination numbers (3–4) play a significant role in the formation of gels in purely attractive systems.[17]

Accordingly, the relative population of particles in various environments can be quantified from simulation trajectories and ensemble averages calculated according to any of the three parameters of interest. If an equilibrium process, the energy "holding" particles in a cluster should be an energy barrier, possibly described as an Arhenius or activated process, which can be tested by determined the average value as a function of cluster size and location within a cluster. Whether a particle is in the process of being expelled or withheld is determined by the directionality of the total force relative to its location from the cluster center of mass, shown by the arrows in Fig. 8.1. If indeed Arhenius, then a rate of exchange and thus, a cluster lifetime can be estimated. Similarly, if the percolation threshold is surpassed, the formation of the percolated network can be decomposed into the association of smaller clusters in a manner similar to the work performed previously for systems with purely attractive interactions.[17] Additionally, altering the cut-off distance defining connectivity as discussed in Chapter 3 could help in identifying "dominant" cluster sizes in network formation.

Finally, the viscosity model developed in the Appendix was qualitatively based

on previously developed models of multi-component HS fluids and one-component interacting systems.[1, 8, 9, 10] However, combining these contributions to quantitatively capture the viscosity in a pseudo-multi-component interacting system, which clustering systems can be approximated as, requires derivation of complex fluid mechanics and hydrodynamics. Even this complicated description of a cluster fluid is a simplification of these materials considering their dynamic nature. Therefore, a derivation of the expected dependence of the diffusivity of clusters as a function of size, volume fraction, and interaction parameters should be pursued in future work. Although the proposed viscosity model is an empirical function of attractive and repulsive forces, if combined with a better representation of cluster size determined from the diffusivity and more appropriate function of inter-cluster interaction strength, then it may provide accurate estimates of the viscosity in cluster forming solutions.

### 8.2.3 Representing Colloidal Shape and Interaction Anisotropy by the Reference Interaction Site Model

Proteins have been observed to interact by an effective combination of short range attraction and long range repulsion. However, the physical origin of the attractive forces is not entirely understood. The study of clustering in several monoclonal antibody formulations has lead to distinctly different hypothesizes. Within this dissertation, mAb1 and mAb3 (discussed in Chapter 6 and Chapter 7, respectively) were differentiated as having short range attractive interactions driven by electrostatic and hydrophobic forces, respectively. As such, understanding the connection between the biochemistry and effective interactions would make a colloidal representation of protein solutions significantly more powerful. Therefore, this field of research would benefit from further progress in representing the complex structure of proteins and the subsequent influence it has on the protein-protein interactions.

An obvious means of distinguishing proteins is by their underlying chemistry, from which the effective interactions originate. Although these proteins are all composed of the same 20 $\alpha$-amino acids acting as fundamental units, the shear size of the

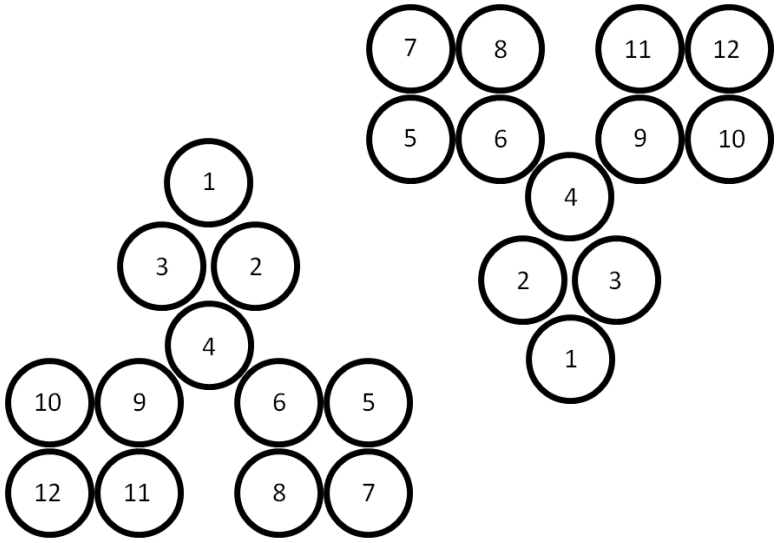


**Figure 8.2:** Two 12 sphere representations of monoclonal antibodies are shown side by side with each position labeled as it would in the RISM formalism.

primary sequence, which contains roughly 1300 building blocks for antibodies, allows for a nearly infinite number of permutations. As a result, the intra-protein structure and inter-protein interactions will vary widely, though all should be considered potentially capable of interacting by SALR interactions. The complex structure of monoclonal antibodies can be captured using a coarse-grained representation using a geometric combination spheres, as demonstrated by the model developed in Chapter 7. However, this leaves a gap in representing the effective interactions, which are currently still represented by mean field isotropic potentials.

The next progression in more accurate calculations of inter-protein interactions is to incorporate the anisotropic structure using the reference interaction site model (RISM) formalism.[3] Similar to the antibody form factor model, RISM represents a fluid of identical structures, each with a combination of $n$ points with a specific, rigid orientation. An example of such a representation following the 12 bead monoclonal antibody structural model is shown in Fig. 8.2. Every combination of points then has a unique interaction potential, totaling $n(n+1)/2$ site-site interactions. In the context

of integral equation theory as described in Chapter 2, the radial distribution function of two particles ($\alpha$ and $\beta$) is $g_{\alpha\beta}(r)$ and the correlation function is $h_{\alpha\beta}(r) = g_{\alpha\beta}(r) - 1$, while the direct correlation function is represented as $c_{\alpha\beta}(r)$ and the intra-structure correlation function as $w_{\alpha\beta}(r)$. Taking the Fourier transform of the Ornstein-Zernike equation, the resulting function of $n$ x $n$ matrices is

$$\hat{H}(k) = \hat{W}(k)\hat{C}(k)\hat{W}(k) + \rho\hat{W}(k)\hat{C}(k)\hat{H}(k) \tag{8.1}$$

which is the multi-component equivalent of Eq. 2.8 in Chapter 2. Correspondingly, Eq. 8.1 is solved in exactly the same manner as the one-component OZ equation using an appropriate closure relation. However, depending on the choice of interaction potential, the number of parameters to be varied/defined becomes significant. For example, using the HSDY potential that includes 4 parameters with the 12 sphere representation of a mAb would require $4\text{x}12(12+1)/2 = 312$ variables. An immediate simplification would be to constrain intra-molecular site-site interactions to be represented by a HS potential. Additionally, while effective mAb-mAb interactions appear to have both a short-range attractive and long-range repulsive component, each individual site interaction may be purely attractive or repulsive, which could provide a means to further reduce the number of variables.

## REFERENCES


[1] Brady, J. F. The rheological behavior of concentrated colloidal dispersions. *J. Chem. Phys. 99*, 1 (1993), 567.

[2] Campbell, A., Anderson, V., van Duijneveldt, J. S., and Bartlett, P. Dynamical Arrest in Attractive Colloids: The Effect of Long-Range Repulsion. *Phys. Rev. Lett. 94*, 20 (May 2005), 1.

[3] Chandler, D., and Andersen, H. C. Optimized Cluster Expansions for Classical Fluids. II. Theory of Molecular Liquids. *J. Chem. Phys. 57*, 5 (1972), 1930–1937.

[4] Eberle, A. P. R., Castañeda Priego, R., Kim, J. M., and Wagner, N. J. Dynamical arrest, percolation, gelation, and glass formation in model nanoparticle dispersions with thermoreversible adhesive interactions. *Langmuir 28*, 3 (Jan. 2012), 1866–78.

[5] Eberle, A. P. R., Wagner, N. J., Akgun, B., and Satija, S. K. Temperature-dependent nanostructure of an end-tethered octadecane brush in tetradecane and nanoparticle phase behavior. *Langmuir 26*, 5 (Mar. 2010), 3003–7.

[6] Godfrin, P. D., Hudson, S. D., Hong, K., Porcar, L., Falus, P., Wagner, N. J., and Liu, Y. Excess viscous response from intrinsic structural heterogeneity caused by competing potential features. *Submitt. to Phys. Rev. Lett.* (2015).

[7] Israelachvili, J. N. *Intermolecular and Surface Forces*, 3rd editio ed. Elsevier, 2011.

[8] Kaplan, P., Yodh, A., and Pine, D. Diffusion and structure in dense binary suspensions. *Phys. Rev. Lett. 68*, 3 (1992), 393–396.

[9] Krishnamurthy, L.-N., and Wagner, N. J. The influence of weak attractive forces on the microstructure and rheology of colloidal dispersions. *J. Rheol. (N. Y. N. Y). 49*, 2 (2005), 475.

[10] Lionberger, R. Viscosity of bimodal and polydisperse colloidal suspensions. *Phys. Rev. E 65*, 6 (June 2002), 061408.

[11] Mossa, S., Sciortino, F., Tartaglia, P., and Zaccarelli, E. Ground-state clusters for short-range attractive and long-range repulsive potentials. *Langmuir 20*, 24 (2004), 10756–10763.

[12] Sciortino, F., Mossa, S., Zaccarelli, E., and Tartaglia, P. Equilibrium Cluster Phases and Low-Density Arrested Disordered States: The Role of Short-Range Attraction and Long-Range Repulsion. *Phys. Rev. Lett. 93*, 5 (July 2004), 5.

[13] Sciortino, F., Tartaglia, P., and Zaccarelli, E. One-dimensional cluster growth and branching gels in colloidal systems with short-range depletion attraction and screened electrostatic repulsion. *J. Phys. Chem. B 109*, 46 (2005), 21942.

[14] Sedgwick, H., Egelhaaf, S. U., and Poon, W. C. K. Clusters and gels in systems of sticky particles. *J. Phys. Condens. Matter 16*, 42 (Oct. 2004), S4913–S4922.

[15] Segrè, P., Prasad, V., Schofield, A., and Weitz, D. A. Glasslike Kinetic Arrest at the Colloidal-Gelation Transition. *Phys. Rev. Lett. 86*, 26 (June 2001), 6042.

[16] Stradner, A., Sedgwick, H., Cardinaux, F., Poon, W. C. K., Egelhaaf, S. U., and Schurtenberger, P. Equilibrium cluster formation in concentrated protein solutions and colloids. *Nature 432*, 7016 (Nov. 2004), 492.

[17] Zia, R. N., Landrum, B. J., Russel, W. B., Landrum, B. J., and Russel, W. B. A micro-mechanical study of coarsening and rheology of colloidal gels :

Cage building , cage hopping , and Smoluchowski ' s ratchet. *J. Rheol. (N. Y. N. Y). 1121*, 5 (2014), 1121–1157.

# Appendix

# A MICROMECHANICAL MODEL OF CLUSTER FLUID DYNAMICS AND VISCOSITY

## A.1 Introduction

Throughout this dissertation, various thermodynamic relationships developed previously for colloidal systems with purely attractive and purely repulsive interactions have been used to rationalize and understand the behavior of materials that interact by a combination of these two forces. For example, Chapter 4 normalized states of systems with SALR interactions by the purely attractive phase diagram to show a unique localization of cluster fluid states. Now, the influence of competing interactions on the dynamics and viscosity are of interest. However, as is repeatedly discussed in Chapters 5 – 7, no models currently exist to represent the properties of these novel systems. Therefore, previous research on "simpler" systems is again used as a basis to help develop an empirical equation to accurately represent the observed effective short-time diffusion and zero-shear viscosity in systems with SALR interactions.

The inter-dependence of the interactions, structure, and dynamics introduces both a benefit and a complication to quantifying SALR interactions from experimental observations. First, the benefit arises from the unique combination of structural and dynamic features of competing interactions such as the formation of an IRO peak in $S(q)$ and large hydrodynamic radii observed in NSE measurements that will help identify the presence of this particular combination of forces. However, representing these types of interactions is complicated by the finite lifetime of association into clusters and the inherent polydispersity and heterogeneity in the structure.[9, 20] As an equilibrium state, particles in cluster fluids freely exchange between cluster and bulk (or monomer)

environments. Therefore, to maintain a consistent representation of structural contributions to both dynamics and viscosity, these two properties are developed in tandem to simultaneously extract representative parameters of cluster formation.

Previous work has highlighted the importance of particle interactions, structure, and dynamics on the viscosity,[5, 19] which can be decomposed into individual microstructural contributions.[5, 17] Several models have incorporated these contributions into a single effective parameter, the Huggins coefficient, for semi-dilute HS suspensions,[3, 24] charged colloids,[5] and weakly attractive particles.[4, 7] Unfortunately, these models assume small, homogeneous perturbations to the equilibrium microstructure. This is important for systems with attractive interactions where a large fraction of particles are in contact that can significantly disrupted by shear forces pulling two these particles apart. This limits the applicability of these micromechanical models to weak attractive forces, where the microstructure is still relatively well dispersed.

SALR systems are unique in their ability to form IRO, which is essentially local heterogeneity, in a variety of microstructural states.[8, 10, 18] The heterogeneity occurs over lengthscales of roughly $2\pi/q_{IRO}$ and smaller, but remain homogeneous fluids over macroscopic lengthscales. Thus, a mean field model to describe the viscosity is still appropriate. Interestingly, cluster formation helps fulfill the assumption of weak perturbations to the equilibrium solution structure. Specifically, if clusters are long-lived, they remain dynamically correlated and can be considered as a single entity. In other words, it is assumed that the internal cluster configuration is unaffected by shear and is also not a significant contribution to the viscosity. The common link between the influence of cluster formation on the dynamics and viscosity is the short-time self diffusivity, $D_S$, which from previous research is known to have significant contributions to the viscosity[5] and represent the effective hydrodynamic cluster size.[20]

## A.2 Modeling the Effect of Competing Interactions on the Dynamics

Theoretical descriptions of self diffusion as a function of volume fraction have been developed for a variety of colloidal systems, on which the current model will be based. A model of hard sphere diffusion[16] has been validated by comparison with simulation[14] and experimental[22] results. Functions also exist for repulsive systems[1] and those with weakly attractive interactions.[7] Here, a model is developed to estimate an effective diffusion coefficient, $D_{eff}(q)$ for systems with SALR interactions, specifically those that lead to the formation of a preferred cluster size in equilibrium with monomers. The fundamental assumption is that these populations can be treated independently with a monomer diffusion coefficient, $D_m$, and a cluster diffusion coefficient, $D_c$. Therefore, the $D_{eff}(q)$ extracted from fitting the intermediate scattering function (ISF), $F_S(q,t)$, obtained by NSE experiments with a single exponential function can be related with a weighted average of both monomer and cluster diffusion

$$\begin{aligned} F_S(q,t)/F_S(q,0) &= C\exp[-q^2 t D_{eff}(q)] \\ &= C_m \exp[-q^2 t D_m(q)] + C_c \exp[-q^2 t D_c(q)]. \end{aligned} \tag{A.1}$$

The weighting function is

$$C_i = \phi_i V_i (\Delta\rho_i)^2 P_i(q), \tag{A.2}$$

where $\phi_i$ is the volume fraction, $V_i$ is the volume, $\Delta\rho_i$ is the neutron SLD contrast and $P_i(q)$ is the particle form factor of component $i$ ($i = m$ for monomers and $i = c$ for clusters). Previous simulation studies of SALR systems have shown the cross correlation structure factor between monomers and clusters to be negligible and therefore the term is excluded here for the sake of simplicity.[8] After some simple arithmetic, the derivative is taken with respect to time. In the short-time limit, the exponential functions approach a value of one and the $q$-dependence disappears resulting in a simplified expression under these conditions. The resulting function represents the effective short-time self diffusion in terms of the individual diffusivities of the two components within

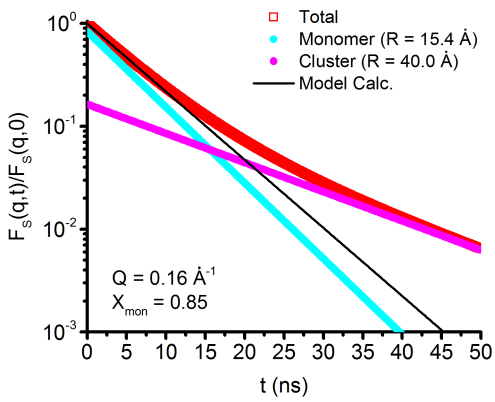


**Figure A.1:** The effective ISF (red squares) for a hypothetical two-component system of HS particles with radii of 1.54 nm (blue circles) and 4 nm (purple circles) is plotted relative to the model of short-time diffusivity (line) of an SALR system of monomers and clusters.

the system

$$D_{eff} = D_m + \frac{A}{1+A}[D_c - D_m], \tag{A.3}$$

where $A = C_c/C_m$. A hypothetical calculation is shown in Fig. A.1 for the given $q$-value, fraction of monomers and two radii of a bimodal system of HS particles shown in the figure along with the corresponding small and large particle correlation functions, the actual effective correlation function and the estimate using Eq. A.3, which is shown to accurately capture the short-time limit.

The expression for Eq. A.3 fits the limits of a monodisperse system of monomers or clusters, as the parameter $A$ approaches zero when no clusters are present and the ratio of $A/(1+A)$ approaches one in the limit of zero monomers. The value of A can be reduced to

$$A = \frac{\phi_c V_c P_c(q)}{\phi_m V_m P_m(q)} = \frac{\phi_c R_c^3 S_C(q,N)}{\phi_m R_m^3}, \tag{A.4}$$

where the internal structure of a cluster of $N$ particles is now contained within the effective hydrodynamic radius of a cluster, $R_c$, and the cluster structure factor, $S_C(q,N)$.

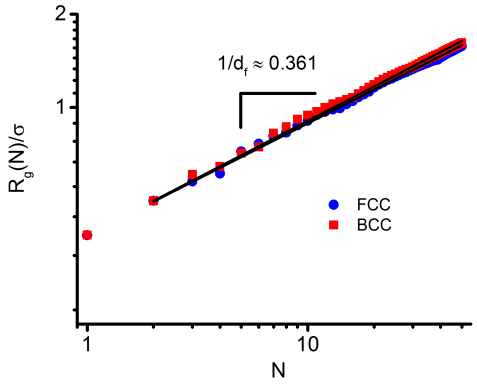


**Figure A.2:** The radii of gyration are plotted as a function of cluster size, $N$, or spherical clusters with FCC (circles) and BCC (squares) crystal structures along with a line representative of the expected power-law for a fractal dimension, $d_f$, of 2.77.

Calculations of $R_c$ are determined as the product of the estimated radius of gyration, $R_g$, and the ratio of hydrodynamic radius, $R_h$, and $R_g$ according to

$$\frac{R_c}{R_0} = \left(\frac{R_h}{R_g}\right)\left(\frac{R_g}{R_0}\right) = \frac{N^{1/d_f}}{\Gamma(2+1/d_f)}, \tag{A.5}$$

where both contributions are functions of fractal dimension, $d_f$. The fractal dimension can be used as a fitting parameter or, if held constant, a representative value of actual cluster structures formed in SALR systems can be used.[23] An example of the power-law relationship between $R_g$ and $N$ used to extract values of $d_f$ is shown in Fig. A.2 for the face-centered and body-centered crystal (FCC and BCC, respectively) structures. The same structures are used to calculate the structure factor contribution, $S_C(q, N)$, to the weighting parameter $A$ as a function of $N$ and $d_f$.

In order to estimate the relative magnitude of monomer and cluster contributions to the signal obtained in NSE experiments, the intensity of the structure factor in the range of $q$-values used to calculate self-diffusion coefficients must be modeled as a function of cluster size (since this is not known *a priori*). The function $S_C(q, N)$ can be averaged within the $q$-range used to extract the short-time self diffusion from NSE

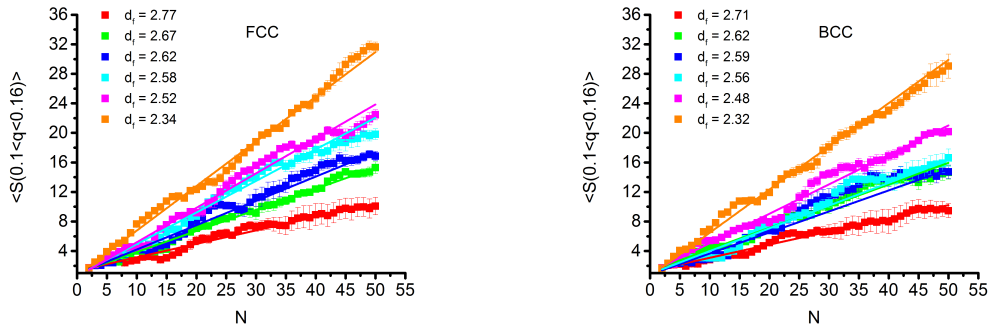


**Figure A.3:** The magnitude of $S(q)$ for an FCC (left) and BCC (right) cluster structure as a function of $N$ and several values of $d_f$.

data ($0.1$ Å$^{-1} < q < 0.16$ Å$^{-1}$) over a range of cluster sizes and fractal dimensions for two crystal matrices. Different values of $d_f$ are obtained by removing particles from inside an initial "perfect" spherical cluster and placing them on corresponding lattice sites on the surface. The trend in the average value of $S(q)$ over this $q$-range is plotted in Fig. A.3 for the FCC and BCC structures as a function of fractal dimension and cluster size.

Each of the lines in Fig. A.3 capture the rate of change in the structure factor intensity as a function of cluster size at each of the fractal dimensions listed. The slopes, $dS/dN$, are then plotted as a function of $d_f$ in Fig. A.4 to allow for tuning the impact of diffusivity on the viscosity by playing with $d_f$. In terms of these parameters, numerical calculations of spherical close packed cluster structures suggest that $S_C(q, N)$ can be approximated by

$$S_C(q, N) = 1 + N(2.88 - 0.98d_f). \tag{A.6}$$

Finally, a representative function of the individual diffusivities must be developed for each of the two components. In the case of a two-component system, as cluster fluids are approximated here, the effective mobility of each species is influenced by the population of both components.[12, 15] Therefore, combinations of previously

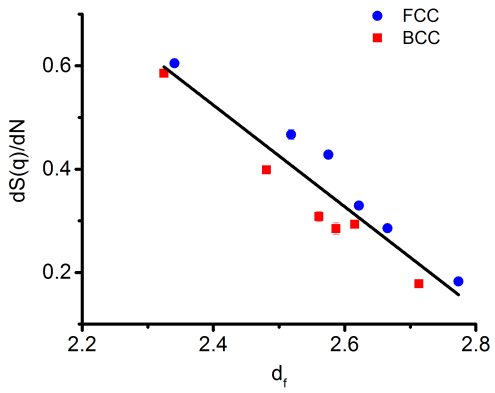


**Figure A.4:** The change in $S(q)$ magnitude with cluster size, $N$, is plotted as a function of fractal dimension for an FCC (circles) and BCC (squares) internal cluster structure and a line of best fit represented by Eq. A.6.

developed Huggins coefficients will be utilized to relate the diffusivity with the volume fraction of each species. Monomer diffusion is estimated according to

$$\frac{D_m}{D_0} = 1 - \phi_m(1.8315 + 0.295/\tau_B) - 0.42\phi_c/(R_c/R_0), \tag{A.7}$$

where the monomer-monomer contribution is a previously developed model for purely attractive particles[7] and the monomer-cluster term is the known first-order $\phi$-dependence of hard sphere excluded volume.[16] While accurately capturing the coupling between these two species would require predicting hydrodynamic mobility functions for the specific ratio of cluster and monomer radii,[11] this rough estimation qualitatively captures the $D_m$–$\phi_c$ dependence. Similarly, cluster diffusion is represented by

$$\frac{D_c}{D_0} = 1 - 2.5\phi_c^{4/3}/(R_c/R_0) - 0.42\phi_m, \tag{A.8}$$

where the contribution from inter-cluster interactions is represented by a function derived for purely repulsive forces,[1] as clusters are expected to interact repulsively.[21] In addition to the excluded volume of the individual particles clusters are composed of, the diffusivity is inversely proportional to the cluster radius according to the Stokes-Einstein relation. With these functions, both the self diffusion and viscosity data can

be fit simultaneously to extract an effective cluster size and population at each solution condition.

### A.3 Modeling the Effect of Competing Interactions on the Viscosity

Theoretical understanding of colloidal suspension viscosity has been well studied, leading to numerous models that accurately account for the effects of concentration, interactions, polydispersity, aspect ratio, etc. An important achievement of these developments is the realization that the viscosity of spherical particles can be decomposed into contributions from hydrodynamic ($\eta_H$), Brownian ($\eta_B$), and inter-particle interactions ($\eta_P$) due to the linearity of stress contributions in the limit of Stokes flow (i.e., low Péclet number).[5] The zero shear viscosity is then a summation of these three contributions:

$$\eta_{r0} = 1 + \eta_H + \eta_B + \eta_P. \tag{A.9}$$

More importantly, by representing the microstructure in terms of statistical mechanical functions, integral equation theory can be used to numerically determine an ensemble average density distribution that can be integrated into the viscosity calculation. Here, the new model builds upon these previous efforts to construct a function for the viscosity of systems with competing interactions, particularly focusing on the impact of cluster formation, developing a functional form for each of the three contributions listed above.

The hydrodynamic contribution is not significantly affected by Brownian motion and is therefore well represented by the high frequency dynamic viscosity. Here, the functional form developed by Lionberger[16] is used:

$$1 + \eta_H = \frac{\eta'_\infty}{\mu} = \frac{1 + 1.5\phi(1 + \phi - 0.189\phi^2)}{1 - \phi(1 + \phi - 0.189\phi^2)}. \tag{A.10}$$

Repulsive interactions are known to reduce the high frequency dynamic viscosity due to the smaller probability of finding particles in contact.[19] Although the combined effect of attraction and repulsion is uncertain, the possibility of forming clusters ensures

a significant population of particles in contact. Therefore, we utilize the hard sphere model.

The Brownian component represents the relative resistance to shear flow from the steady state structure, which arises from both the external and thermodynamic driving forces and the structural relaxation due to thermal motion. Using a statistical mechanical representation of the equilibrium microstructure, the Brownian term is represented by

$$\eta_B = (12/5)(D_0/D_S)\phi^2 g(2), \tag{A.11}$$

where $g(2)$ and $f(2) = 4/3$ are the pair distribution function and equilibrium perturbation function, respectively, at contact and $D_S/D_0$ is the normalized self-diffusion coefficient. Hard sphere models for the self-diffusion coefficient have been explored extensively in the literature, but here we utilize the functional form proposed by Lionberger[16] that accurately approximates simulations by Shikata and Pearson[22]

$$D_S^{HS}/D_0 = (1 - 1.56\phi)(1 - 0.27\phi). \tag{A.12}$$

The hard sphere pair distribution function at contact is well represented by the Carnahan-Starling equation of state[6]

$$g^{HS}(2) = \frac{1 - 0.5\phi}{(1-\phi)^3}. \tag{A.13}$$

Assuming a homogeneous hard sphere fluid under shear, Brady obtained a value for $f(2)$ of 4/3, used here, which corresponds well with the value of 1.43 obtained by solving exact two-body hydrodynamics.[2] Considering the difficulty in estimating the hard sphere value of $f(2)$, doing so for systems with complex interactions is infeasible. Therefore, throughout the remainder of the paper we rely on the hard sphere value of $f(2)$ and replace it with other models when possible.

The contribution from particle interactions is similarly a function of $f(r)$, $g(r)$ and the interaction potential, $U(r)$:

$$\eta_P = -(24/5)(D_0/D_S)\phi^2(\int_1^\infty dU(r)/dr g(r) dr. \tag{A.14}$$

Clearly, this contribution is zero for HS data, which we will see is the cause of the severe discrepancy between the model and the lysozyme data. However, the Brady model compares well with the RWM-MCT model at the volume fractions of interest.

In order to more accurately represent the effect of competing interactions on the zero shear viscosity, the interaction contribution needs to be further decomposed. Specifically, the attractive and repulsive regions of the interaction potential are split in the integration of $\eta_P$

$$\eta_P = -(24/5)(D_0/D_S)\phi^2\left(\int_1^{r_m} dU(r)/dr g(r)dr + \int_{r_m}^{\infty} dU(r)/dr g(r)dr\right), \qquad \text{(A.15)}$$

where $r_m$ is the point of maximum energy in the HSDY potential. The first integrand, which accounts for the attractive portion of the full potential, is accounted for by the KW model.[13] Since attractive interactions produce a microstructure with significant aggregation, the value of $g(2)$ is large compared to a HS fluid. Further, this structure will likely be distorted under flow resulting in a significant perturbation and consequently very different values of $f(2)$ from the HS fluid. Therefore, representing this contribution with a mean field model avoids relying on the severely inaccurate HS value of $f(2)$ for attractive interactions. The resulting form of the model using this representation is

$$\eta_{r0} = (\eta'_\infty/\mu + \eta_B^{HS})(1 + (1.9\phi^2)/\tau_B) + \eta_P^{rep}, \qquad \text{(A.16)}$$

where $\eta_P^{rep}$ incorporates only the second integrand of $\eta_P$. The second purely repulsive integrand is calculated using the parameters extracted from the SANS data. As pointed out by Brady,[5] repulsive systems can be approximated with the HS value of $f(2)$ and an effective particle size accounting for the range of repulsion.

## A.4 Cluster-Cluster Interactions

Due to competing interactions, there is an additional contribution to the viscosity other than the pure two-particle interactions. In particular, the formation of a distribution of cluster sizes will produce a pseudo-multi-component system with effective interactions between these various cluster "species". Further, clusters in SALR

systems are unique in that their stability relies on sufficient repulsion to stabilize their size. Thus, as pointed out previously, clusters will interact with each other by purely repulsive effective interactions.[21] Therefore, these additional interactions can be incorporated into the total viscosity by including additional terms in the $\eta_P^{rep}$ equation. However, previously developed models of polydisperse HS systems require the pair distribution functions for all combinations of species to be known,[15] which for the purposes of this model is impractical. Therefore, the contribution of effective cluster interactions is simplified to a two-component system of monomers and clusters characterized by an average size, $N$, and population $x_c/N$, where $x_c$ is the fraction of particles contained in clusters.

Here we make a quick note on including cluster contributions to the solution viscosity. The distribution of cluster sizes present in clustered fluids is an interpretation of the microstructure. Clusters are a manifestation of the distance defining connectivity. Therefore, a particle will never be in "contact" with a cluster since its proximity will cause it to become a member of that cluster. As the Brownian term represents the contribution of particle mobility and interactions bringing particles in contact, it is appropriate for the Brownian term to keep the functional form of a disperse monomer system in order to accurately account for the equilibrium content of particles in contact.

When including effective cluster interactions, the total repulsive interaction contribution is capture by

$$\begin{aligned}\eta_P^{rep} = -(24/5)(D_0/D_S)\Bigg(&\phi_m^2 \int_{r_m}^{\infty} (dU_{mm}(r))/dr g(r) dr + \\ &\phi_m \phi_c \int_{r_m}^{\infty} (dU_{mc}(r))/dr g(r) dr + \phi_c^2 \int_{r_c}^{\infty} (dU_{cc}(r))/dr g(r) dr\Bigg),\end{aligned} \tag{A.17}$$

where $\phi_m$ and $\phi_c$ are the volume fraction of monomers and clusters, respectively, defined as

$$\begin{aligned}\phi_m &= (1 - x_c)\phi \\ \phi_c &= (x_c \phi)/\phi_n \\ \phi_n &= N[R_0/R(N, d_f)]^3.\end{aligned} \tag{A.18}$$

Here, $\phi_n$ is the volume fraction of particles within a cluster represented as a sphere with an effective radius, $R$, determined according to a representative fractal dimension, $d_f$.

Each interaction is represented by either monomer-monomer interactions, $U_{mm}$, monomer-cluster interactions, $U_{mc}$, or cluster-cluster interactions, $U_{cc}$. Effective monomer-cluster and cluster-cluster interactions can be calculated integrating the two-body HSDY interaction over the effective volume of the cluster(s). The resulting expression for the monomer-cluster interactions is

$$\frac{U_{mc}(r,R)}{kT} = \frac{1}{r}(-(A(z_1,R)K_1e^{-z_1(r-1)} + A(z_2,R)K_2e^{-z_2(r-1)}), \tag{A.19}$$

where the hard sphere definition is left out, and the expression for cluster-cluster interactions is

$$\frac{U_{cc}(r,R)}{kT} = \frac{1}{2\pi r}(-[A(z_1,R)]^2K_1e^{-z_1(r-1)} + [A(z_2,R)]^2K_2e^{-z_2(r-1)}), \tag{A.20}$$

with the function $A(z_i,R)$ defined as

$$A(z_i,R) = \frac{12\phi_n}{z_i^3}\left[(Rz_i+1)e^{-Rz_i} + (Rz_i-1)e^{Rz_i}\right]. \tag{A.21}$$

The integration to arrive at the expressions $U_{mc}$ and $U_{cc}$ assumes a monodisperse sphere that is most closely represented by a spherical close packed structure. Therefore, $\phi_n$ is calculated according to $R/R_0 = N^{1/d_f}$ using a fractal dimension of roughly 2.77.

Figure A.5 demonstrates the characteristic difference between $R/R_0$ and $R_c/R_0$ for a few different cluster structures, indicating that cluster interactions are represented by a smaller, more compact effective sphere (red) compared to cluster diffusivities that are represented by a larger hydrodynamic radius (gold).

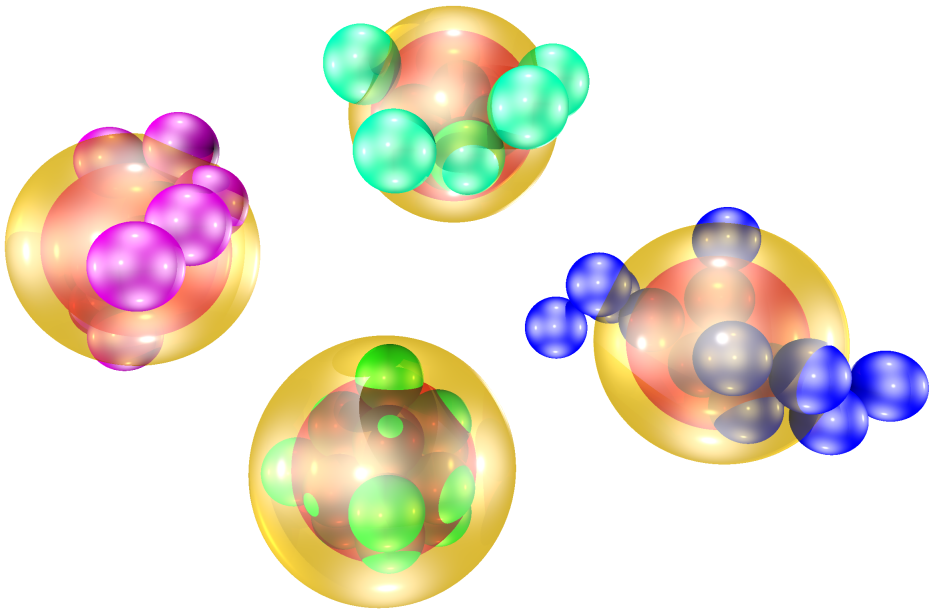

**Figure A.5:** The hydrodynamic (gold) and effective compact cluster (red) radii are represented relative to clusters of 16, 12, 10, and 14 particle (clockwise from bottom). The bottom cluster (green) is a spherical FCC cluster on which the calculations of the effective (red) sphere sizes are partially based. The remaining clusters are characteristic of those expected to form in lysozyme systems, for which the hydrodynamic radii capture the more diffuse structure.

## REFERENCES


[1] Banchio, A. J., and Nägele, G. Short-time transport properties in dense suspensions: from neutral to charge-stabilized colloidal spheres. *J. Chem. Phys. 128*, 10 (Mar. 2008), 104903.

[2] Batchelor, G. K. The effect of Brownian motion on the bulk stress in a suspension of spherical particles. *J. Fluid Mech. 83* (Apr. 1977), 97.

[3] Bergenholtz, J., Brady, J. F., and Vicic, M. The non-Newtonian rheology of dilute colloidal suspensions. *J. Fluid Mech. 456* (Apr. 2002), 239–275.

[4] Bergenholtz, J., and Wagner, N. J. The Huggins Coefficient for the Square-Well Colloidal Fluid. *Ind. Eng. Chem. Res. 33*, 10 (1994), 2391–2397.

[5] Brady, J. F. The rheological behavior of concentrated colloidal dispersions. *J. Chem. Phys. 99*, 1 (1993), 567.

[6] Carnahan, N. F., and Starling, K. E. Equation of State for Nonattracting Rigid Spheres. *J. Chem. Phys. 51*, 2 (1969), 635.

[7] Cichocki, B., and Felderhof, B. U. Diffusion coefficients and effective viscosity of suspensions of sticky hard spheres with hydrodynamic interactions. *J. Chem. Phys. 93*, September (1990), 4427.

[8] Godfrin, P. D., Castañeda Priego, R., Liu, Y., and Wagner, N. J. Intermediate range order and structure in colloidal dispersions with competing interactions. *J. Chem. Phys. 139*, 15 (2013), 154904.

[9] Godfrin, P. D., Hudson, S. D., Hong, K., Porcar, L., Falus, P., Wagner, N. J., and Liu, Y. Excess viscous response from intrinsic structural heterogeneity caused by competing potential features. *Submitt. to Phys. Rev. Lett.* (2015).

[10] Godfrin, P. D., Valadez-Pérez, N. E., Castañeda Priego, R., Wagner, N. J., and Liu, Y. Generalized phase behavior of cluster formation in colloidal dispersions with competing interactions. *Soft Matter 10* (2014), 5061.

[11] Jeffrey, D. J., and Onishi, Y. Calculation of the resistance and mobility functions for two unequal rigid spheres in low-Reynolds-number flow. *J. Fluid Mech. 139* (1984), 261.

[12] Kaplan, P., Yodh, A., and Pine, D. Diffusion and structure in dense binary suspensions. *Phys. Rev. Lett. 68*, 3 (1992), 393–396.

[13] Krishnamurthy, L.-N., and Wagner, N. J. The influence of weak attractive forces on the microstructure and rheology of colloidal dispersions. *J. Rheol. (N. Y. N. Y). 49*, 2 (2005), 475.

[14] Ladd, A. J. C. Hydrodynamic transport coefficients of random dispersions of hard spheres. *J. Chem. Phys. 93*, 5 (1990), 3484.

[15] Lionberger, R. Viscosity of bimodal and polydisperse colloidal suspensions. *Phys. Rev. E 65*, 6 (June 2002), 061408.

[16] Lionberger, R. A., and Russel, W. B. A Smoluchowski theory with simple approximations for hydrodynamic interactions in concentrated dispersions. *J. Rheol. (N. Y. N. Y). 41*, 2 (Mar. 1997), 399.

[17] Lionberger, R. A., and Russel, W. B. Microscopic theories of the rheology of stable colloidal dispersions. *Adv. Chem. Phys. 111* (2000), 399–474.

[18] Liu, Y., Porcar, L., Chen, J., Chen, W.-r., Falus, P., Faraone, A., Fratini, E., Hong, K., and Baglioni, P. Lysozyme protein solution with an intermediate range order structure. *J. Phys. Chem. B 115*, 22 (June 2011), 7238.

[19] Mewis, J., and Wagner, N. J. *Colloidal Suspension Rheology.* Cambridge University Press, New York, 2012.

[20] Porcar, L., Falus, P., Chen, W.-R., Faraone, A., Fratini, E., Hong, K., Baglioni, P., and Liu, Y. Formation of the Dynamic Clusters in Concentrated Lysozyme Protein Solutions. *J. Phys. Chem. Lett. 1*, 1 (Jan. 2010), 126.

[21] Sciortino, F., Mossa, S., Zaccarelli, E., and Tartaglia, P. Equilibrium Cluster Phases and Low-Density Arrested Disordered States: The Role of Short-Range Attraction and Long-Range Repulsion. *Phys. Rev. Lett. 93*, 5 (July 2004), 5.

[22] Shikata, T., and Pearson, D. S. Viscoelastic behavior of concentrated spherical suspensions. *J. Rheol. (N. Y. N. Y). 38*, 3 (May 1994), 601.

[23] Valadez-Pérez, N. E., Castañeda Priego, R., and Liu, Y. Percolation in colloidal systems with competing interactions: the role of long-range repulsion. *RSC Adv. 3* (2013), 25110.

[24] Wagner, N. J., and Woutersen, A. T. J. M. The viscosity of bimodal and polydisperse suspensions of hard spheres in the dilute limit. *J. Fluid Mech. 278* (1994), 267–287.